UNIVERSITY OF CAMBRIDGE

# Dynamical and radiative processes in the Upper Troposphere/Lower Stratosphere

Alison Donna Ming

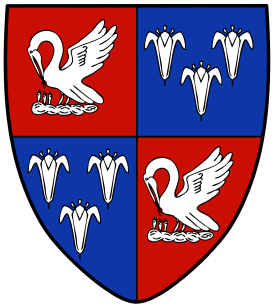

Corpus Christi College

This dissertation is submitted on 30 September 2015 for the degree of Doctor of Philosophy

**Dynamical and radiative processes in the Upper Troposphere/Lower Stratosphere**

*Alison Ming*

# Abstract

The overall aim of this thesis is to gain a better understanding of certain key attributes and processes in the Upper Troposphere/Lower Stratosphere (UTLS). This work involves exploring the interactions between radiation and dynamics which ultimately affect the destination of chemical constituents. A recently identified feature of the extratropical upper troposphere and lower stratosphere is a region of stable air located just above the tropopause known as the tropopause inversion layer (TIL) which appears as a peak in the stratification. The first main chapter of the thesis focuses on elucidating the large scale dynamical mechanisms which lead to the formation of the TIL by exploring the downward influence of the stratosphere on the UTLS region. Model experiments illustrate that the TIL can arise as a result of the dynamics and the wave driving leads to an upwelling structure that results in a TIL. The maximum value and the shape of the TIL peak vary considerable depending on how the observational data is processed. A common method involves averaging with respect to the tropopause. The details of this averaging are found to affect the shape and strength of the TIL. There exist a double peak in the radiative heating (and correspondingly in the upwelling) in the tropical lower stratosphere and radiative calculations reveal that part of it can be considered as imposed. Radiative process are usually thought of as relaxational with waves being regarded as driving the circulation. Idealised model experiments show that imposing a heating leads to an upwelling and the structure of the latter depends on the aspect ratio of the imposed heating. In such experiments, the waves form part of the response. The last core chapter looks at the relatively large annual cycle in temperatures at around 70 hPa in the UTLS. The annual cycle has peak to peak amplitude of about 7 K in observational data. Using radiative experiments that take into account the time evolution of trace gases, the effect of ozone and water vapour on temperatures is quantified. Water vapour is found to play a significant role in this region, especially lower down in the region of the cold point, with important non local influences on temperature. A further set of experiments reveals how the temperatures are affected by the interactions between the dynamics and radiation.

# Declaration

This dissertation is the result of my own work and includes nothing which is the outcome of work done in collaboration except as declared in the Preface and specified in the text. It is not substantially the same as any that I have submitted, or, is being concurrently submitted for a degree or diploma or other qualification at the University of Cambridge or any other University or similar institution except as declared in the Preface and specified in the text. I further state that no substantial part of my dissertation has already been submitted, or, is being concurrently submitted for any such degree, diploma or other qualification at the University of Cambridge or any other University of similar institution except as declared in the Preface and specified in the text.

Alison Donna Ming
February, 2016

# Preface

The work in Chapter 3 follows on from work done towards an MSc degree at the University of Cambridge. In the previous work, the model was set up and the static stability structure investigated. The results in this thesis have since revisited and substantially extended the previous work.

The work in Chapter 4 forms the basis of two accepted papers that are due to be published in the Journal of Atmospheric Sciences [Ming et al. (2016a), Ming et al. (2016b)].

# Acknowledgements

I would to thank my supervisor, Peter Haynes for his patience, insight and guidance through my PhD as well as for the freedom to explore the problems that were of interest to me. Many people have provided valuable help along the way, for which I am grateful.

Fenwick Cooper helped with setting up the model when I first started my PhD and made sure I was suitably afraid of bad statistics. Peter Hitchcock endured the lunchtime conversations where he provided many constructive comments on my results and reiterated the need for good statistics. Amanda Maycock shared her knowledge of radiation codes and the many conversations we had improved my understanding of the complexities of water vapour in the atmosphere.

Various people who are or have been associated with the Atmos-Ocean dynamics group namely, Tom Flannaghan, Emma Boland, Sue Liu, Stephan Fueglistaler, John Taylor, Mike Davey and Megan Stamper also provided support and insight in my work. John Pyle and his group, Amee O'Callaghan and Angus Ferraro all shared an enthusiasm for studying the atmosphere and for climate modelling and I thank them for their interest in my work.

Lorna Ayton and Ewa Karczeweska also contributed to the enjoyment of many cups of tea.

Most importantly, Graeme Morgan was invaluable in getting under brackets aligned in LaTeX and has always supported me throughout my PhD.

I would also like to acknowledge PhD funding from the European Research Council for the ERC project 267760-ACCI.

# Contents

# Chapter 1

## Introduction

As the atmosphere thins out into space with increasing altitude, the pressure decreases but the thermal characteristics, chemical composition and dynamical properties exhibit a complex behaviour. We can divide the atmosphere into five distinct layers bounded by "pauses" at which we see significant changes in these characteristics. The lowermost layer, the troposphere, is where most of the weather occurs. The height of the troposphere varies with latitude and is larger in the tropical regions than at the poles with temperature broadly decreasing with altitude throughout the troposphere. Uneven surface heating by the sun causes convective overturning, and large scale patterns of winds move heat and moisture around the globe. Above the troposphere, in the layer known as the stratosphere, ozone is abundant and water vapour concentrations are low. Ozone heating leads to temperature increasing with height which sets up a stable stratification. The next three layers of the atmosphere are the mesosphere, thermosphere and the exosphere (Figure 1.1); however this thesis will only be concerned with the lower two layers.

The troposphere and stratosphere are separated by a notional boundary known as the tropopause. The region within about 5 km of the tropopause sees a transition between tropospheric and stratospheric properties and is referred to as the Upper Troposphere/Lower Stratosphere (UTLS) region. The UTLS plays a key role in influencing both layers of the atmosphere that it couples. Relatively low temperatures in this region cause it to be particularly sensitive to changes in radiatively active gases, effectively controlling how radiation from the troposphere escapes to space and hence the surface climate. Dynamical variability in the UTLS also modulates atmospheric waves propagating upwards, transferring momentum and energy from the surface and the troposphere to the region above. These waves provide a torque to

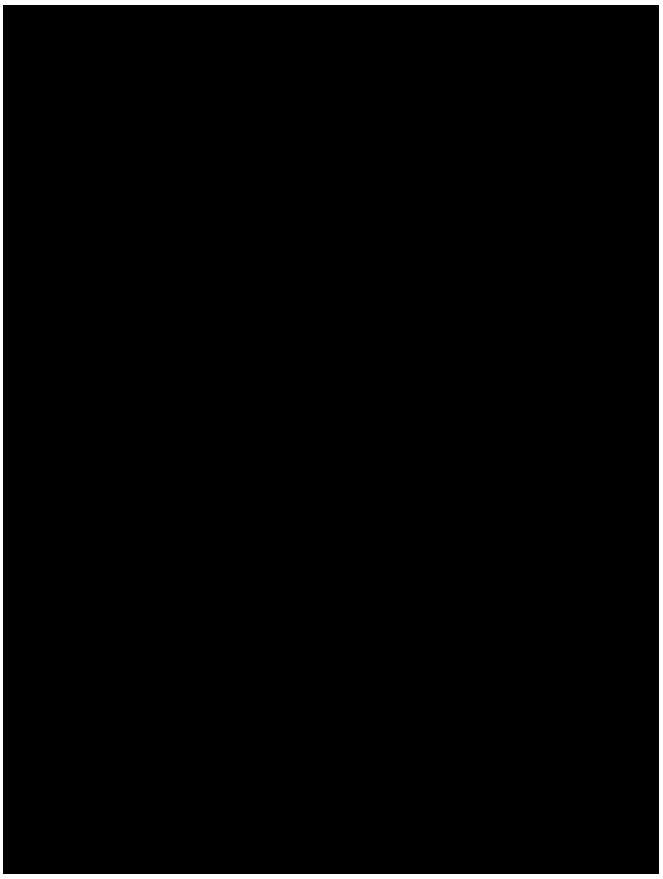

**Figure 1.1:** [From Brasseur et al. (1999)] Vertical profile of the temperature between the surface and 100 km altitude as as defined in the U.S. Standard Atmosphere (1976) and related atmosphere layers.

the stratosphere that drives a slow persistent equator to pole circulation. In addition, stratosphere–troposphere exchange across the tropopause impacts the chemistry in both the troposphere and the stratosphere. This strong connectivity between radiative, dynamical, chemical and microphysical processes in the UTLS make it highly sensitive to climate change. Gettelman et al. (2011) review the upper troposphere and lower stratosphere region in the extratropics whilst Fueglistaler et al. (2009a) and more recently Randel and Jensen (2013) look at the tropics. An overview of the transport processes in the stratosphere can be found in Shepherd (2007). Figure 1.2, taken from the Gettelman et al. (2011) review paper illustrates some of the main processes in the UTLS region.

The central aim of this thesis is to gain a better understanding of processes in the UTLS by looking at various large scale features of this region. This is achieved using observational data, radiative calculations and idealised general circulation models which are described in Chapter 2. The vertical temperature structure affects atmo-

**Figure 1.2:** [From Gettelman et al. (2011)] Schematic snapshot of the extratropical UTLS using data from a Northern Hemisphere section along 60° W longitude on 15 February 2006. Wind contours (solid black lines 10 m s$^{-1}$ interval), potential temperature surfaces (dashed black lines), thermal tropopause (red dots), and potential vorticity surface (2 PVU: light blue solid line). Illustrated schematically are the extratropical UTLS (dark and light blue shading), extratropical transition layer (dark blue shading), clouds and fronts (gray shading), static stability contours in the TIL (green shading), quasiisentropic exchange (red wavy arrows), crossisentropic exchange (orange wavy arrows), and the BrewerDobson Circulation (deep, red solid outline; shallow, dotted solid outline).

spheric motions on a wide range of length scales. The temperature stratification is measured by the static stability. This is often defined as a buoyancy frequency, $N$, which is the frequency of the vertical oscillation of a parcel of air displaced from equilibrium adiabatically when the atmosphere is stably stratified. The troposphere in the extratropics is dominated by moist convection and baroclinic eddies and has typical values of $N^2 \approx 1 \times 10^{-4}\,\mathrm{s}^{-2}$. In contrast, the stratosphere sees typical values of $N^2 \approx 5 \times 10^{-4}\,\mathrm{s}^{-2}$. A recently identified feature of the extratropical upper troposphere and lower stratosphere is a region of stable air located just above the tropopause known as the tropopause inversion layer (TIL), as discussed in Birner (2006), Grise et al. (2010) and references therein. The TIL appears as a peak in the stratification with values of $N^2 \approx 7 \times 10^{-4}\,\mathrm{s}^{-2}$ in an annual average. The maximum value of the static stability and the shape of the TIL peak vary considerable depending on how the observational data is processed. Tropopause height variations with time cause the location of the TIL to change and simple averaging leads to a smearing out of the peak. To account for this, Birner (2006) proposed a method of averaging with respect to the tropopause which gives a TIL with a very sharp static stability transition at

the tropopause. Whilst this method does indeed make the TIL peak more prominent, waves propagating through the atmosphere do not see static stability values obtained from tropopause based compositing. Buoyancy is the dominant restoring force for vertical motions and atmospheric waves such as Rossby waves and gravity waves are affected by the fine scale features of the static stability field. Chapter 3 focuses on elucidating the mechanisms that could be responsible by exploring the downward influence of the stratosphere on the UTLS region. We also look at the effects of tropopause based averaging on the shape and strength of the TIL.

Waves impart a force on the mean flow either via the transient local growth and decay of the waves or through processes that generate and dissipate them. The waves drive a stratospheric circulation by pumping air polewards and, in the steady state, have a downward influence on vertical velocities. This process has been widely studied in the literature (e.g. Haynes et al. (1991), Holton et al. (1995)) and is described in more detail in the following section. The notion that the stratospheric wave forcing can be seen as prescribed is widely used and is a reasonable assumption in the extratropics where the wave induced transport of angular momentum is from Rossby waves and internal gravity waves generated non-locally in the troposphere. Considerable attention is devoted to how the wave driving is expected to change with climate change and consistent evidence from a range of current climate models seems to point to a strengthening of the stratospheric circulation [Butchart et al. (2010a)].

As we move closer to the equator, the downward influence of the stratosphere becomes less well defined. The timescale to reach a steady state gets longer and non-linear effects become important. The spatial distribution of the forcing depends on the structure of the mean flow. Far from the equator, the force can be assumed to cause a negligible change to the mean flow. Haynes (1998) showed that as the equator is approached, the force must directly drive a mean flow change leading to a non-linear problem. Moreover, with frictional relaxation, one can have a thin equatorial region where a meridional circulation is sustained without a wave forcing [Plumb and Eluszkiewicz (1999)]. Chapter 4 looks more closely at the constraints on the temperature around the tropical region and the consequences for the upwelling. We also challenge the accepted view that the wave driving in the stratosphere can be always be regarded as a specified forcing. In particular, we look at situations where the diabatic heating can be considered as given and investigate the processes that control the structure and strength of upwelling in the tropical lower stratosphere. The work in this chapter was done in collaboration with Dr. Peter Hitchcock who was closely involved in the interpretation of the results as well as developing the theory.

Chapter 5 looks at another aspect of the tropical lower stratosphere which is the relatively large annual cycle in temperatures at around 70 hPa in the UTLS. The annual cycle has peak to peak amplitude of about 7 K in observational data and recent work has speculated that a significant contribution to the temperature cycle could come from the ozone annual cycle [Fueglistaler et al. (2011)]. We build on this work and discuss the possible radiative influences of the major trace gases, ozone, water vapour and carbon dioxide, on temperature in the context of the seasonal cycle. We also design a framework of experiments where the radiative effects, zonally symmetric dynamics and eddy effects are decoupled and their influences on temperature studied independently. The radiation code was set up with the help of Dr. Amanda Maycock and conversations with Drs. Amanda Maycock and Peter Hitchcock have been key in helping me form an understanding of the radiative interactions.

The remainder of this chapter gives a more detailed description of the dynamics and radiative processes in the atmosphere and introduces the tools needed to study the various problems. More details of both the dynamical and radiative processes can be found in Andrews et al. (1987).

## 1.1 Stratospheric circulation

The main entrance pathway of air into the stratosphere from the troposphere occurs via tropical upwelling. The air is subsequently pumped polewards and returned to the troposphere at high latitudes. This slow circulation is known as the Brewer–Dobson circulation after Brewer who first described its existence [Brewer (1949)] and Dobson who suggested that such a circulation might exist based on ozone measurements [Dobson et al. (1929)]. Brewer was investigating why high altitude aircraft left condensation trails. He noticed that no trails formed in the stratosphere in the extratropics. By obtaining measurements of temperature and frost point, Brewer realised that stratospheric air is exceptionally dry and came up with a prediction that the air must be dehydrated before entering the stratosphere. The only region cold enough for this to happen is the tropical lower stratosphere. Dobson observed low ozone concentrations over the tropics and high ozone in the Arctic in spring and reconciled these observations by suggesting a slow poleward drift of air.

Whilst there is little debate as to the existence of a stratospheric circulation, questions remain regarding the precise mechanisms in operation, especially in the tropics. In the extratropics, the time mean meridionally averaged circulation can be understood

as a consequence of the action of wave forces on the meridional circulation and is encapsulated in the "downward control" principle [Haynes et al. (1991)] described in more detail below. The downwelling through a certain level is controlled purely by the distribution of wave drag above that level and not by heating. In the stratosphere, the wave forcing arises from the waves that propagate upwards from the troposphere and break in the middle atmosphere [Holton et al. (1995)].

## 1.2 Dynamical tools

### 1.2.1 Transformed Eulerian Mean framework

The equations of motion for a gas in a rotating frame can be simplified by making various assumptions detailed in Andrews et al. (1987) to give a form useful for application to large and medium scale meteorological phenomena. These equations related to momentum balance in the zonal and meridional directions, hydrostatic balance in the vertical, continuity of mass and the material advection of potential temperature. The horizontal spherical coordinates are the latitude, $\phi$, and longitude, $\lambda$, and the vertical coordinate is a log–pressure altitude given by $z = -H\,\log(p/p_s)$ where $p$ is the pressure, $p_s = 1000\,\mathrm{hPa}$ and $H$ is a scale height taken to be $7\,\mathrm{km}$ in this work. The potential temperature, $\theta$, is related to the temperature, $T$, by $\theta = T\,\left(\frac{p_s}{p}\right)^{\kappa} = T\,\sigma^{-\kappa}$ where $\kappa = R/c_p = 2/7$ or the ratio of the gas constant ($R = 287\,\mathrm{J\,K^{-1}kg^{-1}}$) to the specific heat capacity at constant pressure. Neglecting the horizontal component of the Coriolis force and friction, the primitive equations that govern the evolution of the wind field, $(u, v, w)$, the potential temperature and the geopotential height, $\Phi$, are given by

$$\frac{\mathrm{D}u}{\mathrm{D}t} - \left(f + \frac{u\,\tan\phi}{a}\right) v + \frac{\Phi_\lambda}{a\,\cos\phi} = X, \tag{1.1}$$

$$\frac{\mathrm{D}v}{\mathrm{D}t} - \left(f + \frac{u\,\tan\phi}{a}\right) v + \frac{\Phi_\phi}{a} = Y, \tag{1.2}$$

$$\Phi_z = \frac{R}{H}\,\theta\,\exp(-\frac{\kappa\,z}{H}), \tag{1.3}$$

$$\frac{1}{a\,\cos\phi}\,\left(u_\lambda + (v\,\cos\phi)_\phi\right) + \frac{1}{\rho_0}\,(\rho_0\,w)_z = 0, \tag{1.4}$$

$$\frac{\mathrm{D}\theta}{\mathrm{D}t} = Q, \tag{1.5}$$

where $X$ and $Y$ represent unspecified horizontal components of friction or other non conservative mechanical forcing.

The geopotential height is defined as $d\,\Phi/d\,z^* = g$ where $z^*$ is the geometric height and $g$ is the acceleration due to gravity. The Coriolis parameter, $f = 2\,\Omega\,\sin\phi$ where $\Omega$ is the rotation rate of the Earth. $D/Dt$ is the material derivative following fluid motion. $\rho_0$ is the background density given by $\rho_0 = \rho_s\,\exp(-z/H)$ and $\rho_s$ can be found from the surface temperature and pressure using the ideal gas law. Finally, $Q$ is a diabatic heating rate.

Atmospheric processes can be regarded as involving the interaction of a zonal mean flow with disturbances superimposed. For a variable, $M$, the departure from the zonal mean, $\overline{M}$, is given by

$$M' = M - \overline{M}.$$

The Eulerian mean equations are obtained by separating each variable into a zonal and a disturbance part and substituting into the primitive equations and zonally averaging. These comprise a closed set of equations for predicting the time evolution of the zonal mean flow and contain zonally averaged terms of the form $\overline{M}$ and eddy terms of the form $\overline{M'\,N'}$ where $N$ is a different variable. For example, $\overline{v'\,u'}$ represents an eddy momentum flux and $\overline{v'\,\theta'}$ is an eddy heat flux.

It is convenient to then transform these equations to a different form which makes it easier to anticipate how the zonal mean flow will respond to these eddy terms. The approach is to define a residual mean meridional circulation $(0, \overline{v}^*, \overline{w}^*)$,

$$\overline{v}^* = \overline{v} - \frac{1}{\rho_0}\left(\rho_0\,\frac{\overline{v'\,\theta'}}{\overline{\theta}_z}\right)_z, \tag{1.6a}$$

$$\overline{w}^* = \overline{w} + \frac{1}{a\cos\phi}\left(\cos\phi\,\frac{\overline{v'\,\theta'}}{\overline{\theta}_z}\right)_\phi, \tag{1.6b}$$

such that the effect of eddies enters only in the longitudinal momentum equation through a wave forcing term, $\nabla\cdot\mathbf{F}$, the divergence of the Eliassen–Palm flux (EP flux).

The resulting equations are referred to as the transformed Eulerian mean (TEM)

equations and are

$$\partial_t \overline{u} + \frac{1}{a\,\cos\,\phi}\,\overline{v}^*\,\partial_\phi\,(\overline{u}\,\cos\,\phi) + \overline{w}^*\,\partial_z \overline{u} - f\,\overline{v}^* = \frac{1}{\rho_0\,a\,\cos\,\phi}\nabla\cdot\vec{F} + \overline{X} \tag{1.7a}$$

$$f\,\partial_z \overline{u} + \frac{2\,\tan\,\phi}{a}\overline{u}\,\partial_z \overline{u} + \frac{R}{H}\,\frac{1}{a}\,e^{\frac{-\kappa\,z}{H}}\partial_\phi \overline{\theta} = G \tag{1.7b}$$

$$\frac{1}{a\,\cos\,\phi}\,\partial_\phi\,(\overline{v}^*\,\cos\,\phi) + \frac{1}{\rho_0}\,\partial_z\,(\rho_0 \overline{w}^*) = 0 \tag{1.7c}$$

$$\frac{1}{a}\,\overline{v}^*\,\partial_\phi \overline{\phi} + \overline{w}^*\,\partial_z \overline{\theta} = \overline{Q} - \frac{1}{\rho_0}\partial_z\left[\rho_0\,\left(\overline{v'\,\theta'}\,\frac{\overline{\theta}_\phi}{a\,\overline{\theta}_z} + \overline{w'\,\theta'}\right)\right], \tag{1.7d}$$

where $G$ represents all the components that cause a departure from gradient wind balance between $\overline{u}$ and $\overline{\theta}$. This term is generally small in meteorological application and is often neglected.

The components of the vector $\mathbf{F} = (0, F^\phi, F^z)$ and $\nabla\cdot\mathbf{F}$ for spherical log–pressure coordinates are

$$F^\phi \;=\; \rho_0\,a\cos\phi\,\left(\overline{u}_z\,\frac{\overline{v'\,\theta'}}{\overline{\theta}_z} \;-\; \overline{v'\,u'}\right), \tag{1.8a}$$

$$F^z \;=\; \rho_0\,a\cos\phi\,\left[\left(f \;-\; \frac{1}{a\cos\phi}\,(\overline{u}\cos\phi)_\phi\right)\,\frac{\overline{v'\,u'}}{\overline{\theta}_z} \;-\; \overline{w'\,u'}\right], \tag{1.8b}$$

$$\nabla\cdot\mathbf{F} \;=\; \frac{1}{a\cos\phi}\,\frac{\partial}{\partial\phi}(F^\phi\cos\phi) \;+\; \frac{\partial F^z}{\partial z}. \tag{1.8c}$$

Tropical stratospheric air enters the lower stratosphere via the tropical tropopause, is transported poleward to the extratropics, and descends into the troposphere. The rapid rotation rate of the Earth means that the angular momentum per unit mass of the atmosphere is dominated by the rotation and only weakly affected by air motions relative the surface. Surfaces of constant angular momentum are roughly vertical in the extratropics and any poleward mean flow has to cross those surfaces. Changing the angular momentum of parcels of air requires the existence in the atmosphere of an eddy–induced mean zonal force, $\nabla\cdot\mathbf{F}$. The forcing can be associated with dissipative eddy processes such gravity and Rossby waves breaking. If this torque on the atmosphere were to be switched off [Haynes et al. (1991) and references therein], the circulation would die down and temperatures would relax towards their radiative equilibrium values [Fels (1985)]. Where the circulation pushes air parcels downwards in the high latitudes, temperatures are driven above their radiative equilibrium values by adiabatic warming and conversely in the tropical stratosphere, the air parcels being

pulled up results in adiabatic cooling.

### 1.2.2 Downward control principle

The mean residual vertical velocity at a given height can be related to the forcing above that level and forms the basis for the downward control principle. This follows from the TEM equations and the method used in Haynes et al. (1991) will be briefly repeated here.

The zonal momentum TEM equation in $(\phi,\, z)$ coordinates has the form

$$\frac{\partial \overline{u}}{\partial t} \,+\, \overline{v}^* \left[\frac{1}{a\cos\phi}\frac{\partial}{\partial\phi}\left(\overline{u}\cos\phi\right) \,-\, 2\,\Omega\sin\phi\right] \,+\, \overline{w}^*\,\frac{\partial \overline{u}}{\partial z} \,=\, \frac{1}{\rho_0\, a\cos\phi}\,\nabla\cdot\mathbf{F}, \qquad (1.9)$$

where $a$ is the radius of the Earth and $\Omega$ is the rotation rate.

The mass continuity equation is

$$\frac{1}{a\cos\phi}\frac{\partial}{\partial\phi}\left(\overline{v}^*\cos\phi\right) \,+\, \frac{1}{\rho_0}\,\frac{\partial}{\partial z}\left(\rho_0\,\overline{w}^*\right) \,=\, 0. \qquad (1.10)$$

The mean residual velocities can be written in terms of a streamfunction, $\psi(\phi, z)$, as

$$\overline{v}^* \,=\, -\,\frac{1}{\rho_0\,\cos\phi}\,\frac{\partial\psi^*}{\partial z}, \quad \overline{w}^* \,=\, \frac{1}{a\,\rho_0\,\cos\phi}\,\frac{\partial\psi^*}{\partial\phi}. \qquad (1.11)$$

In the steady state, the momentum equation (Equation 1.9) can be written in terms of the streamfunction as

$$\frac{\partial(\psi,\overline{m})}{\partial(\psi,z)} \,=\, \frac{\partial\psi}{\partial\phi}\,\frac{\partial\overline{m}}{\partial z} \,-\, \frac{\partial\psi}{\partial z}\,\frac{\partial\overline{m}}{\partial\phi} \,=\, a\cos\phi\,\nabla\cdot\mathbf{F}, \qquad (1.12)$$

where $\overline{m} = a\cos\phi\,(\overline{u} + a\,\Omega\cos\phi)$, the angular momentum per unit mass.

Dividing throughout by $\overline{m}_\phi = \partial(\overline{m}, z)/\partial\phi, z$ in Equation 1.12 gives

$$\frac{\partial(\psi,\overline{m})}{\partial(\overline{m},z)} \,=\, \frac{a\cos\phi\,\nabla\cdot\mathbf{F}}{\overline{m}_\phi}. \qquad (1.13)$$

The term on the left of Equation 1.13 is equal to $-\,(\partial\psi/\partial z)|_{\overline{m}}$ where the derivative is along a line of constant $\overline{m}$. This equation can be integrated to give the streamfunction

in terms of the divergence of the Eliassen–Palm flux,

$$\psi^* = \int_z^\infty \left. \frac{a \cos\phi \nabla \cdot \mathbf{F}}{\overline{m}_\phi} \right|_{\phi=\phi(z')} \mathrm{d}z'. \tag{1.14}$$

The constant of integration is fixed using the convention that $\psi \to \infty$ and the requirement that $\rho_0 \overline{w}^* \to 0$ as $z \to 0$. Using Equation 1.11, we can deduce that

$$\overline{w(z)}^* = \frac{1}{\rho_0(z) \cos\phi} \frac{\partial}{\partial\phi} \left[ \int_z^\infty \left. \frac{\cos\phi \nabla \cdot \mathbf{F}}{\overline{m}_\phi} \right|_{\phi=\phi(z')} \mathrm{d}z' \right].$$

In the midlatitudes, the angular momentum contours are nearly vertical (Figure 1.3) and it is convenient to do the integral at constant latitude using the quasi–geostrophic limit where $|\overline{u}| \ll 2\,\Omega\,a\,|\sin\phi|$.

**Figure 1.3:** [Figure 1 from Haynes et al. (1991)] Zonally averaged absolute angular momentum distribution in the middle atmosphere for January, April, July and October in units of $6.4 \times 7\,\mathrm{m^2\,s^{-2}}$. Calculated from the zonal wind fields in Marks (1989)

Hence $\overline{m}_\phi \simeq -2\,\Omega\,a^2 \sin\phi \cos\phi$. The downward control equation can be written as

$$\overline{w(z)}^* = \frac{1}{a\,\rho_0(z) \cos\phi} \frac{\partial}{\partial\phi} \left[ \int_z^\infty \left. \frac{\nabla \cdot \mathbf{F}}{2\,a\,\Omega \sin\phi} \right|_{\phi=\text{const.}} \mathrm{d}z' \right]. \tag{1.15}$$

Holton et al. (1995) performed a set of idealized numerical experiments on the response of the mean stratospheric zonally symmetric circulation to a westward force which

has a sinusoidal time dependence with a frequency of $\sigma$. The diabatic heating in the atmosphere can be split into a shortwave term and a longwave term. The longwave heating is essentially relaxational and can be written as $-\alpha T$ where $\alpha$ is the radiative relaxation rate. The response, shown in Figure 1.4, depends on the ratio of $\sigma$ to $\alpha$. As $\sigma/\alpha \to 0$, the steady state limit applies and the vertical velocity through a given pressure level at a given latitude is entirely determined by the applied force above that that region.

Scott (2002) showed that the interaction between the transient parts of the meridional circulation and the angular momentum, $m$, gives rise to a set of additional terms. The numerator in the integral in Equation 1.15 can be modified to $a\,\rho\,\cos\phi\,\nabla\cdot\mathbf{F}+\mathbf{J}$ where $\mathbf{J}=\left\langle\overline{v^*}'\,\partial_y\overline{u}'\right\rangle\;+\;\left\langle\overline{w^*}'\,\partial_z\overline{u}'\right\rangle$. Angle brackets denote time averages and primes denote the deviations from the time average.

Applying the downward control principle to the tropics becomes problematic as the zonal wind distribution allows for the possibility of closed angular momentum contours. It is then possible for a closed meridional circulation to exist along the closed contours without the need for wave driving. Conservation of mass on any pressure level dictates that there must be upwelling in the tropics to compensate for the persistent downwelling seen in the extratropics and this is indeed seen in observational data. We will return to this problem in Chapter 4.

### 1.2.3 Potential vorticity

Another quantity of considerable dynamical interest is Ertel's potential vorticity (PV). PV is a scalar materially conserved quantity in a stratified, rotating, inviscid and adiabatic flow. Material conservation follows from the Kelvin circulation theorem [Batchelor (2000)]. PV is a particularly important quantity for understanding balanced flows and is a fundamentally local quantity, yet coupled with the invertibility principle, knowledge of a PV field can be used to determine other dynamical fields such as the wind speeds provided the distribution of potential temperature at the surface and the mass distribution in the atmosphere is known [McIntyre (2003), Hoskins et al. (1985)]. PV is usually given in units of PVU where $1\,\mathrm{PVU}=10^6\,\mathrm{K\,m^2\,kg^{-1}\,s^{-1}}$.

PV can be defined in several ways, one of which is Ertel's formula [Hoskins et al.

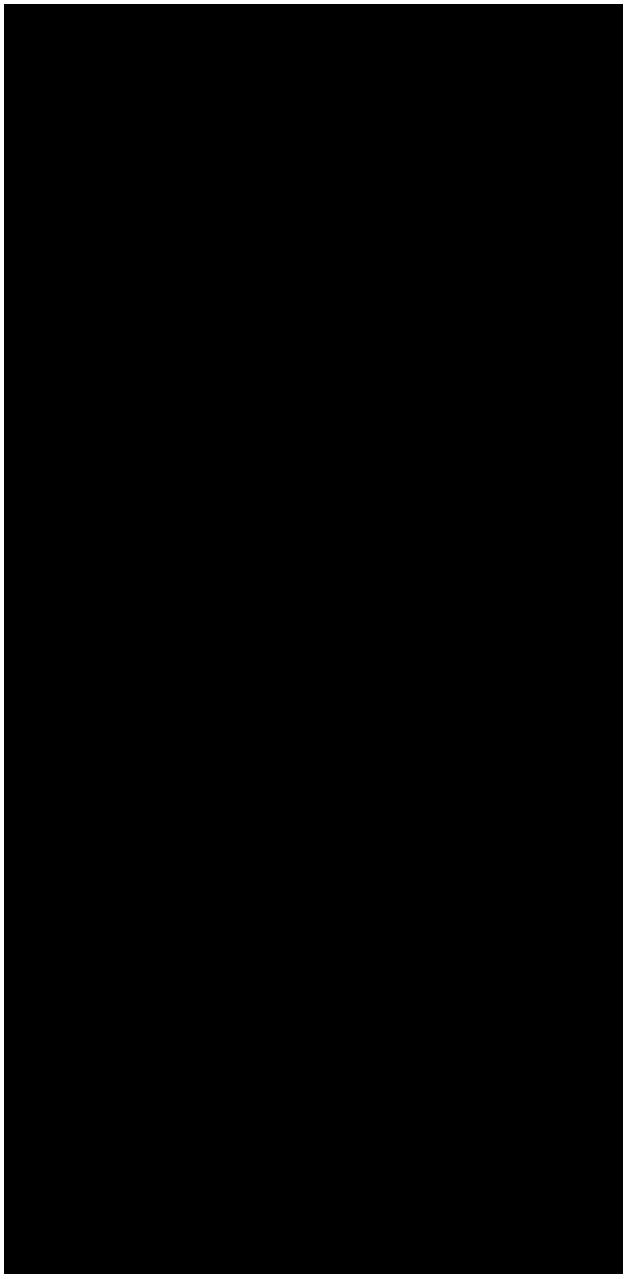

**Figure 1.4:** [Holton et al. (1995)] Idealized numerical experiments on the meridional circulation response of the stratosphere to a longitudinally symmetric westward force applied in the shaded region. Contours are streamlines, with the same contour interval used in each panel (and corresponding to a given mass flux). (a) Adiabatic response for $\sigma/\alpha \gg 1$. A smaller contour interval in this case would shown opposite signed circulation cell above the shaded region and extension of the lower circulation cell well into the opposite hemisphere. (b) Response for $\sigma/\alpha \simeq 0.34$, corresponding to annual frequency and 20 day radiative damping timescale; the solid and dashed contours show the response that is respectively in phase and 90° out of phase with the forcing. (c) Steady state response ($\sigma/\alpha \ll 1$,). Note that the magnitude of the response in the mass stream function increases as $\sigma/\alpha$ decreases and that it is given qualitatively by Equation 1.8 for (c). The model is unbounded below so the ordinate has arbitrary origin.

(1985)] which in a rotating reference frame is given by

$$PV = \frac{\boldsymbol{\zeta}^a \cdot \boldsymbol{\nabla}\theta}{\rho} = \frac{(\boldsymbol{\zeta}^r + 2\boldsymbol{\Omega}) \cdot \boldsymbol{\nabla}\theta}{\rho}, \tag{1.16}$$

where,

$\boldsymbol{\zeta}^r$ = relative vorticity vector, $\theta$ = potential temperature,
$\boldsymbol{\Omega}$ = angular velocity of the rotating frame, $\rho$ = density.

Material conservation of PV can be written as

$$\frac{\mathrm{D}[PV]}{\mathrm{D}t} = \left[\frac{\partial}{\partial t} + \boldsymbol{u} \cdot \nabla\right](PV) = 0,$$

where $t$ is time and $\boldsymbol{u}$ is a velocity vector.

## 1.3 Radiative transfer

Radiative transfer in the atmosphere refers to the process by which electromagnetic radiation is exchanged between different regions of the atmosphere and is often taken to happen vertically in a column since the distance a photon has to travel to encounter a significant temperature change is much shorter in the vertical than the horizontal. Short-wave (SW) radiation (wavelengths of less than 4 $\mu$m) from the Sun, is incident on Earth and subsequently absorbed, emitted and scattered by the various gases and particles in the atmosphere and the surface. The photons that are emitted from the surface and the atmosphere have a longer wavelength than 4 $\mu$m and make up longwave (LW) radiation. LW radiation has a strong temperature dependence. The major radiatively active trace gases in the lower two layers of the atmosphere are carbon dioxide, water vapour and ozone. Figure 1.5 shows a plot of the solar spectrum and the main regions where the radiation interacts with the major trace gases. The resulting vertical distribution of heating due to the longwave and shortwave components of some important trace gases is shown in Figure 1.6

In the stratosphere, the net diabatic heating rate is a result of the imbalance between the local absorption of SW and radiative heat loss. As detailed in Dickinson (1973), the local exchange of photons around a region of the atmosphere can be neglected and the heat loss is dominated by a cooling to space term. If dynamical disturbances to the temperature are sufficiently small, the Planck function can be linearized such that

**Figure 1.5:** [From Fu (2003)] Solar spectrum at the top of the atmosphere and at the surface for a solar zenith angle of 60° in a clear atmosphere. Absorption and scattering regions are indicated.

**Figure 1.6:** [From Andrews et al. (1987)] Vertical distribution of heating due to the absorption of solar radiation (right) and cooling due to the emission of infrared radiation (left) in units of $\mathrm{K\,day^{-1}}$.

the heating is a linear function of the local temperature. Moreover, carbon dioxide is the main emitter in the stratosphere and is well mixed which justifies using the

temperature as a measure of heating rates and neglecting variations in constituents. Hence, the longwave cooling term can be approximated as a linear damping with a coefficient that varies in space and time. This is known as the Newtonian cooling approximation. These approximations do not hold in the troposphere where the abundance of water vapour and its condensed states mean that local exchange terms become important. The impact of the major trace gases, ozone and water vapour, on temperatures in the tropical UTLS will be studied further in Chapter 5.

A very brief overview of radiative transfer will now follow; detailed descriptions may be found in Goody and Yung (1989) and Andrews et al. (1987). The change in intensity as a result of the interaction between radiation and matter can be summed up in the equation of radiative transfer, Equation 1.17, first given in this form by Schwarzschild:

$$\frac{\mathrm{d}I_\nu(\hat{\mathbf{\Omega}})}{\mathrm{d}s} = -\kappa_\nu \, \rho_a \, [I_\nu(\hat{\mathbf{\Omega}})) \; - \; J_\nu(\hat{\mathbf{\Omega}}))]. \tag{1.17}$$

This equation represents the rate of change of the intensity, $I_\nu$, of a monochromatic beam of frequency $\nu$ along a length element $\mathrm{d}s$ in the direction $\hat{\mathbf{\Omega}}$. $\rho_a$ is the density of the radiatively active gas and $\kappa_\nu$ is the extinction coefficient. $\kappa_\nu$ can be written as the sum of an absorption coefficient and a scattering coefficient. The last quantity in the equation, $J_\nu$ is a source function of the radiation. Scattering of radiation contributes to the source function. The source function is made up of thermal emission from the gas which is isotropic and the scattering contribution which depends on the angular distribution of the scattered radiation. For a gas in local thermal equilibrium (LTE) with no scattering, the source function is equal to the Planck function. Local thermal equilibrium holds in the atmosphere for the important radiatively active gases for pressures greater than about 0.1 hPa where the velocities of the molecules are distributed according to a Maxwell–Boltzman distribution. With scattering, the source function is a combination of the Planck function, $B_\nu(T)$, and the intensity integrated over all incident angles for the scattered photons. The Planck function is dependent on the local temperature, $T$.

Due to the aspect ratio of the atmosphere, we can make two approximations to the radiative transfer theory. Firstly, we assume that the curvature of the level surfaces from the sphericity of the Earth is negligible. Secondly, radiative properties of the medium depend only on the vertical coordinate. These form the plane–parallel atmosphere approximation and the net flux is vertical. It is convenient to express the angular dependence of the intensity in terms of polar coordinates $(\theta, \phi)$ so that $\theta$ is the zenith angle (measured from the vertical). The intensity is independent of $\phi$. The

upward and downward flux densities for each wavenumber are given by:

$$F^{\uparrow}(z)_{\nu} = 2\pi \int_0^{\frac{\pi}{2}} I_{\nu}(\theta, z) \cos\theta \sin\theta \, \mathrm{d}\theta, \quad F^{\downarrow}(z)_{\nu} = 2\pi \int_{\pi}^{\frac{\pi}{2}} I_{\nu}(\theta, z) \cos\theta \sin\theta \, \mathrm{d}\theta, \tag{1.18}$$

where $z$ is the vertical coordinate.

Under the assumptions of LTE and a plane parallel atmosphere, $I_{\nu}$ can be expressed in terms of a transmittance function, $\mathcal{T}_{\nu}$:

$$I_{\nu}(z) = I_{\nu}(0) + \int_0^z B_{\nu}(T(z')) \frac{\mathrm{d}\mathcal{T}_{\nu}(z, z')}{\mathrm{d}z'} \, \mathrm{d}z', \tag{1.19}$$

Radiation codes for the atmosphere aim to estimate the transmittance function efficiently and various methods are used to do this:

- Line by line codes: These are the most accurate method of estimating the transmittance and involve explicitly calculating the contribution from each spectral line to the absorption.
- Band models: The average transmittance over a band of spectral values is estimated by making assumptions about the Planck function over each spectral interval. Band models are faster than line by line codes.
- Correlated–k method: By grouping spectral intervals with similar absorption coefficients, the number of times similar radiative transfer equations have to be solved can be reduced. This method is computationally fast with accuracies comparable to line by line codes [Lacis and Oinas (1991)].

The last two types of radiation codes will be used in this thesis.

# Chapter 2

## Data and Methods

A brief description of the datasets and models used throughout this thesis is included in this short chapter.

## 2.1 ERA-Interim data

By optimally combining atmospheric observational data with a climate model, one can obtain a global numerical description of the climate known as a reanalysis dataset. Data that is assimilated in the model would typically come from a variety of sources such as satellite observations, radiosonde, ground based weather stations and aircraft measurements. The data often has sparse coverage and rarely spans the whole time period. In this thesis, we make use of the ECMWF ERA-Interim reanalysis dataset [Dee et al. (2011)] which includes a number of atmospheric fields output on different grids from 1979 onwards and is a widely used reanalysis dataset. Unless stated otherwise, we use the data output every six hours on the a $1^\circ \times 1^\circ$ horizontal grid and 60 pressure levels. Surface data of a similar resolution is also used. We also use dynamical and radiative tendencies [Fueglistaler et al. (2009b)] that are output as a forecast field every six hours.

## 2.2 CHAMP radio occultation data

In Chapter 3, we require high vertical resolution data to observed the global behaviour of the tropopause inversion layer. The CHAllenging Mini-Satellite Payload

(CHAMP) satellite uses the GPS network to provide limb sounding measurements of the atmosphere. About 270 profiles of temperature with a high vertical resolution were generated daily between 2001 and 2006 from refractivity measurements. This data has been used in previous studies of the TIL [Schmidt et al. (2010), Grise et al. (2010)]. The suitability of CHAMP data as a climate benchmark data has also been the subject of numerous studies [e.g Ho et al. (2009), Kuo et al. (2004), Foelsche et al. (2008)].

The processed profiles can be retrieved from the UCAR COSMIC Data Analysis and Archive Center (CDAAC) (http://cosmic-io.cosmic.ucar.edu/cdaac/index.html). A description of the retrieval algorithms used by UCAR can be found in the work of Kuo et al. (2004). A brief description of the radio occultation technique can be found in Schmidt et al. (2010) and references therein.

## 2.3 SWOOSH dataset

The Stratospheric Water and OzOne Satellite Homogenized (SWOOSH) data set is a record formed from a combination of measurements from various limb and solar occultation satellites since 1984 to the present (http://www.esrl.noaa.gov/csd/groups/csd8/swoosh/). The data comes from the SAGE-II/III, UARS HALOE, UARS MLS, and Aura MLS instruments. The measurements are homogenized by applying corrections that are calculated from data taken during time periods of instrument overlap. The seasonal cycle climatology in SWOOSH used data from 1984 to 2012.

Although this dataset is relatively new, it has been used in a study of stratospheric water vapour trends [Maycock et al. (2014)] and makes uses of HALOE and Aura MLS which have been widely validated in the literature [Harries et al. (1996), Brühl et al. (1996), Lambert et al. (2007)].

## 2.4 Idealised general circulation model

### 2.4.1 Model description

All the numerical experiments are done in a idealised global circulation model make use of some configuration of the Reading IGCM which solves the dry primitive equations

[Forster et al. (2000)]. The model is set up as follows unless otherwise described. The lower boundary has no topography, and zero mass flux is imposed as the top boundary condition. Frictional damping is imposed in the lower levels to simulate the turbulent dissipation of energy in a planetary boundary layer. The model is set up with an initial uniform temperature state and the temperature evolves with Newtonian relaxation to a forcing temperature profile. The model is allowed to 'spin-up' where the system evolves towards a steady state and proceeds for an additional amount of time to generate data. At each time step, fields are transformed between spectral and grid-point representation. Linear terms are evaluated in spectral space and non-linear terms in grid-point space. In the model, each variable is represented by a series of Legendre polynomials. The set of corresponding spectral coefficients has to be truncated at some finite wavenumber and this determines the resolution of the model. For instance, T42L40 represents triangular truncation at wavenumber 42, corresponding to a $4.5° \times 4.5°$ horizontal grid (approximately 480 km spacing). The vertical coordinate in the model is $\sigma$ which is defined as the ratio of the pressure to the surface pressure. $\sigma$ has a value of one at the surface and zero at the top of the atmosphere. L40 indicates a vertical resolution of 40 levels equally spaced in $\log \sigma$. In the model experiments in Chapters 3 and 4, the model top is chosen to be at 28 km and the vertical spacing is about 700 m for L40. In Chapter 5, the model top is chosen to be at 50 km with L60 and the vertical spacing is about 830 m. The levels are illustrated in Figure 2.1.

The model is hydrostatic. Further details of the spectral method and the semi-implicit time scheme used in the model can be found in Hoskins and Simmons (1975). A hyperdiffusion term of the form $\nabla^8$ is used in the vorticity, divergence and temperature equation to provide small scale dissipation. It can be thought of as a way of parametrising the cascade of energy to sub-grid scales before dissipation. The e-folding time for the smallest wave in the model is set to 0.1 days. A description of the effect of including hyperdiffusion can be found in Lauritzen et al. (2011).

### 2.4.2 Model resolution and parameters

The parameters needed to determine the model resolution and the number of spectral coefficients are described in Table 2.1. The number of even spectral coefficients (NWJ2) is equal to the value of $\frac{1}{4}\,\mathrm{MM}\,(\mathrm{MM}+2)$ rounded up to the nearest integer. For a jagged triangular truncation (see section below), this equals the number of odd coefficients.

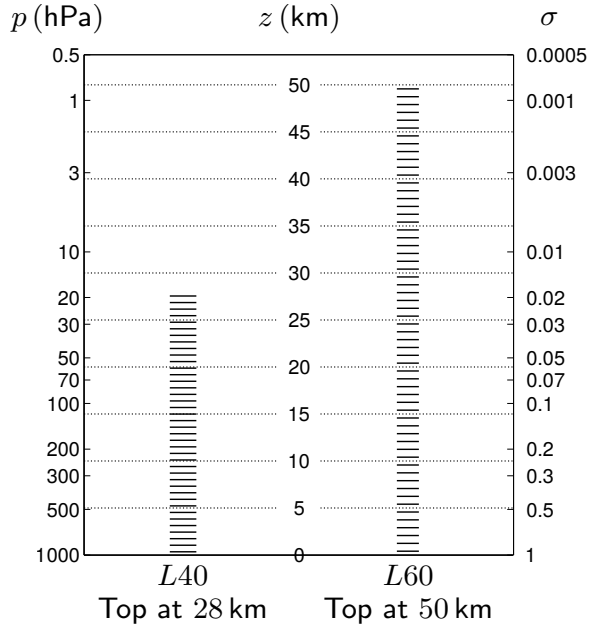


**Figure 2.1:** Plot of the model levels in IGCM for model runs with L40 used in Chapters 3 and 4 and L60 used in Chapter 5. The model uses $\sigma$ coordinates in the vertical. The pressure values shown assume a surface pressure of 1000 hPa. $z$ is a log pressure height such that $z = H \log \sigma$ where $H = 7\,\text{km}$.

The grid size and horizontal grid spacing, $L$, are calculated assuming 2 MM points fit around the equator. $D$ is a typical vertical length scale as calculated from the Prandtl number, $Pr = \frac{D}{L} = \frac{f}{N^2}$. For instance, near the mid-latitude tropopause, a typical value of $N^2$ is $5 \times 10^{-4}\,\text{s}^{-2}$. These values at relevant to the results in Chapter 3.

### 2.4.3 Jagged triangular truncation

The spectral coefficients are truncated such that there are an equal number of even and odd coefficients for each field at each level. In the history file, for each day and each level, even coefficients precede odd ones for the surface pressure, temperature and divergence fields and odd precede even ones for the vorticity. Within each set of coefficients, storage is with increasing n within increasing m. Figure 2.2 shows a T5 triangular truncation.

### 2.4.4 Implementation of relaxation temperature profile

The Held and Suarez (1994) profile has gained considerable acceptance as a simplistic way to parametrise forcing and dissipation in an idealised climate model whilst

| Parameter | Description |
|---|---|
| MM | highest zonal wavenumber, m, retained in spectral series. |
| NN | highest zonal wavenumber, n, retained in spectral series. |
| NL | number of vertical levels. |
| MG | number of longitudes in the transform grid. It has to be of the form $2^p 3^q$ where $p \geq 1$ and $p, q \in \mathbb{Z}_{\geq 0}$. MG $\geq 3\,\mathrm{MM} + 1$ is required for a global run to prevent aliasing of quadratic terms. |
| JG | number of Gaussian latitudes between pole to equator. It must satisfy JG $\geq \frac{1}{4}(3\,\mathrm{MM} + 1)$. |

**Table 2.1:** Parameters describing the model resolution of the Reading IGCM and their descriptions.

| Resolution | MG | JG | NWJ2 | Grid size | $L$ (km) | $D$ (km) |
|---|---|---|---|---|---|---|
| T21 | 64 | 16 | 121 | 8.6° × 8.6° | 950 | 4.3 |
| T42 | 128 | 32 | 462 | 4.2° × 4.2° | 480 | 2.1 |
| T63 | 192 | 48 | 1024 | 2.9° × 2.9° | 320 | 1.5 |
| T85 | 256 | 64 | 1849 | 2.1° × 2.1° | 240 | 1.1 |
| T106 | 324 | 80 | 2862 | 1.7° × 1.7° | 190 | 0.9 |

**Table 2.2:** Table of model parameters used with various resolutions, grid spacing and typical vertical and horizontal length scales.

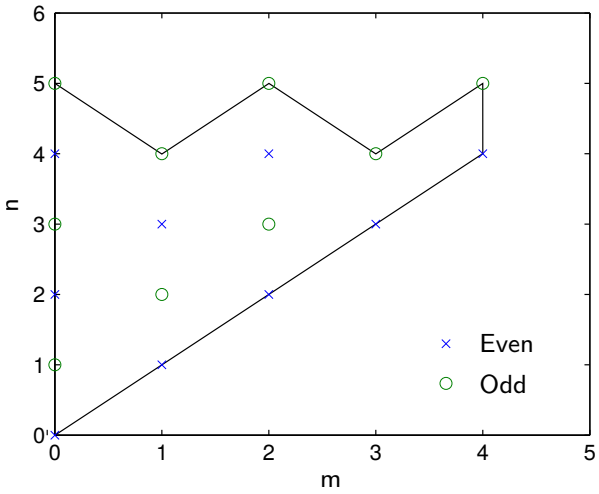


**Figure 2.2:** Plot of total wavenumber, n, against zonal wavenumber, m, showing the coefficients retained after a T5 jagged triangular truncation.

producing reasonably realistic circulations. This profile will be widely used in this thesis and the equilibrium fields generated have been validated against those in Held and Suarez (1994).

The relevant equations describing the Held and Suarez restoration profile are:

$$\frac{\partial v}{\partial t} = \ldots - k_v(\sigma)\, v$$

$$\frac{\partial T}{\partial t} = \ldots - k_T(\phi, \sigma)\, [T - T_{eq}(\phi, \sigma)]$$

$$T_{eq} = \max\left\{200\text{K},\ \left[315\text{K} - (\Delta T)_y\, \sin^2\phi - (\Delta\theta)_z\, \log\sigma\, \cos^2\phi\right]\, \sigma^\kappa\right\}$$

$$k_T = k_a + (k_s - k_a)\, \max\left(0,\ \frac{\sigma - \sigma_b}{1 - \sigma_b}\right)\, \cos^4\phi$$

$$k_v = k_f\, \max\left(0,\ \frac{\sigma - \sigma_b}{1 - \sigma_b}\right)$$

$$k_f = 1\,\text{day}^{-1} \qquad k_a = \frac{1}{40}\,\text{day}^{-1} \qquad k_s = \frac{1}{4}\,\text{day}^{-1}$$

$$\sigma_b = 0.7 \qquad (\Delta T)_y = 60\,\text{K} \qquad (\Delta\theta)_z = 10\,\text{K}$$

$$p_0 = 1000\,\text{mb} \qquad \kappa = \frac{R}{c_p} = \frac{2}{7} \qquad c_p = 1004\,\text{J kg}^{-1}\,\text{K}^{-1}$$

$$\Omega = 7.292 \times 10^{-5}\,\text{s}^{-1} \qquad g = 9.8\,\text{m s}^{-2} \qquad a = 6.371 \times 10^6\,\text{m}$$

The temperature in the relaxation profile decreases in height in the tropopause up to 200 K after which it is uniform (representing the stratosphere), as shown in figure 2.3. The radiative relaxation time scale $1/k_T$ is 40 days in most of the atmosphere except close to the surface. Dissipation is provided by linear damping of velocities of strength proportional to $\sigma$. Damping is non-zero only in the layers near the surface with $\sigma > 0.7$.

## 2.5 Radiation codes

### 2.5.1 Zhong and Haigh code

The Zhong and Haigh radiation code is a broad-band radiative transfer model based on the original scheme by Morcrette (1991) with improvements to the water vapour emissivities implemented by Zhong and Haigh (1995). This radiation code is included

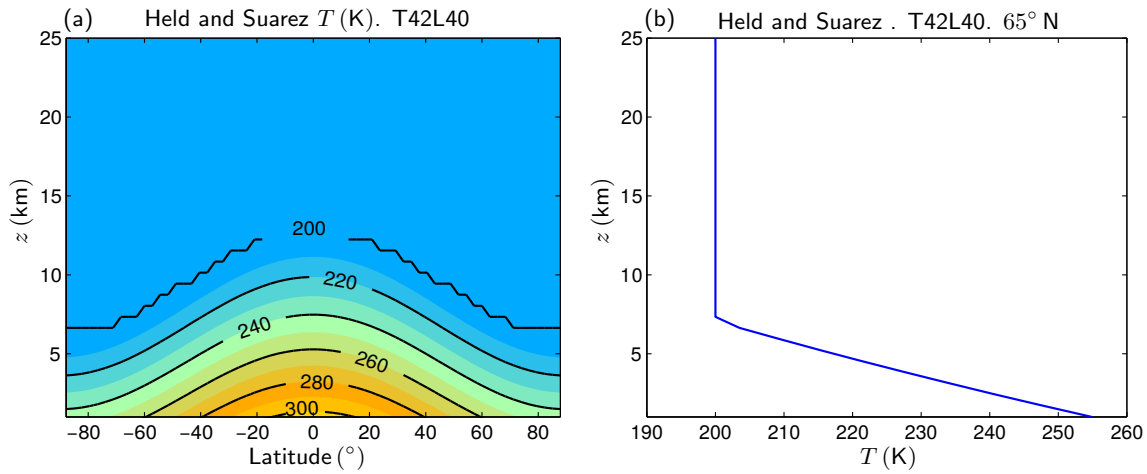


**Figure 2.3:** (a)Held and Suarez temperature relaxation profile. The temperature is constant at 200 K in the stratosphere. (b) Plot of the relaxation temperature with height, z, at latitude 65 ° N.

in version 3.1 of the Reading IGCM used in Chapter 5 of this thesis and has previously been used in the Integrated Forecast System (IFS) atmospheric model of the European Centre for Medium Range Weather Forecasts. The longwave part of the code has eight bands in the thermal infrared: 0–350 $\mathrm{cm}^{-1}$ and 1450–1880 $\mathrm{cm}^{-1}$ combined band, 350–500 $\mathrm{cm}^{-1}$, 500–800 $\mathrm{cm}^{-1}$, 800–970 $\mathrm{cm}^{-1}$, 970–1110 $\mathrm{cm}^{-1}$, 1110–1250 $\mathrm{cm}^{-1}$, 1250–1450 $\mathrm{cm}^{-1}$ and 1880–3000 $\mathrm{cm}^{-1}$. The shortwave scheme uses two bands and includes the effects of water vapour, ozone and uniformly-mixed gases. In this thesis, we will only be concerned with the radiative effect of the major trace gases: carbon dioxide, water vapour and ozone. The mixing ratio of other trace gases and aerosols is set to zero. Clear sky calculations are performed unless otherwise stated. The surface albedo is set to the time mean zonally averaged value obtained from ERA-Interim using the years 1979 to 2013.

In the offline calculation, solar insolation is calculated at each latitude and the short wave heating rates take into account diurnal variations by using a Gaussian quadrature method with three zenith angles. In the model radiation code, the diurnal cycle is not taken into account. The solar constant is set to 1376 $\mathrm{W\,m}^{-2}$.

The sets of vertical pressure levels used are:

- 50 pressure levels: 1, 2, 4, 6, 8, 10, 12, 14, 16, 18, 20, 25, 30, 40, 50, 60, 70, 80, 90, 100, 110, 120, 130, 140, 150, 160, 170, 180, 200, 210, 220, 230, 240, 250, 260, 270, 280, 290, 300, 330, 350, 370, 400, 450, 500, 600, 700, 800, 900, 1000 hPa

- 100 pressure levels: 1, 2, 3, 4, 5, 6, 7, 8, 9, 10, 11, 12, 13, 14, 15, 16, 17, 18, 19, 20, 22, 25, 27, 30, 35, 40, 45, 50, 55, 60, 65, 70, 75, 80, 85, 90, 93, 95, 97, 100, 103, 105, 107, 110, 113, 115, 117, 120, 123, 125, 127, 130, 133, 135, 137, 140, 145, 150, 155, 160, 165, 170, 175, 180, 185, 190, 200, 205, 210, 215, 220, 225, 230, 235, 240, 245, 250, 255, 260, 265, 270, 275, 280, 285, 290, 295, 300, 320, 330, 340, 350, 370, 400, 450, 500, 600, 700, 800, 900, 1000 hPa.

Most calculations in Chapters 4 and 5 are done using 50 levels. This is adequate for the resolution of the input data. A higher resolution of 100 levels is used in some calculations (see Chapter 5) when we investigate the non local contribution of ozone and water vapour changes from different regions in the vertical.

### 2.5.2 RRTM

The Rapid Radiative Transfer Model (RRTM) uses a correlated-k approach [Mlawer et al. (1997)] to calculate the heating rates where the k coefficients are obtained directly from a line by line code (LBLRRTM) [Clough et al. (1992), Clough and Iacono (1995)]. The longwave part of the RRTM code will be used in Chapter 4 to calculate longwave diabatic heating rates for comparison with ERA-Interim. The IFS model used to generate the ERA-Interim dataset currently makes use of the RRTM code [Morcrette et al. (2001)]. The longwave code used 16 spectral bands within which radiative transfer calculations are performed covering the 0 to 3000 $cm^{-1}$ spectral region. In our calculations, we only look at the clear-sky radiative effects of carbon dioxide, water vapour and ozone. The trace gas concentrations are interpolated to the 60 model pressure levels used in ERA-Interim which are:

0.10, 0.29, 0.51, 0.80, 1.15, 1.57, 2.07, 2.67, 3.36, 4.19, 5.20, 6.44, 7.98, 9.89, 12.3, 15.2, 18.8, 23.3, 28.9, 35.8, 44.3, 54.6, 66.6, 80.4, 96.0, 113, 133, 154, 177, 202, 229, 257, 288, 320, 353, 388, 425, 462, 500, 539, 577, 616, 654, 692, 728, 763, 796, 828, 857, 884, 908, 930, 949, 965, 979, 990, 998, 1004, 1009, 1012 hPa.

Exact values of these levels can be found in the ERA-Interim model documentation (http://www.ecmwf.int/en/forecasts/documentation-and-support/60-model-levels).

In Chapter 5, we make used of the RRTM code implemented in a version of the IGCM 3.1 model. In this calculation, the radiative transfer calculation is done on the same 60 sigma levels used by the model.

## 2.6 Statistical methods

Both reanalysis data and model data contain serial correlations which must be taken into account when estimating confidence intervals. In this thesis, we follow the method described in Zwiers and von Storch (1995) which entails estimating an effective number of degrees of freedom, $n_e$, from the autocorrelation function, $\rho(t)$, of the time series of total length $n$. The effective number of degrees of freedom is given by

$$n_e = \frac{n}{1 + 2\sum_{t=1}^{n-1}\left(1 - \frac{t}{n}\right)\,\rho(t)}. \tag{2.1}$$

Adequate convergence of the sum in the denominator can be obtained if terms in the autocorrelation function are retained up to the lag where $\rho$ falls below 0.1. This corresponds to about a lag of 100 days in the model runs in Chapter 4. In these runs, long timescale processes such as the annual cycle and quasibiennial oscillation are not present. Once $n_e$ is obtained, it can be used to produce an adjusted sample variance, $s/(n_e)^{1/2}$, where $s^2$ is the sample variance, and confidence intervals are obtained from a Student's t-test. When the method described here is used, it will be referred to as the adjusted Student's t-test.

In cases where the quantity of interest is known to have long serial correlations and the dataset is short, for example for correlations due to the quasibiennial oscillation in a twenty year ERA-Interim dataset, $n_e$ is likely to be less than 30. In these cases where $n_e$ is difficult to estimate at certain latitudes, a subjective best guess estimate is obtained by taking into account estimates of $n_e$ at neighbouring latitudes on the same pressure level. A further check on the uncertainty estimates is performed by splitting the dataset into smaller continuous time series to see if the uncertainties scale as expected. Further examples will be given in the Appendix of Chapter 4.

## 2.7 Contour plots

Two colour schemes are used for contour plots throughout this thesis (excluding plots from external sources). In one scheme, the colours transition from blue to green to orange with blue representing low values and orange representing high values. The other colour scheme runs from blue to white to orange and is primarily used for

data that has a range spanning zero such as differences of a quantity from its mean. These schemes are colour-blind friendly. In addition black or grey label contours are superimposed and labelled with the contour value. Coloured contours are plotted at half the interval of the black/grey contours.

# Chapter 3

## Extratropical tropopause inversion layer

## 3.1 Introduction

A key feature of the extratropical upper troposphere and lower stratosphere is a region of stable air located just above the tropopause. This region is commonly referred to as the tropopause inversion layer (TIL) since it is directly related to an inversion in the vertical temperature gradient i.e the vertical temperature gradient changes from a roughly steady decrease in the troposphere to a strong increase just above the tropopause. The TIL is a few kilometers thick and is located about 0–1 km above the extratropical tropopause. Figure 3.1 is an illustration of the lower part of the atmosphere together with the extratropical TIL.

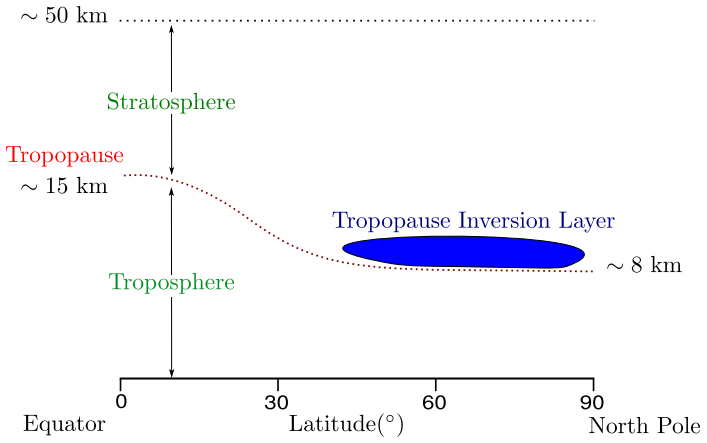


**Figure 3.1:** Schematic diagram of the lower part of the atmosphere showing the rough location of the TIL. The stratosphere is followed upwards by the mesosphere, thermosphere and exosphere. The diagram is not to scale.

Birner et al. (2002) noted the presence of this feature by looking at observational data. Figure 3.2, modified from Figure 1 in Birner et al. (2002), shows profiles of temperature and buoyancy frequency squared. The buoyancy frequency is a measure of how stable a parcel of air is with respect to its surroundings, i.e. its static stability. The troposphere is characterized by low values of static stability and the stratosphere by higher values. The fields shown come from radiosonde data and from the ECMWF reanalysis data set (ERA-40) [Uppala et al. (2005)]. Reanalysis data products are generated by assimilating observational data from a wide range of sources such as radiosonde, aircraft and satellite measurements into a model. The vertical coordinate used by Birner et al. (2002) is a tropopause based height where the profiles are shifted so that the vertical variation in tropopause height over time is accounted for. This process is also referred to as compositing. The tropopause height can be defined in various ways and Birner et al. (2002) use the one based on the vertical temperature gradient. Further details on defining the tropopause will be given in the next section. The horizontal lines in Figure 3.2 represent the tropopause and the sharp peak above the tropopause can be identified as the extratropical TIL. A simple vertical coordinate average does not capture the sharp transition in static stability seen in a tropopause based average.

**Figure 3.2:** [Modified from Figure 1 in Birner et al. (2002)] Mean profiles and corresponding relative standard deviations of (a) temperature, (b) buoyancy frequency squared for Munich. Black full lines represent averages for radiosonde data. Dotted lines denote mean ERA-profiles. Profiles are time-averaged (denoted by the overbar) relative to the respective tropopause height (horizontal lines). The grey shading indicates the tropopause region.

The TIL is in a region characterized by a strong connectivity between radiative, dynamical, chemical and microphysical processes and as a result is highly sensitive to climate change. Its presence can play a crucial role in affecting chemical transport

across the extratropical tropopause. Processes that contribute to the formation of the TIL are still not well understood and are a matter of active research. Understanding the structure of the static stability in the atmosphere is important because static stability is central to dispersion relations for atmospheric waves such as gravity and Rossby waves which all depend to some extent on the restoring force associated with buoyancy.

The midlatitude troposphere is dominated by eddies which affect the stratification. Wirth (2003) looks more closely at the effect of those eddies and suggests that the asymmetry between upper level cyclones and anticyclones affects the local stratification around the tropopause in such a way that for anticyclonic flow, composited profiles of static stability reveal a TIL in the climatological mean. Randel et al. (2007b) points out that although the strength of the TIL is modulated by the local circulation, as expected from balanced dynamics [Wirth (2003)], the fact that the inversion layer is also present for cyclonic flow suggest additional forcing mechanisms. Randel et al. (2007b) conducted a set of radiative transfer calculations and showed that the lower stratospheric structure of ozone and water vapour produce the right pattern of temperature changes to force and maintain a TIL. However, a radiative mechanism also inherently includes transport effects by assuming the dynamics lead to the observed ozone and water vapour distributions. In the stratosphere, air rising from the tropical pipe is transported polewards and then descends over the high latitudes. This circulation is called the Brewer–Dobson circulation [Haynes (2005)]. Birner et al. (2006) examined the properties of the downwelling branch of the Brewer–Dobson circulation. Results from the Canadian Middle Atmosphere Model (CMAM) and ERA-40 reanalysis showed that the strong vertical gradients in the downwelling just above the tropopause help create a TIL. The time–dependent equation for the static stability derived in Birner et al. (2006) contains the gradient of the vertical velocity as a crucial forcing term.

The TIL has been shown to be present in reanalysis data [Birner (2006)] and quasi realistic global circulation models [Birner (2006), Miyazaki et al. (2010)] and in satellite temperature profiles [Randel et al. (2007b), Grise et al. (2010)]. Models produce a TIL which is broader and smoother than observational data, and the peak is not significantly enhanced by tropopause based (TB) averaging; in particular, the sharp transition in static stability is not seen. This has been attributed to their coarse vertical resolution and Hegglin et al. (2010) show that they behave similarly to observations where the high vertical resolution is degraded. Son and Polvani (2007) ran a simple general circulation model which did not include a realistic radiative forcings from

chemical species and found a broad TIL to be present in a TB vertical coordinate but did not compare to the simple averaged case. These results show that the TIL emerges as a result of the dynamics but Son and Polvani (2007) do not offer a dynamical mechanism.

In this chapter, we first explain the process of tropopause based averaging in Section 3.2. Section 3.3 then shows static stability plots from satellite data and the effect of different methods of averaging on the data. Next, using a similar approach to Son and Polvani (2007), we attempt to reproduce a TIL in a simple general circulation model. The model and results are described in Section 4.5 and the sensitivity to model resolution is discussed. We also present a case where the model does not produce a TIL. Building on the model results from Section 3.4, Section 3.5 focuses on a possible dynamical mechanism for the formation of the TIL by focussing on the meridional circulation. We look in detail at the vertical velocity distribution above the tropopause but in contrast to Birner et al. (2006), we consider the steady state case and how wave forcings in the stratosphere can give rise to an upwelling that is consistent with increased static stability. Finally, Section 3.6 examines the effects of tropopause based averaging on idealised profiles of static stability. A brief summary and some concluding remarks are given in Section 3.7.

## 3.2 Tropopause based (TB) averaging

The following section explains the process of tropopause based averaging. The description is based on that in Birner (2006).

There is no unique definition used to describe the tropopause. A conventional definition is based on the rate at which temperature, $T$, falls with geometric height, $z$, known as the lapse rate ($-\partial_z T$) and relies on the fact that the troposphere and the stratosphere have a different thermal stratification. The troposphere is observed to have a small but stable stratification with a typical lapse rate $\gtrsim 5\,\mathrm{K\,km^{-1}}$. The stratosphere is comparatively strongly and stably stratified with a lapse rate $\lesssim 0\,\mathrm{K\,km^{-1}}$. According to the World Meteorological Society definition [WMO (1957)], the thermal tropopause is located at the lowest level at which the lapse rate decreases to $2\,\mathrm{K\,km^{-1}}$ or less, provided that the average lapse rate between this level and all higher levels within 2 km does not exceed $2\,\mathrm{K\,km^{-1}}$.

Conventionally, a sea-level based coordinate system is used to compute averages of

climate variables using, for example, geometric height, $z$ or pressure, $p$, as the vertical coordinate. The vertical coordinate system is fixed in time and horizontal space and averaging quantities that vary in time results in features being smeared out. At a given location in the extratropics, the height of the tropopause changes considerably, by a few kilometers, with time. A simple average of vertical temperature profiles would result in a blurred transition as illustrated Figure 3.3(a). Tropopause based averaging preserves the characteristics of the tropopause by defining a coordinate system centred on the tropopause which varies in location and time. The profiles at one location can be composited to give an average where the tropopause is present as a sharp transition. This concept is illustrated in Figure 3.3(b). Let $G(t, z)$ be a time and height dependent quantity of interest. We can define a new vertical coordinate, $\tilde{z}$, which depends on the height of the tropopause at time $t$, $z_{\mathrm{TP}}(t)$, as $\tilde{z} = z - z_{TP} + \overline{z_{\mathrm{TP}}}$, where the overline denotes time averaging. The tropopause based average is then given by $\overline{G(t, z - z_{\mathrm{TP}})}$. Essentially, the set of profiles at one grid point is vertically shifted so that the instantaneous tropopause coincides with the mean tropopause height there. Our method uses a cubic spline interpolation to obtain the quantities in $\tilde{z}$ based coordinates from $z$ coordinates before time averaging.

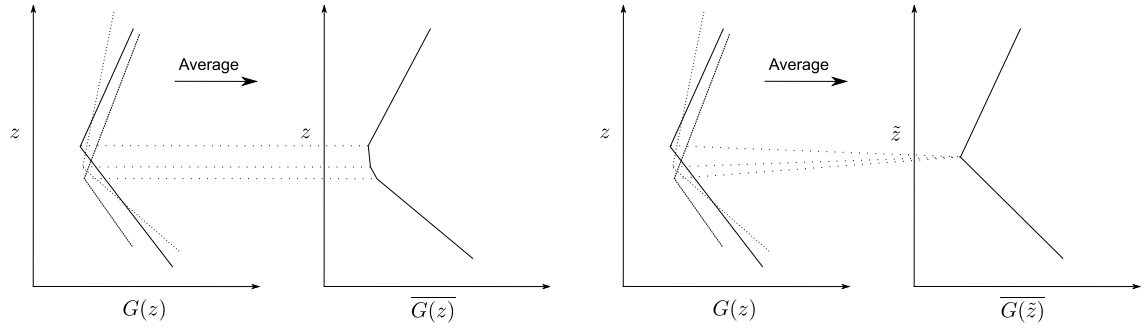


**(a)** Simple **(b)** Tropopause based

**Figure 3.3:** An illustration of how simple averaging, (a), results in smeared out features in the quantity G in contrast to tropopause based averaging, (b), which produces a sharp kink in G.

## 3.3 TIL in CHAMP observational data

The calculation of the static stability from CHAMP radio occultation data involves truncating the dry temperature, pressure and height profiles down to the region of interest; the 3 to 25 km range. The number of vertical levels in each profile varies from 1000 to 5000. By using a simple cubic interpolation, we compress each profile to 200

vertical levels so all the profiles have a vertical resolution of 110 m. The temperature difference between any initial temperature profile and the resulting compressed profile is less than the uncertainty associated with the retrieval method used. This uncertainty is about 1 K [Kuo et al. (2004)] for the data used. Figure 3.4(a) shows six typical profiles of static stability from CHAMP data. Tropopause heights are calculated using the WMO lapse rate definition and are additionally constrained to lie between 8 to 12 km. The sample profiles that have been tropopause adjusted are shown in Figure 3.4(b).

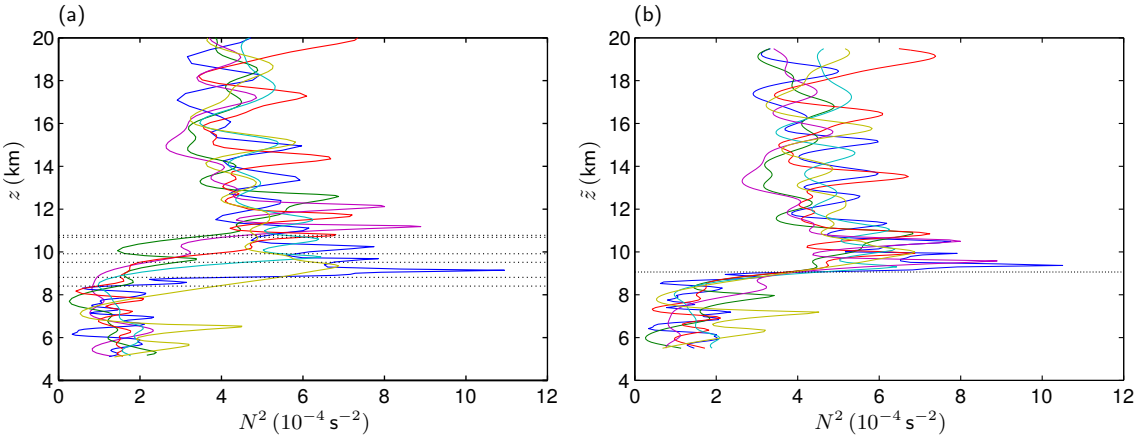


**Figure 3.4:** Plot of six static stability profiles taken from CHAMP data for January 2002. The profiles are located within the 60 to 70° N band and are shown plotted against geometric height in (a) and tropopause based height in (b) as the vertical coordinate. Horizontal lines represent the tropopause height.

The static stability averaged over the months of January to June 2002 in the latitude range 60-65° N is shown in Figure 3.5. Tropopause based averaging produces a considerably sharper and stronger TIL than the simple averaging. The amplitude of the peak (taken as the difference between the maximum value and the value in the stratosphere) is more than twice as large in the TB averaged case compared to simple averaging. Our TB averaged results agree with other observational data plots of the TIL [Randel et al. (2007b), Grise et al. (2010), Schmidt et al. (2010)]. Note that although there is a strong seasonal variation in the strength of the TIL [Bell and Geller (2008)], this calculation is purely to illustrate the effect of tropopause based averaging and a similar result will be obtained if a different time period is chosen.

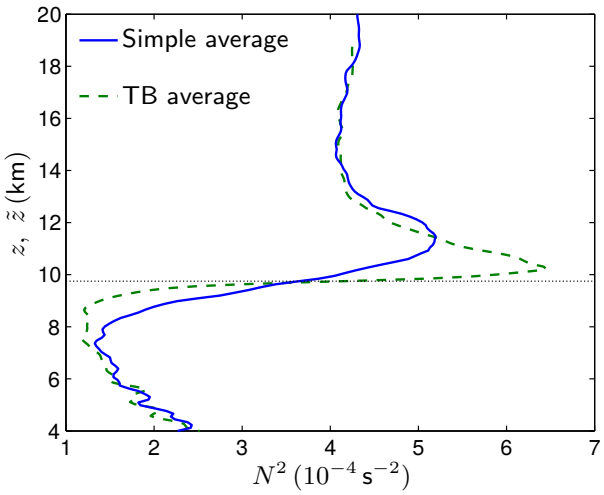


**Figure 3.5:** Plot of TB and simple averaged static stability obtained from CHAMP data for the months of January to June 2002 in the latitude range 60-65° N. 463 profiles were averaged. The horizontal line represents the mean tropopause height.

## 3.4 Modelling the TIL

The TIL is modelled using the Reading IGCM set up with the temperature relaxed to a restoration temperature profile. Two such profiles are used in our experiments: the Held and Suarez (1994) profile (HS), described in Section 2.4.4 and the Haynes, Scinocca, and Greenslade (2001) profile (HSG).

### 3.4.1 Held and Suarez (HS) profile

#### 3.4.1.1 Static stability field

The Brunt-Väisälä frequency, N, is a measure of the frequency of oscillation of a parcel of air when displaced vertically in a density stratified environment that is statically stable. $N^2$ is used as a measure of static stability and can be defined in terms of the potential temperature, $\theta$, as follows

$$N^2 = \frac{g}{\theta}\frac{\partial\theta}{\partial z}, \tag{3.1}$$

where $g$ is the acceleration due to gravity $9.81\,\mathrm{m\,s^{-1}}$. Potential temperature is a conserved quantity in adiabatic flow and is preferred to temperature since a fluid

parcel undergoing an adiabatic pressure change can expand or contract, resulting in a temperature change. Only diabatic contributions such as heating can cause a change in the potential temperature. The usual definition of potential temperature, $\theta = T\,(\sigma)^{-\kappa}$ (with $\kappa$ being a constant equal to 2/7 for a dry atmosphere) is the temperature that a parcel of fluid would have if it was moved adiabatically down to some reference pressure, $p_0$ (usually 1000 hPa, the pressure at the Earth's surface) [Vallis (2006)]. The temperature in the atmosphere decreases through the troposphere, increases in the stratosphere and decreases again in the next layer of the atmosphere, the mesosphere but the potential temperature accounts for the pressure change and increases from ground level up.

Following the approach of Son and Polvani (2007), we run the model with the HS restoration profile. The static stability of the Held and Suarez restoration state is shown in Figure 3.6(a) and is constant in the stratosphere (does not contain a tropopause inversion layer). In the equilibrium state of the model, a TIL is present and can be identified in the static stability plot, Figure 3.6(b), as a layer of a few kilometers in thickness poleward of 55 °N. This layer is located above the tropopause which is found at a height of about 10 km in the mid latitudes. The thickness of this layer is approximately constant poleward of 55 °N, a feature seen in observational data [Grise et al. (2010)]. The large maximum in $N^2$ in the lower stratosphere in the tropics at around 18 km can be identified as the tropical tropopause layer [Fueglistaler et al. (2009a)].

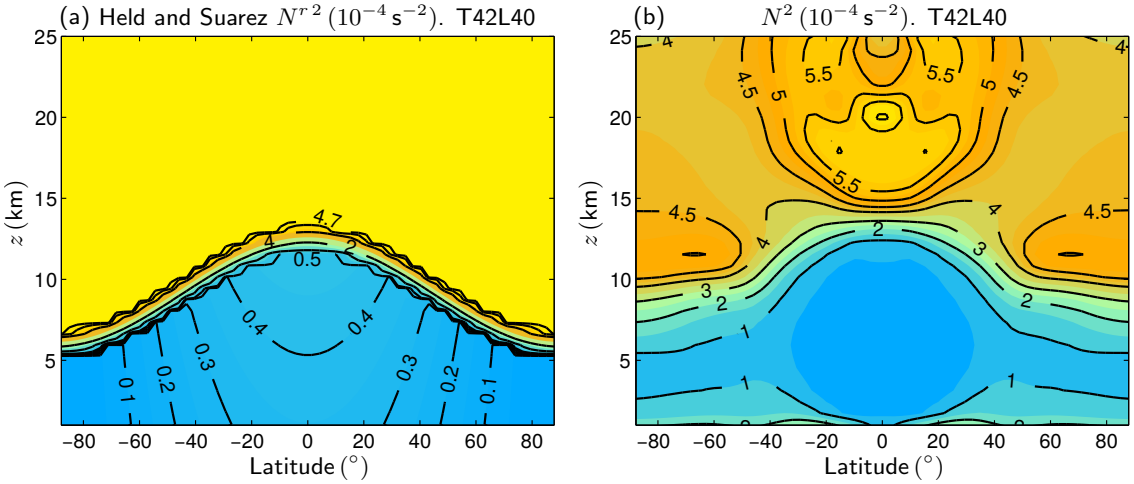


**Figure 3.6:** (a) Static stability, $N^{r\,2}$ for the Held and Suarez restoration state. The superscript, $r$ denotes the restoration state. (b) Simple zonal mean and time average of static stability for the equilibrium state when the idealised model is relaxed towards the Held and Suarez restoration state. The model resolution is T42L40.

#### 3.4.1.2 Simple versus TB averaging in model data

Since the TIL is relatively uniform in latitudes in the extratropics, we considered a single latitude (65 ° N) and compute the simple and TB averages of the static stability profile for the model run with the HS restoration profile. Figure 3.7 shows a plot of the simple and tropopause based average static stability for a T42L40 run. TB averaging tends to slightly sharpen the maximum in static stability. In contrast, TB averaging in radiosonde data (Figure 3.2) causes a distinct change to the shape of the peak above the tropopause, resulting in a sharp spike. Also the TIL was only uncovered by tropopause based averaging of the radiosonde data and is otherwise considerably smeared out.

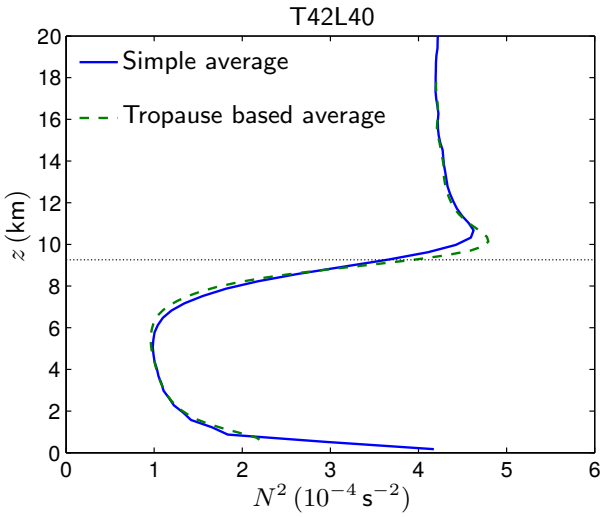


**Figure 3.7:** Simple average and tropopause based average $N^2$ at latitude 65° N and a single longitude for the T42L40 run. The dotted lines represent the time mean tropopause height.

We therefore propose a way of distinguishing between the maximum found in TB averaged data from that in simply averaged data. We will refer to a type I TIL as the enhanced region of static stability seen in simply averaged static stability profiles and a type II as the sharp spike seen in a TB average. The radiosonde data presented in Birner et al. (2002) shows a weak ($N^2 \sim 5 \times 10^{-4}\,s^{-2}$) type I TIL in the conventional average and a stronger ($N^2 \sim 7 \times 10^{-4}\,s^{-2}$) type II TIL after TB averaging. A similar effect was seen in the CHAMP data in the previous section, Figure 3.5.

The static stability profiles show that our model produces a weak type I TIL. Birner et al. (2006) used a more comprehensive model (CMAM) which incorporates interactive chemistry but the results still fail to produce a sharp type II TIL.

#### 3.4.1.3 Sensitivity of TIL to model resolution

We test the sensitivity of the static stability profiles to model resolution by keeping either the vertical or the horizontal resolution fixed and varying the other. Plots of such experiments are shown in Figure 3.8. These results independently confirm those by Son and Polvani (2007) and show a higher sensitivity to horizontal resolution which Son and Polvani (2007) attribute to the choice of the sub-grid scale diffusion. Our experiments are done to a much higher model resolution and we find that past a certain resolution, the curves start to converge. This can be explained by considering the vertical and horizontal grid spacing. For a given horizontal grid spacing, $L$, there is an associated natural vertical scale $D$. The ratio of the two quantities can is given by the dimensionless Prandtl's ratio of scales, $Pr = \frac{D}{L} = \frac{f}{N}$ [Joseph Pedlosky (1987)]. Using a typical value of $N^2 \approx 5 \times 10^{-4}\,\mathrm{s}^{-2}$ near the mid-latitude tropopause, a Prandtl number of 0.006 is obtained. Consider a model resolution where the vertical grid spacing is less than the vertical lengthscale, $D$. The horizontal resolution is then increased with fixed vertical resolution. The vertical grid spacing eventually becomes the limiting factor.

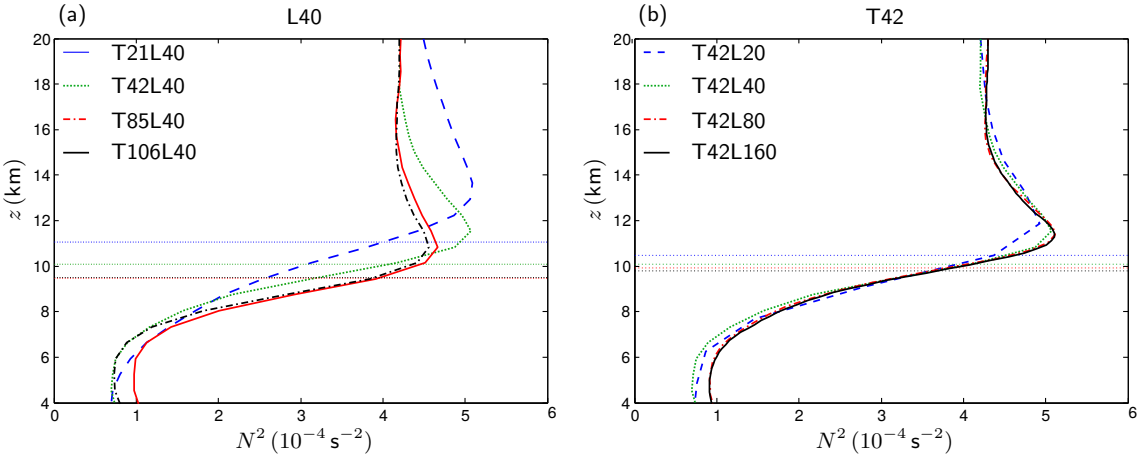


**Figure 3.8:** Simply averaged $N^2$ profiles at latitude 65° N and a single longitude for runs with (a) 40 levels at T21, T42, T85 and T106 and (b) T42 with 20, 40, 80 and 160 levels. The dotted lines represent the time mean tropopause height for the corresponding resolution.

The model has an inherent aspect ratio which means that for a given horizontal resolution, there is no further gain by increasing the vertical resolution past a certain point. For example, for T42, higher resolution than L40 do not improve the representation of the model TIL.

#### 3.4.1.4 Potential vorticity

Work in this section is motivated by some results obtained in Wirth (2003) which suggest that the asymmetry between upper level cyclones and anticyclones affects the local stratification around the tropopause. In the case of anticyclonic vorticity, composited profiles of static stability reveal a TIL in the climatological mean despite the initial background state not containing one. The TIL arises as a result of the balanced dynamics [Bühler (2009)] in which the potential vorticity is a conserved quantity.

Wirth (2003) set up a model in which the background atmosphere is characterized by smooth gradients in the troposphere and stratosphere and a linear increase in the tropopause height with horizontal distance. The background static stability profile consists of two constant values, one in the troposphere and a higher value in the stratosphere with a smooth transition over a few hundred metres. The cyclones and anticyclones (baroclinic eddies) are generated as follows. The background state is locally disturbed by horizontal advection across the background gradients, creating a local PV anomaly. This anomaly is smoothly cut off and is purely axisymmetric. The PV field obtained is subsequently inverted to obtain the wind and temperature, from which static stability can be derived. The resulting anticyclones are characterized by a sharp peak in $N^2$ right above the tropopause in the vortex centre whilst cyclones show a smooth transition from tropospheric to stratospheric $N^2$ values. The tropopause based average of $N^2$ is dominated by the anticyclonic peak. These results imply that the TIL is a feature that arises after compositing because of the cyclonic-anticyclonic asymmetry and has to be attributed to the effects of balanced dynamics. We argue that in our model the TIL is not due to the transient effects of eddies on the static stability and that an inherent feature is present in the background PV field.

The plot of Ertel's PV, Figure 3.9(a), shows that PV increases vertically upwards and towards the pole as expected from Equation 1.16. The sign of the absolute vorticity in each hemisphere determines the sign of the PV (positive in the northern hemisphere). PV increases smoothly towards the poles since the vertical component of the absolute vorticity increases. PV also increases with height as the density falls.

PV is also used to define a tropopause height and a range of values from 1.5 to 3.5 PVU can be found in the literature [Hoerling et al. (1991), Holton et al. (1995)]. We choose a value of 2 PVU which gives a dynamical tropopause that follows a path about 2 km below that obtained from the lapse rate definition in the extratropics in our model

results.

Since the PV increases upwards, a local maximum in the vertical structure can be hidden. We propose computing a modified potential vorticity (mPV) quantity which varies like the static stability and is still materially conserved. By construction, this quantity is independent of height in an isothermal atmosphere. This is done by replacing $\theta$ in Equation 1.16 by a well behaved function of $\theta$,

$$\text{mPV} = \frac{\boldsymbol{\zeta}^a \cdot \nabla f(\theta)}{\rho} = \frac{\boldsymbol{\zeta}^{\boldsymbol{a}} \cdot \nabla \theta}{\rho} f'(\theta) = \text{PV}\, f'(\theta) = \text{PV}\, g(\theta).$$

Material conservation holds as both PV and $\theta$ are materially conserved quantities. We choose $g(\theta) = \theta^{-\frac{1}{\kappa}-1}$ to account density change with height. The modified PV then is given by:

$$\text{mPV} = \text{PV}\ \theta^{-\frac{1}{\kappa}-1} = \text{PV}\ \theta^{-4.5}.$$

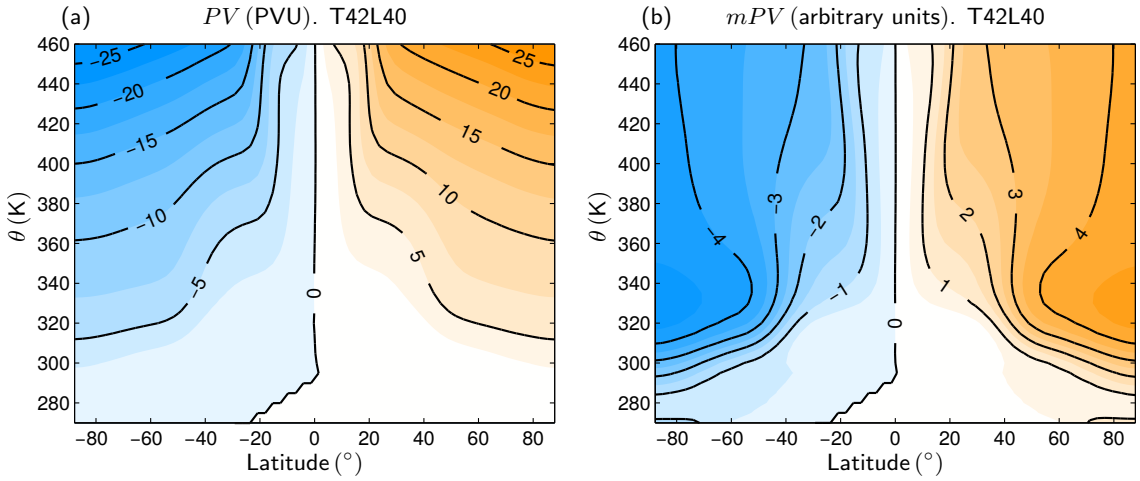


**Figure 3.9:** (a) PV and and (b) mPV (in arbitrary units) at a single longitude for T42L40.

Comparing the structure of PV in Figure 3.9(a) and mPV in Figure 3.9(b), the equilibrium state displays a weak maximum in mPV but not in PV. The plot of mPV shows that the potential vorticity and the static stability structure of the upper troposphere/lower stratosphere region are intimately related.

Note that there are no PV anomalies in the restoration state but the dynamics lead to there being a maximum in the mPV field in the steady state which is present even without compositing. Our results differ from Wirth (2003) in that we claim that

there is a persistent feature in PV in contrast to transient PV anomalies generated by baroclinic dynamics. This has wider implications for the climate system; for instance, a persistent TIL will affect the propagation of waves such as Rossby waves from the troposphere to the stratosphere [Bühler (2009)]. Those waves with a timescale longer than that of baroclinic eddies, i.e. of order greater than a few days, will be affected by a TIL in the background PV.

### 3.4.2 Haynes, Scinocca and Greenslade (HSG) profile

Son and Polvani (2007) made use of three different restorations profiles in the idealised model and all profiles lead to the formation of a TIL. We will now demonstrate that it is possible for the TIL not to form in an idealised model experiment. We implement a modified version of the restoration profile described in Haynes et al. (2001). The main feature of this restoration profile is the lack of a clear distinction between the stratosphere and the troposphere. Unlike the HS restoration profile, the temperature in the HSG profile is a smooth and continuous function of height and latitude. The timescale for temperature relaxation is chosen to be 25 days. The area weighted latitudinal average of $T_{\mathrm{HSG}}(\phi, z)$ is given by $T_0(z) = 285\,\mathrm{K} - 70\,\mathrm{K}\,\tanh(z/10000)$. The $\phi$–dependent part of $T_{\mathrm{HSG}}(\phi, z)$ is in thermal wind balance with a longitudinal velocity field in solid body rotation at a rate that increases linearly with height, $u_r(\phi, z) = 6 \times 10^{-3}\, z\, \exp(-z/40 \times 10^3) \cos\phi$.

No surface topography or heat fluxes are imposed in the model. Frictional drag is imposed in the bottom layers ($\sigma < 0.7$). Unlike Haynes et al. (2001), we find it convenient to set the initial temperature to 250 K at all grid points as we are only interested in the statistical steady state and data generated during the model spin-up is not used. The model top is at 28 km and there is no sponge layer. Plots of the static stability in the HSG restoration profiles is shown in Figure 3.10(a). In the steady state, a TIL is not produced in the static stability field, Figure 3.10(b).

## 3.5 Dynamical explanation for the presence of the TIL

Having demonstrated that the steady state dynamics and the TIL are linked, we will use the transformed Eulerian mean framework (Section 1.2.1) to explain how a

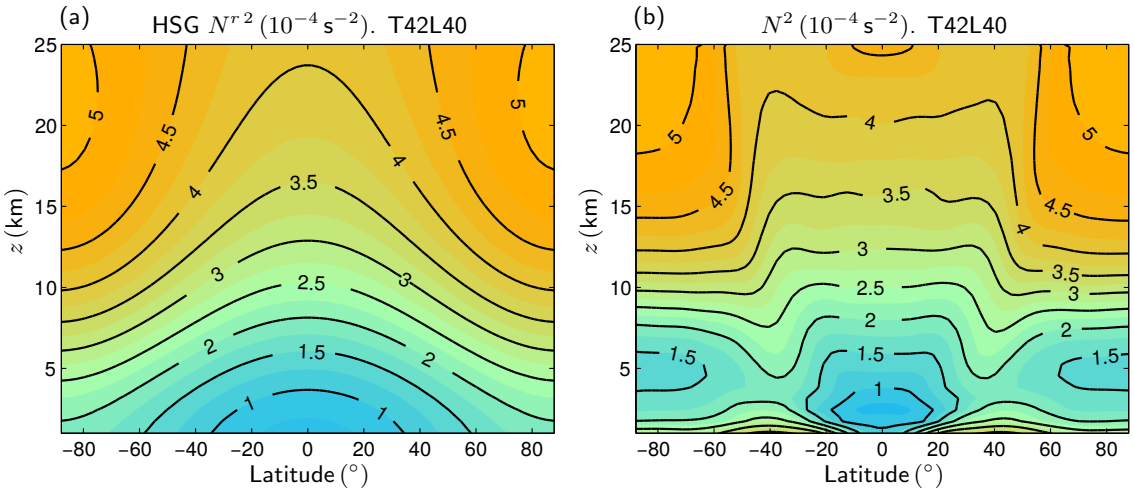


**Figure 3.10:** (a) Static stability in the Haynes, Scinocca and Greenslade restoration profile. (b) Simply averaged static stability for the equilibrium state for a model resolution of T42L40 at a specific longitude and averaged over 1000 days.

TIL forms in the model. Using the TEM equations, we can construct a relationship between the static stability and the divergence of the Eliassen-Palm flux in an attempt to provide a dynamical explanation for the TIL that is present in the steady state model data.

The thermodynamic equation in TEM form is:

$$\frac{\partial \overline{\theta}}{\partial t} + \frac{1}{a}\,\overline{v}^{*}\,\frac{\partial \overline{\theta}}{\partial z} + \overline{w}^{*}\,\frac{\partial \overline{\theta}}{\partial z} - \overline{Q} = -\frac{1}{\rho_0}\left[\rho_0\left(\frac{\overline{v'\,\theta'}}{a}\,\frac{\overline{\theta}_{\phi}}{\overline{\theta}_{z}} + \overline{w'\,\theta'}\right)\right]_{z}, \tag{3.2}$$

where $\overline{Q} = \alpha\,(\overline{\theta^{r}} - \overline{\theta})$ and $\theta^{r}$ is the restoration potential temperature. $\alpha$ is the radiative relaxation rate and is equal to $k_T = 1/40\,\text{days}^{-1}$ for the Held and Suarez case (Section 2.4.4)

In the steady state, the time derivative in Equation 3.2 is zero and in the region near the midlatitude tropopause, the diabatic heating $\overline{Q}$ is balanced by the term $\overline{w}^{*}\,\overline{\theta}_{z}$. Terms on the right hand side of Equation 3.2 can be neglected in the midlatitude lower stratosphere, see Birner (2010). The term $\frac{1}{a}\overline{v}^{*}\overline{\theta}_{z}$ is also small in the model results and is neglected. Hence,

$$\overline{w}^{*}\,\frac{\partial \overline{\theta}}{\partial z} = \alpha\,(\overline{\theta^{r}} - \overline{\theta}). \tag{3.3}$$

We can derive an expression for the static stability from Equation 3.3 as follows. The

expression in Equation 3.3 is rearranged to get an expression for $\theta$,

$$\overline{\theta} = \overline{\theta^r} - \frac{\overline{w}^*}{\alpha}\frac{\partial\overline{\theta}}{\partial z}. \tag{3.4}$$

Using the fact that $\theta \simeq \theta^r$ is a good first approximation,

$$\overline{\theta} = \overline{\theta^r} - \frac{\overline{w}^*}{\alpha}\overline{\theta^r}. \tag{3.5}$$

The above expression for $\theta$ substituted back into Equation 3.4 to give,

$$\begin{aligned}
\overline{\theta} &= \overline{\theta^r} - \frac{\overline{w}^*}{\alpha}\left(\overline{\theta^r} - \frac{\overline{w}^*}{\alpha}\overline{\theta^r}_z\right)_z, \\
\overline{\theta} &\simeq \overline{\theta^r} - \frac{\overline{w}^*}{\alpha}\overline{\theta^r}_z - \frac{\overline{w}^*}{\alpha}\left(\frac{\overline{w}^*}{\alpha}\overline{\theta}_z\right)_z, \\
\overline{\theta} &\simeq \overline{\theta^r} - \frac{\overline{w}^*}{\alpha}\overline{\theta^r}_z,
\end{aligned}$$

where terms to first order in $\frac{\overline{w}^*}{\alpha}$ have been kept.

An expression for $N^2$ can then be constructed as shown

$$\begin{aligned}
\overline{N^2} = \frac{g}{\overline{\theta}}\frac{\partial\overline{\theta}}{\partial z} &\simeq \frac{g}{\overline{\theta^r} - \frac{\overline{w}^*}{\alpha}\overline{\theta^r}_z}\left[\overline{\theta^r} - \frac{\overline{w}^*}{\alpha}\overline{\theta^r}\right]_z \\
&\simeq \frac{g}{\overline{\theta^r} - \frac{\overline{w}^*}{\alpha}\overline{\theta^r}_z}\left[\overline{\theta^r}_z - \frac{\overline{w}^*}{\alpha}\overline{\theta^r}_{zz} - \frac{\overline{w}^*_z}{\alpha}\overline{\theta^r}_z\right] \\
&\simeq N^{r\,2} + g\frac{\overline{w}^*}{\alpha}\frac{\overline{\theta^r}_z^{\,2}}{\overline{\theta^r}^2} - g\frac{\overline{w}^*}{\alpha}\frac{\overline{\theta^r}_{zz}}{\overline{\theta^r}} - g\frac{\overline{w}^*_z}{\alpha}\frac{\overline{\theta^r}_z}{\overline{\theta^r}},
\end{aligned}$$

where $N^{r\,2}$ is the static stability corresponding to the temperature restoration profile.

For the Held and Suarez restoration profile, in the region of the mid latitude tropopause, $\theta^r = 200\, e^{\frac{\kappa z}{H}}$, hence the expression for the static stability simplifies to

$$N^2 \simeq N^{r\,2}\left[1 - \frac{\overline{w}^*_z}{\alpha}\right]. \tag{3.6}$$

The divergence of the Eliassen-Palm flux, $\nabla\cdot\mathbf{F}$, is shown in Figure 3.11(a) for the Held and Suarez run and a large region of convergence is present in the extratropical stratosphere (above 13 km). The mean residual vertical velocity is related to $\nabla\cdot\mathbf{F}$ via

the downward control principle (Section 1.2.2). The downward control principle relates the forcing above a certain level to the upwelling through that level. Figure 3.11(b) shows the $\overline{w}^*$ obtained from a full downward control calculation (Equation 1.2.2) and Figure 3.11(c) shows the same field obtained directly from the dynamical quantities in the model. Comparing these last two figures shows that the mean residual vertical velocity is consistent with the Eliassen-Palm flux in the model.

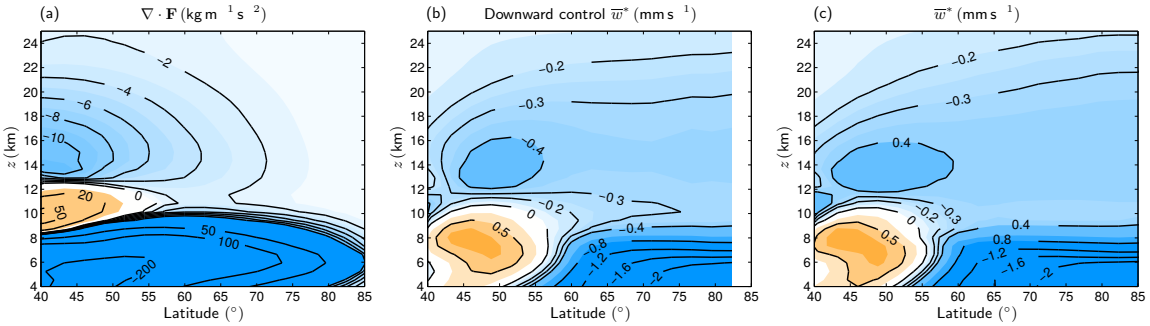


**Figure 3.11:** (a)The term $\nabla \cdot \mathbf{F}$ for the model run with T42L40 and the Held and Suarez restoration profile. (b) The mean residual vertical velocity, $\overline{w}^*$, calculated by applying the full downward control principle using the divergence of the Eliassen-Palm flux shown in (a). (c) The mean residual vertical velocity, $\overline{w}^*$, calculated from the dynamical quantities obtained directly from the model.

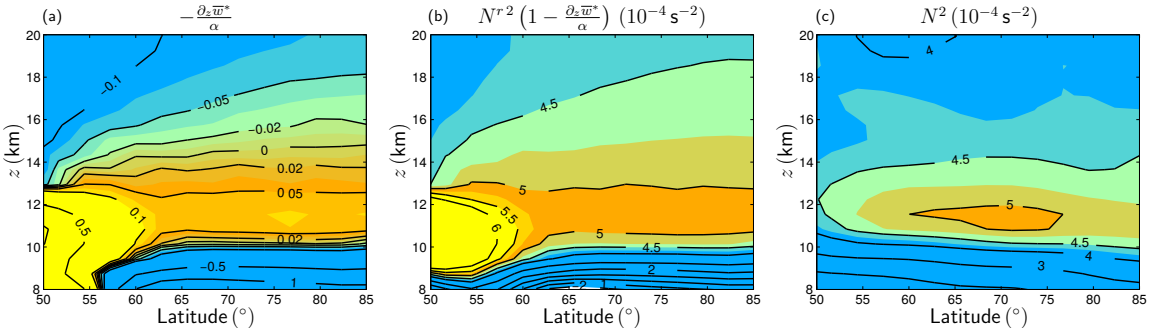


**Figure 3.12:** (a) The term $-\partial_z \overline{w}^*/\alpha$. (b) The static stability estimated as $N^{r\,2}(1-\partial_z \overline{w}^*/\alpha)$ (c) The static stability calculated from the model (same as Figure 3.6). All the plots are for a model resolution of T42L40 using the Held and Suarez restoration profile and averaged over 1000 days.

From Equation 3.6, we expect a maximum in the static stability to correspond to a maximum in $\partial_z \overline{w}^*$ since both $N^{r\,2}$ and $\alpha$ are constant in the region of the TIL. Figure 3.12(a) shows a clear maximum around 12 km where the TIL is located. Comparing the static stability estimated using Equation 3.6, Figure 3.12(b), and that obtained directly from the temperature in the model, Figure 3.12(c), we can see that our expression for the static stability in Equation 3.6 is able to reproduce the location

and magnitude of the TIL to a good approximation. This calculation establishes a clear link between the structure of the static stability in the TIL and the structure in the wave driving. There is a large maximum in the convergence of $\nabla \cdot \mathbf{F}$ in the troposphere and a second weaker region of convergence in the stratosphere. The separation between the two maxima in $\nabla \cdot \mathbf{F}$ is necessary to provide the right pattern of upwelling such that a maximum in static stability emerges just above the tropopause.

We further decompose $\nabla \cdot \mathbf{F}$ into its wavenumber components in an attempt to find out if different processes are contributing to each maximum. To find the EP flux contribution due to a wavenumber, m, we set all the spectral coefficients other than those for wavenumbers m and zero (the mean) to zero after all the time steps have been done in the model and before derived quantities, like the EP flux, are calculated. The model runs with all the wavenumbers but the derived quantities are only calculated for each m. If the components of the EP flux for each value of m are summed, the full EP flux field is obtained. The wavenumber dependence of the EP flux at 65 °N is shown in the contour plots in Figure 3.13(a).

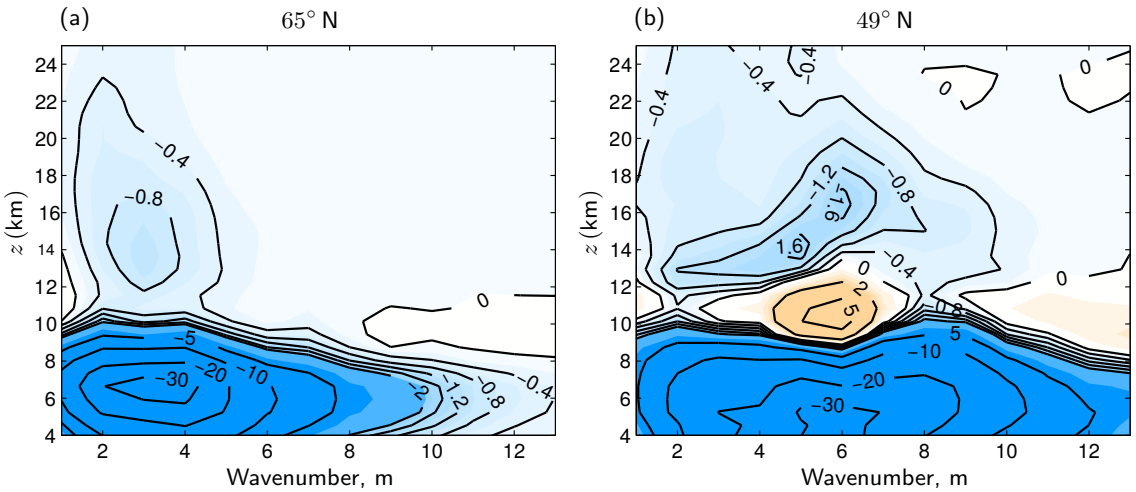


**Figure 3.13:** Contributions to $\nabla \cdot \mathbf{F}$ ($\mathrm{kg\,m^{-1}\,s^{-2}}$), from different wavenumbers for a model resolution of T42L40 with the Held and Suarez restoration profile at (a) 65 °N and (b) 49 °N.

Again, the 2 distinct regions of convergence of the EP flux divergence can be seen and broadly span wavenumbers 1 to 6. We chose to define this range as the region over which the peak value of $\nabla \cdot \mathbf{F}$ (centred around wavenumber 3) drops by a factor of e. We expect the tropospheric maximum to be caused by baroclinic eddies which in a typical primitive equation model would have wavenumber 5 to 7 [Gall (1976)]. This is not the case in our model at 65 °N. At lower latitudes such as 49 °N, the maximum in the EP flux in the troposphere is centred on wavenumber 6, Figure 3.13(b). The

second region of convergence in the stratosphere is also centred on approximately the same wavenumber as the peak in the troposphere for both latitudes. This indicates that the same mechanism may be causing both peaks.

Birner (2010) shows that the only dynamical forcing term to the time dependent static stability budget at the level of maximum static stability is of the form $-\overline{N^2}\partial_z\overline{w^*}$ and argues that the vertical structure of the residual circulation results in a dipole forcing structure with negative $N^2$ forcing just below the tropopause and positive just above. This forcing acts to sharpen the tropopause. Our theory differs in that we associate the static stability structure in the steady state to certain structure in the vertical residual circulation and further relate this to the divergence of the Eliassen–Palm flux via the downward control principle.

In the case of the HSG restoration profile, the TIL is not present. The $\nabla \cdot \mathbf{F}$ profile, Figure 3.14, lacks the second minimum in the stratosphere and has a region of convergence in the stratosphere while the Held and Suarez case has a region of divergence, Figure 3.11(a). The large minimum in the troposphere is still present.

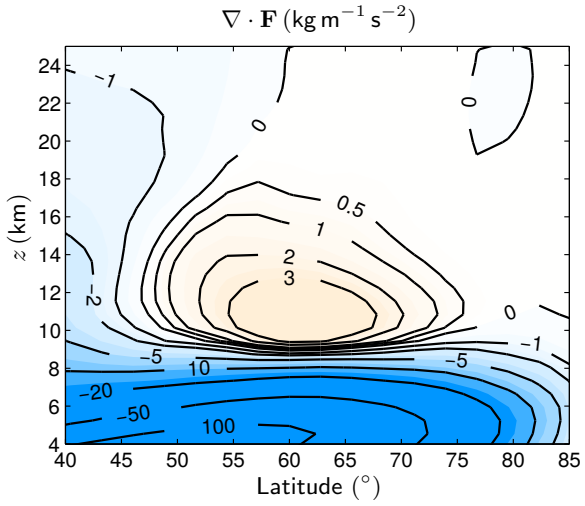


**Figure 3.14:** $\nabla \cdot \mathbf{F}$ in the steady state of the model run with T42L40 and the Haynes, Scinocca and Greenslade restoration profile. Unlike the Held and Suarez (1994) case, there is no separate region of convergence in the lower stratosphere.

We have shown that it is possible for an idealised dynamical model to produce a steady state temperature structure that lacks a TIL by changing the radiative relaxation state. The formation of a TIL depends on a certain dynamical regime where there is a separate region of convergence of the Eliassen-Palm flux in the stratosphere. If this region is absent, a TIL does not form. It is not the case that a TIL is always present in the model independent of the dynamics.

## 3.6 Effects of TB averaging on fluctuations in a profile

Since introduced in the paper by Birner et al. (2002), TB based plots have been widely used in literature describing the TIL. As we have shown in the previous sections, simply averaging static stability profiles does reveal a TIL. In observational data, for instance the CHAMP dataset, there are large fluctuations in static stability that could be attributed to gravity waves. TB averaging lines up the local tropopause in each profile and leading to the peaks in static stability just above the tropopause to coincide with decreasing correlation with height. The end result of compositing is a sharp peak above the tropopause. Model data displays much smaller and smoother fluctuations than observational data and compositing does not result in a sharp TIL. We argue that the lack of sharp TIL in models is not entirely due to the resolution being lower but also from large amplitude small scale vertical wave oscillations of the order of a few kilometres not being present. We attempt to find a class of fluctuations which would result in the significant strengthening and sharpening of the TIL after compositing.

Consider the effect of compositing on small amplitude fluctuations. A set of temperature profiles is generated by adding small fluctuations to a base temperature profile, $T_0$, chosen such that the resulting static stability is monotonically increasing.

For convenience, we will be considering a quantity $N(z)$ which is proportional to the static stability,

$$N(z) = \frac{1}{T}\left[T' + \Gamma\right], \tag{3.7}$$

where the temperature, $T$, is a function of the height, $z$, and $\Gamma$ is a constant (the dry adiabatic lapse rate). $(\cdot)'$ represents a derivative with respect to z.

Consider a set of small random fluctuations, $\delta T(z)$, on an initial temperature profile $T_0(z)$. This causes fluctuations in the tropopause height.

$$\begin{aligned} T(z) &= T_0(z) + \delta T(z), \\ z^T &= z_0^T + \delta z^T, \end{aligned}$$

where $\langle \delta T(z) \rangle = 0$.

Define a new TB coordinate, $\tilde{z}$,

$$\begin{aligned} \tilde{z} &= z - z^T, \\ z &= \tilde{z} + z_0^T + \delta z^T. \end{aligned}$$

In both the base profile and set of profiles with fluctuations, the lapse rate condition determines the tropopause height, i.e.

$$T_0'(z)|_{z_0^T} = -\Gamma, \tag{3.8}$$

$$T'(z)|_{z^T} = -\Gamma. \tag{3.9}$$

We then substitute for $T(z)$ and $z_0^T$ into Equation 3.9 and perform a Taylor expansion about $z_0^T$ to second order in $\delta z^T$. Using Equation 3.8 and averaging over all fluctuations, we can form an expression for $\delta z^T$ to second order,

$$\langle \delta z^T \rangle = -\frac{1}{2} \left. \frac{T_0'''}{T_0''} \right|_{z_0^T} \langle (\delta z^T)^2 \rangle. \tag{3.10}$$

Now consider the effect of this change of coordinates on $N(z)$,

$$\begin{aligned} \langle N(z) \rangle &= \langle (N_0 + \delta N)(\tilde{z} + z_0^T + \delta z^T) \rangle \\ &= \langle N_0(\tilde{z} + z_0^T) \rangle + \langle N_0'(\tilde{z} + z_0^T)\, \delta z^T \rangle + \langle \frac{1}{2} N_0''(\tilde{z} + z_0^T)\, (\delta z^T)^2 \rangle \\ &+ \langle \delta N(\tilde{z} + z_0^T) \rangle + \langle \delta N'(\tilde{z} + z_0^T)\, (\delta z^T) \rangle + O(\delta^3). \end{aligned} \tag{3.11}$$

We will now compute each of the terms in the expression for $N(z)$. $N_0'$ and $N_0''$ can be obtained by differentiating the expression for $N$, Equation 3.7, and comparing the relative magnitudes of the terms. When $\frac{dT}{T} << 1$,

$$N_0' \approx g \frac{T_0''}{T_0}, \qquad N_0'' \approx g \frac{T_0'''}{T_0}. \tag{3.12}$$

Similarly we can derive expressions for $\langle \delta N \rangle$ and $\langle \delta N' \delta z^T \rangle$ in terms of the temperature fluctuations by expanding $\delta N$ to second order in $\delta T$ and $\delta T'$ and averaging. Comparing the magnitudes of the different terms, we find that $\langle \delta T''\, \delta z^T \rangle$ dominates over $\langle \delta N \rangle$ and is given by

$$\langle \delta N'\, \delta z^T \rangle = \frac{g}{T_0(\tilde{z} + z_0^T)} \langle \delta T''(\tilde{z} + z_0^T)\, \delta z^T \rangle. \tag{3.13}$$

Substituting the expressions from equations 3.12, 3.10 and 3.13 into the Taylor

expansion (Equation 3.11), the TB averaged static stability is given by

$$\langle N(z)\rangle = \langle N_0(\tilde{z} + z_0^T)\rangle \; + \Delta N \tag{3.14}$$

where

$$\Delta N = \underbrace{-\, g\, \frac{T_0''(\tilde{z}+z_0^T)}{T_0(\tilde{z}+z_0^T)} \left[\frac{1}{2}\, \frac{T_0'''(z_0^T)}{T_0''(z_0^T)}\right] \langle(\delta z^T)^2\rangle}_{\text{A term}} + \underbrace{\frac{1}{2}\, g\, \frac{T_0'''(\tilde{z}+z_0^T)}{T_0(\tilde{z}+z_0^T)}\, \langle(\delta z^T)^2\rangle}_{\text{B term}}$$

$$+ \underbrace{\frac{g}{T_0(\tilde{z}+z_0^T)}\, \langle \delta T''(\tilde{z}+z_0^T)\, \delta z^T\rangle}_{\text{C term}}\,.$$

Terms A and B depend on the size of the fluctuations in tropopause height and are large in the region where $N$ changes rapidly. Term C is the correlation between $T$ over the whole profile and tropopause height fluctuations. This will be large around the tropopause.

Consider a temperature profile with constant lapse rates in the troposphere and the stratosphere and a smooth transition region in between:

$$\begin{aligned}
T(z) &= a\,(z - z_{10}) + b\, \ln[\cosh(\alpha(z - z_{10}))],\\
T'(z) &= a + b\,\alpha\, \tanh[\alpha(z - z_{10})],\\
T''(z) &= b\,\alpha^2\, \mathrm{sech}^2[\alpha(z - z_{10})],\\
T'''(z) &= -2\,b\,\alpha^3\, \mathrm{sech}^2[\alpha(z - z_{10})]\; \tanh[\alpha(z - z_{10})],
\end{aligned}$$

where $a = -3.5 \times 10^{-3}$, $b = 3.5$, $\alpha = 1 \times 10^{-3}$ and $z_{10} = 10\,\mathrm{km}$.

The following sections describe some numerical experiments to calculate the TB deviation and compare it to that predicted by Equation 3.14.

Note that when the TB deviation in static stability is calculated numerically, we take into accounts the fact that terms in $\langle \delta T\rangle$ and $\langle \delta T'\rangle$ are non-zero and these are subtracted from the numerical value of $\Delta N$.

### 3.6.1 Small amplitude random fluctuations in T

Fluctuations in T are generated by constructing cubic splines between Gaussian distributed random values of $\delta T$ at equally spaced values of $z$ (typical vertical lengthscale of the fluctuations). The Gaussian distribution has a standard deviation of 0.01. Each temperature profile has a different random vertical lengthscale taken from a uniform distribution ranging from 200 m to 800 m.

Figure 3.15 shows that tropopause based averaging produces a deviation in the value of $N$ which agrees with the expression predicted in Equation 3.14. The results show that small amplitude perturbations in a profile, when tropopause averaged, lead to an artificially enhanced static stability peak above the tropopause but also a minimum of a similar magnitude below.

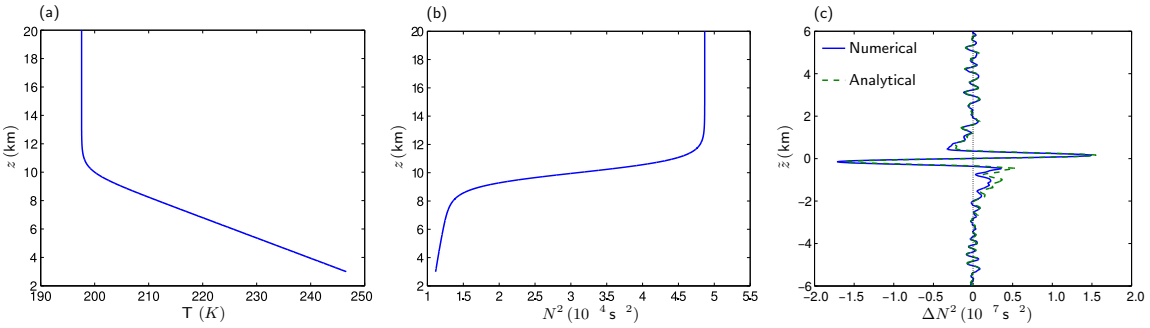


**Figure 3.15:** (a) Idealised temperature profile to which perturbations will be applied. (b) Static stability profile corresponding to (a). (c) Change in the static stability resulting from tropopause based averaging compare to simple averaging for small amplitude random fluctuations to the temperature profile in (a). The numerical result is compared to that predicted in Equation 3.14.

### 3.6.2 Large amplitude fluctuations in temperature

Using the smoothed random fluctuations described above, we test the effect of TB based averaging on large fluctuations in the temperature profile. An additional term is included in the base temperature profile used such that the static stability contains a maximum (TIL) just above the tropopause,

$$T(z) = a\,(z - z_{10}) + b\,\ln[\cosh(\alpha\,(z - z_{10}))] + 3\,[1 + \tanh((z - z_{10}) \times 10^{-3})] \quad (3.16)$$

where $a = -3.5 \times 10^{-3}$ and $b = 3.5$.

The amplitude of the fluctuations follows a random Gaussian distribution along the profile and has a standard deviation of 0.5 K. Each has a typical vertical length scale taken from a uniform distribution ranging from 500 m to 1500 m. These values correspond roughly to the fluctuations that are seen in CHAMP satellite data (Figure 3.4). The base temperature profile is plotted in Figure 3.16(a) and a set of four profiles with fluctuations are shown in Figure 3.16(b). 4000 vertical levels were used in each of the 20000 profiles averaged. The results are robust to increasing the vertical resolution.

Figure 3.16(c) illustrates the resulting deviation from the based static stability profile that emerges after TB based averaging. The results show that for large amplitude fluctuations in the base temperature profile, tropopause based averaging introduces artefacts in the static stability profile by sharpening the TIL but does not increase the strength of the peak. The sample CHAMP profiles, Figure 3.4, suggest that the real fluctuations in temperature may have a larger amplitude and smaller lengthscale just above the tropopause which could lead to a larger composited TIL. Our idealised calculation demonstrates that tropopause based compositing is affected by fluctuations in the data which can lead to the artificial enhancement of the TIL. Whilst this effect can make the TIL more easily distinguishable in observational data, this composited TIL is not relevant to the dynamics.

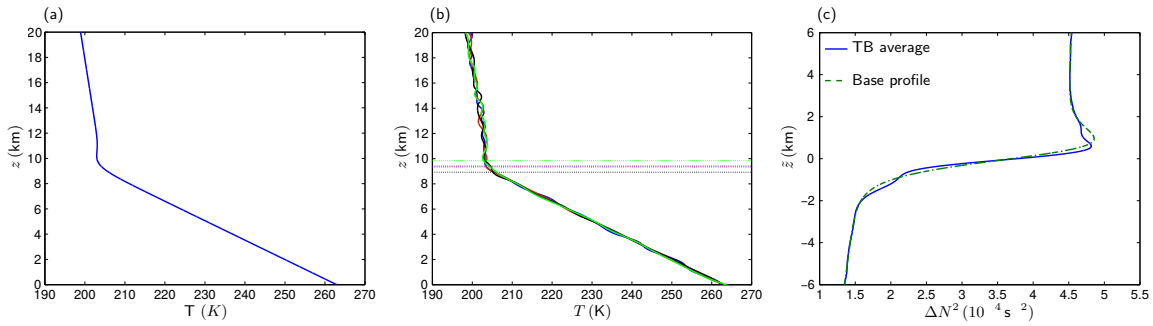


**Figure 3.16:** (a) Idealised temperature profile to which perturbations will be applied. This profile contains a TIL. (b) Example set of profiles with large amplitude perturbations. Horizontal dotted lines represent the tropopause height for each of the profiles. (c) Change in the static stability resulting from tropopause based averaging with large amplitude random fluctuations to the temperature profile in (a). The simple average gives the same static stability as the base profile (not shown).

## 3.7 Discussion

In this chapter, there are two lines of enquiry. The first is based on numerical modelling studies continuing on from the work of Son and Polvani (2007) who demonstrated the formation of a TIL in a dry primitive equation model using the Held and Suarez (1994) restoration profile but did not discuss mechanisms. We reproduce their results and also demonstrate that the model TIL is not significantly sharpened by compositing. Son and Polvani (2007) raise the issue of the sensitivity of the model TIL to resolution and we investigate this by running our model to much higher resolutions and conclude that a natural aspect ratio, given by Prandtl's ratio of scales, can be associated to the dynamics in the model. For instance, increasing the horizontal resolution at fixed vertical resolution will eventually cause profiles of model fields to converge as the vertical resolution becomes a limiting factor.

Son and Polvani (2007) makes use of two distinct restoration profiles and both produce a TIL. Our experiments demonstrate that one can find a restoration profile, similar to that in Haynes et al. (2001), where a TIL does not form.

This study also focuses on the mechanisms by which a persistent TIL forms in the model. Wirth (2003) attributed the TIL to the effect of compositing on transient PV anomalies. Anticyclonic anomalies enhance the static stability above the tropopause and cyclonic anomalies do not. Compositing brings out this asymmetry. Birner (2010) proposed that the only dynamical forcing term in the time dependent static stability equation involves the gradient of the vertical mean residual velocity and the structure of the residual circulation is such that a TIL emerges.

Our proposed mechanism differs in that the $\overline{w^*}$ structure is in the steady state and is shown to correspond to an enhanced static stability. $\overline{w^*}$ can then be linked to the divergence of the Eliassen-Palm flux via the downward control principle and we find that the presence of two separate regions of convergence in $\nabla \cdot \mathbf{F}$, one in the troposphere and the other in the stratosphere, are necessary to the formation of the TIL. This pattern in $\nabla \cdot \mathbf{F}$ is seen in a model run with the Held and Suarez (1994) restoration profile. In contrast, the $\nabla \cdot \mathbf{F}$ field from the Haynes et al. (2001) restoration profile model run only contains one region of convergence in the troposphere and no TIL forms, further supporting our proposed mechanism. It is important to note that our results do not explain the dynamics leading to the regions of convergence occur in the model.

The second line of enquiry focuses on looking more closely at the process of tropopause based averaging. This is relevant to the dynamical significance of the TIL. We analysed the tropopause inversion layer by looking at CHAMP radio occultation data. Simple averaging produces a broad TIL which is sharpened and strengthened when the profiles are composited. Individual temperature profiles show strong short wavelength fluctuations and we have tried to find an appropriate family of fluctuations that would cause a significant TIL signal with compositing. It is hypothesized that the fluctuations in the observational data are aligned in such a way that a sharp spike in static stability is created above the tropopause. This feature is smeared out by simple averaging. Whilst there is some indication from the results that random fluctuations with certain characteristics can sharpen the TIL, there are no clear cases where the fluctuations enhance the static stability to the extent seen in observational data. Thus a preliminary conclusion is that the strong TIL structure is present in the absence of fluctuations and that the main effect of compositing is to cause some sharpening of the TIL without increasing its strength. It remains an open question as to why the composited TIL should be both so strong and sharp and conversely what limits the latter.

In summary, our work highlights the importance of the EP flux structure in causing the TIL and also the need to completely understand how tropopause based averaging affects the shape of the peak.

# Chapter 4

## Structure of tropical upwelling

## 4.1 Introduction

The Brewer-Dobson circulation is recognised as an important component of the chemistry-climate system. In the lower and middle stratosphere the circulation is upward at low latitudes and downward at high latitudes and therefore controls the rate at which chemical species with tropospheric sources are taken into the stratosphere and correspondingly the rate at which species with sources in the stratosphere and mesosphere are removed to the troposphere. Brewer's important paper [Brewer (1949)], deducing the existence of a global-scale circulation on the basis of a small number of extratropical water vapour measurements, noted that if such a circulation existed then an explanation would be needed for the angular momentum balance (but did not attempt to provide such an explanation).

Subsequent theoretical and modelling studies have established the steady component of the Brewer-Dobson circulation (i.e. what would be observed from a multi-year average), as a 'wave-driven circulation in which the Coriolis force associated with poleward flow, is balanced by the wave force due to dissipating Rossby waves and gravity waves (see e.g. Plumb (2002), Butchart et al. (2014)). The relation between the wave force and the circulation is encapsulated in the 'downward control' principle derived by Haynes et al. (1991) who consider the zonally symmetric response of a radiatively damped atmosphere to a prescribed zonally symmetric force. The upwelling or downwelling through a certain level is controlled purely by the distribution of the wave force above that level. In this steady regime a zonally symmetric applied heating will not drive a circulation – the response to such a heating is simply an adjustment in

temperatures such that the applied heating is balanced by a change in the long-wave radiative heating.

While this analysis based on zonally symmetric dynamics makes the important point that there cannot be a circulation without a wave force (or a systematic change in circulation without a change in wave force) it cannot predict the actual response of the real atmosphere or a modelled atmosphere to a zonally symmetric applied heating, which may be that there is a change (through the three-dimensional dynamics of propagating and dissipating waves) in the wave force and that this change will correspondingly drive a steady meridional circulation. A well-known example of this is the response of the middle atmosphere to increased greenhouse gases – the direct forcing of the system is a heating but this results in a change in the wave force and hence a change in the meridional circulation [e.g. Butchart et al. (2010a), Garcia and Randel (2008), Shepherd and McLandress (2010), Butchart and Scaife (2001)]. The decadal changes in meridional circulation due to the ozone hole might provide another example.

This work is motivated by the low-latitude structure of the upwelling meridional circulation in observations and certain model simulations. A feature of the upwelling velocity is the presence of two local maxima at about 20° N-S in the ERA-Interim reanalysis dataset as shown by Seviour et al. (2012) (Figure 4.1(a)). The feature of the upwelling is seen in the multi model mean of the Coupled Model Intercomparison Project 5 (CMIP5) ensemble as can be seen in Figure 4.1(b) taken from Hardiman et al. (2014) (their Figure 5). In both the ERA-Interim data and the CMIP5 ensemble, whilst the region and strength of the upwelling is modulated by the seasonal cycle, the two distinct maxima in upwelling are present year round. It is also present in various of the coupled chemistry-climate models [Butchart et al. (2010b),Butchart et al. (2006)].

Figure 4.2(a) shows different measures of the upwelling at 70 hPa calculated from ERA-Interim fields. The solid line shows the mean residual vertical velocity, $\overline{w}^*$, calculated from the meridional velocity and temperature. Equation 1.6a is used to calculate $\overline{v}^*$ from $v$ and $\theta$. The residual mass streamfunction, $\psi$ is computed from the pressure integral $\psi = \int_{\mathrm{TOA}}^{p} \overline{v}^* \, \mathrm{d}p'$ (TOA denoting the top of the atmosphere). $\overline{w}^*$ is then obtained from $\psi$. This method means that $\overline{w}$, a noisy field in ERA-Interim, does not enter the computation and $\overline{w}^*$ is obtained through mass balance from $\overline{v}^*$. The calculated $\overline{w}^*$ is in good agreement with that shown by Seviour et al. (2012). The dashed line shows the upwelling inferred from the total diabatic heating rates, i.e.

**Figure 4.1:** (a) [Figure 4(a) from Seviour et al. (2012)] Monthly and latitudinal variations of monthly mean $\overline{w}^*$ at 70 hPa for ERA-Interim data for 1989-2009. Contours are in units $\mathrm{mm\,s^{-1}}$, with the zero contour in bold. Dashed contours represent negative values. (b) [Figure 5 from Hardiman et al. (2014)] The multi-model mean (MMM) seasonal cycle of the latitudinal distribution of $\overline{w}^*$ $\mathrm{mm\,s^{-1}}$ at 70 hPa, averaged 1960-2000 (historical simulations).

the 'diabatic residual-mean vertical velocity' defined by (8) of Butchart et al. (2014). Both methods of calculating the mean residual vertical velocity show that there are two local maxima in the upwelling at 70 hPa centred around 20° N and 20° S. This calculation is intended as a simple estimate of the upwelling from the diabatic heating and we do not impose the constraint that the globally averaged upwelling is zero. A 95 % confidence interval is also shown as a shaded region using an adjusted Student's t-test as described in Section 2.6.

A similar double peak structure is present in the diabatic heating rates at these levels in ERA-Interim [Fueglistaler et al. (2009b)]. Figure 4.2(b) show the total diabatic heating rate plotted as a difference from the equatorial value (this is helpful in emphasising latitudinal variations, particularly for quantities that have a large vertical gradient). The latitudinal structure in the heating rates is also present in other reanalysis datasets such as the Modern Era Retrospective Analysis for Research and Applications (MERRA) dataset and the Climate Forecast System Reanalysis (CFSR) but with less pronounced peaks [Wright and Fueglistaler (2013)] as shown in Figure 4.3. The structure and magnitude of the peaks vary with seasons and with the phase of the quasi-biennial oscillation (QBO) [Fueglistaler et al. (2009b)], but they are present in the multi-year average and are not simply associated with a particular phase of the seasonal cycle or of the QBO. The double peak of upwelling has to be consistent with the angular momentum transport, and, for example, off-equatorial maxima in upwelling might arise if the planetary scale and synoptic scale Rossby

waves propagating from mid-latitudes dissipated in the subtropics so that the resulting westward wave force was confined away from the Equator.

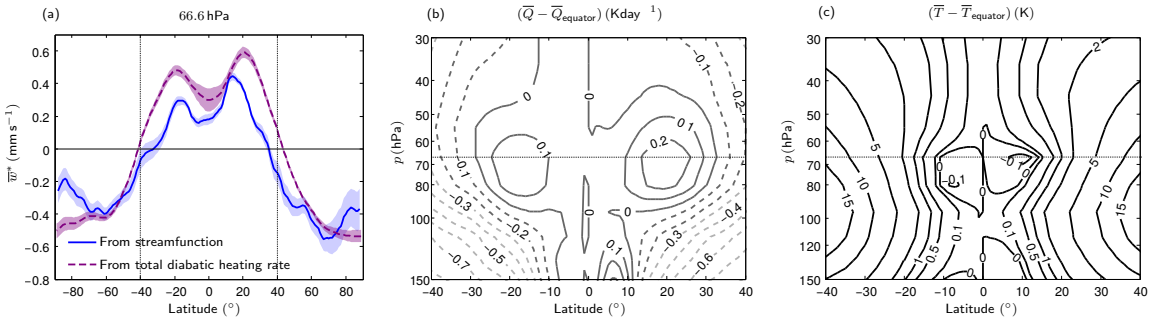


**Figure 4.2:** Zonally and time averaged ERA-Interim data from 1991 to 2010. (a) Plot of the mean vertical residual velocity ($\mathrm{mm\,s^{-1}}$) at 66.6 hPa. The 95% confidence intervals are calculated from an adjusted Students' t-test. (b) Heating rate ($\mathrm{K\,day^{-1}}$) difference from the value at the Equator (c) Temperature difference (K) from the temperature at the Equator. Dotted lines are intended as guides for the pressure level of 66.6 hPa and the latitude range 40° N-S plotted in (b) and (c).

**Figure 4.3:** [Top row of Figure 2 from Wright and Fueglistaler (2013)] Zonal mean total diabatic heating averaged over the period 2001-2010 according to the (a) MERRA, (b) ERAI, (c) CFSR, (d) JRA, and (e) NCEP reanalysis data sets. The 340, 350, 380, and 450 K isentropic surfaces from each reanalysis are shown as black contours.

In contrast, the temperature does not have the same latitudinal structure across the Equator, as shown in Figure 4.2(c). The difference from the equatorial value is only about 0.1 K at 15° N–S and about 2 K at 25° N–S and furthermore the temperature increases away from the Equator. Therefore an estimate of the contribution of the local temperature to the diabatic heating through a Newtonian cooling approximation would imply, relative to the Equator, cooling rather than heating at the location of the peaks. Furthermore estimates of the radiative timescale in this region range between 25 days [Hitchcock et al. (2010)] and 100 days [Mlynczak et al. (1999), Randel et al. (2002)]. Even with the smallest estimate of 25 days the corresponding difference in heating would be less than 0.1 $\mathrm{K\,days^{-1}}$, i.e. not only of the wrong sign but modest compared to the magnitude of the peaks shown in Figure 4.2(b).

However, consistency is not the same as deducing a mechanism for the pattern of

upwelling. It is natural to think of the upwelling as being caused by the dynamics. Consider a situation where the wave dynamics give rise to a distribution of wave force that is suitably confined away from the Equator and leads to off-equatorial maxima in upwelling (and a corresponding equatorial minimum). Within the downward control framework, an applied force will generate a circulation. In order to satisfy the thermodynamic budget, a diabatic term is needed. In a background atmosphere where the radiative relaxation temperature has very little structure across the tropics, for the diabatic heating to have the observed structure, the downward control framework would require that it arises from the temperatures adjusting. This argument is broken by the fact that the temperatures are observed to lack such fine scale meridional structures. The observed temperatures from the ERA-Interim reanalysis dataset are also relatively independent of latitude.

An alternative would be that there is some structure in the radiative relaxation temperature and the waves cause an upwelling with just the right dynamical heating to flatten the temperature gradients. It is unlikely that these two effects always produce a flat temperature structure by pure coincidence. It is more likely that the diabatic heating and the torque from the waves are related and the aim of this study is to gain an understanding of the structure of the tropical upwelling by considering a diabatic term that contributes to the forcing in the system.

The aim of the work reported in this chapter is to determine the cause of the observed double peak in upwelling (or equivalently diabatic heating). The structure is as follows. In Section 4.2, we review the structure of the upwelling, temperature and diabatic heating in ERA-Interim data and show that the wave force is indeed consistent with the double-peak structure in upwelling. Then in Section 4.3, we consider in more detail at how the pattern in diabatic heating rates seen in ERA-Interim data arises, first by considering contributions from individual processes to the total diabatic heating rate and then using an off-line radiative code to gain further insight into how the long-wave heating is determined by the temperature field and by the concentrations of different radiatively active constituents. The diagnostic calculations carried out in these two sections do not by themselves establish the cause of the double peak structure, but they are very useful in motivating a relevant dynamical investigation of the response of the lower stratospheric circulation to imposed heating perturbations. A heuristic dynamical discussion is presented in Section 4.4 and identifies a potentially relevant response in which imposed heating is balanced by upwelling. Section 4.5 describes an idealised model experiment which verifies this response and Section 4.6 describes an extended set of experiments which, by varying the parameters defining the imposed

heating field, clarifies the conditions under which it occurs.

The findings of Sections 4.4-4.6 are also relevant to understanding the response to an imposed mechanical forcing, rather than an imposed heating, and this problem is discussed briefly in Section 4.7. This relates to recent discussions of the driving of the Brewer-Dobson circulation by Cohen et al. (2013, 2014). Finally Section 4.8 contains a discussion of some of the main findings and gives some conclusions.

## 4.2 Off-equatorial maxima in upwelling

In this section we will demonstrate that there are two local maxima in the upwelling in the tropics at 70 hPa and that the features are consistent with the angular momentum distribution. We make use of the downward control approach [Haynes et al. (1991)] (Section 1.2.2) with careful treatment of the region close to the Equator.

Data is taken from the ERA-Interim dataset [Dee et al. (2011)] covering the period 1991 to 2010. The data at a horizontal resolution of 1° and is produced at 6-hourly analysis time intervals (0000, 0006, 0012 and 0018 UTC). For the calculation of the upwelling, we make use of the data provided on 37 pressure levels. The European Centre for Medium-range Weather Forecasts (ECMWF) also provides diabatic and physics tendencies from the forecast model used to generate the ERA-Interim dataset, accumulated over 12-hour periods with the same horizontal resolution. These diabatic tendencies are provided on 60 model eta (hybrid) levels and are interpolated to 60 pressure levels taking account of surface pressure data. In the following we shall refer to these tendencies simply as ERA-Interim diabatic heating rates.

The observed structure in upwelling is consistent with angular momentum transport. We can make use of the downward control principle [Haynes et al. (1991)] to calculate the upwelling from the divergence of the Eliassen palm flux, $\nabla \cdot \mathbf{F}$, in ERA-Interim. Figure 4.4 shows the upwelling calculated using both the full integral (Equation 1.2.2) and the QG approximation (Equation 1.15). ERA-Interim also provides a zonal wind tendency field that is the momentum forcing due to unresolved processes (including gravity wave drag), bearing in mind that in models there is often a significant contribution to the driving of the Brewer-Dobson circulation from parametrised processes (e.g. Butchart et al. (2011)). The tendency leads to a force on the atmosphere and the part associated with gravity waves is a part of $\nabla \cdot \mathbf{F}$ in equation 1.2.2. The addition of this tendency to the zonal wind into the full integral does not change the upwelling

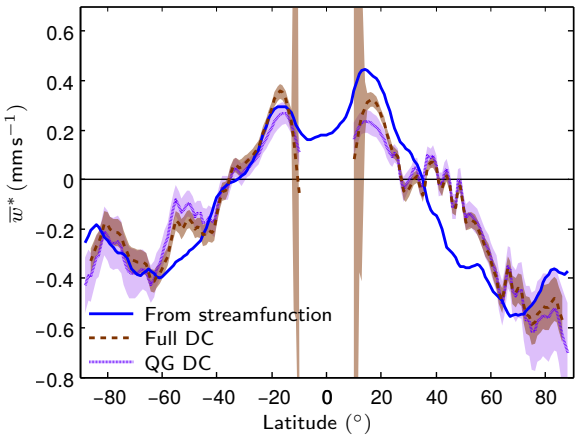


**Figure 4.4:** Plot of the mean vertical residual velocity (mm s$^{-1}$) at 70 hPa from ERA-Interim calculated directly from the streamfunction (same as in Figure 4.2) and from the Eliassen-Palm fluxes using the full and quasigeostrophic approximation to the downward control integral. For the last two lines, 95% confidence intervals are calculated from an adjusted Students' t-test. The uncertainty diverges for the full downward control case as the meridional gradient in angular momentum becomes small.

calculated to within the uncertainty in the calculations in region of interest (around latitude 20°) and these results are not included in Figure 4.4.

The QG and full calculations agree in the extratropics. In the tropics, the structure in the angular momentum contours affects the value of upwelling computed and the full integral produces an upwelling that is about 0.1 mm s$^{-1}$ larger at the location of the double peaks. The uncertainty in the full downward control integral is large close to the Equator since the meridional gradient of the angular momentum, $\overline{m}_\phi$ becomes small and strong serial correlations in the data from the annual cycle and quasibiennial oscillation result in a small number of degrees of freedom remaining in the 20 year dataset used. The term **J** (see Section 1.2.2), which represents the time varying components of the streamfunction and angular momentum, is not included in this calculation as this quantity is only comparable to $\nabla \cdot \mathbf{F}$ in the region within 5° of the Equator and its contribution is dominated by the uncertainty in the data.

Although the uncertainty in the downward control calculations becomes large near the Equator, a double peak structure in the upwelling in the tropics is present in both calculations, demonstrating that the wave force, as represented by ERA-Interim data, has a structure consistent with the upwelling. In the data, the resolved part of the wave force is important and the parametrised tendencies do not play a role in the tropics. The contribution of the **J** term is dominated by uncertainty in the ERA-Interim dataset but not in the longer models runs shown later in this work.

## 4.3 Origin of the diabatic heating structures at 70 hPa

As noted previously, there is a corresponding double peak structure in the diabatic heating rates at the same location as those in the upwelling. Using offline radiative calculations we will explain how the double peak structure in the heating emerges and to what extent it can be regarded as externally imposed. The difference between the total ERA-Interim diabatic heating rate and the equatorial value has previously been shown in Fig. 4.2(b). Fig. 4.5(a) shows the corresponding field without subtracting the equatorial value. The double peak structure at about 70 hPa with maxima centred around 20° N–S is clear. The ERA-Interim also provides individual radiative components of the diabatic heating. These are clear sky (radiative transfer without clouds) heating and an all sky (with clouds) heating, each further divided into shortwave (SW) radiation and longwave (LW) contributions. The non-radiative components which represent a combination of latent heating and diffusive and turbulent heat transport can be computed as a residual (Fueglistaler et al., 2009b). The total contribution from radiative processes is shown in Fig. 4.5(b) which is composed of the clear sky shortwave (Fig. 4.5(c)), the clear sky longwave (Fig. 4.5(d)) and the net heating (LW and SW) from clouds (Fig. 4.5(e)). Fig. 4.5(f) shows the non radiative components.

### 4.3.1 Clear sky shortwave

Fig. 4.5(c) shows the SW clear sky contribution. There is a strong increase with height, but also a latitudinally varying part which increases away from the Equator and hence contributes to the double peak structure. These features are reproduced by the offline calculation. The shortwave scheme in the ERA-Interim reanalysis is based on a two-stream method by Fouquart and Bonnel (1980). For the offline clear sky shortwave (SW) calculations, we instead use the Zhong and Haigh shortwave code (Zhong and Haigh, 1995). A three point Gaussian quadrature method is used to account for the diurnal variation in the solar zenith angle. The albedo is taken from ERA-Interim.

The results are shown in Fig. 4.6(a). The radiative calculation uses zonally and time averaged (1991 to 2010) climatologies of water vapour and temperature and the

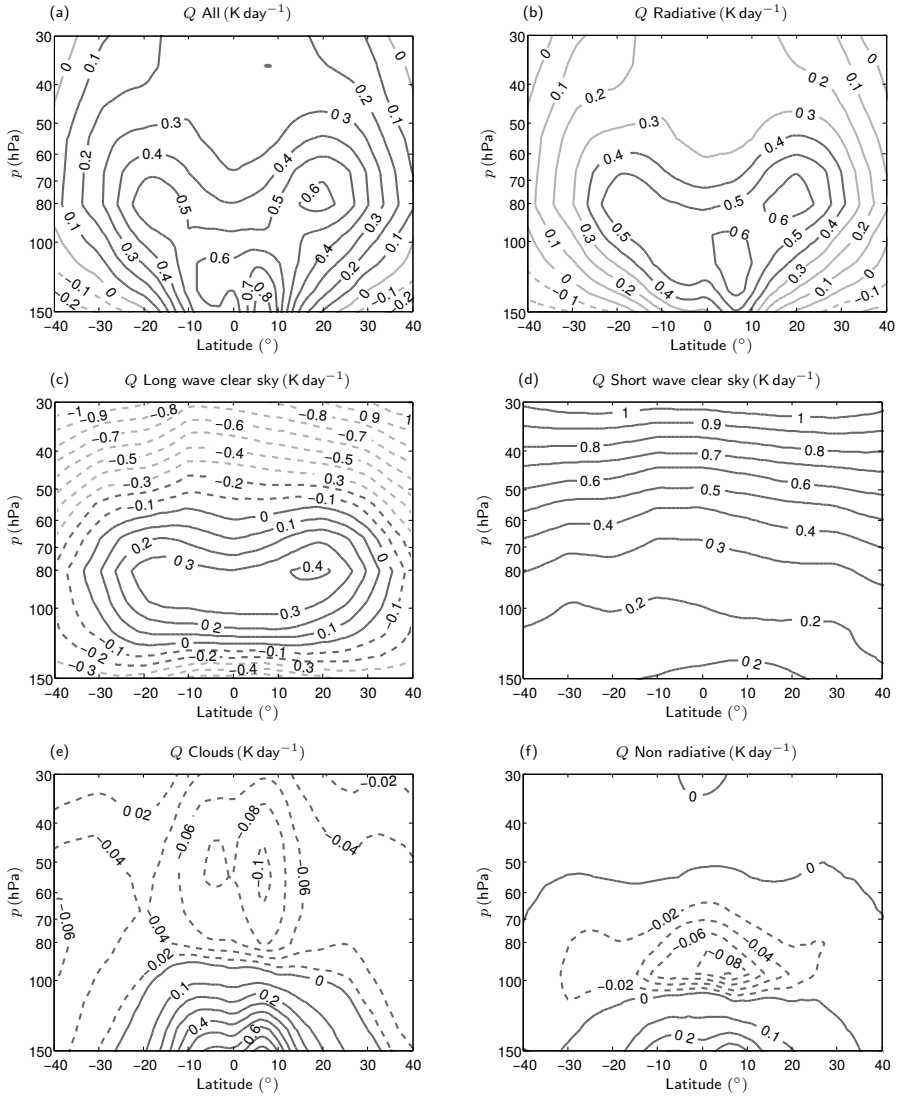


**Figure 4.5:** Zonal mean diabatic heating rates ($\mathrm{K\,day^{-1}}$) from ERA-Interim averaged over the years 1991 to 2010. (a) Total diabatic heating rate. (b) All sky diabatic heating rate from radiative processes. Equal to the sum of (c), (d) and (e). (c) Clear sky shortwave heating rate. (d) Clear sky longwave heating rate. (e) Radiative contribution from clouds (both in the LW and SW). (f) Non radiative, diabatic processes calculated as a residual ((a) - (b)). Contour intervals are $0.1\,\mathrm{K\,day^{-1}}$ with additional contours at $0.02\,\mathrm{K\,day^{-1}}$ for the negative values in (e) and (f).

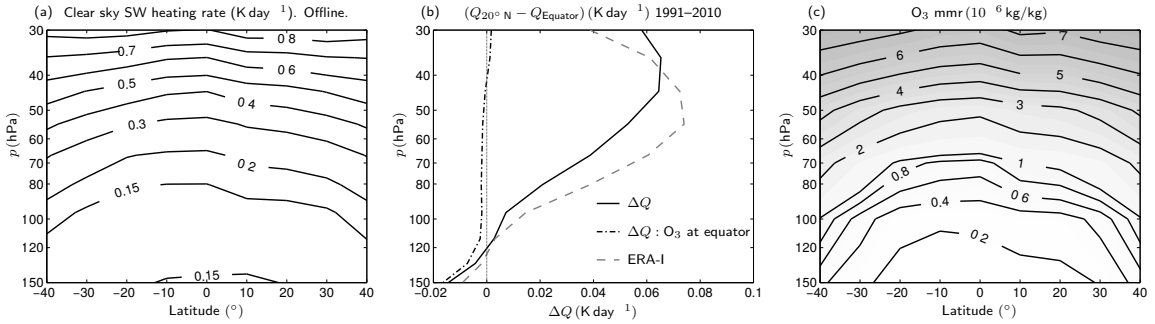


**Figure 4.6:** (a) Zonal mean clear sky shortwave heating rates ($\mathrm{K\,day^{-1}}$) obtained from an offline calculation with the Zhong and Haigh (1995) radiation code. (b) Difference between 20° N and the Equator of the zonal mean diabatic heating rate. The solid line is using the same data as in (a). For the dash-dotted line, ozone is kept at the values at the Equator. The dashed line is using ERA-Interim clear sky shortwave data. (c) Zonal and time mean Fortuin and Kelder ozone climatology.

monthly mean Fortuin and Kelder ozone climatology. [1] The calculation is done daily and the heating rates are time averaged. There are small differences between the offline calculation (Fig. 4.6(a)) and the ERA-Interim values (Fig. 4.5(c)) of about $0.1\,\mathrm{K\,day^{-1}}$ at 70 hPa which are likely to be due to the use of a zonally averaged water vapour climatology and differences in the radiation code.

Fig. 4.6(b) shows the difference in the heating rate between 20° N and the Equator according to the offline calculation (solid curve) and according to ERA-interim (dashed curve). There is a contribution of about $0.05\,\mathrm{K\,day^{-1}}$ to the total diabatic heating shown in Fig. 4.2(b). This contribution is primarily due to the latitudinal gradient in ozone evident in Fig. 4.6(c). The offline radiative calculation is repeated at 20° N with the ozone profile held fixed at the equatorial profile and the difference between the clear sky shortwave heating at 20° N and the Equator is shown as the dash-dotted line. This difference therefore results only from the latitudinal variation in incident shortwave radiation and, as can be seen, it is negligible. Hence, the latitudinal gradient in ozone plays the dominant role in determining the latitudinal gradient in the clear sky shortwave heating rates. The ozone gradient is also present in more recent climatologies such in HALOE and MLS measurements (not shown).

[1] ERA-Interim uses the older Fortuin and Langematz (1994) ozone climatology instead. The offline heating rates obtained using this climatology are in better agreement with the ERA-Interim heating rates and the results can be found in Ming et al. (2016a). The use of a different ozone climatology in this thesis does not change the main conclusions in this Chapter.

### 4.3.2 Clouds and non-radiative effects

The radiative effect of clouds on the lower stratosphere, Fig. 4.5(e), is essentially that optically thick clouds in the upper troposphere suppress the upwelling longwave radiation and hence reduce long-wave heating due to ozone absorption in the lower stratosphere (Doherty et al., 1984; Hartmann et al., 2001; Gettelman et al., 2004). The reduced longwave heating effect of clouds in the lower stratosphere is largest at the Equator and hence acts to increase the latitudinal gradients away from the Equator in the double peak structure. Non-radiative diabatic effects, shown in Fig. 4.5(f), are important near the tropopause. Although their contribution decreases rapidly with height above 90 hPa, they lead to a relative cooling at 70 hPa over the Equator of a magnitude similar to the cloud effect. The contribution of the different components of the diabatic heating to the double-peak structure is summarised in Fig. 4.7 by showing for each component the difference between 20° N and the Equator as a function of height. At 70 hPa, there is a 0.29 K day$^{-1}$ difference in the heating between 20° N and the Equator, of which 0.18 K day$^{-1}$ is due to the clear sky longwave, 0.06 K day$^{-1}$ due to the clear sky shortwave, 0.02 K day$^{-1}$ from the cloud effect and remainder from non-radiative effects.

### 4.3.3 Clear sky longwave

Since from the above it appears that the clear sky longwave component is a large contributor to the overall double peak structure in the heating, we now analyse this component further to establish how it arises from the distribution of temperature and trace gas concentrations using the RRTM radiation code as described in section 2.5.2.

We will first demonstrate that it is possible to reproduce the double peak structure seen in the longwave clear sky radiative heating rates in ERA-Interim using an offline calculation with the longwave RRTM radiation code. A single year (2000) is chosen as it allows a comprehensive approach where the radiative calculation is carried out daily and independently at twelve equally spaced longitudes.

Fig. 4.8(a) and (b) compares the zonally averaged clear sky longwave heating rate for the year 2000 from ERA-Interim and the offline RRTM calculation. Both are plotted as differences from the equatorial value. The offline calculation shows that it is possible to reproduce the double peak structure in the LW heating although the values at the peak of the heating are about 30% smaller than in ERA-Interim. Further

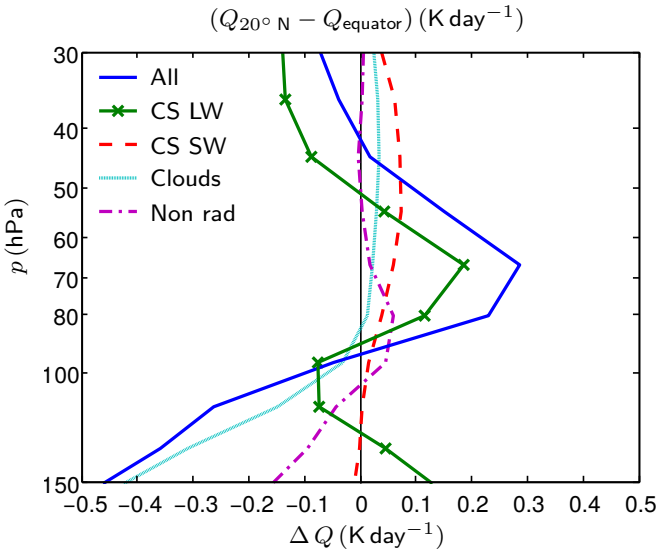


**Figure 4.7:** Difference between the zonal mean diabatic heating rates ($\mathrm{K\,day^{-1}}$) at 20° N and the Equator from ERA-Interim averaged over the years 1991 to 2010. The dashed line for the clear sky shortwave is the same as that in Fig. 4.6.

radiative calculations show that the contribution to the heating rate in this region from nitrous oxide, methane, CFC-11 and CFC-12, as prescribed in ERA-Interim, is negligible. Background stratospheric aerosols were not included but their radiative impact, estimated using results reported by Ramachandran et al. (2000), suggests that the diabatic heating rate contribution in the region of the double peak in heating is of an order of magnitude smaller.

We will now demonstrate that it is possible to reproduce the double peak structure seen in the long wave clear sky radiative heating rates in ERA-Interim using an offline calculation. In this analysis we make use of off-line calculations with the rapid radiative transfer model (RRTM) code [Mlawer et al. (1997)]. A similar radiation code is used by the version of the ECMWF model that is the basis for the ERA-Interim reanalysis dataset [Morcrette et al. (2001)]. RRTM employs a correlated-k approach to calculate the heating rates where the k coefficients are obtained directly from a line by line code (LBLRRTM). Within the ERA-Interim reanalysis calculation the radiative code uses an imposed Fortuin and Kelder (1998) ozone climatology and the water vapour that is calculated through the assimilation process. For the off-line calculation with the RRTM radiative code we therefore provide as input the daily zonal averages from the same Fortuin and Kelder (1998) ozone climatology and ERA-Interim water vapour and temperature and set the carbon dioxide mixing ratio everywhere to 370 ppmv. The input fields to the radiation code are on pressure levels corresponding to the

60 model levels used by the ECMWF model. Ozone from the Fortuin and Kelder (1998) climatology is linearly interpolated to these pressure levels. A surface emissivity of 0.99 was used and the surface temperature was set to the skin temperature from ERA-Interim.

A single year (2000) is chosen as it allows a comprehensive approach where the radiative calculation is carried out daily and independently at a twelve equally spaced longitudes. The double peak in heating in ERA-Interim is present year round but the size of the peak compared to the value at the Equator is modulated by an annual cycle and by inter-annual variations such as the QBO [Fueglistaler et al. (2009b)]. We will discuss the year to year temperature variability further at the end of this section. Figure 4.8(a) shows the offline calculation from RRTM of the clear sky longwave heating rate at latitude 10° N, longitude 60° E and time 12:00 on 1 January 2000 (solid line) as an example. The ERA-Interim dataset contains temperature tendencies that are accumulated for six hours. The dotted and dashed lines show two estimates of the heating rates at 12:00 from ERA-Interim using tendencies accumulated from 12:00 to 18:00 and from 06:00 to 12:00 respectively. The overall agreement of the offline calculation with the ERA-Interim data is good with some differences at the top of the model and the surface. Surface differences are likely due to a surface emissivity values being different (we use a constant value of 0.99). The differences at the top could be due to the way the top of the atmosphere fluxes are handled in the offline radiation code being different to the model. The offline code produces no longwave heating at the top model level. The inset in Figure 4.8(a) focuses on the region of interest around 70 hPa and shows that the offline calculation is able to reproduce the ERA-Interim heating rates in the tropical lower stratosphere at a single location. Similar results are obtained for other locations in the tropics.

Figure 4.8(a) and (b) compares the zonally averaged clear sky long wave heating rate for the year 2000 from ERA-Interim and the offline RRTM calculation. Both are plotted as differences from the equatorial value. The offline calculation shows that it is possible to reproduce the double peak structure in the LW heating although the values at the peak of the heating are about 30% smaller than in ERA-Interim. Further radiative calculations show that the contribution to the heating rate in this region from nitrous oxide, methane, CFC-11 and CFC-12, as prescribed in ERA-Interim, is negligible. Background stratospheric aerosols were not included but their radiative impact, estimated using results in Ramachandran et al. (2000), suggests that the diabatic heating rate contribution in the region of the double peak in heating is of an order of magnitude smaller. We have not attempted to completely reproduce the

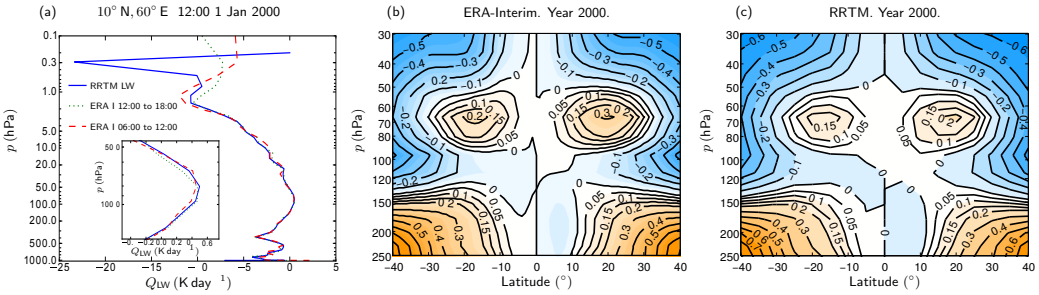


**Figure 4.8:** Long wave clear sky diabatic heating rates for the year 2000. (a) At a single location from RRTM and ERA-Interim. Inset shows the same data but focussing on the region around 70 hPa. (b) Zonally averaged ERA-Interim data (c) Calculation with the RRTM radiation code, using the Fortuin and Kelder ozone climatology and daily values of water vapour and temperature from ERA-Interim and a $CO_2$ mixing ratio of 370 ppmv. The calculation is done on 12 longitudes and zonally averaged. More details can be found in the main text.

ERA-Interim heating as the main focus of this section is to show that the double peak feature is not an artefact of the reanalysis process.

To understand how the structure of the double peak in heating arises in the climatological mean, we run a set of one dimensional radiative calculations with data averaged between 1991 and 2010. For these multi-year, time and zonally averaged profiles of temperature, water vapour and ozone are used to produce the clear-sky longwave heating rate at the Equator. The calculation is repeated using the temperature profile from 20° N whilst keeping the water vapour and ozone profiles at the values on the Equator. The mixing ratio for carbon dioxide and other trace gases is the same as in previous calculation. The difference between these two calculations is shown in Figure 4.9 by curve A, which shows the contribution of the latitudinal temperature difference between 20° N and the Equator to the difference in heating rate. The contributions of the latitudinal differences in ozone and in water vapour indicated by Curves B and C, calculated in a similar way to A but with ozone and water vapour individually being changed rather than temperature. The sum of the three contributions is shown as curve A+B+C and gives very good agreement to the total heating rate at 20° N implying that the contributions may be captured by a linear calculation. The effect of overlapping spectral bands Clough and Iacono (1995) therefore appears to be small in this region.

At 73 hPa, the latitudinal difference in heating rate is 0.13 $\mathrm{Kday}^{-1}$ of which 0.08 $\mathrm{Kday}^{-1}$ comes from the latitudinal difference in ozone. The contribution from the latitudinal difference in temperature is 0.03 $\mathrm{Kday}^{-1}$ and the remainder comes from water vapour. The ozone contribution arises from the fact that in the tropical lower stratosphere,

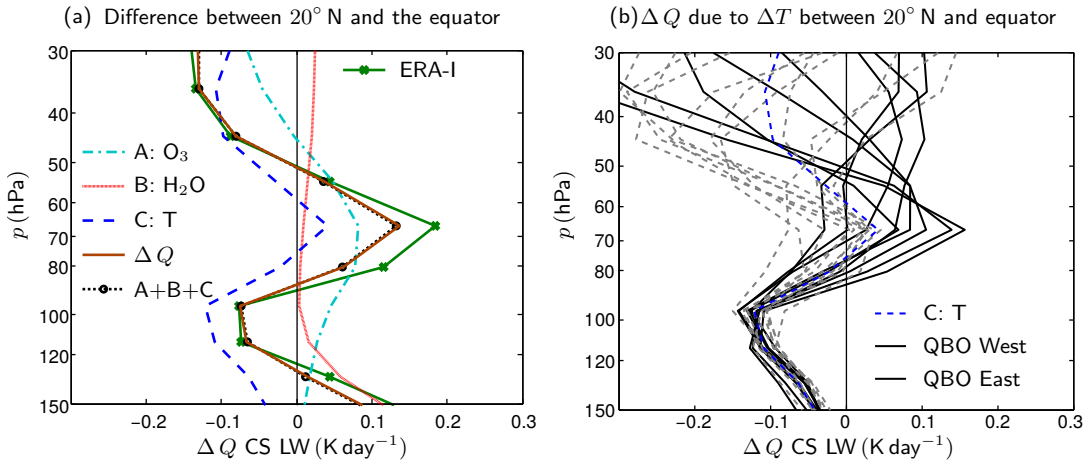


**Figure 4.9:** (a) Radiative calculations using the RRTM code to show the effect of the meridional gradients in temperature and ozone between the Equator and 20° N on the long wave heating rate. Profiles of temperature, ozone and water vapour input into the radiation code are averaged zonally and between 1991 to 2010. Curve A is the difference in long wave heating rate calculated at the Equator from using the ozone profile at 20° N with water vapour and temperature held at equatorial values. Curves B and C are similar to A but for the water vapour and temperature meridional gradients respectively. The solid line labelled $\Delta Q$ is the difference in heating between the two latitudes taken from the same calculation as for Figure 4.8(b). For reference, the same plot of clear sky long wave heating rate difference from ERA-Interim is shown as a solid grey line. (b) Similar calculation used in (a) to produce Curve C but repeated for each of the twenty years in 1991 to 2010 separately and classified depending on the QBO phase (based on the sign of the zonal mean zonal wind at 50 hPa and the Equator). Curve C is repeated in this plot.

around 73 hPa, there are larger ozone mixing ratios and hence more effective absorption of upwelling long-wave radiation off the Equator than at the Equator. The radiative calculation also shows that there is more cooling over the Equator due to water vapour in the region of interest but this is of secondary importance.

The latitudinal temperature difference leads to a relative warming in the longwave at 73 hPa, notwithstanding the fact that at this level, as noted previously, temperatures are higher at 20° N than on the Equator, Figure 4.2(c). The explanation is provided by the vertical non-locality of the dependence of heating rate on temperature. Figure 4.10 shows the contribution to the difference between 20° N and the Equator in clear-sky long wave heating rate at 73 hPa from the corresponding temperature at each of the individual pressure levels. Ozone and water vapour profiles are held at their equatorial values and radiative calculations are carried out at the Equator with the temperature at individual pressure levels perturbed to the value at 20° N. The difference in heating rate as a result of this perturbation is then plotted against the pressure level of the perturbation. The individual contributions add linearly, i.e. the sum of the heating

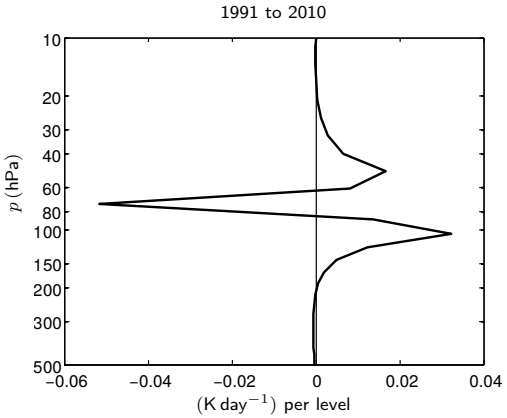


**Figure 4.10:** Plot of the contribution to the clear-sky long wave heating rates from the temperature difference between 20° N and the Equator from individual pressure levels using the RRTM LW code with ERA-Interim data averaged from 1991 to 2010.

rate changes due to all pressure levels as shown by the solid curve will give the total contribution from temperature to the clear sky long wave heating at 73 hPa. The solid curve shows that the positive contribution of latitudinal difference in temperature (at all levels) to latitudinal difference in heating at 73 hPa comes from layers above and below 73 hPa which dominate the local effect of the latitudinal difference in temperature at the 73 hPa itself. The non local temperature effect, particularly in the region below 100 hPa, is decoupled from the dynamical processes around 70 hPa and forms part of the diabatic forcing in the long wave at that level.

There is a significant amount of inter-annual variability in the temperature contribution to the peak in heating around 70 hPa. Additional radiative calculations using individual years from 1991 to 2010 give a temperature contribution ranging from $-0.08\,\mathrm{K\,day^{-1}}$ to $0.16\,\mathrm{K\,day^{-1}}$ at 70 hPa as shown in Figure 4.9. A rough classification depending on the phase of the QBO is shown and we use the annual averaged zonal mean zonal wind at the Equator and 50 hPa to do so following a similar method in Holton and Tan (1980) to illustrate the significant influence of the QBO at 70 hPa. This is consistent with the significant modulation of the heating rate noted by Fueglistaler et al. (2009b), but we emphasise again that the double peak in heating is a clear feature of the time average.

In the above we have shown that the major contributions to the double-peak structure in diabatic heating are the latitudinal variations in ozone concentration which give rise to a corresponding variation in heating due to long-wave absorption and the latitudinal variations in temperature in the atmospheric layers below and above the level of the double peak. The latitudinal variation of temperature at the level of

the double peak in heating itself if anything acts to reduce the double peak. This motivates the hypothesis that the double peak in heating, which is largely confined to the 90 hPa to 60 hPa layer is forced by aspects of radiative heating that are external to the temperature structure and indeed the dynamics of that layer, in particular by the ozone concentrations within that layer and by the temperature structure in the layers above, in the middle stratosphere, and below, in the upper troposphere. This hypothesis motivates the dynamical study reported in the following sections of this chapter.

## 4.4 Dynamical considerations

For a dynamical interpretation of the above we turn to the transformed Eulerian mean equations (equation 1.7) in spherical coordinates and log pressure coordinates, which in the steady-state limit take the form:

$$\frac{1}{a\,\cos\,\phi}\,\overline{v}^*\,\partial_\phi\,(\overline{u}\,\cos\,\phi) + \overline{w}^*\,\partial_z\overline{u} - f\,\overline{v}^* = \frac{1}{\rho_0\,a\,\cos\,\phi}\nabla\cdot\vec{F} = G([\overline{u}(.,.)],\phi,z), \quad (4.1a)$$

$$f\,\partial_z\overline{u} + \frac{R}{H}\,\frac{1}{a}\,\partial_\phi\overline{T} = 0, \quad (4.1b)$$

$$\frac{1}{a\,\cos\,\phi}\,\partial_\phi\,(\overline{v}^*\,\cos\,\phi) + \frac{1}{\rho_0}\,\partial_z\,(\rho_0\overline{w}^*) = 0, \quad (4.1c)$$

$$\frac{1}{a}\,\overline{v}^*\,\partial_\phi\overline{T} + \overline{S}\,\overline{w}^* = \overline{Q} - \alpha\,\overline{T}. \quad (4.1d)$$

where $\overline{S} = \partial\overline{T}/\partial z + g/c_p$ is a measure of the static stability and $c_p$ is the specific heat at constant pressure. The terms on the right-hand side of (4.1d) represent radiative heating, with $\overline{Q}$ envisaged as imposed. In the specific context discussed in Sections 4.2 and 4.3, $\overline{Q}$ might be the heating in the lower stratosphere that results from absorption of upwelling long wave radiation by ozone and does not depend on local temperatures, whereas the $-\alpha\,\overline{T}$ term is a simple Newtonian cooling representation of the dependence of the diabatic heating field on local temperatures.

We assume that the horizontal components of friction and other non conservative mechanical forcings are negligible. Equation 4.1b assumes that thermal wind balance dominates over the eddy terms. Some eddy terms in Equation 4.1d have also been neglected as they are small in the region of interest. In the following analysis we will neglect the first two terms in (4.1a) and the first term in (4.1d). The equations are then essentially in their quasi-geostrophic form.

An important aspect of the Eliassen-Palm flux term on the right-hand side is that it depends on the mean flow (because the propagation and breaking of waves is affected by the structure of the mean flow). This is emphasised by the representation $G([\overline{u}(.,.)], \phi, z)$ The dependence on $\overline{u}$ is non-local and, of course, the explicit form of $G(.)$ for the real atmosphere remains unknown.

We now proceed to analyse the response to a given imposed heating $\overline{Q}$. We have noted previously, in Sections 4.2 and 4.3 and in particular from Figure 4.2c, that the double-peak structure in heating is not matched by a corresponding structure in temperature. Starting from the heuristic assumption that at leading-order in Equation 4.1d, $\overline{Q}$ is balanced by the term $\overline{S}\overline{w}^*$ rather than the term $\alpha\overline{T}$. Note the immediate caveat that there is a constraint that the global average value of $\overline{w}^*$ on each $z$-level, implying that the assumed balance cannot be perfect. We return to this point in the next section.

Note that all the dependent variables in equations 4.1a) to 4.1d will change as a result of the imposed heating, including $G$, because of its dependence on $\overline{u}$. It is convenient to introduce $\Delta U$ as a typical magnitude of the response in $\overline{u}$ and $\Delta G$ as a typical magnitude of the response in $G$. For the moment we do not attempt to relate $\Delta U$ and $\Delta G$. However we assume that the horizontal and vertical scales of both these responses are approximately the same as the horizontal and vertical length scales of the imposed heating, which we take to be $L_Q$ and $D_Q$ respectively.

From Equation 4.1a it follows that $\overline{v}^* \sim \Delta G/f$ and then from Equation 4.1c that $\overline{w}^* \sim \Delta G\, D_Q/(f\, L_Q)$. From Equation 4.1b it follows that $\overline{T} \sim H\, L_Q\, f\, \Delta U/(R\, D_Q)$. The sizes of the two terms that can balance $\overline{Q}$ in (4.1a) are therefore $\overline{S}\, \Delta G\, D_Q/(f\, L_Q)$ (the vertical advection term) and $\alpha\, H\, L_Q\, f\, \Delta U/(R\, D_Q)$ (the Newtonian cooling term).

Noting that $R\, S/H$ is the square of the buoyancy frequency, $N$, it follows that the relative sizes of the vertical advection term and the Newtonian cooling term are given by the quantity

$$\frac{\Delta G}{\Delta U}\, \frac{N^2\, D_Q^2}{\alpha\, f^2\, L_Q^2} \sim K\, \frac{N^2\, D_Q^2}{\alpha\, f^2\, L_Q^2}, \tag{4.2}$$

where $K$ is a typical value of the ratio $\Delta G/\Delta U$, i.e. of the sensitivity of the wave force $G$ to the velocity.

In the case where the heating is applied close to the Equator then $f$ must be replaced

by $\beta L_Q$ in the above and the relative size is

$$\frac{\Delta G}{\Delta U}\,\frac{N^2\,D_Q^2}{\alpha\,\beta^2\,L_Q^4} \sim K\frac{N^2\;D_Q^2}{\alpha\,\beta^2\,L_Q^4}. \tag{4.3}$$

The quantities appearing in expressions 4.2 and 4.3 must be large if the heuristic assumption $\overline{Q}$ is balanced by the term $\overline{S}\overline{w}^*$ is to be self-consistent. They represent 'dynamical aspect ratios' that determine whether, in an appropriate sense, the imposed heating is 'deep' or 'shallow'. If the dynamical aspect ratio is large then the heating is 'deep' and the majority of the imposed heating is balanced by upwelling. If it is small then the heating is 'shallow' and, in simple cases, the majority of the imposed heating is balanced by Newtonian cooling. (The latter cannot be deduced directly from the previously presented argument, but is straightforward to deduce from a simple modification to it.)

For given $D_Q$, $\alpha$ and $K$ the heating is deeper at low latitudes than at high latitudes. Indeed expression 4.2 implies that however large $D_Q$, the deep response is always seen sufficiently close to the Equator. The quantities in the expressions 4.2 and 4.3 and the distinction between the 'shallow' and 'deep' response have been identified and discussed in many previous papers including Dickinson (1971), Fels et al. (1980), Garcia (1987), Plumb and Eluszkiewicz (1999) and Haynes (2005), making specific assumptions about the form of $G(.)$, essentially that it can be represented by a Rayleigh friction so that $G = -\kappa\,\overline{u}$ where $\kappa$ is the Rayleigh damping coefficient. $\kappa$ then replaces $K$ in the expressions 4.2 and 4.3. However it is generally accepted that Rayleigh friction is a non-physical and very poor representation of the wave forces that operate in the stratosphere. The difference here is that we are taking $K$ to be a rough quantitative description of a more general $G(.)$ that, as emphasised previously, is an unknown, non-local and possibly very complicated function of $\overline{u}$. Evaluating $K$ as the ratio $\Delta G/\Delta U$ in any precise way will be difficult. But the fact is that in any given problem, provided that the applied heating perturbation is not too large, there will be some rough proportionality between the typical magnitude of change of $\overline{u}$ and of $G$ and there will be some $K$ which captures that proportionality.

## 4.5 Model calculations of response to the equatorial applied heating

### 4.5.1 Model description

We now describe detailed model simulations of the response to an applied heating. Bearing in mind the arguments in the previous section, we expect that the change in the wave force will be an important part of the overall response and use a three-dimensional model in which the wave field, and hence the wave force, are free to vary. In particular we choose the well-known idealised system first defined by Held and Suarez (1994), in which there is a simple thermal relaxation to a temperature field, $T_{\mathrm{HnS}}$, with horizontal temperature gradients. The relaxation state leads, under three-dimensional dynamics that incorporates longitudinal as well as latitudinal and vertical variations, to an active baroclinic eddy field and to a statistical equilibrium state which is maintained away from the thermal relaxation state by the action of the eddies, and which includes, for example, well-defined subtropical jets (see Held and Suarez (1994) for further details). We use the Reading IGCM which is described in Chapter 2.4.1. Since there is no imposed inhomogeneity in longitude there is no stationary planetary wave field. However there are transient waves on a range of longitudinal scales (e.g. see Held and Suarez (1994), Figure 4) including synoptic-scale and planetary-scale and it is these that provide the wave force in the subtropical lower stratosphere. The Eliassen-Palm fluxes in the Held and Suarez model integration are generally upwards and equatorwards and in each hemisphere, there are two main regions of convergence, one in the troposphere and one in the stratosphere as shown in Figure 4.11. The broad region of convergence in the stratosphere has a maximum around latitude 40° and 70 hPa with significant contributions from wave numbers 1 to 7. Previous studies (e.g. Randel et al. (2008), Shepherd and McLandress (2011)) have emphasised the range of wave types that give rise to the wave force in the subtropical lower stratosphere in the real atmosphere and in general circulation models, with no evidence for a dominant role for stationary planetary waves, and on this basis we regarded the Held-Suarez configuration as suitable for the study reported here.

The response to applied heating is calculated by taking the difference between integrations with and without a specified steady heating perturbation added to the Held-Suarez configuration. In each case the model is integrated from an initial state of rest with small-amplitude random noise added for a total of 100000 days, with

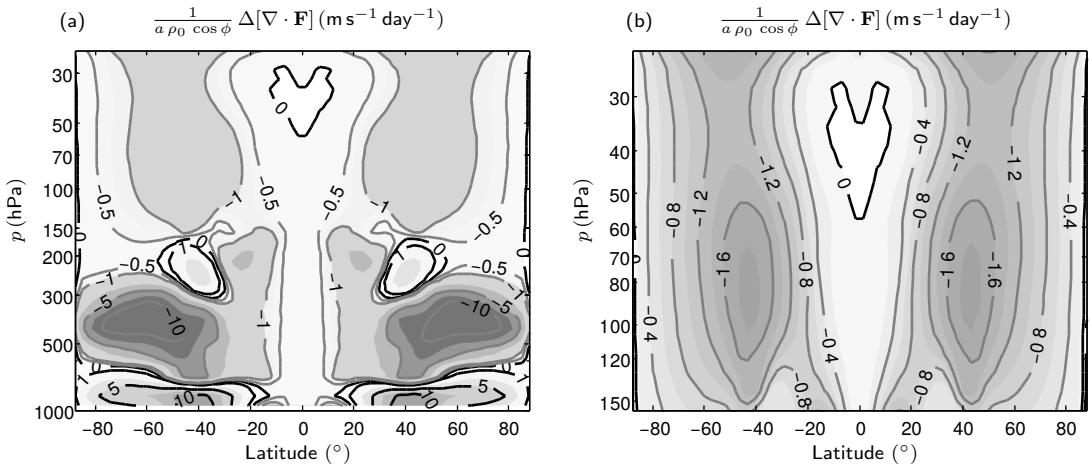


**Figure 4.11:** (a) Wave force due to the divergence of the Eliassen-Palm flux in the idealised model run (T42L40) with the Held and Suarez (1994) restoration state. (b) is similar to (a) but focuses on the stratosphere which will be of primary interest and shown in later figures.

the first 10000 days discarded to eliminate the period of spin-up from rest. The long integrations are needed in order to allow the response to the specified heating perturbation to be distinguished clearly from differences due to internal dynamical variability. The heating perturbation, which is a function only of latitude and height, is added to the right-hand side of the thermodynamic equation to give

$$\frac{\partial T}{\partial t} = \ldots - \alpha(\phi,\sigma)\,[T - T_{\mathrm{HnS}}(\phi,\sigma)] + Q_{\mathrm{double}}(\phi,\sigma) \tag{4.4}$$

$$Q_{\mathrm{double}} = Q_d^+ + Q_d^- \tag{4.5}$$

$$Q_d^{\pm} = Q_A\,\exp\left[-\frac{(\phi \pm \phi_{\max})^2}{2\,\Delta\phi^2} - \frac{(z - z_{\max})^2}{2\,\Delta z^2}\right].$$

The first term on the right-hand side of (4.4) is that used in the standard Held-Suarez configuration with a Newtonian cooling term proportional to the difference between the actual temperature and the temperature as specified by the thermal relaxation state (Section 2.4.4). The value of the Newtonian cooling coefficient, outside of a shallow boundary layer is taken at 0.025 days$^{-1}$. The second term is the specified heating perturbation.

In the first integration to be reported

$$\begin{aligned} Q_A = 0.125\,\mathrm{K\,day^{-1}}, \quad \phi_{\max} = 15^\circ, \quad z_{\max} &= 18\,\mathrm{km}, \\ \Delta\phi = 5^\circ, \quad \Delta z &= 1.5\,\mathrm{km}. \end{aligned}$$

with the amplitude and latitude-height structure of the heating perturbation chosen to make it a simple representation of the double peak structure in the ERA-Interim heating rates.

### 4.5.2 Response to imposed heating

Figures 4.12(a) to (e) show the imposed perturbation to the diabatic heating, $\Delta Q = \alpha\,(T_{\text{double}} - T_{\text{HnS}})$, and the resulting changes in the upwelling, temperature, zonal wind and divergence of the Eliassen-Palm flux respectively. The response in the upwelling has a spatial structure that broadly resembles the imposed heating and indeed in the regions of the applied heating, the upwelling term $\overline{S}\,\overline{w}^*$ in the thermodynamic equation balances the applied heating to good approximation. The upwelling in the regions of the applied heating is part of a larger pattern in meridional circulation with a double cell in each hemisphere. The downwelling outside of the regions of applied heating cause a temperature increase. The overall result is that the temperature response at 78 hPa (peak in heating) is much broader than the imposed diabatic heating and to a first approximation flat over the Equator. The existence of meridional circulation cells in the response requires a non-trivial balance in the zonal momentum equation. Where there is latitudinal flow there is an implied Coriolis torque, which is balanced by a change in $\nabla \cdot \mathbf{F}$. The heating perturbation shifts the region of convergence in $\nabla \cdot \mathbf{F}$ upwards and equatorwards. The change in $\nabla \cdot \mathbf{F}$ is negative above and polewards of the heating region and positive below and polewards of the heating region. There is also a corresponding change in the zonal wind, primarily in the region above the heating, with a large decrease over the Equator and two regions on either side of this where $u$ increases. Note that the change in the wave force has a significantly different spatial structure to the change in the zonal wind.

To demonstrate that there is a consistent angular momentum balance in the response, we calculate the upwelling using the downward control integral. Figure 4.12(f) shows that upwelling from the model is in agreement with that inferred from the quasi-geostrophic and full downward control equations at 70 hPa. The solid line shows the upwelling calculated from the wind and temperature response in the model. The downward control calculation is calculated using the time averaged changes in $\nabla \cdot \mathbf{F}$ and $u$. The upwelling estimated from the wave torque has a double peak structure which is similar to the one obtained from the direct calculation from the velocity fields in the model. In the extratropics, both the quasi-geostrophic and full downward control agree. In the tropical region between 25° S to 25° N, the quasi-geostrophic

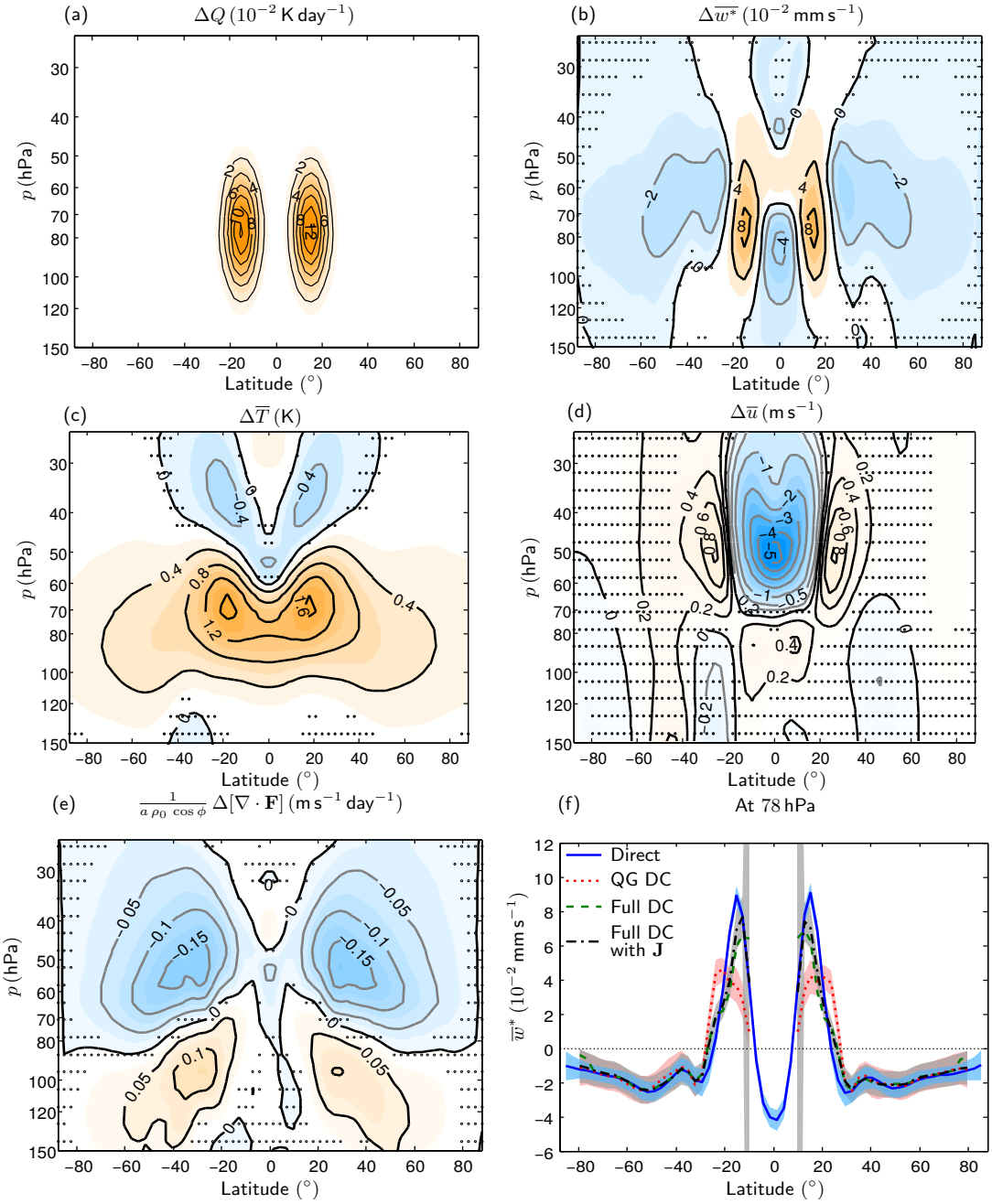


**Figure 4.12:** (a) Imposed change in diabatic heating, $\Delta Q = \alpha\,(T_{\mathrm{double}} - T_{\mathrm{HnS}})$, $(10^{-2}\,\mathrm{K\,day^{-1}})$ (Equation 4.4) in a full model run at a resolution of T42L40. More details can be found in the main text. (b) Change in $\overline{w}^*$ $(10^{-2}\,\mathrm{mm\,s^{-1}})$. (c) Change in $\overline{T}$ (K). (d) Change in $\overline{u}$ $(\mathrm{m\,s^{-1}})$. (e) Change in $1/(a\,\rho_0\,\cos\phi)\,\nabla\cdot\mathbf{F}$ $(\mathrm{m\,s^{-1}\,day^{-1}})$. The regions stippled are not significant at the 95% confidence level as determined by an adjusted Student's t-test. More details of the statistics can be found in the Appendix. (f) $\overline{w}^*\,(\mathrm{mm\,s^{-1}})$ at 78 hPa. The direct and three downward control (DC) calculations are shown. The latter are done with the quasi-geostrophic approximation and the full calculation using $\nabla\cdot\mathbf{F}$, and with the full calculation using $\nabla\cdot\mathbf{F}-\mathbf{J}$. The 95% confidence intervals are shown for all lines except for the full calculation with $\nabla\cdot\mathbf{F}$ in the interest of clarity. The confidence interval for this line is similar to that for $\nabla\cdot\mathbf{F}-\mathbf{J}$.

approximation to the integral is not able to capture the upwelling and the change in the angular momentum contours must be taken into account. In this calculation, we also show the effect of the **J** term from Scott (2002) which is only important close to the Equator. Unlike the ERA-Interim data, the model runs are sufficiently long to allow the inclusion of this term.

The response to applied heating found here is in broad agreement with the combination of double peak in upwelling and flat temperature structure observed in ERA-Interim, previously described in Section 4.2.

Now consider the changes in the various terms in the (time-averaged) thermodynamic Equation 4.1d when a heating $\Delta Q$ is applied, with $\Delta(\cdot)$ indicating the change in the quantity $(\cdot)$.

$$\Delta(\overline{S}\,\overline{w}^*) = \Delta\overline{S}\,\overline{w}^*_0 + \overline{S}_0\,\Delta\overline{w}^* + \Delta\overline{S}\,\Delta\overline{w}^* = \Delta Q - \alpha\,\Delta\overline{T} \tag{4.6}$$

where $\overline{w}^*_0$ and $\overline{S}_0$ are the vertical velocity and static stability respectively in the standard Held-Suarez configuration. This equation indicates that the heating perturbation may be balanced by a combination of change in vertical velocity, change in temperature and change in static stability, with the latter two quantities, of course, being very closely related, since $\Delta\overline{S} = \partial\Delta\overline{T}/\partial z$.

The impression from Figures 4.12(a) and (b) is the balance comes primarily from the change of vertical velocity. However, this has to be consistent with the constraint that $\langle\overline{w}^*\rangle = 0$ where $\langle(\cdot)\rangle = \int_{-\frac{\pi}{2}}^{\frac{\pi}{2}}(\cdot)\cos\phi\,\mathrm{d}\phi / \int_{-\frac{\pi}{2}}^{\frac{\pi}{2}}\cos\phi\,\mathrm{d}\phi$ denotes the global average on a $z$-level.

Assuming that the third term on the left-hand side of (4.6) is small, we divide throughout by $\overline{S}_0$ and take the global average to give

$$\langle\Delta\overline{w}^*\rangle = \left\langle\frac{\Delta Q}{\overline{S}_0}\right\rangle - \alpha\left\langle\frac{\Delta\overline{T}}{\overline{S}_0}\right\rangle - \left\langle\frac{\Delta\overline{S}\,\overline{w}^*_0}{\overline{S}_0}\right\rangle = 0. \tag{4.7}$$

It follows that only if $\langle\Delta Q/\overline{S}_0\rangle = 0$ can the heating perturbation be entirely balanced by $\Delta\overline{w}^*$ and therefore that in assessing the balance in (4.6) it is more appropriate to consider the correspondence between $\overline{S}_0\,\Delta\overline{w}^*$ and $\Delta\widetilde{Q} = \Delta Q - \overline{S}_0\,\langle\Delta Q/\overline{S}_0\rangle$ rather than $\Delta Q$ itself. Note that $\overline{S}_0$ has mean value of about $1\times10^{-3}\,\mathrm{K\,m^{-1}}$ and the difference between the value in the tropics and the extratropics is about 25%. This latitudinal structure in $\overline{S}_0$ is taken into account in $\Delta\widetilde{Q}$.

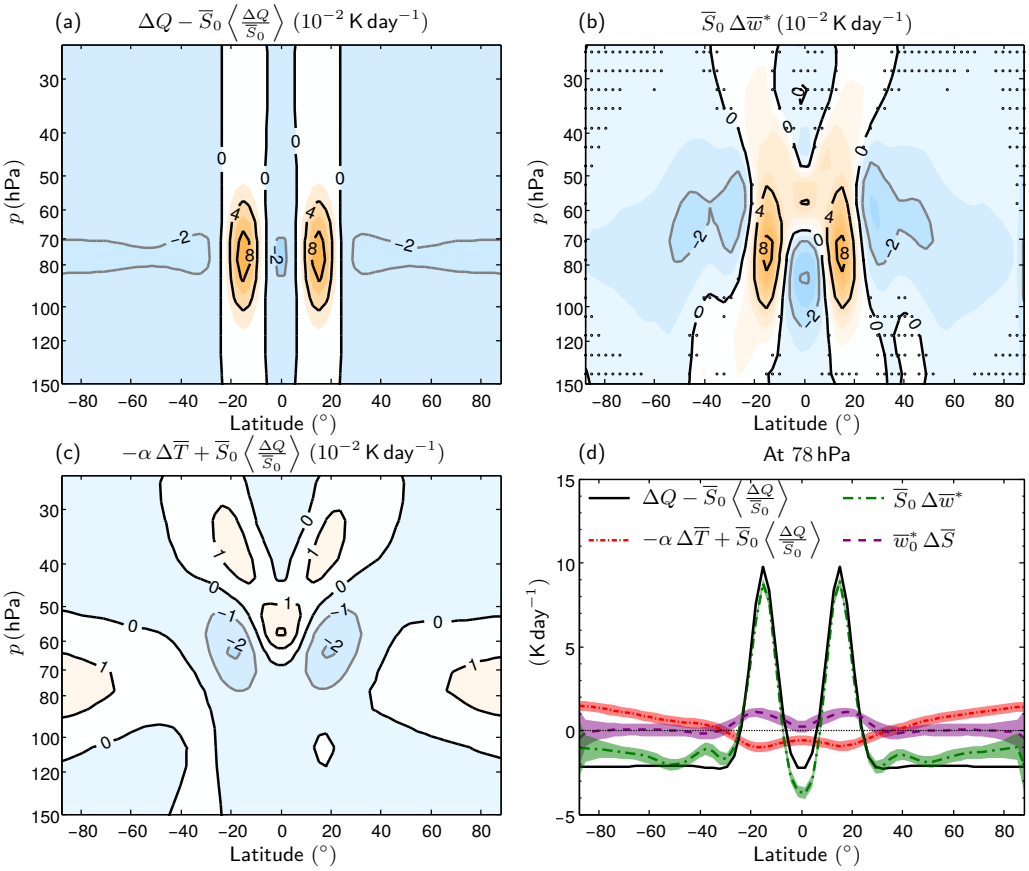


**Figure 4.13:** (a) Heating perturbation with a global mean removed ($\Delta Q - <\overline{S}_0\,\Delta Q/\overline{S}_0>$) for the case shown in Figure 4.12(a). (b) $\overline{S}_0\,\Delta\overline{w}^*$ (c) $-\alpha\,\Delta\overline{T} + <\overline{S}_0\,\Delta Q/\overline{S}_0>$. (d) Plot of the terms in (a)–(c) at 78 hPa. All plots are in units of $10^{-2}\,\mathrm{K\,day^{-1}}$. The regions stippled are not significant at the 95% confidence level as determined by an adjusted Student's t-test. A similar calculation produces the 95% confidence intervals shown in (d).

Figures 4.13(a) and (b) show respectively the quantities $\Delta\widetilde{Q}$ and $\overline{S}_0\,\Delta\overline{w}^*$. The good quantitative agreement between the two quantities in the region where the heating perturbation is applied is clear. Figure 4.13(c) shows the sum $-\alpha\,\Delta\overline{T} + \langle\overline{S}_0\,\Delta Q/\overline{S}_0\rangle$, which would be the difference between the quantities in (a) and (b) if the term $\overline{w}^*_0\,\Delta\overline{S}$ was negligible. In fact the latter tends to oppose $-\alpha\,\Delta\overline{T} + \langle\overline{S}_0\,\Delta Q/\overline{S}_0\rangle$ in the region where the heating perturbation is applied. This is clear from Figure 4.13(d) which shows the latitudinal structure at 78 hPa in all of the various quantities and confirms the very close agreement between $\Delta\widetilde{Q}$ and $\overline{S}_0\,\Delta\overline{w}^*$.

The balance in the thermodynamic equation (4.6) can be assessed fully only by considering the height-latitude variation of the various quantities shown in Figures 4.13(a)-(c). However it is convenient for some purposes to find simple quantitative measures of this balance and in particular we will use the ratio $\overline{S}_0\,\Delta\overline{w}^*/\Delta\widetilde{Q}$, evaluated at the centre

of one of the double peaks in applied heating as a measure of the extent to which the applied heating is balance by a response in upwelling. This ratio has a value of $1.04 \pm 0.04$ in the case reported above.

### 4.5.3 Zonally symmetric simulations with Rayleigh friction

We next provide some illustrative results for the case where the wave force $G$ is represented by Rayleigh friction. This was the basis for many of the earlier studies of the driving of the mean meridional circulation (e.g. Dickinson (1971), Fels et al. (1980), Garcia (1987)) and incorporates the $u$-dependence of $G$, but in a highly simplified manner that is not believed to be realistic. Under certain simplifying assumptions, essentially weak departures from a latitudinally independent state, analytical progress is possible using Hough function expansions (e.g. Garcia (1987)). Here it is most convenient simply to calculate the response using a zonally symmetric version of the full numerical model described previously. This allows incorporation of latitude-dependent temperature structure, for example.

The standard Held and Suarez (1994) configuration described above is modified as follows. Rayleigh friction with a constant friction coefficient, $\kappa$, is added throughout the whole domain. All dynamical fields are constrained to be zonally symmetric. This means, for example, that there is no baroclinic instability. The first 1000 days of the model run are discarded as spin up and the model state after this is analysed.

A set of experiments were performed in the axisymmetric model with values of $1/\kappa$ of 1, 10 and 30 days. The applied heating field, defined by the Equation 4.4, again with the peaks located at latitudes of 15° N–S, is shown in Figure 4.12(a). The corresponding changes in temperature, zonal wind and vertical wind are shown in Figure 4.14.

For large values of $\kappa$ ($1/\kappa$ equal to 1, 10 and 30 days) the system adjusts such that the dominant balance in the thermodynamic equation is between the vertical upwelling and the heating. (Compare Figure 4.12(a) and Figures 4.14 (c), (f) and (i).). Given the vertical wind response, the continuity equation implies a change in $v$. For this change in $v$, the balance between the Coriolis torque and the Rayleigh drag in the momentum equation sets the structure of $u$. Finally, thermal wind balance will related the change in the wind, $u$, to a temperature change. Note that within this large-$\kappa$ regime, whilst the vertical velocity (and hence the latitudinal velocity) changes very little as $\kappa$ varies, at least in the region of the applied heating, there is a substantial change in $\overline{u}$. This change in $\overline{u}$ has a magnitude inversely proportional to $\kappa$ and a

horizontal structure that is broad for large $\kappa$ and which narrows as $\kappa$ decreases.

We can think of $\kappa$ as setting the width of some tropical region over which the circulation generated by the heating can spread. As $\kappa$ is decreased, this region becomes smaller and the temperature and zonal wind changes become increasingly confined to the region of heating. This can also be seen in the location of the regions of downwelling in the right hand column of Figure 4.14. Conservation of mass on each pressure levels means that the upwelling generated has to be balanced by a downwelling and this becomes stronger over the Equator as the circulation becomes more latitudinally confined.

For a smaller value of $\kappa$ ($1/\kappa$ equal to 30) there are clear quantitative differences between the applied heating Figure 4.12(a) and the vertical upwelling (Figures 4.14 (i)). (Note, for example, that the magnitude of the equatorial downwelling relative to the subtropical upwelling is much larger for larger values of $\kappa$.) It follows that the

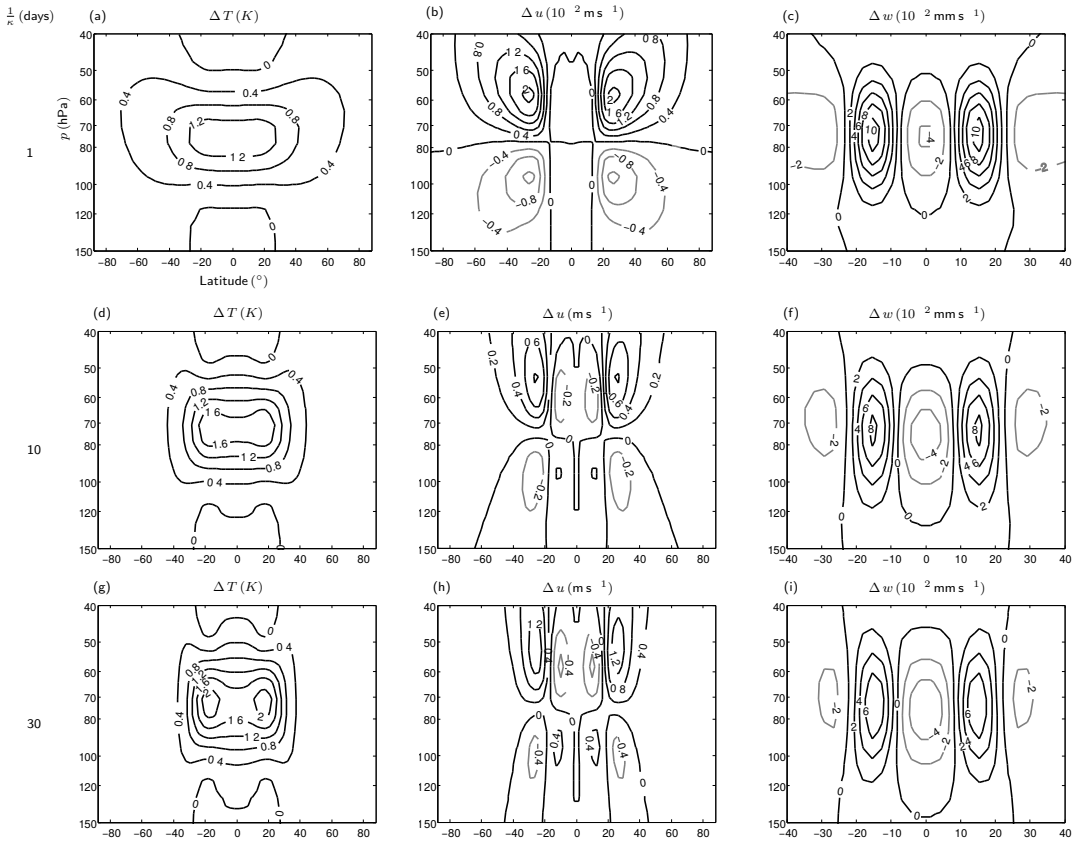


**Figure 4.14:** (a), (d), (g): Change in $T$ (K) for the imposed heating from Figure 4.12 in an axisymmetic version of the T42L40 model with Rayleigh drag for values of $1/\kappa$ equal to 1, 10 and 30 days respectively. (b), (e), (h): Change in $u$ (Note that the units of $u$ change down the column). (c), (f), (i): Change in $\overline{w}$ ($10^{-2}\,\mathrm{mm\,s^{-1}}$).

Newtonian cooling term is an important part of the balance in the thermodynamic equation. For reference the value of the dynamical aspect ratio (expression 4.2), setting $K = \kappa$, for the three values of $\kappa^{-1}$: 1, 10 and 30 days is respectively 20, 2 and 0.7, confirming that the scaling arguments given previously are consistent with the calculated response.

These results for axisymmetric dynamics with Rayleigh friction may be compared with the full three-dimensional dynamical response shown in Figure 4.12(b)–(d). The three dimensional response is very similar to that with large Rayleigh friction in that there is a balance between applied heating and upwelling, but the temperature and zonal wind responses are quite different. This is because, in this dynamical regime, the change in zonal wind (and hence, through thermal wind balance, the change in temperature) is determined by the requirement that there is balance in the momentum equation and this change therefore depends on the details of the function $G([\overline{u}(.,.)], \phi, z)$. The same point has been noted above with respect to different values of the Rayleigh friction. In other words, in this dynamical regime, the response in the vertical and latitudinal velocities, is robust and insensitive to the precise form of $G([\overline{u}(.,.)], \phi, z)$, but the change in zonal wind and temperature is not.

Note in particular that, whereas for the Rayleigh friction case the change in force has, by definition, the same shape in the latitude-height plane as the change in velocity since they are proportional to each other, the same is not true for the three-dimensional case where the change in the acceleration due to the waves $1/(a\,\rho_0\,\cos\phi)\,\nabla\cdot\mathbf{F}$ (Figure 4.12(e)) differs from zonal wind change (Figure 4.12(d)).

## 4.6 Model response to different types of applied heating

Having established the possibility of a dynamical response to applied heating in which the heating is balanced by upwelling and the wave force adjusts to balance the corresponding Coriolis torque, we now investigate the implications of variations in the latitude, width and strength of the heating. The next subsections report details of a set of experiments in the three-dimensional model in which these quantities are varied. The parameters for this set of experiments are listed in table 4.1. Note that the first experiment described above is also repeated in each group for completeness and indicated by an asterisk. Whereas this first experiment was motivated specifically by

| Group | $Q_A$(K day$^{-1}$) | $\phi_{\max}$ | $\Delta\phi$ | |
|---|---|---|---|---|
| A: | 0.125 | 10 ° | 5 ° | |
| | 0.125 | 15 ° | 5 ° | * |
| | 0.125 | 20 ° | 5 ° | |
| | 0.125 | 30 ° | 5 ° | |
| | 0.125 | 40 ° | 5 ° | |
| | 0.125 | 50 ° | 5 ° | |
| | 0.125 | 60 ° | 5 ° | |
| B: | 0.025 | 15 ° | 5 ° | |
| | 0.125 | 15 ° | 5 ° | * |
| | 0.250 | 15 ° | 5 ° | |
| | 0.500 | 15 ° | 5 ° | |
| | 1.000 | 15 ° | 5 ° | |

| Group | $Q_A$(K day$^{-1}$) | $\phi_{\max}$ | $\Delta\phi$ | |
|---|---|---|---|---|
| C: | 0.125 | 15 ° | 5 ° | * |
| | 0.125 | 15 ° | 10 ° | |
| | 0.125 | 15 ° | 20 ° | |
| | 0.125 | 60 ° | 5 ° | |
| | 0.125 | 60 ° | 10 ° | |
| | 0.125 | 60 ° | 20 ° | |
| | 0.125 | 60 ° | 40 ° | |

**Table 4.1:** Sets of experiments with different values of some of the parameters in Equation 4.4 to test the response of the model when the latitude (Group A), strength (Group B) or width (Group C) of the applied heating is changed. The case marked by an * is repeated for completeness and is described by Equation 4.4 and plotted in Figure 4.12.

the radiative calculations in the first part of this chapter, the wider set of experiments are intended to explore the range of dynamical behaviour rather than to model specific aspects of the real atmosphere.

The next sections detail a set of experiments in the full model to test the sensitivity to latitude, strength and width of the heating. The parameters for this set of experiments are listed in table 4.1. Note that the case described above is also listed in each group for completeness and indicated by an asterisk.

### 4.6.1 Varying the latitude of the maximum heating (A)

Figure 4.15 shows the temperature, upwelling and divergence of the Eliassen-Palm flux response to a heating perturbation located at 10, 20, 40 and 60 ° N–S (group A of table 4.1). This experiment is not intended to model realistic heating perturbations but explore the dynamical behaviour in the extratropics. It is worth noting that although the experiment is set up such that the response should have hemispheric symmetry, there are some asymmetries that are especially prominent in $u$ and $1/(a\,\rho_0\,\cos\phi)\,\nabla\cdot\mathbf{F}$. The statistical test used picks out changes that are statistically different to zero at the 95% confidence level not how different the values are between hemispheres. These hemispheric differences could be due to long timescales in the tropospheric jets which

are known to occur in dynamical cores such as the one we are using. They are unlikely to be a signal directly associated with the imposed diabatic heating in the lower stratosphere. A further statistical test shows at the 95% confidence level that the response is not different between the hemispheres.

For this set of experiments, as the applied heating is moved away from the Equator the dominant structure of the upwelling response continues to match that of the applied heating, even when the latter is located in the extratropics. Further quantitative detail is given by Figure 4.16 which shows the ratio $\overline{S}_0\,\Delta\overline{w}^*/\Delta\widetilde{Q}$ evaluated at the centre of one of the double peaks in applied heating. For this particular shape of applied heating, the ratio remains close to one for all latitudes plotted. Whilst this result might initially seem surprising, bearing in mind the $f$ dependence implied by (4.2), it is consistent with (4.2) provided that $K$ is sufficiently large, i.e. the wave force is sufficiently sensitive to the zonal velocity. Indeed the same behaviour is observed in the Rayleigh drag case for large enough values of $\kappa$ as may be seen from the additional grey curves in Figure 4.16. These were obtained through a calculation involving the use of Hough function expansions (e.g. Garcia (1987)). The numerical calculation requires a large number of Hough functions to converge close to the Equator and adequate convergence was obtained using the first 1000 eigenfunctions. This method is a simplification of the Rayleigh drag calculation performed using the model (described in Section 4.5.3) since the squared of the buoyancy frequency is set to a constant value typical of the stratosphere in the Held and Suarez case ($N^2 = 3.35 \times 10^{-4}$). However it provides a useful indication of the behaviour of the ratio $\overline{S}_0\,\Delta\overline{w}^*/\Delta\widetilde{Q}$ as $\kappa$ is increased. The dot-dash curve also shows that the term $\overline{w}^*_0\,\Delta\overline{S}/\Delta\widetilde{Q}$, which has contributions from the change in static stability, is small.

### 4.6.2 Varying the strength of the heating (B)

For the case where the peaks are centred at 15° N–S, the strength of the heating is varied from 0.025 K day$^{-1}$ to 1 K day$^{-1}$. Recall that typical heating perturbations that are observed in reanalysis diabatic heating rates are about 0.03 K day$^{-1}$ (Figure 4.7). The response to the heating in all the cases looks quantitatively similar with a roughly linear relationship between the maximum heating $Q_A$ and the amplitude of the response, even for large values of the heating perturbation up to 0.5 K day$^{-1}$ with a hint of non linearity beyond that (arising from the term $\Delta\overline{S}\,\Delta\overline{w}^*$ becoming larger). This is illustrated by the relation between $Q_A$ and the vertical velocity measured at the location of the maximum heating shown in Figure 4.17(a).

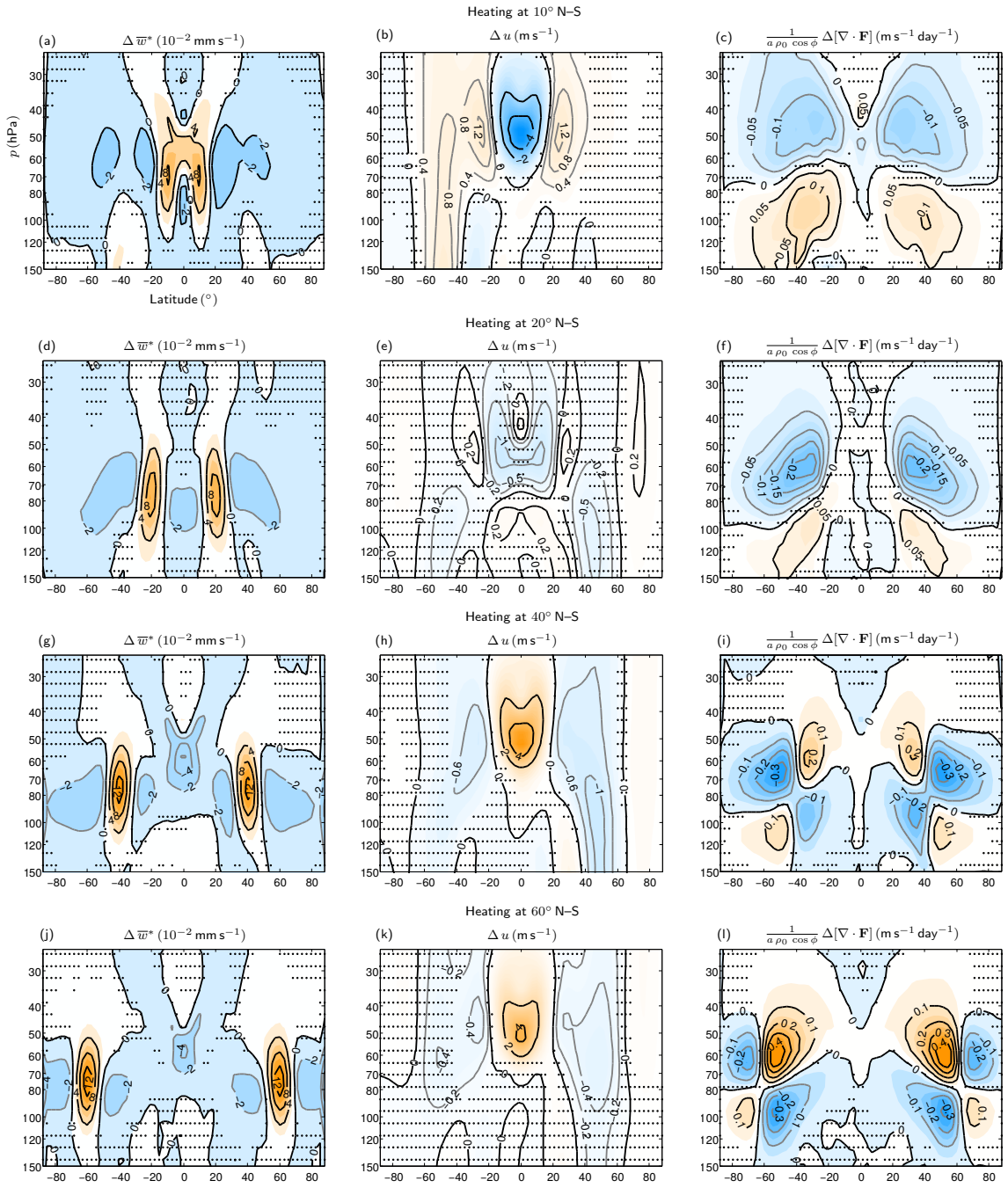


**Figure 4.15:** Changes in (a) $\overline{w}^*$ ($10^{-2}\,\mathrm{mm\,s^{-1}}$), (b) $\overline{u}$ ($\mathrm{m\,s^{-1}}$) and (c) $1/(a\,\rho_0\,\cos\phi)\,\nabla\cdot\mathbf{F}$ ($\mathrm{m\,s^{-1}\,day^{-1}}$) due to an imposed change in diabatic heating with peaks at 10, 20, 40 and 60 ° N–S. Group A in table 4.1.

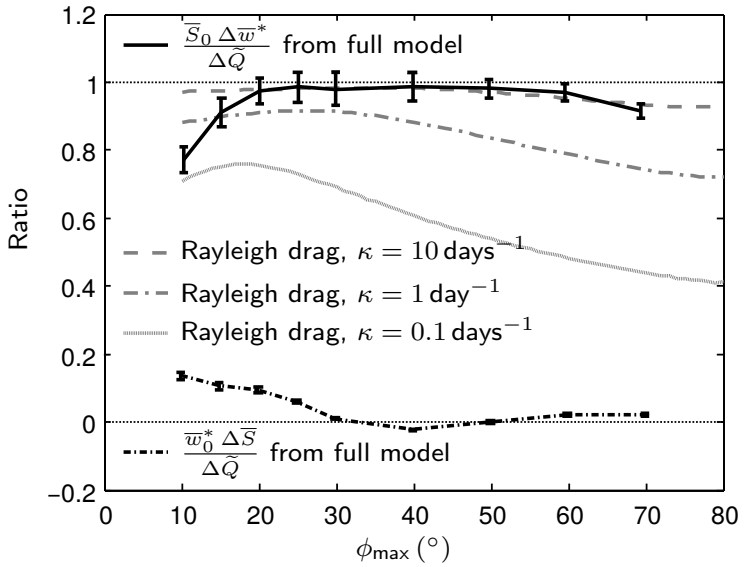


**Figure 4.16:** Plots of the ratio $\overline{S}_0\,\Delta\overline{w}^*/\Delta\widetilde{Q}$ and $\overline{w}_0^*\,\Delta\overline{S}/\Delta\widetilde{Q}$,, against the latitude of the maximum heating perturbation from the model runs with $Q_A = 0.125\,\text{K}\,\text{day}^{-1}$. The ratio is calculated at the location of the maximum in heating. The 95% confidence intervals are calculated using an adjusted Student's t-test. The ratio $\overline{S}_0\,\Delta\overline{w}^*/\Delta\widetilde{Q}$ is also plotted for the Rayleigh drag cases with $\kappa$ equal to 10, 1 and 0.1 $\text{days}^{-1}$ from the Hough function calculation.

The ratio of the imposed heating to the upwelling term plotted in Figure 4.17(b) shows the ratio is close to one which is consistent with the fact that the dynamical aspect ratio (expression 4.2) does not include a dependence on the size of the heating. For small $Q_A$ the statistical uncertainty in the ratio is large and, whilst there is a hint that the ratio may be smaller for very small $Q_A$ it is not clear that this would stand up to further scrutiny.

The conclusion from this set of experiments is that over the range of heating amplitudes (up to $1\,\text{K}\,\text{day}^{-1}$) considered the response is essentially linear and there is no change in the property (for this particular heating field) that upwelling provides the dominant balance to the applied heating. Larger amplitudes of applied heating might give rise to non linear effects but are not likely to be relevant to the tropical lower stratosphere.

### 4.6.3 Varying the width of the heating (C)

The experiments in group C address the change in response as the width of the double peaks is increased. As shown by the results in Figure 4.18(a) and (b), for

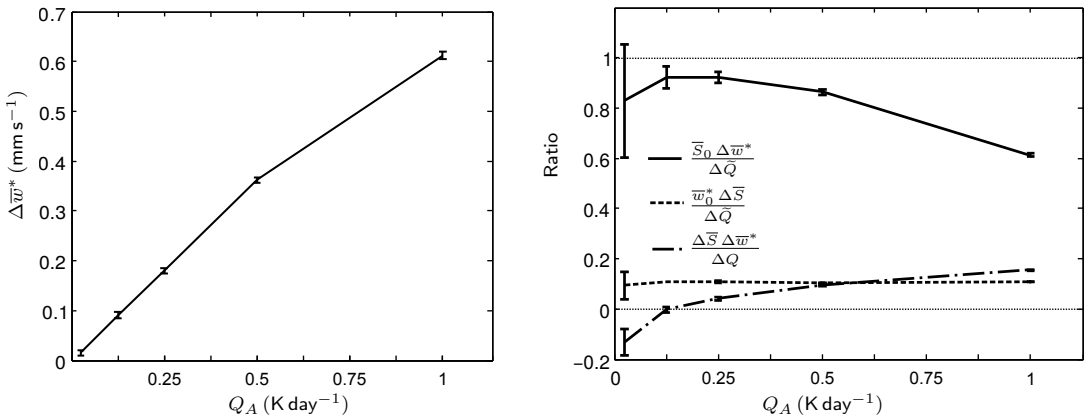


**Figure 4.17:** Group B in table 4.1. (a) Plot of the change in upwelling against the size of the heating perturbation, $Q_A$, in the model experiments. (b)The plot shows the ratio of various quantities in the thermodynamic equation to the heating plotted against the size of the heating perturbation when the double peaks in heating are centred at 15° N–S. The 95% confidence intervals are calculated using an adjusted Student's t-test.

cases with a $\phi_{\max} = 15°$ N–S and at $\phi_{\max} = 60°$ N–S, as the width of the perturbation is increased, the upwelling term no longer provides the dominant balance in the thermodynamic equation to the applied heating and other terms become as important. For $\phi_{\max} = 15°$ N–S the static stability term $\overline{w}^*_0\,\Delta\overline{S}$ becomes increasingly important as the width increases. Figure 4.18(c) shows that the broad heating at 15° N–S ($\Delta\phi = 20°$) causes a significant change in the static stability of about 13% of the background value at the location of the peak in heating compared to 4% for the narrow heating ($\Delta\phi = 5°$). This change is of a similar magnitude to the latitudinal variation in $\overline{S}$.

For $\phi_{\max} = 60°$ N–S both the $\overline{w}^*_0\,\Delta\overline{S}$ and $-\alpha\,\Delta\overline{T}$ terms become important. The fact that these tend to cancel at the centre of the applied heating means that $\overline{S}_0\,\Delta\overline{w}^*/\Delta\widetilde{Q}$, evaluated at the centre of the applied heating, which we have previously used as a measure of the role of upwelling, decreases relatively little with width. However inspection of the height-latitude structure of the response in various fields confirms that, as width increases, there is a clear change from a response in which upwelling essentially matches heating, as seen in the cases in Figure 4.15 for narrow heating, to a more complicated response.

An example of the detailed response to a broad heating, for the case ($\phi_{\max} = 15°, Q_A = 0.125\,\mathrm{K\,day^{-1}}, \Delta\phi = 20°$), is shown in Figure 4.19. Note in particular that the region of upwelling (b) is much narrower that the applied heating (a) and furthermore that the maximum in upwelling is shifted significantly upwards relative to the region of

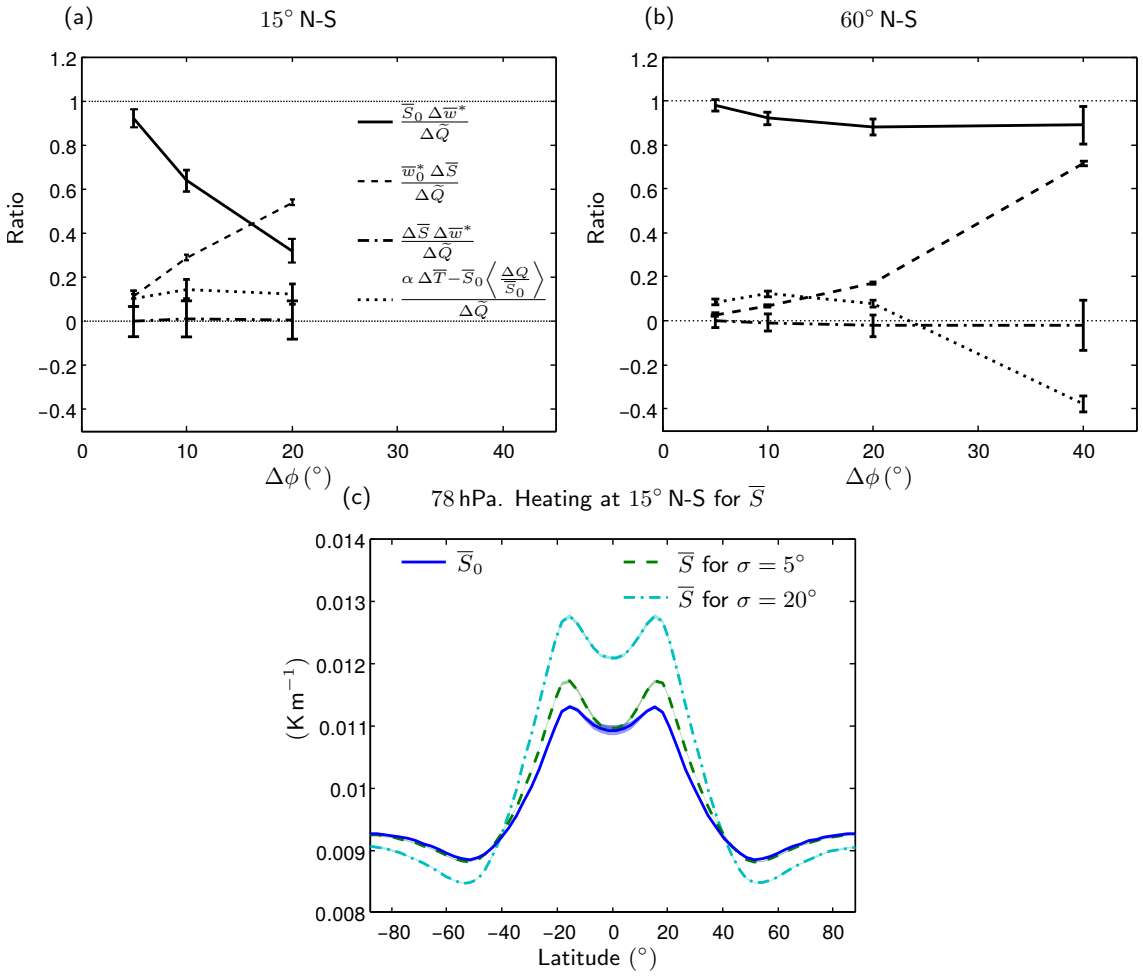


**Figure 4.18:** Group C in table 4.1. Plots of the ratios of the various terms in Equation 4.6 to the diabatic heating against the width of the double peaks in heating when they are centred at (a) 15° N–S and (b) 60 ° N–S. The 95% confidence intervals shown. The legend for the two plots is the same. (c) The plot shows the static stability at 78 hPa for the Held and Suarez, $\overline{S}_0$ case and when the heating is at 15° N–S with a width of 5° and 20°.

heating. Figure 4.19(f) summarises the role of the different terms in the thermodynamic equation at 78hPa. While some of the heating is balanced by an upwelling, the static stability change becomes equally as important in the tropical region with the term $\overline{w}^*_0\,\Delta\overline{S}$ becoming significant as shown in Figure 4.19(d). The $\Delta\overline{w}^*\,\Delta\overline{S}$ term remains small as shown in Figure 4.19(e).

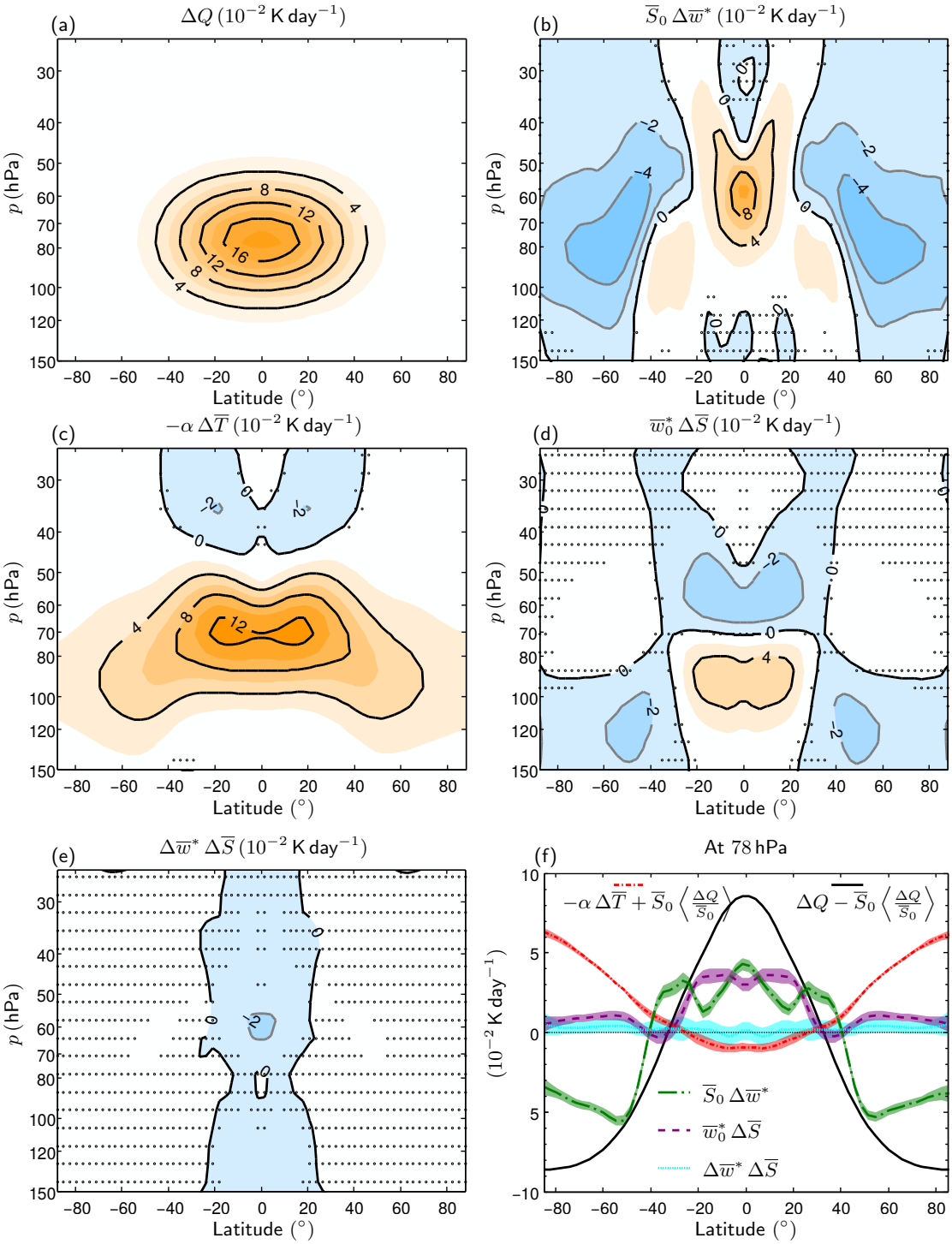


**Figure 4.19:** Plots of the various terms in the thermodynamic equation for the model experiment where the heating is at 15° with amplitude $0.125\,\mathrm{K\,day^{-1}}$ and width 20°. (a) Change in imposed heating. (b) Change in $\overline{S}_0\,\Delta\overline{w}^*$. (c) Change in $-\alpha\,\Delta T$. (d) Change in $\overline{w}^*_0\,\Delta\overline{S}$. (e) Change in $\Delta\overline{w}^*\,\Delta\overline{S}$. Stippled regions are not statistically significant at the 95% level. (f) The same terms plotted at 78 hPa. The global mean heating term, $\overline{S}_0\,\langle\Delta Q/\overline{S}_0\rangle$, is removed from $\Delta Q$. All terms are in units of $10^{-2}\,\mathrm{K\,day^{-1}}$. The 95% confidence intervals are shown as a shaded region.

### 4.6.4 Idealised orography

The idealized Held-Suarez configuration is a convenient vehicle for a first exploration the response of a system with synoptic-scale and planetary-scale eddies to applied heating in the tropical lower stratosphere. However it is not defensible as an accurate quantitative model of the troposphere-stratosphere system and it is important to establish whether the results reported so far are robust to changes in this idealized configuration. As a first step, a crude representation of orography is added to the northern hemisphere in the model run with the heating at 15 N–S. A wave one perturbation is added to the surface geopotential height as a sine wave in longitude and a half a sine wave between 25 and 45° N with an amplitude of 500 m. Figure 4.20 shows the same quantities as Figure 4.15 (b) to (e) but for the case with orography. Comparing Figure 4.20(a) and Figure 4.15(b), we find that the upwelling response is qualitatively similar in the case with a mountain and the case without. The ratio $\overline{S}_0\,\Delta\overline{w}^*/\Delta\,\widetilde{Q}$ in the case with the mountain is still close to one and has a value of $1.2 \pm 0.05$.

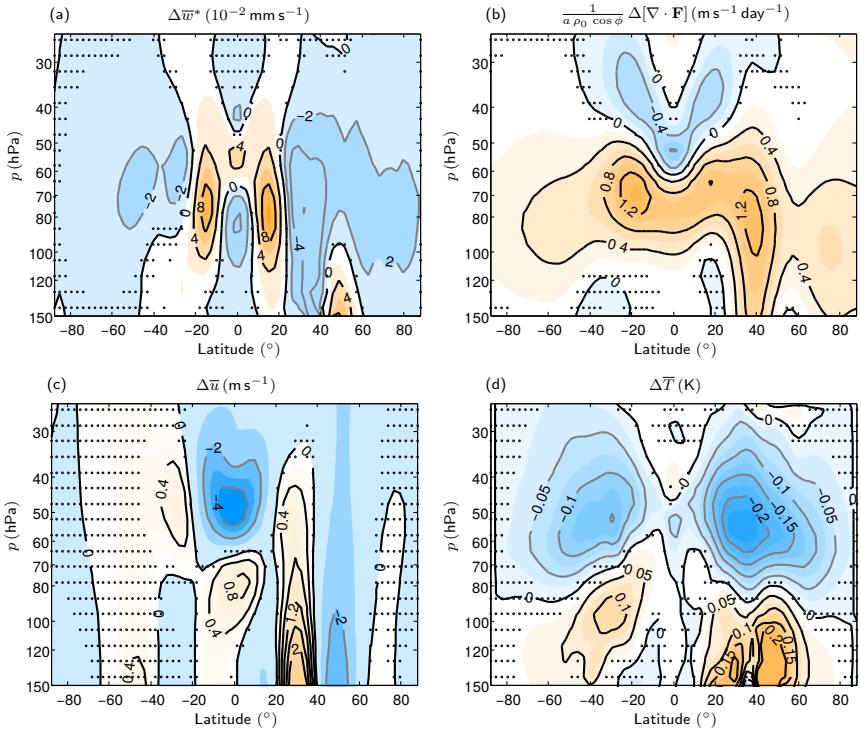


**Figure 4.20:** Full model run with heating at 15° N and amplitude 5 K (Figure 4.15(a)) but with a wave one surface geopotential height perturbation. (a) Change in $\overline{w}^*$ ($10^{-2}$ mm s$^{-1}$). (b) Change in $\overline{T}$ (K). (c) Change in $u$ (m s$^{-1}$) (d) Change in $1/(a\,\rho_0\,\cos\phi)\,\nabla\cdot\mathbf{F}$ (m s$^{-1}$ day$^{-1}$).The regions stippled are not significant at the 95% confidence level as determined by an adjusted Student's t-test.

The downwelling response is also stronger and has a smaller meridional lengthscale. This is consistent with the larger divergence of the Eliassen-Palm flux. These results are broadly consistent with what has been noted previously. Since both hemispheres are in the appropriate dynamical regime of strong dependence of the wave force to the zonal velocity, the dominant balance in the thermodynamic equation is that the upwelling balances the applied heating. Therefore the vertical velocity response is relatively insensitive to the details of the wave force and, in the experiment reported above, is similar between the two hemispheres. The responses in the zonal wind and temperature, on the other hand, are more sensitive to the details of the wave force, and these therefore differ between the two hemispheres.

## 4.7 Response to an imposed force

Having observed a dynamical regime where there is significant compensation between an imposed narrow and tall heating by the upwelling response, we briefly explore the response to an imposed force. This is motivated by recent discussion (Cohen et al. (2013, 2014)) of the dynamics of model-predicted increases in the strength of the Brewer-Dobson circulation due to increases in the concentrations of long-lived greenhouse gases (e.g. Butchart et al. (2014)). It has been previously noted (e.g. Cohen et al. (2013)) that whilst the predicted rate of increase in the strength of the circulation is broadly consistent across many models at about 2% per decade, there is significant variation across the models in the quantitative contribution to the change in wave force from different wave types. In some models the change is primarily from parametrized gravity waves and in others it is primarily from synoptic-scale and planetary-scale Rossby waves that are resolved by the model dynamics. Cohen et al. (2013) have characterised this as a 'compensation' by which the Brewer-Dobson circulation response to changes to the parametrized gravity waves, for example, is compensated by the Brewer-Dobson circulation response to consequential changes in the resolved waves. Cohen et al. (2013, 2014) have discussed possible mechanisms for this compensation, including a role for barotropic instability, though the relevance of the latter mechanism has been questioned by Sigmond and Shepherd (2014)), who studied compensation in a general circulation model, and by Watson and Gray (2015), who studied it in a stratosphere-mesosphere model.

Returning to the arguments of Section 4.4, consider the wave force $G(.)$ appearing in (4.1a) to be a function not only of the zonal mean state, but also of some set of

external parameters $\mathbf{h} = h_1, h_2, h_3, \ldots$. These parameters could, for example, represent orography on different scales, or parameters in a gravity wave scheme. A key point, noted by Cohen et al. (2013) and others, is that if one or more of these external parameters is changed, then the resulting change in $G()$ will be due in part to the change in the zonal mean state, i.e. the zonal mean zonal wind and temperature field. We could express this formally by writing the change in $G()$ as a part that involves partial derivatives with respect to $\mathbf{h}$ and a part the involves partial derivatives (or functional derivatives) with respect to flow variables. A convenient simplification would be to say that the change $\Delta G$ is to some approximation the sum of two parts: an imposed force, $\Delta G_{\mathbf{h}}$ and a force which has to be determined as part of the response, $\Delta G_u$.

Just as previously we have asked whether an applied heating perturbation is balanced by upwelling or by a change in Newtonian cooling (or more generally long-wave radiative heating) due to a change in temperature, here we ask whether the change in force $\Delta G_{\mathbf{h}}$ arising directly from changing external parameters is balanced by the Coriolis force due to a change in meridional circulation or by a compensating change $\Delta G_u$ in the wave force. The horizontal and vertical scales of $\Delta G_{\mathbf{h}}$ are assumed, respectively, to be $L_G$ and $D_G$. Again a heuristic approach is to assume a typical change $\Delta u$ in zonal velocity and then progress through equations 4.1b, 4.1c and 4.1d to deduce the corresponding change in latitudinal velocity.

It follows that the relative sizes of the $\Delta G_u$ term and the Coriolis force term in the zonal momentum equation is

$$\delta G N^2 D_G^2 / \alpha f^2 L_G^2 \delta U \sim K N^2 D_G^2 / \alpha f^2 L_G^2. \tag{4.8}$$

where again $K$ is a typical value of the ratio $\delta G / \delta U$, i.e. of the sensitivity of the wave force $G$ to the velocity. This is simply the expression (4.2) with the length scales $L_Q$, $D_Q$ of the heating replaced by the length scales $L_G$, $D_G$ of the externally determined part of the change in wave force $\Delta G_{\mathbf{h}}$. There is a corresponding simple modification of the expression in 4.3 that applies when $\Delta G_{\mathbf{h}}$ is located in the tropics. The implication is that when $\Delta G_{\mathbf{h}}$ is relatively deep and narrow, in a sense made precise by the dynamical aspect ratio (4.8), it is balanced primarily by the adjustment $\Delta G_u$ in the wave force rather than by a Coriolis force, in other words it is ineffective in driving a meridional circulation.

The imposed force has the form of a single Gaussian peak centred at $\phi_{\max} = 30^\circ$ S

and all other corresponding parameters describing the height and width of the forcing are set to those used in the heating case in Equation 4.4. The amplitude (analogous to $Q_A$ in Equation 4.4) is set to $1\,\mathrm{kg\,m^{-1}\,s^{-2}}$. The perturbation for the $\Delta\phi = 5°$ and $\Delta\phi = 10°$ cases are shown in Figure 4.21(a). We explore a range of widths, $\Delta\phi = 5°, 6°, 8°, 10°, 12°$, and plot the ratio of the response, $\Delta G_u$, to the imposed forcing, $\Delta G_{\mathbf{h}}$, at the location of the maximum in the impose Gaussian, in Figure 4.21(b). To investigate this further, we carry out a series of model experiments similar to those described in Section 4.6.3 but rather than adding an imposed heating to the right hand side of the thermodynamic equation (4.1d), we add an imposed force to the right hand side of the zonal momentum equation (4.1a). For the narrow forcing, there is significant compensation of the imposed wave force by the wave response. The amount of compensation decreases as the forcing gets wider. The change in the wave force in the narrow forcing case ($\Delta\phi = 5°$), Figure 4.21(c), has a similar spatial structure to the imposed forcing. The compensation is not perfect and the remaining wave torque drives a meridional circulation as shown by the plot of the residual mean meridional velocity in Figure 4.21(e). Corresponding plots to Figures 4.21(c) and (e) for a wider forcing case ($\Delta\phi = 10°$) are shown in Figures 4.21(d) and (f). The amplitude of the response is smaller than the imposed torque and the response extends into the other hemisphere and the Coriolis term is larger as can be seen from the plot of $\Delta\overline{v}^*$ in Figure 4.21(f).

Our findings are consistent with the results reported by Cohen et al. (2013) who in seeking to explain the compensation in the driving of the meridional circulation between the resolved waves and the parametrized waves, carried out numerical experiments where a given force (corresponding to our $\Delta G_{\mathbf{h}}$) was applied and the resolved waves, and hence the wave force due to those waves (corresponding to our $\Delta G_u$), were allowed to a change as part of the response. They found that narrower $\Delta G_{\mathbf{h}}$ gave more compensation than broader $\Delta G_{\mathbf{h}}$.

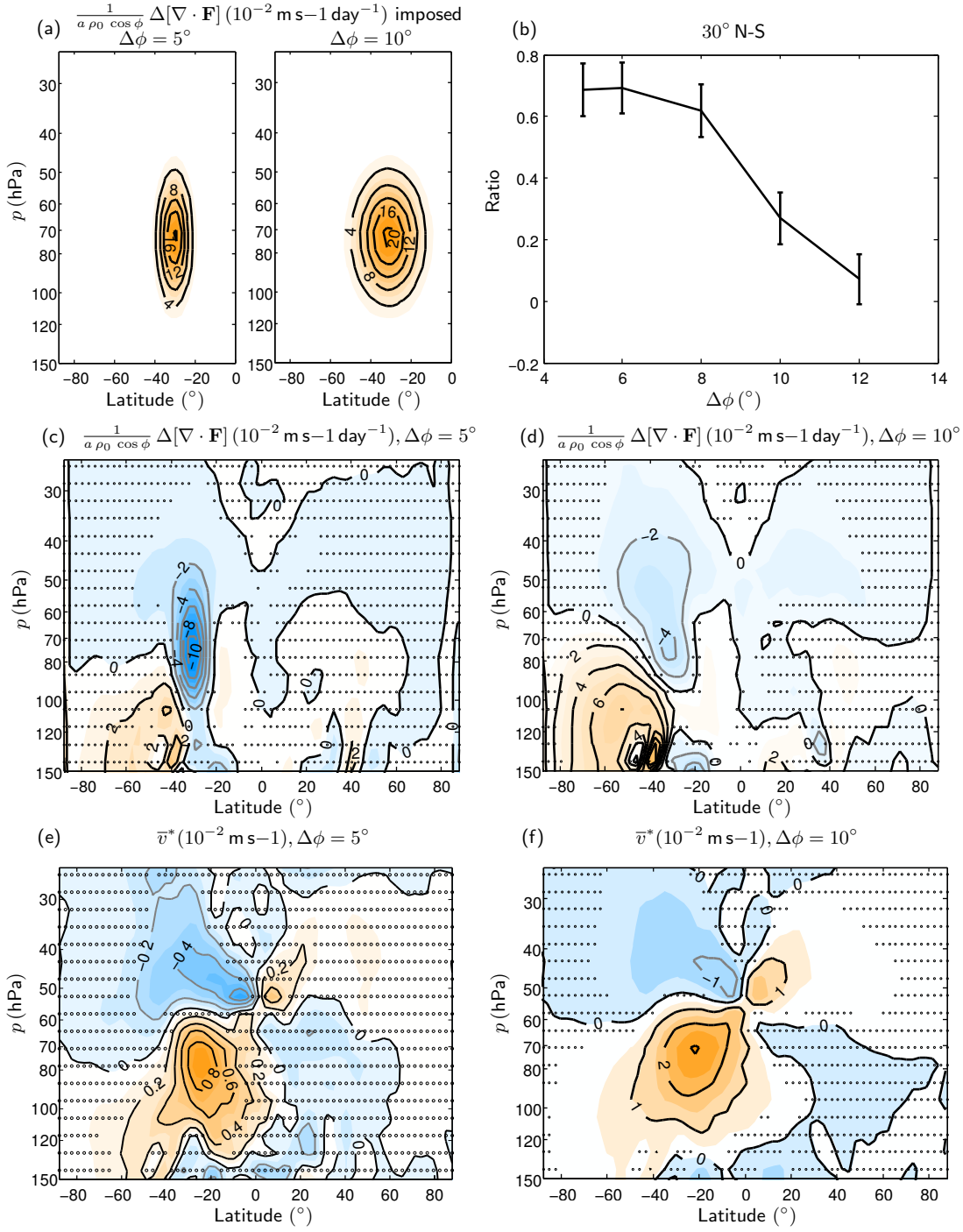


**Figure 4.21:** (a)Imposed Gaussian perturbation in $1/(a\,\rho_0\,\cos\phi)\,\nabla\cdot\mathbf{F}$ located at 30° S only. Two different widths ($\Delta\phi = 5°$ and $\Delta\phi = 10°$) are shown. Note that only the Southern Hemisphere is shown. The perturbation is only in one hemisphere. (b) Ratio of $-\nabla\cdot\mathbf{F}/\nabla\cdot\mathbf{F}_{\mathrm{imposed}}$ at the maximum of the perturbation (30° S, 78 hPa) plotted against the width of the perturbation, $\Delta\phi$. (c) Change in the $1/(a\,\rho_0\,\cos\phi)\,\nabla\cdot\mathbf{F}$ for a perturbation of width $\Delta\phi = 5°$. (d) Similar to (c) but for a width of $\Delta\phi = 10°$. (e) Change in $\overline{a}\overline{v}\overline{g}\overline{v}^*$ for $\Delta\phi = 5°$. (f) Similar to (e) but for $\Delta\phi = 10°$. The regions stippled are not significant at the 95% confidence level as determined by an adjusted Student's t-test.

However in discussing relevant mechanisms Cohen et al. (2013) argued that a narrower force would tend to give rise to change in sign of potential vorticity gradients and that the resulting dynamical instability would give rise to a redistribution of the wave force. Our argument, on the other hand, simply asserts that there will be, as part of the response to an applied heating or an applied perturbation to part of the wave force, ($\Delta G_{\mathbf{h}}$) in our notation), a change of the total wave force because the propagation and dissipation of waves will change as the zonal flow changes. The fact that we found in the three-dimensional simulations with applied heating that the amplitude of the response is linear in the amplitude of the applied heating suggests that no particular instability threshold has to be exceeded to give the required dynamical effect and the same conclusion might be drawn from the results of Watson and Gray (2015) who found that changing the sign of the applied force simply changed the sign of the response. We argue further that the overall magnitude of this change is usefully captured by the quantity $K$ and that this through expression 4.8 determines the nature of the response.

## 4.8 Discussion

In this chapter we have examined the double-peak structure in the low-latitude low stratosphere seen in the ERA-Interim dataset in both diabatic heating (Fueglistaler et al. (2009b)) and correspondingly in the upwelling vertical velocity (Seviour et al. (2012)). The upwelling was shown to be consistent with that inferred from the downward control principle, with better agreement when the actual angular momentum distribution is taken into account, rather than assuming that for a resting atmosphere. This consistency is solid evidence that the double peak in upwelling is not an artefact of the reanalysis process. We examined the various contributions to diabatic heating in more detail using an offline radiative code, taking account of up-to-date estimates of ozone and water vapour distributions. This calculation, independent of ERA-Interim except for the temperature and water vapour distributions, could account for the double-peak structure in the diabatic heating, though the amplitude was less than that implied by the ERA-Interim dataset.

The difference between 20 °N and the Equator at 66 hPa in clear sky longwave heating rates averaged from 1991 to 2010 can be broken down as follows: 60% can be attributed to the ozone meridional gradient and 30% to the temperature changes with smaller contributions from water vapour. There is a significant amount of inter-annual

variability in the temperature contribution to the double peak largely associated with the lower stratospheric temperature signal of the QBO. Whether or not there is inter-annual variability in the ozone contribution is not revealed by our study since a fixed ozone climatology is used in the radiative code of ERA-Interim.

We argued that, bearing in mind the corresponding structure in temperature, which does not show a double peak and is relatively flat across low latitudes, the double peak in upwelling is likely to be caused by latitudinal structure in the radiative heating rather than being a response to latitudinal structure in the wave force. This argument implicitly requires that a long-term change in the meridional circulation is caused by a change in radiative heating. For this to be possible there has to be a self-consistent angular momentum balance and hence also a change in the wave force. We investigated this further in a simple three-dimensional dynamical model, set up in the Held and Suarez (1994) configuration, which we argued captured the essential wave dynamics relevant to the subtropical lower stratosphere. A radiative heating perturbation was imposed by adding two localised regions of heating to the standard configuration. The response to the heating was deduced by taking the difference between the time average circulation and temperature in this perturbed configuration and that in the standard configuration. We found that for a latitudinally confined diabatic heating perturbation, the dominant balance in the thermodynamic equation, in the region of the heating perturbation, is between the heating and the upwelling terms. The temperature change makes a relatively small contribution (through the Newtonian cooling term) to the thermodynamic equation in this region and the latitudinal scale of the overall temperature change is much broader than the scale of the heating perturbation, with weak temperature gradients across the tropics and subtropics. Angular momentum balance is maintained by a change in Eliassen-Palm flux, so that the change in wave force balances the Coriolis force associated with the change in meridional circulation. In this regime the upwelling response can simply be deduced from the heating perturbation and is insensitive to the details of the dependence of the wave force on the zonal velocity.

We set out scaling arguments to provide some dynamical insight into this circulation response. These arguments assumed that the typical magnitude of the change in wave force was $K$ times the typical magnitude of the change in zonal velocity, with $K$ having the dimensions of inverse time. According to these arguments an applied heating would be primarily balanced by an upwelling provided that the dynamical aspect ratio $K\,N^2\,D_Q^2/\alpha\,f^2\,L_Q^2 \gg 1$ (expression 4.2), i.e. the heating was relatively deep and narrow in a sense that depends on the various parameters $K$, $N$, $f$ and $\alpha$, with in

particular large $K$ and/or small $f$ (i.e. low latitude) making it more likely that the condition is satisfied. The scaling arguments are similar to, but potentially have wider applicability than, those applied by previous authors (e.g. Fels et al. (1980), Garcia (1987)) in considering the zonally symmetric response to heating when the wave force is represented by Rayleigh friction ($K$ is then simply the Rayleigh friction coefficient). We presented some explicit zonally symmetric calculations with Rayleigh friction for comparison purposes. These calculations capture the balance between applied heating and upwelling seen in the three-dimensional simulations when the heating is deep and narrow (comparing Figure 4.12(b) and the third column in Figure 4.14). But even in that case they do not capture, for example, the response in zonal velocity (comparing Figure 4.12(d) and the second column in Figure 4.14), which is determined by the details of the dependence of the wave force on the zonal velocity and which in the three-dimensional simulations very clearly does not correspond to Rayleigh friction.

We demonstrated by varying the width $L_Q$ of the region of applied heating that the scaling arguments gave useful insight, i.e. that as the width increased the change in upwelling no longer provided the dominant balance in the thermodynamic equation for the heating perturbation $\Delta Q$. Instead other terms in the thermodynamic equation became more important, both the Newtonian cooling term and the term representing the effect of the change in static stability. Both have to be taken into account, together with the change in upwelling to understand how the heating is balanced.

Perhaps surprisingly, when the width for the applied heating was taken to be its smallest value ($\Delta\phi = 5°$) and the latitude of the heating changed from low latitudes to mid and high latitudes the response continued to be dominated by upwelling, suggesting that the value of $K$ was at each latitude sufficiently large to ensure large values of the expression 4.2. However it is not clear that any aspect of the real atmosphere naturally motivates such narrow applied heating in mid latitudes and certainly broader heating, as might represent the effect of mid-latitude ozone trends, for example, gives a significant temperature response.

From the radiative calculations in Section 4.3 and the dynamical calculations in Section 4.4 we deduce that an important part of the latitudinal structure in radiative heating that causes the double peak in upwelling is due to the ozone distribution. In reality, of course, the ozone distribution is determined by transport processes, but not just vertical advection, also horizontal mixing/exchange with the extratropics. This is not captured by our dynamical calculations, in which the structure of the

applied heating is simply imposed, but these calculations might be seen as a first step towards understanding the latitudinal structure of the low-latitude upwelling in a system, where, as the in real atmosphere, dynamics, radiation and chemistry are fully coupled. A further important point is a fixed dynamical heating calculation, often used as to infer temperature changes that result from changes in constituents such as ozone, would not be relevant here – it is precisely the dynamical heating that is the main response to the structure in the ozone field.

Finally we have noted that the dynamical discussion leading to expression 4.2 can be extended to consider the response to an applied force added to the flow-dependent wave force. In this case when the applied force is relatively narrow and deep in the sense of the aspect ratio, expression 4.8, being large, the applied force is primarily balanced by an adjustment to the flow-dependent wave force rather than by the Coriolis torque. The response in the meridional circulation is therefore small. If it is accepted that differences in parametrised waves correspond to narrow and deep applied forces, which is naturally motivated by the results of Cohen et al. (2013) (see their Figures 4b and 5d) and Sigmond and Shepherd (2014) (see their Figure 2) then this potentially offers an overall dynamical principle that explains the compensation (in the changes in the Brewer-Dobson circulation driven by resolved waves and by parametrized waves) observed in climate model simulations. Of course, if the aspect ratio, expression 4.8, is to be of quantitative use then the sensitivity $K$ must be estimated and, as we have emphasised previously, this is by no means straightforward, since it essentially requires a parametrisation of wave force for an arbitrary mean flow.

# Appendix: Adjusted Students' t-test

The reanalysis data contains serial correlations which must be taken into account when testing statistical significance and estimating confidence intervals. Consider a time series, $x$, with sample size $n$ and sample mean $\overline{x}$. We follow the method described in Zwiers and von Storch (1995) which entails estimating an effective number of degrees of freedom, $n_e$, from the autocorrelation function, $\rho(t)$, of the time series (Section 2.6). Confidence intervals are based on a modified estimate of the standard deviation of the sample mean, $\hat{\sigma}_\mu = \hat{s}\,\hat{n}_e^{-1/2}$, where $\hat{s}$ is the standard deviation of the time series and $\hat{n}_e$ is the effective number of degrees of freedom, Equation 2.1.

A further check on the uncertainty estimates is performed by splitting the dataset into a set of smaller continuous sub samples of length $N$ and means $\hat{m}_i$ where the subscript

$i$ denotes a sub sample. Two different estimators for the standard deviation of the sub sample means, $\hat{\sigma}_m(N)$ and $\hat{\sigma}_\mu(N)$, are obtained and compared as $N$ is changed. The first method involves scaling the later with $N$ to give $\hat{\sigma}_\mu(N) = (\hat{n}_e\, n/N)^{-1/2}\, \hat{s}$. The second estimate, $\hat{\sigma}_m(N)$, is given by the standard deviation of the means $\hat{m}_i$. These estimates should converge if the adjusted standard deviation for the whole time series $\hat{\sigma}_\mu(n)$ is reasonable.

An example of this convergence for $\overline{w}^*$ from ERA-Interim at 20° N and 66 hPa is plotted in Fig. 4.22 showing good agreement with $n_e \sim 4100$ ($n = 29200$).

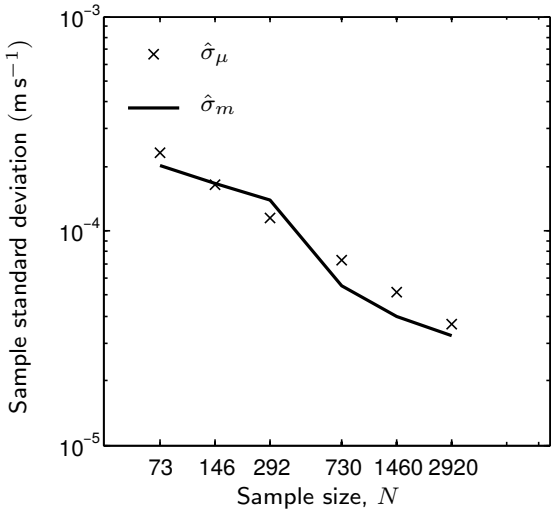


**Figure 4.22:** Estimates of the standard deviation in $\overline{w}^*$ from ERA-Interim at 20° N and 66 hPa computed from 6-hourly data from 1991 to 2010 ($n = 29200$). $n_e = 4100$.

The method used to estimate the statistical significance of the difference between two quantities is closely related to that described above. The effective number of degrees of freedom, $n_e$ is estimated in the same way. In the model experiments, we showed calculations of the difference of the means between two time series $X$ and $Y$ and tested the null hypothesis $H_0 : \mu_X = \mu_Y$. One of the two sets of formula in von Storch and Zwiers (2001) is used to calculated the test statistic

$$t = \frac{\hat{\mu}_X - \hat{\mu}_Y}{\sqrt{\hat{s}_X^2/\hat{n}_{e\,X} + \hat{s}_Y^2/\hat{n}_{e\,Y}}}, \tag{4.9}$$

and the approximate degrees of freedom given by

$$df = \frac{(\hat{s}_X^2/\hat{n}_{e\,X} + \hat{s}_Y^2/\hat{n}_{e\,Y})^2}{\frac{(\hat{s}_X^2/\hat{n}_{e\,X})^2}{\hat{n}_{e\,X}-1} + \frac{(\hat{s}_Y^2/\hat{n}_{e\,Y})^2}{\hat{n}_{e\,Y}-1}}. \tag{4.10}$$

We check this calculation, within features likely to be relevant to the conclusions in this work, by dividing the time series into sub samples of size $N$ and calculating $\hat{\sigma}_{\mu_X-\mu_Y}(N)$ and $\hat{\sigma}_{m_X-m_Y}(N)$. As described in Part I, these two quantities should converge as $N$ tends to $n$.

An example of this calculation is shown in Fig. 4.23 for the temperature change when the heating is applied at latitude 15° as described in Section 4.5. Let $X$ be a time series for the unperturbed Held-Suarez run (with mean $\mu_X$) and $Y$ be a time series with a heating perturbation (with mean $\mu_Y$). Each time series is 90 000 days long and has $n_{e\,X} = 470$ and $n_{e\,Y} = 490$. Fig. 4.23 shows the two quantities can be seen to converge. For changes in the zonal wind near the top of the model over the Equator, long timescales in the data means that the calculation of $\hat{n}_e$ does not always converge and it is necessary to sum to where the lag falls below $e^{-3}$ in

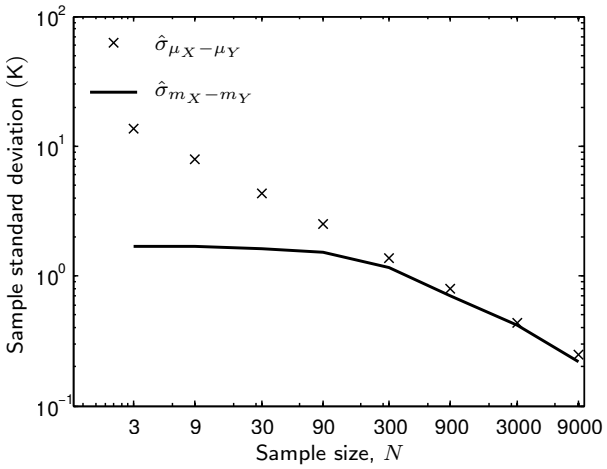


**Figure 4.23:** Sample standard deviation for the temperature difference calculated at 78 hPa and 15° N for the heating located at latitude 15° (case described in section 4.5). The crosses are the sample standard deviation calculated by scaling the effective number of degrees of freedom with sample size. The line is obtained by estimated the standard deviation of the sample.

# Chapter 5

## Annual cycle in tropical lower stratospheric temperatures

## 5.1 Introduction

The previous chapter focused on time averaged features of the UTLS region. This chapter moves towards discussing the annual variation in tropical lower stratospheric temperatures. Temperatures in the tropical tropopause layer exhibit a marked annual cycle [Reed and Vicek (1969)] whilst one would naïvely expect that there would be a semi-annual cycle based on the fact the sun goes over the Equator twice in a year as the tilt of the Earth changes. The annual cycle climatology in temperature in ERA-Interim, constructed using data from 1991 to 2010, is shown in Figure 5.1. The temperature variations appear coherent over a region from about 125 hPa to 25 hPa with a maximum around 70 hPa of 7 K peak to peak. Above this region temperature variations are dominated by the semi annual oscillation and below the temperature is controlled by upper tropospheric processes [Fueglistaler et al. (2009a)].

Many explanations have been put forth to explain the annual cycle in temperatures. Initial explanations by Reed and Vicek (1969) and Reid and Gage (1981) involved the tropospheric Hadley circulation penetrating into the stratosphere. A completely different mechanism was proposed by Yulaeva et al. (1994). They noted that in the Microwave Sounding Unit channel 4 (MSU-4) temperature data there was significant compensation between tropical and extratropical temperature variations as defined by the area weighted averages inside and outside of latitude 30° respectively. Each of these annual cycles has an amplitude of about 2 K and the global mean annual cycle has a residual of only about 0.2 K. They proposed that the tropical annual cycle

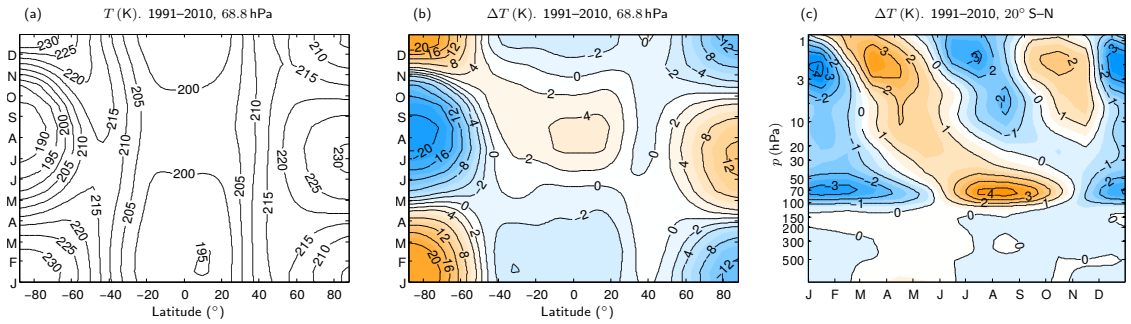


**Figure 5.1:** Seasonal climatology in ERA-Interim temperature constructed by averaging from 1991 to 2010. (a) Temperature (K) at 68.8 hPa. (b) Difference in temperature (K) from annual mean value at 68.8 hPa. (c) Difference in temperature (K) from annual mean averaged between 20° N–S.

is not caused by tropospheric processes but by stratospheric processes, in particular the stratospheric circulation. When the circulation is strongest in boreal winter, the ascending branch drives strong adiabatic cooling and hence lower temperatures. The opposite is true in the descending branch and this would lead the compensation observed in the temperatures. Yulaeva et al. (1994) also show that the small residual global annual cycle in temperatures follows the equatorial total ozone cycle with a lag of a few weeks. A similar analysis of tropical and extratropical temperatures was done by Young et al. (2011) throughout the depth of the stratosphere and their results in the lower stratosphere using MSU-TLS temperatures agree with Yulaeva et al. (1994).

Kerr-Munslow and Norton (2006) argue that the annual cycle in temperature is driven by tropical wave driving rather than wave dissipation in the extratropics. Whilst the annual variation in dynamical cooling is likely to lead to the main component of the annual cycle, we will show that the annual cycle in trace gases is also important. Fueglistaler et al. (2011) revisit the Yulaeva et al. (1994) analysis of MSU-4 data and find that the strong degree of compensation is an artefact of the MSU-4 weighting function and does not hold on individual pressure levels. Whilst they agree with Yulaeva et al. (1994) that there is an important role for the residual circulation in the annual cycle in temperatures, they argue that the latitudinal structure in both the static stability and radiative equilibrium temperatures from the ozone annual cycle cannot be neglected. Ozone variations at 70 hPa make significant contributions to the temperature cycle in the tropics as shown by radiative calculations in Fueglistaler et al. (2011). They use a seasonally evolving fixed dynamical heating (SEFDH) framework (described in more detail below) with the ozone concentrations from HALOE measurements to show that about a third of the temperature variations can be attributed to ozone.

The importance of ozone is further supported by calculations from Chae and Sherwood (2007) done in a one dimensional radiative-convective model with an imposed upwelling in the stratosphere. They attribute about 3 K of the peak to peak amplitude in the annual cycle to ozone. However, their calculations also make use of constant water vapour and they claim that the role of water vapour is negligible. We will revisit this assertion in this chapter.

Ozone is strongly linked to the circulation and it is difficult to determine what drives the ozone annual cycle. Stronger upwelling in the tropics in boreal winter leads to ozone poor tropospheric air being brought into the tropical lower stratosphere which accounts for part of the amplitude of the annual cycle variation. The other part arises from an annual variation in in-mixing between the tropics and the midlatitudes [Randel et al. (2007a), Konopka et al. (2010)]. Stolarski et al. (2014) recently showed that the whilst these two effects are in phase in the Northern Hemisphere, they are not in the Southern Hemisphere and that the tropics cannot be treated as a latitudinally homogeneous region.

Whilst it is established that the ozone contribution is substantial, the only quantitative estimate that takes into account the seasonal evolution and that shows the latitudinal structure of the temperature change is from a seasonally evolving fixed dynamical heating calculation (see Section 5.3 for more details) [Fueglistaler et al. (2011)]. This calculation will be examined more closely in this Chapter. Such a calculation although not widely used has the potential to explore various aspects of the vertical coupling from radiative transfer as we will demonstrate. Moreover, the contribution from water vapour which is another major radiatively active trace gas has not been addressed. There is a pronounced annual cycle in water vapour in the tropical UTLS which maximises around 100 hPa with a signal that is evident up to about 20 hPa as can be seen in the work of Randel et al. (2001) and in plots in later sections of this chapter. Various studies have shown that water vapour makes a significant contribution to the energy balance in this region. Maycock et al. (2011) used a set of radiative calculations to show that a uniform increase in stratospheric water vapour gives rise to a cooling that is largest in the lower stratosphere at all latitudes.

Before looking at dynamical interactions, it is important to first understand the temperature changes. Temperature is a key state variable that connects the dynamical processes to the radiative and chemical processes. In particular, the annual temperature changes at the cold point determine the structure of the water vapour tape recorder signal, Figure 5.2. The amount of water vapour that is freeze dried out of a parcel of

air as it travels upwards depends on the coldest temperature encountered and it can be argued that the annual cycle in temperatures is more relevant in setting the saturation vapour mixing ratio than the annual mean value. The rapid decrease with height in water vapour content past the cold point is schematically represented by a sharp gradient in colour in Figure 5.3. In contrast, the mixing ratio of ozone is increasing sharply with height with more photochemical production in stratosphere.

**Figure 5.2:** From Mote et al. (1996). Variable part of total hydrogen from HALOE data. 12° S to 12° N. The total hydrogen include both water vapour and methane.

Whilst existing studies have focussed on the decadal trends in ozone [e.g Forster et al. (1997)] and water vapour and their subsequent impact on the circulation and surface climate, the annual cycle aspect of water vapour in the UTLS and its radiative impact in this region has been neglected. Various radiative studies have shown that changes in stratospheric water vapour have a significant impact on temperature trends in the stratosphere and the surface (e.g Forster and Shine (1999), Forster and Shine (2002), Solomon et al. (2010)). Changes in stratospheric temperatures will affect the circulation and to date, a small number of climate model simulations have established a link between stratospheric water vapour changes and the stratospheric flow [MacKenzie (2004), Rind and Lonergan (1995)] and to the tropospheric climate [Joshi et al. (2006)]. Maycock et al. (2014) also looks at some aspects of the dynamical response to changes in water vapour but do not look in detail at the annual cycle aspect of water vapour changes. With the many complex interactions between the dynamics, radiation and chemistry in this region, the current modelling studies have either focused on very idealised single column radiative perturbations or fully comprehensive climate models which take into account a range of feedbacks from the eddies and on the transport of the trace gases. We will attempt to bridge this gap in the hierarchy of models by setting out a set of experiments of increasing complexity to separate the different interactions.

An often used linearisation in the atmosphere and in climate models is to describe heating perturbations as being proportional to the local temperature change and this

can be written as $-\alpha\,(T - T_{\mathrm{rad}})$ where $T_{\mathrm{rad}}$ is the temperature that the atmosphere would have without the dynamics (the radiative relaxation temperature) [Fels et al. (1980)] and $\alpha$ is the radiative relaxation rate. This approximation was used in general circulation model parametrisations in the previous two chapters. Conceptually, it is convenient to think of the atmosphere responding to a heating with a certain timescale, given by $1/\alpha$, which gives to a first approximation an idea of how stiff the atmospheric radiative spring is. Estimates of $\alpha$ have been calculated in many studies [e.g. Dickinson (1973), Mlynczak et al. (1999), Hitchcock et al. (2010)]. In the context of the annual cycle in temperature, Randel et al. (2007a) argue that the location of the maximum in the amplitude of the temperature annual cycle at 70 hPa can be attributed to the peak in the radiative timescales at this level [Randel et al. (2002)]. We will make use of an SEFDH-like calculation to revisit this problem.

The motivation for this chapter is to investigate the various processes that contribute to the annual cycle in temperature. We will revisit the calculations by Fueglistaler et al. (2011) on the ozone cycle contribution and address the water vapour contribution to the temperature annual cycle. Furthermore, we will clarify the importance of vertical gradients in the annual cycle in trace gases. The water vapour contribution has previously been argued to be negligible in Fueglistaler et al. (2011) and Chae and Sherwood (2007). The interactions between radiation and dynamics in this region are complex and we built a framework in which these effects can be studied separately. Chemistry climate models are generally able to reproduce the phase of the annual cycle in ozone and water vapour in the TTL but there is a wide spread in the values with a corresponding spread in cold point temperatures [Gettelman et al. (2010)]. Hence understanding the radiative effect of the annual cycle of ozone and water vapour on the cold point temperature is relevant to future model development.

Figure 5.3 is a simplified schematic diagram that illustrates some of the key processes and complex interactions in the TTL. The two pressure levels shown are of particular interest in this work. Both the temperature and ozone annual cycles maximise at around 70 hPa [Randel et al. (2007a)] but the amplitude of the water vapour cycle is largest at 100 hPa [Randel et al. (2001)].

The chapter is organised as follows. The first section gives a brief overview of a widely used technique, the fixed dynamical heating (FDH) calculation, to estimate temperature changes from constituent changes using a single column radiation code. We then extend the radiative calculations to understand how individual species contribute to the heating rate and how the radiative adjustment happens. Section 5.3 then

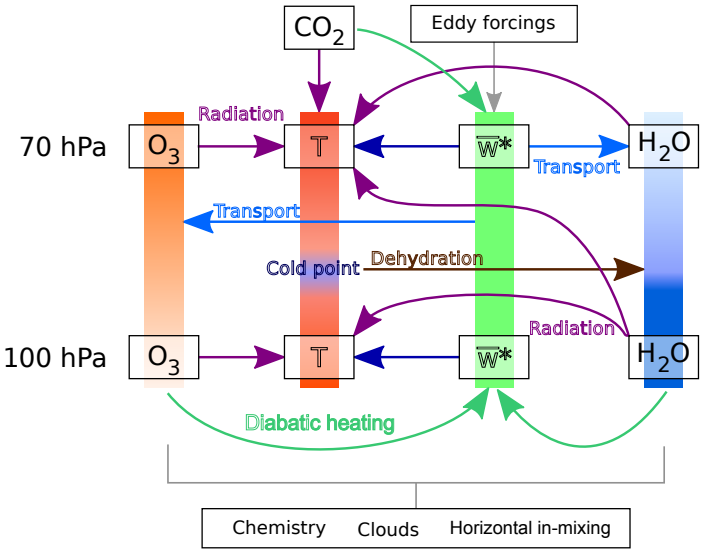


**Figure 5.3:** Schematic diagram illustrating some of the key processes taking place in the tropical tropopause layer. The color gradients for the temperature and upwelling are intended as a visual guide to show how these quantities change with height. Purple arrows show the radiative influence. The blue arrows indicate a dynamical link. The brown arrow shows that the cold point temperature influences the amount of water vapour entering the stratosphere. The grey arrows shows that eddies influence the upwelling.

describes a similar calculation for the seasonally evolving case where we demonstrate that water vapour plays an important role in the annual cycle in the UTLS and exerts a non-local influence on temperature changes. In Section 5.4 we perform a corresponding set of experiments with the same radiation code in a zonally symmetric dynamical model to include the effects of the zonally symmetric dynamics. Finally, Section 5.6 contains a discussion and some conclusions.

## 5.2 Fixed dynamical heating (FDH) calculations

The fixed dynamical heating calculation is a method to estimate the effect of a change in a trace gas on the temperature under the assumptions that no circulation changes are produced and the stratosphere adjusts radiatively to a heating perturbation [Fels et al. (1980), Ramanathan and Dickinson (1979)]. The purpose of this section is to revisit the widely used FDH technique and show how water vapour and ozone perturbations lead to a temperature change in such a calculation. These calculations illustrate various aspects of the radiative response that will become important in later discussion. These idealised calculations can also be used as a benchmark to compare to results from other radiation codes.

The timescale on which the stratosphere reacts to such perturbations is relatively short compared to the troposphere; about 40 days in the lower stratosphere and less than a week near the stratopause [Hitchcock et al. (2010)]. In contrast, the tropospheric response is affected by the slow adjustment of the ocean. Hence it is common in FDH calculations to keep tropospheric temperatures fixed. Numerous radiative studies have made use of FDH calculations often in the context of stratospheric temperature trends [Ramaswamy et al. (2001)]. FDH temperature changes have also been shown to be in good agreement with GCM results [Fels et al. (1980), Forster and Shine (1999, 2002)] except in the winter extratropical stratosphere where dynamical interactions are important. Figure 5.4 summarises these processes. Compared to Figure 5.3, we have only kept the radiative influence of carbon dioxide, ozone and water vapour via a heating perturbation on the temperatures. The dynamical heating is assumed to be constant.

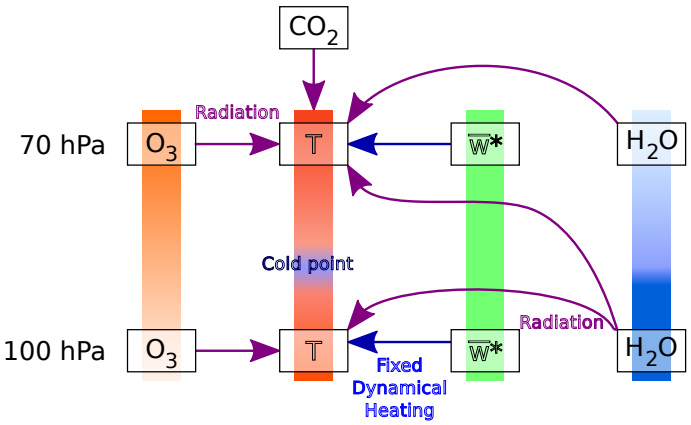


**Figure 5.4:** Schematic diagram illustrating some of the processes included in the fixed dynamical heating calculation.

The thermodynamic equation (written in a simplified form in Equation 5.1) relates the rate of change of temperature of a parcel of air to the amount of dynamical, $Q_{\text{dyn}}$, and radiative, $Q_{\text{rad}}$, heating. The radiative heating can be broken down into a temperature dependent longwave (LW) component and a shortwave (SW) heating which to a good approximation is temperature independent in the region of the atmosphere under consideration.

$$\partial_t T^0 + Q_{\text{dyn}} = Q_{\text{rad}}(T^0, \chi^0) = Q_{\text{LW}}(T^0, \chi^0) + Q_{\text{SW}}(\chi^0), \tag{5.1}$$

where $T^0$ is the temperature and $\chi^0$ represents the concentrations of all radiatively

active trace gases. The superscript $(.)^0$ will be used to denote the base state and $(.)'$, the perturbed state. In the steady state, the rate of change of temperature is zero and $Q_{\rm dyn}$ balances $Q_{\rm rad}(T^0, \chi^0)$. For a given profile of trace constituents and temperature, the dynamical heating can be estimated by assuming it is equal to $Q_{\rm rad}(T^0, \chi^0)$. When a trace gas is perturbed from $\chi^0$ to $\chi'$, the radiative heating changes and under the fixed dynamical heating approximation, the temperature is adjusted (to $T'$) until a new equilibrium holds with the dynamical heating held constant,

$$Q_{\rm dyn} = Q_{\rm LW}(T', \chi') + Q_{\rm SW}(\chi'). \tag{5.2}$$

Numerically, this is done by iterating the temperatures forward with a time step of one day using the longwave heating rates until the change in temperature and the fluxes between levels between consecutive time steps falls below $5 \times 10^{-4}$ K and $1 \times 10^{-7}$ K m$^{-1}$ respectively. These values were found to produce adequate convergence. In practice, these thresholds are reached after about 500 days which is much larger than any radiative timescales in the stratosphere, hence, ensuring that the temperatures in the stratosphere have converged.

Two FDH calculations with ozone and water vapour perturbations will now be included to illustrate the radiative effects of these gases in the tropical lower stratosphere. The Zhong and Haigh radiation code with 50 pressure levels (described in Section 2.5.1) is set up to do an FDH calculation. The base profiles of ozone and water vapour used are from the SWOOSH dataset at the equator and time averaged. These are shown as the solid lines in Figures 5.5(a) and 5.6(a) respectively. The dynamical heating is estimated as being equal to the radiative heating in the unperturbed case for the ozone and water vapour profiles. The ozone is now perturbed in the lower stratosphere to the profile shown by the dashed line. This is done by removing a Gaussian perturbation of the form $0.5 \times 10^{-6}$ exp$[-(z - 18.6)^2/4]$ where $z = -7 \log(p/1 \times 10^5)$ km, from the region between 30 and 200 hPa.

A similar perturbation is removed from the water vapour profile of the form $1 \times 10^{-6}$ exp$[-(z - 18.6)^2)/8]$ (dashed line in Figure 5.6(a)). A mixing ratio of 285 ppmv was used for carbon dioxide but since carbon dioxide is well mixed and this is purely an illustrative calculation, the particular choice of value is not critical. The horizontal line at 200 hPa indicates the highest level at which the temperatures are not adjusted (troposphere-like). This level will be referred to as the FDH 'tropopause'. The temperature change under the FDH assumptions is shown in Figures 5.5(b) and 5.6(b). The time scale to balance a radiative heating is of the order of the radiative time scales.

Estimates in the atmosphere range from 25 days [Hitchcock et al. (2010)] to 100 days [Mlynczak et al. (1999), Randel et al. (2002)] in the lower stratosphere. In our FDH calculations, a good approximation to the final temperature change is obtained after about 50 days although to satisfy the convergence conditions on the heating rates and fluxes just described, the FDH iteration runs for about 500 days.

### 5.2.1 Ozone perturbation

Figure 5.5(c) shows that the dominant instantaneous response to a decrease in ozone in the lower stratosphere is a local decrease in the long wave heating rate, $Q_{\mathrm{LW}}$ where 'local' refers to the region around the perturbation. A weaker local decrease in shortwave heating is also seen as a result of less absorption. Ozone concentrations are low in the troposphere allowing the upwelling longwave radiation of wavelength relevant to ozone (9.6 $\mu$m-band) to reach the stratosphere. Decreasing the ozone mixing ratio in the lower stratosphere will cause less local absorption of upwelling longwave radiation in the region where the ozone is removed leading to a local cooling. The longwave is then absorbed by ozone present at higher altitudes causing heating above the perturbation. As the temperature changes, both carbon dioxide and to a lesser extent water vapour and ozone act to damp out the temperature change as shown in Figure 5.5(d). Removing ozone around 70 hPa will induce a shortwave cooling. The temperatures will response such that a local heating in the longwave is produced to balance the short wave cooling. The equilibrium temperature change is dominated by local decrease around 70 hPa (Figure 5.5(b)). Note that sharp changes in the heating rate at 200 hPa (FDH 'tropopause') are due to the discontinuity in the temperature gradient resulting from holding temperatures below this level fixed in the FDH calculation.

The main conclusion from this calculation is that a local decrease in ozone results in a local decrease in temperature in an FDH calculation.

### 5.2.2 Water vapour perturbation

Figure 5.6 is similar to Figure 5.5 but for the water vapour perturbation. The abundance of water vapour in the troposphere means it is relatively opaque to upwelling longwave radiation. One day after the perturbation, the effect of locally reducing the water vapour in the lower stratosphere is to cause less emission of longwave radiation to

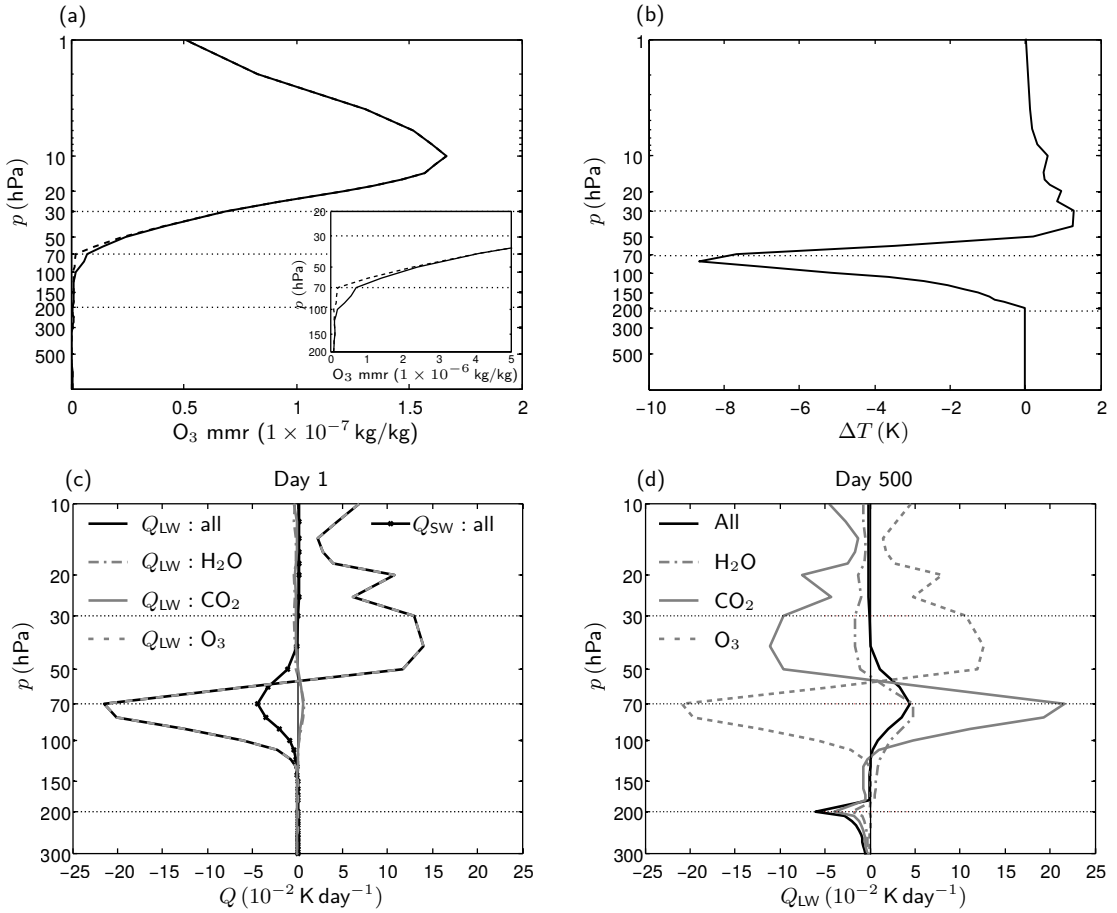


**Figure 5.5:** (a) Ozone reference profile (solid) and perturbed profile (dashed) used in the FDH calculation. The inset panel shows a close up plot of the perturbed profile. (b) Temperature change resulting from the ozone perturbation. The calculation is done at 10° N on January 1 but the results should be qualitatively similar for other times and latitudes. The horizontal lines are intended as visual guides for a subset of the pressure levels. The line at 200 hPa denotes the FDH 'tropopause'. (c) The clear sky long wave and short wave heating rate one day after the perturbation was applied with the longwave broken down by species. (d) Similar to (c) but at steady state. The short wave heating is not shown but will not change as the temperature evolves. Note that the vertical scale in (a) and (b) is different to (c) and (d).

surrounding regions resulting in local heating and a non-local cooling in the region below. Less water vapour also results in less shortwave being absorbed locally.

Similar to the ozone perturbation, Figure 5.6(d) shows carbon dioxide, ozone and water vapour act to damp out the initial temperature change that the long wave heating rate changes are driving. Emission dominates over absorption locally for water vapour and the local temperature rises. The removal of the water vapour absorber also allows more upwelling radiation through. The local increase in temperatures will cause more

longwave emission in the bands relevant to carbon dioxide which is absorbed by carbon dioxide further up causing a small amount of warming above the perturbation. This non-local behaviour cannot be modelled by a Newtonian cooling approximation.

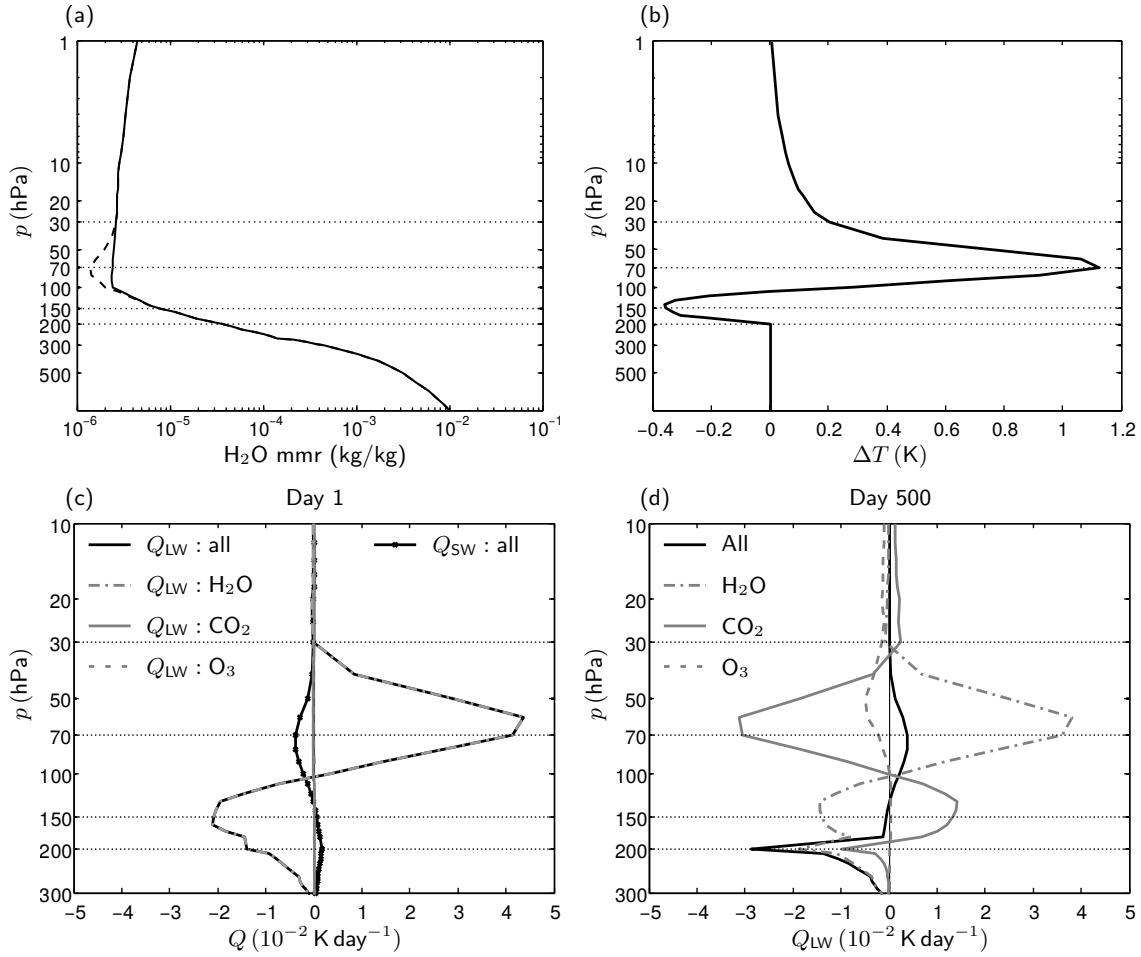


**Figure 5.6:** Similar to the plots in Figure 5.5 but for water vapour. (a) Water vapour profile (solid) and perturbation (dashed) used in the FDH calculation. The horizontal lines are intended as visual guides for a subset of the pressure levels. (b) Temperature change resulting from the water vapour perturbation. The calculation is done at 10° N on January 1 but the results should be quantitatively similar for other times and latitudes. (c) Heating rate change one day after the perturbation. (d) Heating rate change at steady state. Note that the vertical scale in (a) and (b) is different to (c) and (d).

### 5.2.3 Dependence on amplitude of perturbation

The amplitude of the Gaussian perturbations in ozone and water vapour are varied and the peak value of the temperature change under an FDH calculation is plotted against the maximum value of the perturbation in Figure 5.7. The figures show how

the FDH temperature changes vary with both ozone and water vapour perturbations in the tropical lower stratosphere. In the context of the annual cycle, the amplitude of the ozone perturbation as a mass mixing ratio is about $0.2 \times 10^{-6}$ kg/kg at 70 hPa and the results show that increases in ozone of this amplitude above the background value would produce a temperature change of about 0.83 K compared to a decrease of 0.8 K for an ozone decrease of the same amplitude. The amplitude of the water vapour perturbation is about $0.4 \times 10^{-6}$ kg/kg at 70 hPa and Figure 5.7(b) shows that the temperature change is about 0.2 K for both an increase and a decrease in water vapour. The calculations shows that the ozone and water vapour annual cycle perturbations are in the approximately linear regime.

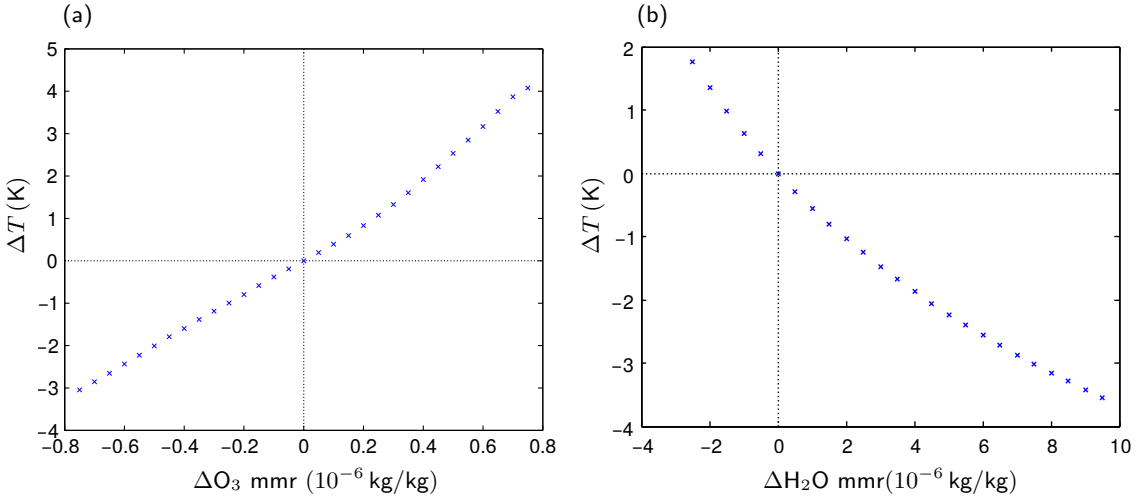


**Figure 5.7:** FDH temperature change resulting from different Gaussian perturbations in (a) ozone and (b) water vapour calculated from a similar experiment to those shown in Figures 5.5(a) and 5.6(a) respectively. The horizontal axis shows the amplitude of the perturbation at 70 hPa (the centre of Gaussian). At 70 hPa, the background mixing ratio for ozone is 0.73 ppm (kg/kg) and for water vapour is 2.9 ppm (kg/kg). The calculations are done at the Equator.

## 5.3 Seasonally Evolving Fixed Dynamical Heating (SEFDH) calculations

Since the radiative timescales in the tropical lower stratosphere are not a negligible fraction of a year, temperatures will take a few months to adjust and trace gas concentrations will have evolved. To study the radiative contribution of ozone and water vapour on the annual cycle temperatures, we make use of a modified FDH calculation that takes into account the time dependence of the dynamical heating

[Forster et al. (1997)]. When the trace gas concentration is perturbed from $\chi^0$ to a time dependent profile, $\chi'(t)$, the temperatures are adjusted iteratively using

$$\partial_t T'(t) = Q'_{\text{rad}}(T', \chi'(t), t) + Q_{\text{dyn}}(t), \tag{5.3}$$

where $Q_{\text{dyn}}(t)$ can be estimated using

$$Q_{\text{dyn}}(t) = \partial_t T^0(t) - Q^0_{\text{rad}}(T^0(t), \chi^0).$$

until a new time evolving equilibrium state in temperatures, $T'(t)$, is obtained. The dynamical heating, $Q_{\text{dyn}}(t)$, is estimated using the annual mean ozone and water vapour values and the annual cycle temperature climatology. The variation of the zenith angle throughout the year is also taken into account.

This quasi steady state takes about two years to achieve and we run the iteration for five years. The SEFDH technique is less widely used than FDH and we will first attempt to reproduce an earlier SEFDH calculation [Forster et al. (1997)]. We will then use the SEFDH technique to investigate the effects of ozone and water vapour on the annual cycle.

### 5.3.1 Reproducing the SEFDH calculation by Forster et al. (1997)

The SEFDH with the Zhong and Haigh radiation code is tested by reproducing Figure 2a from Forster et al. (1997). The ozone concentration at 80° S is depleted by 50% for the month of October to simulate an ozone hole. We follow the procedure detailed in the paper with the following changes. We use ozone and water vapour values from the SWOOSH dataset and set the carbon dioxide mixing ratio to 279 ppmv to match Forster et al. (1997). The temperature climatology and albedo value are taken from an ERA-Interim climatology. We set the tropopause level to 200 hPa and use 50 pressure levels between 1 and 1000 hPa as detailed in Chapter 2. Figure 5.8 shows that we are able to reproduce the SEFDH results of the Forster et al. (1997) paper. The structure and magnitude of the temperature change produced are similar but there are differences of up to 1 K in the temperature change close to the peak of the perturbation. Taking into account difference in the data and radiative code, we are satisfied that the SEFDH calculation has been correctly implemented.

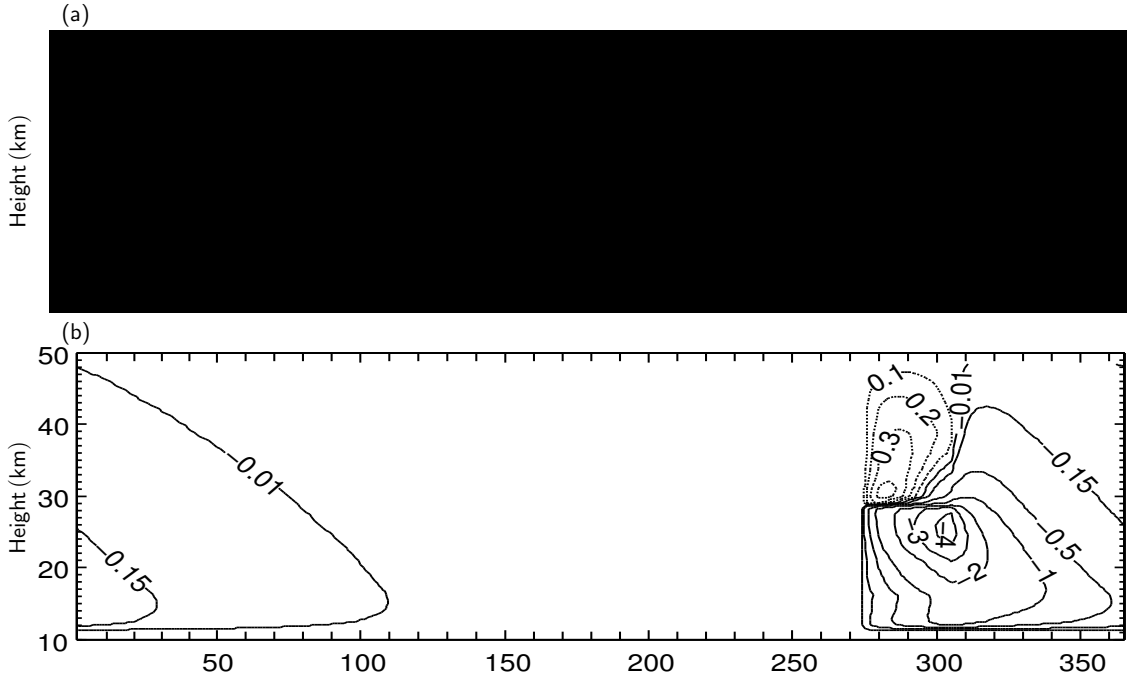


**Figure 5.8:** (a) [Figure 2a from Forster et al. (1997)] Stratospheric temperature change (K) from the SEFDH model as a function of day of the year and height, for 80° S. Ozone has been depleted between 12–28 km by 50%, during October only.The tropopause is fixed at 12 km and the tropospheric temperatures are fixed at their mid-January values. The contour values are at irregular intervals and are printed on each contour. (b) Attempt to reproduce the method in the Forster et al. (1997) using the Zhong and Haigh radiation code, ERA-Interim temperatures and SWOOSH ozone and water vapour.

### 5.3.2 Ozone annual cycle

The distribution of ozone with height over the equatorial region is shown in Figures 5.9(a) to (c). Figure 5.9(a) shows that the ozone mixing ratio increases away from the Equator at 70 hPa and that there is a pronounced annual cycle over the tropics. Figure 5.10 from Stolarski et al. (2014) shows the tropical region in more detail. They make use of a different dataset, Aura MLS, and a comparison of Figure 5.9(a) and Figure 5.10 show that the main features of the ozone annual cycle are similar between the two plots. Their analysis shows that the ozone annual cycle in the southern tropics is dominated by the seasonality of upwelling whereas in the northern tropics, seasonality in mixing is more important. Differences in the magnitude and phase of the variations in upwelling and mixing contribute to the observed structure. Figure 5.9(b) shows that the mixing ratio of ozone increases with height in the stratosphere. This is due to increasing photochemical production of ozone [Fueglistaler et al. (2009b)]. The annual cycle in ozone over the equator, as measured by the change in the mixing

ratio shown in Figure 5.9(c), also increases in amplitude with height. There are local maxima in the percentage change in ozone compared to the background value at around 70 hPa and 100 hPa. Randel et al. (2007a) show that in HALOE data, the maximum in the relative ozone cycle amplitude occurs at 83 hPa while this strong maximum is not resolved by MLS data. They emphasize the need for high resolution measurements to accurately resolve the vertical structure of the annual cycle. The SWOOSH dataset ozone values are provided at 68.1, 82.5 and 100.0 hPa in this region and whilst we believe the SWOOSH dataset to be an improvement over single satellite measurements, the vertical resolution is similar to the data used in Randel et al. (2007a) and measurements of ozone at higher vertical resolution would be desirable.

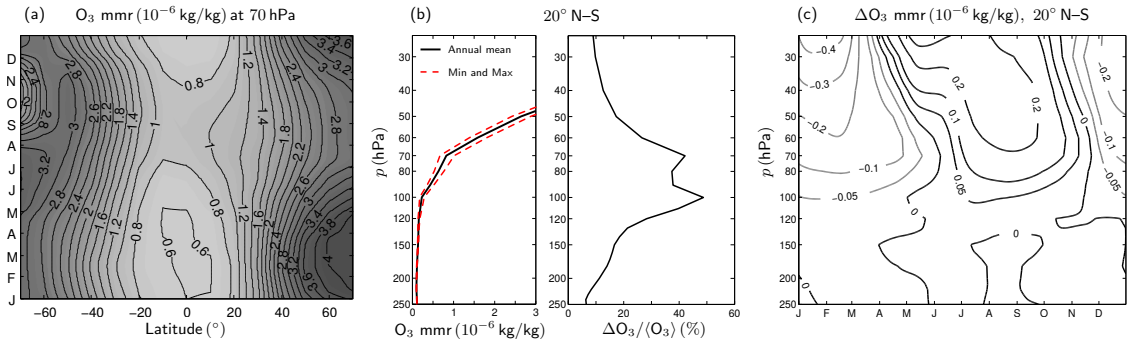


**Figure 5.9:** Ozone mass mixing ratio ($10^{-6}$ kg/kg) from SWOOSH and temperature change from an SEFDH calculation. (a) Ozone at 70 hPa on a latitude-time plot. (b) Left: Annual mean ($\langle O_3 \rangle$), maximum and minimum values of ozone. Right: Amplitude of ozone annual cycle as a percentage of the annual mean. Both plots show averages over the region 20° N–S. (c) Pressure versus time plot of ozone anomaly from the time mean averaged over 20° N–S.

Figure 5.11(a) shows the change in the ozone annual cycle from the annual mean at 70 hPa and Figure 5.11(b) shows the corresponding SEFDH temperature change at that level. In this and future calculations, the carbon dioxide mixing ratio is set to 350 ppmv which is close to the value at the start of the ERA-Interim period used. The sensitivity to this value will be discussed later in this chapter. The time dependent diabatic heating term is estimated using a climatological annual cycle of temperature from ERA-interim between 1991 and 2010 and annual mean values of ozone and water vapour from the SWOOSH dataset.

The annual cycle in ozone contributes to a temperature annual cycle of about 3.5 K peak to peak over the equator. The structure of the annual cycle in temperature in Figure 5.9(b) broadly resembles that of the ozone change in figure 5.9(a) with a lag of about 1.5 months. The meridional structure of the temperature change is set by several competing factors. The change in the ozone mixing ratio Figure 5.9(a), has

**Figure 5.10:** [Figure 8 from Stolarski et al. (2014)] Latitude/time plot of mixing ratio of 82 hPa ozone from the measurements on Aura MLS. Ozone mixing ratios are in parts per million by volume. Results are from a monthly mean climatology in 2° latitude bands repeated with 18 months shown from April through September. Red arrows are drawn from the 0.6 contour to the 0.4 contour in the summer of the northern and southern tropics to emphasize the apparent strong mixing into the northern tropics. Blue dashed lines are drawn at 20° S, equator, and 20° N to show the two tropical regions considered in the analysis. The figure is constructed from 8 years of monthly mean ozone and the months April to September are shown twice. Note that this figure shows volume mixing ratios while Figure 5.9 shows the mass mixing ratio

two minima in February at about 10° N and at 40° S. The minimum in ozone and the larger shortwave heating rates close to the equator both contribute to the large temperature change at 10° N in March–April in Figure 5.9(b). As we move south of the equator, the contribution from the shortwave is decreasing but the change in ozone is a local minimum in February at 40° S. The background ozone mixing ratio is also increasing towards the pole leading to increasing opacity to ozone and a smaller temperature change. All these contribute to the amplitude and location of the minimum in temperature being seen closer to the Equator at 30° S. In the vertical, the temperature change in the SEFDH calculation is largest between 70 to 80 hPa where the annual cycle in ozone is large compared to the annual mean value, Figure 5.9(c).

The SEFDH calculation is repeated with the annual cycle imposed between different ranges of pressure levels, namely: $[1, 30)$ hPa, $[30, 50)$ hPa, $[50, 90)$ hPa, and $[90, 1000)$ hPa to determine which levels contribute to the temperature change at 70 hPa. At all other pressure levels, ozone is set to its annual mean value. The

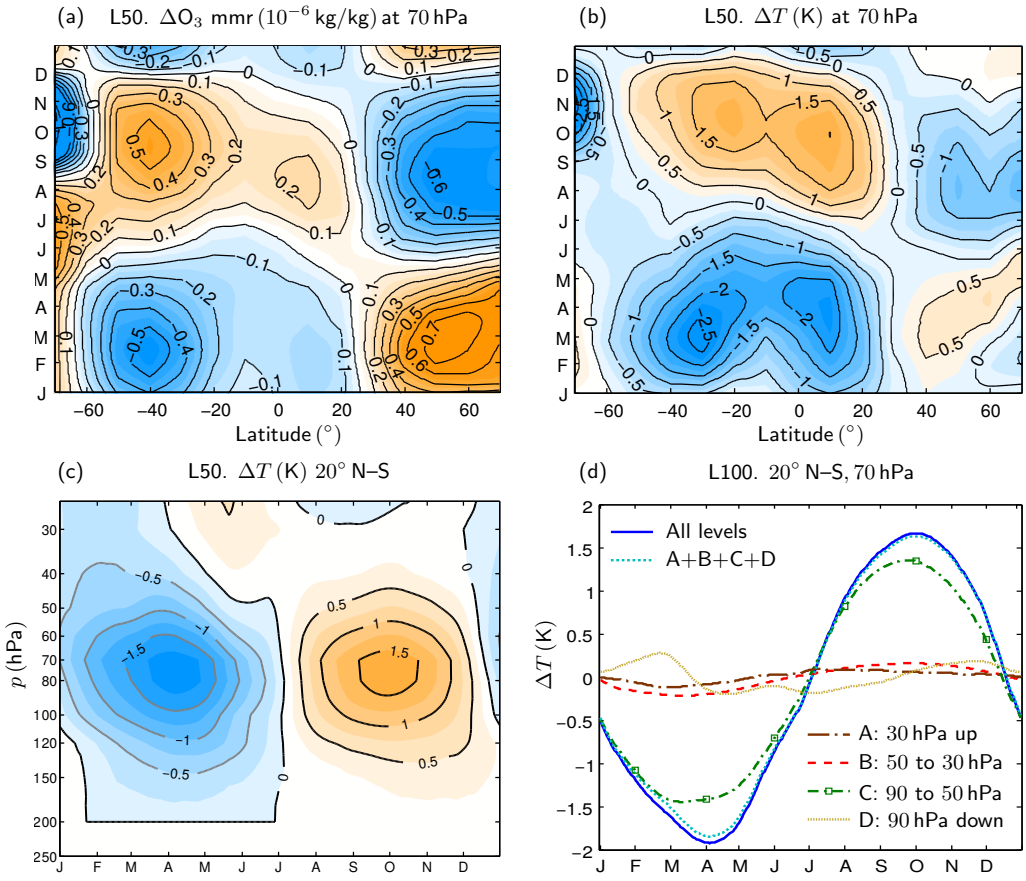


**Figure 5.11:** (a) Change in ozone from the annual mean at 70 hPa. Coloured contours are drawn at intervals of $0.05 \times 10^{-6}$ (kg/kg). The corresponding SEFDH temperature change (K) is plotted in (b), (c) and (d). All other traces gases are kept at their annual mean values. (b) Temperature change at 70 hPa (c) Temperature change averaged between 20° N–S. Coloured contours are at intervals of 0.25, K in (b) and (c). (d) Temperature changes at 70 hPa and averaged between 20° N–S calculated using SEFDH with the annual cycle in ozone imposed within different pressure ranges. Outside of this range and including the pressure level at the lower bound (in terms of height) of the range, the ozone mixing ratio is kept at the annual mean value. The calculation uses 100 vertical levels (instead of 50 in (a)–(c)) to minimise the effect of discontinuities in the ozone perturbation.

vertical resolution is increased to 100 levels (L100) to minimise the effect of these discontinuities. This increase in resolution affects temperature changes by less than 0.02 K. Figure 5.9(f) shows that the annual cycle in ozone in the region 90 to 50 hPa accounts for about 80 % of the temperature annual cycle at 70 hPa which is consistent with the results in Section 5.2.1 where ozone changes in the lower stratosphere drive primarily local temperature changes.

The amplitude of the annual cycle obtained in the calculation with the ozone annual cycle imposed at all levels is larger than that obtained by Fueglistaler et al. (2011) as

shown in Figure 5.12. Figure 5.12(a) and (b) are taken from Figure 5(a) and (b) in Fueglistaler et al. (2011) and 5.12(c) and (d) show the same data as in Figure 5.9(d) and (e) plotted such that a comparison can be made.

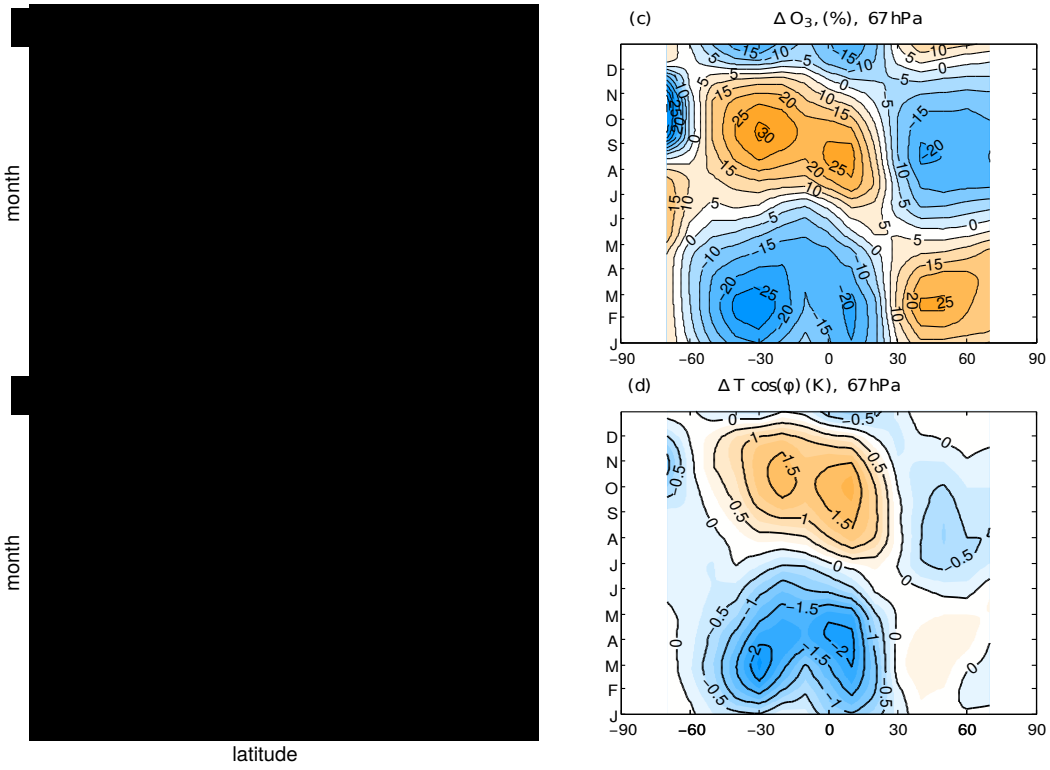


**Figure 5.12:** (a) and (b): Figures 5(a) and 5(b) from Fueglistaler et al. (2011). (a) The climatological mean annual cycle of ozone concentrations from HALOE (anomalies from annual mean, in percent). (b) The corresponding temperature adjustment under the seasonally evolving fixed dynamical heating assumption; area-weighted. (c) Percentage change in ozone concentration from the annual mean in the SWOOSH dataset. (d) Change in temperature due to ozone annual cycle in SWOOSH using an SEFDH calculation. Coloured contours are at an interval of 0.25 K.

The spatial structure of the ozone change in SWOOSH is broadly similar to that in HALOE with a larger minimum in ozone. The annual cycle in ozone in SWOOSH dataset (1984 to 2012) leads that of the HALOE dataset (1994 to 2000) by about a month. Taking into account the differences in the datasets and the fact that the radiative calculation will depend on the background value of the other trace gases, the two calculations shown in Figure 5.12 are broadly consistent in that they both predict similar latitudinal structures in the temperature change from ozone. Datasets such as HALOE contain missing data. SWOOSH was chosen because it is a more recent combined dataset generated by making SAGE-II/III, UARS HALOE, UARS MLS instruments consistent with Aura MLS.

To quantify a few of the factors contributing to the uncertainty in the temperature

change from ozone, we now look at the sensitivity to the background water vapour and carbon dioxide mixing ratios in the following sections. The water vapour perturbations used are in the range of typical values seen from between profiles from different years.

#### Sensitivity to background trace gas concentration

Additional SEFDH radiative calculations show that the temperature annual cycle at 70 hPa due to ozone is not significantly affected by the mean value of tropospheric water vapour within the range of values observed in the SWOOSH dataset. Increasing (decreasing) the annual mean water vapour mixing ratio below 200 hPa by 50 ppmv decreases (increases) the amplitude of the temperature annual cycle by only 0.001 K.

At 70 hPa, the difference between the annual mean values in individual years and the climatological mean can be up to about 0.2 ppmv for ozone and about 1 ppmv for water vapour. Figures 5.13(a) and (b) show a set of experiments where the annual mean values of ozone and water vapour respectively are changed at all heights in the region above 200 hPa. The amplitude of the temperature annual cycle decreases as the background amount of the trace gas (annual mean value) is increased since the opacity of the overlying atmosphere is a factor that will affect the amplitude and structure of the instantaneous heating rate resulting from the perturbation and the resulting equilibrium temperature as shown by Maycock et al. (2011). For the range of annual mean values observed in ozone and water vapour, the SEFDH temperature change due to ozone is most affected by the ozone annual mean as shown by Figures 5.13(a) and (b). Over the period of the SWOOSH dataset, the carbon dioxide mixing ratio changes from about 340 ppmv in 1984 to 390 ppmv in 2012. This corresponds to values of 0.97 to 1.1 $\times$ $CO_2$ in Figure 5.13(c). Variations in carbon dioxide during this time period have a negligible effect.

### 5.3.3 Annual cycle in water vapour

Fueglistaler et al. (2011) and Chae and Sherwood (2007) both claim that the effect of the annual cycle in water vapour is negligible compared that of ozone. We repeat the SEFDH calculation for ozone above but with water vapour. Figure 5.14 is similar to Figure 5.9 but for the water vapour. Figure 5.14(a) shows that water vapour has

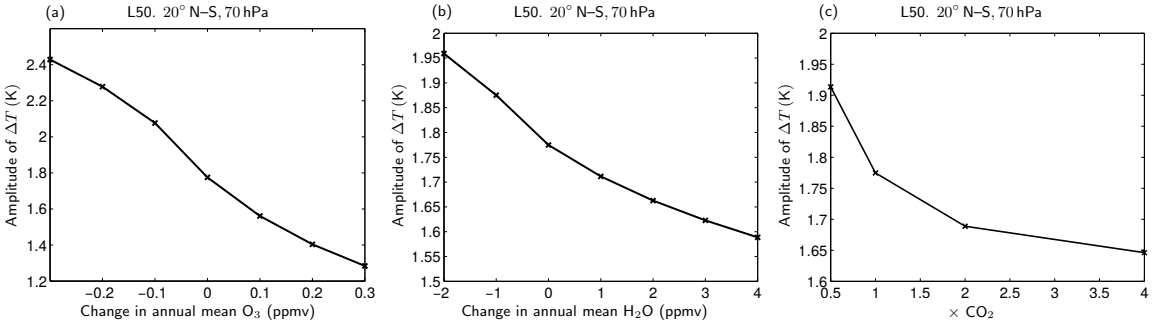


**Figure 5.13:** Amplitude of the annual cycle temperature change (K) averaged between 20° N–S at 70 hPa with an annual cycle in ozone plotted against (a) a constant perturbation to the annual mean value of ozone, (b) a constant perturbation to the annual mean water vapour, (c) different carbon dioxide mixing ratios. $1 \times CO_2 = 360$ ppmv. The perturbation is applied in the region $[1, 200)$ hPa. The amplitude is calculated as half the peak to peak value.

a large annual cycle at 70 hPa but the largest amplitude of the water vapour annual cycle occurs lower down at 100 hPa as seen in Figure 5.14(b). The stratosphere is dry compared to the troposphere and this due to much of the water vapour entering the stratosphere over the tropics being dried out by the low temperatures at the cold point as discussed previously. The cold point in temperature is located at about 90 hPa where there is also an annual cycle in the temperatures (figure 5.1(c)). The annual cycle of temperatures modulate the amount of water vapour entering the stratosphere (the tape-recorder signal), clearly visible in Figure 5.14, as tilted bands of positive and negative water vapour anomalies with respect to the annual mean. Isentropic mixing into the subtropics eventually attenuates the signal [Mote et al. (1998)].

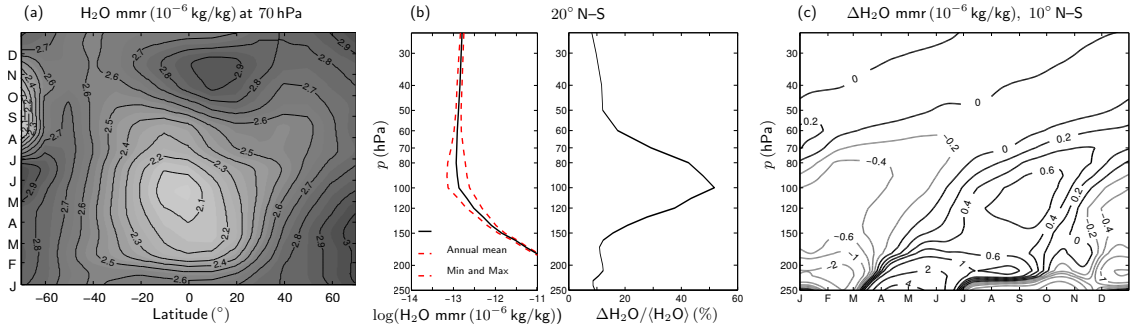


**Figure 5.14:** Water vapour mass mixing ratio ($10^{-6}$ kg/kg) from SWOOSH. (a) Water vapour at 70 hPa. (b) Annual mean, maximum and minimum values of water vapour averaged over the region 20° N–S. (c) Pressure versus time plot of water vapour with annual mean removed and averaged over 20° N–S.

There are hemispheric differences in the water vapour annual cycle, Figure 5.15(a) and (b), and the peak in the annual cycle in water vapour is shifted towards the

Northern Hemisphere. A possible explanation is that this is due to air ascending in the Indian/Southeast Asian monsoon which leads to higher water vapour concentrations during boreal summer [Rosenlof et al. (1997)].

Figure 5.15(c) show the SEFDH temperature change due to water vapour at 70 hPa. The SEFDH temperature change due to water vapour over the tropical region at 70 hPa is smaller than that due to ozone (compare to Figure 5.11(b)) but is not negligible and will act to reduce the temperature change from ozone. The largest contribution from the annual cycle in water vapour in the tropics to the temperatures also occurs further down at around 90 to 100 hPa as shown in Figure 5.15(d). The combined effect of the two trace gases will be discussed in the next section.

The amplitude of the SEFDH temperature change from water vapour at 70 hPa is largest in the Northern Hemisphere and located around 25° N whilst the water vapour annual cycle peaks are centred over the equator, Figure 5.15(a). The temperature structure bears a closer resemblance to the structure of the water vapour changes lower down at 100 hPa, Figure 5.15(b), suggesting there may be significant non-local contribution from water vapour to the temperature change. We will examine this in more detail in Section 5.3.5.

### 5.3.4 Annual cycle in both ozone and water vapour

Figure 5.16(a) shows the combined effect of imposing the annual cycles in ozone and water vapour together in an SEFDH calculation. At 70 hPa (Figure 5.16(a)), ozone causes a peak to peak temperature change of 3.5 K whilst water vapour causes a change of 1 K. Water vapour acts to decrease the amplitude of the temperature change. The temperature change due to water vapour and ozone add linearly to that obtained when the annual cycle in both trace gases is imposed. The combined effect of both trace gases is to produce an annual cycle of about 3 K peak to peak. Note that there is a phase difference between the contributions of the two trace gases.

The cancellation between the temperature changes, at 100 hPa, produced by the water vapour (1.2 K peak to peak) and ozone (2.6 K peak to peak) annual cycles is more prominent (Figure 5.16) with the combined temperature change being about 1.5 K. The amplitude of the water vapour annual cycle is a maximum around 100 hPa whilst for ozone, this occurs around 70 hPa, Figure 5.16(c). The plot reveals that both ozone and water vapour have a substantial radiative influence on the annual cycle in lower stratospheric temperatures. The combined SEFDH temperature change from both

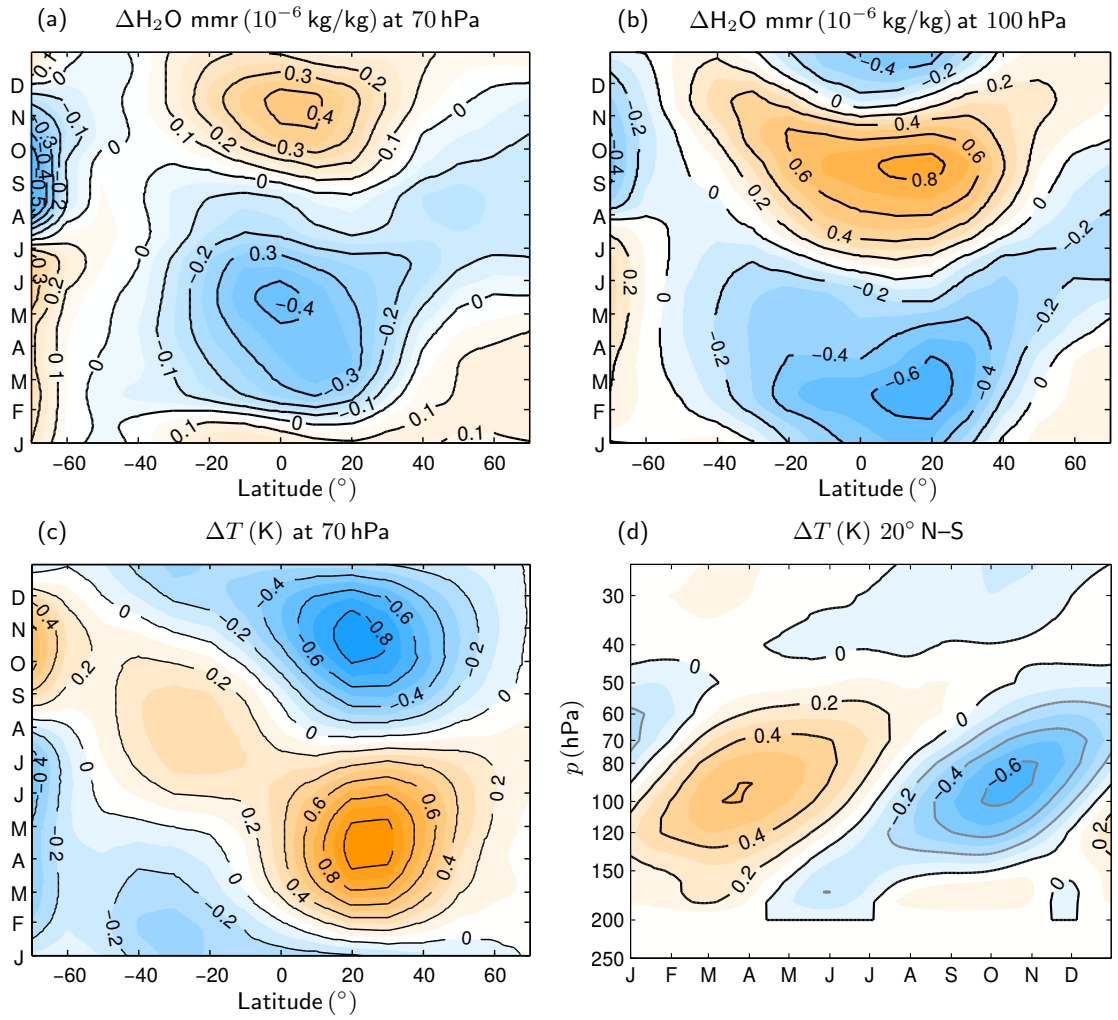


**Figure 5.15:** (a) Water vapour mass mixing ratio ($10^{-6}$ kg/kg) from SWOOSH at 70 hPa with annual mean removed. (b) Same as (a) but at 100 hPa. (c) Temperature change (K) due to the water vapour annual cycle in an SEFDH calculation (c) at 70 hPa and (d) averaged between 20° N–S.

trace gases peaks in amplitude around 70 hPa. The phase of the temperature change is not the same at the ERA-Interim temperature. We need to combine the radiative effect with the dynamical heating to obtain the correct phase of the temperature change and this will be addressed in Section 5.3.6.

### 5.3.5 Non-local influence of water vapour on temperatures

As shown in Section 5.3.3, the temperature change from water vapour at 70 hPa peaks in the northern hemisphere and the latitudinal structure does not resemble that of the local water vapour annual cycle (Figure 5.14(d)). The peak in the water vapour

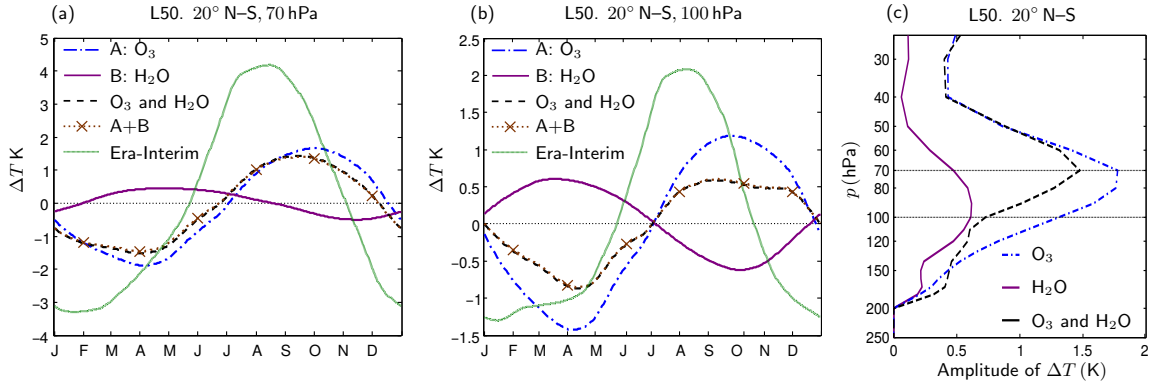


**Figure 5.16:** Temperature changes (K) calculated using SEFDH with annual cycles in ozone and water vapour imposed separately (A and B) and together to show that their radiative effects add linearly. The plots are averaged between 20° N–S at (a) 70 hPa and (b) 100 hPa. The ERA-Interim temperature annual cycle is also shown. Note that the vertical axes are different in (a) and (b). (c) Shows the amplitude of the SEFDH temperature change averaged between 20° N–S calculated as half the difference between the peak to peak value at each level. Note that there is a phase difference between the temperature from the water vapour and ozone annual cycles.

annual cycle is located further North lower down in the tropical tropopause layer as shown in Figure 5.14(c). A similar effect is observed at 100 hPa. This suggests that there is a non-local contribution from changes in water vapour to the temperature. We investigate these non-local contributions further by looking at the temperature annual cycle at 100 hPa where the water vapour annual cycle is a maximum.

Similarly to the ozone calculation in the previous section, the SEFDH calculation with 100 vertical levels, is repeated with the annual cycle imposed between different ranges of pressure levels. Figure 5.17(a) shows the temperature change at 100 hPa in each of these calculations. The total peak to peak temperature change from water vapour at 100 hPa is 1.1 K which can be broken down as follows. There is a large local contribution of 0.8 K from $[70, 120)$ hPa (curve B), a significant contribution of 0.22 K from the region $[120, 150)$ hPa (curve C) below the maximum and 0.14 K from the region further down, $[150, 200)$ hPa (curve D), in the upper troposphere although the temperature change is this region is only important between January and September. Smaller temperature changes come from the regions above and from the troposphere: 0.04 K from $[1, 70)$ hPa (curve A) and 0.04 K from $[200, 1000)$ hPa (curve E). All the contributions add linearly.

In the tropical tropopause layer, unlike the ozone annual cycle, the water vapour annual cycle below a region has a significant non-local radiative effect on the temperature

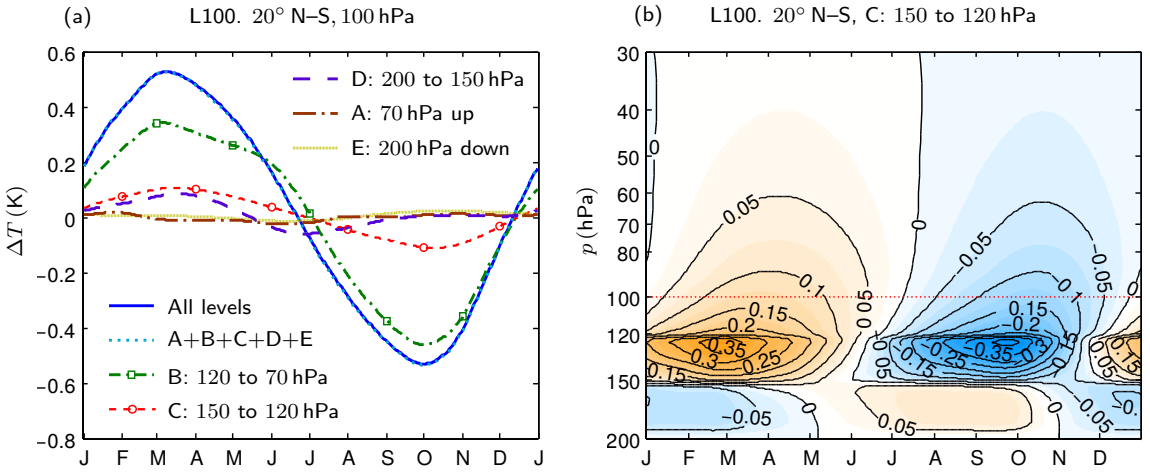


**Figure 5.17:** Annual cycle temperature changes (K) at 100 hPa calculated using SEFDH with the annual cycle in water vapour imposed within different pressure ranges. Outside of this range and on the pressure level at the lower bound (in terms of height) of the range, the water vapour mixing ratio is kept at the annual mean value. The plots are averaged between 20° N–S. (b) Temperature change (K) at all levels for the case C from plot (a) where the water vapour annual cycle is imposed in the pressure range $[120, 150)$ hPa only. The 100 hPa level is marked by a dotted red line.

change in that region. For instance, the region 150 to 120 hPa (curve C) contributes to the temperatures at 100 hPa. The annual cycle in temperature in curve C lags behind the temperature change due to the local water vapour changes, curve B, by about 5 days. This is due to a combination of factors. The water vapour tape recorder signal in the region C lags behind that at 100 hPa by about 20 days at 150 hPa and 7 days at 120 hPa. The water vapour change in the 150 to 120 hPa region causes a local temperature change which lags behind and depends on radiative relaxation time scales. It takes time for this temperature change to have a radiative effect on the layer above and for the temperature of this layer to adjust. When the temperature change reaches 100 hPa, this process adds a further lag as seen in Figure 5.17(b). The plot shows the temperature change in the vertical when the water vapour perturbation is confined to 150 to 120 hPa region. Moreover the local temperature at 100 hPa takes about 22 days to respond to the local water vapour annual cycle. The net effect is that curve C and curve B are nearly in phase. The non-local radiative effect is not confined to the 100 hPa level but occurs throughout the lower stratosphere where water vapour has a significant annual cycle, for example, similar results are obtained when looking at the 70 hPa level. Whilst the water vapour concentrations are set by the temperature at the cold point, the radiative effects extend from below the cold point to the region above.

### 5.3.6 Location of maximum in amplitude of annual cycle

The temperature annual cycle in the lower stratosphere in ERA-Interim occurs in a very narrow range of pressure levels between about 100 to 50 hPa as shown in Figure 5.1(c) with a maximum in amplitude at 70 hPa. Randel et al. (2007a) attributed this to the radiative timescales maximising at this level [Randel et al. (2002)], i.e the largest temperature change occurs where the radiative spring is slack. Whilst this may be one cause of the location of the maximum, the other is that the forcing is greatest at this level. We revisit this problem using an SEFDH-like calculation.

In this experiment, $Q_{\rm dyn}(t)$ from Equation 5.3 is estimated as the heating obtained with the ERA Interim temperatures, $T_0(t)$ and SWOOSH ozone and water vapour, $\chi(t)$, all of which include annual cycles. The aim is to explore how the vertical structure in dynamical heating and in the radiative properties of the system affect the location of the maximum temperature change.

Whilst the mean residual vertical velocity, $\overline{w}^*$, shown in Figure 5.18(a), is relatively flat in the vertical around 70 hPa, the dynamical heating term, $\overline{w}^*\,\overline{S}$, has a local maximum in this region with a significant annual cycle as shown in Figures 5.18(b) and (c). At 70 hPa, the peak to peak amplitude is about $0.2\,\mathrm{K\,day^{-1}}$. The mean residual vertical velocity, $\overline{w}^*$, is noisy and for the purpose of this calculation, the dynamical heating is smoothed by computing monthly averages and interpolating to obtain daily values. The data from ERA interim is provided on hybrid pressure levels and in converting to pressure levels, we have assumed that all quantities below 450 hPa have the same values as those at 450 hPa. This does not affect any of the conclusions in this section.

Both the vertical structure in the upwelling, $\overline{w}^*$, and in $\overline{S}$ determine the vertical structure of the dynamical heating and together lead to a local maximum in the amplitude at around 70 hPa in the tropical lower stratosphere (Figure 5.19(a)). The annual cycle in $\overline{w}^*$ determines most of the structure in the annual cycle of the dynamical heating, Figure 5.19(a). The effect of the annual cycle variation in $\overline{S}$ is small and Figure 5.19(b) shows that using the annual mean value of $\overline{S}$ and an annual cycle in $\overline{w}^*$ produces a slightly larger amplitude dynamical heating around 70 hPa. The static stability change with time and in the vertical is important. This is held constant in the calculation of radiative timescales in Randel et al. (2002).

To isolate the effect of having vertical structure in the annual cycle in dynamical heating, we perturbed the dynamical heating by adding a heating of $-0.1\,\cos(2\pi\,t/365)\,\mathrm{K\,day^{-1}}$ to all pressure levels. The amplitude and phase of the perturbation are chosen to

be similar to that of the annual cycle in the term $\overline{w}^* S - \langle \overline{w}^* S \rangle$ at 70 hPa. A similar iteration to the SEFDH calculation is performed to find the new seasonally evolving temperature. Note that in this experiment, we allow temperatures to adjust everywhere including below 200 hPa (discussed further below). The resulting temperature change is shown in Figure 5.20(a). The plots shows that there is a preferred region around 100 hPa where the temperature change is large despite a lack of vertical structure in the imposed dynamical heating perturbation. This can be directly attributed to the radiative properties of the tropical lower stratosphere and indicates that there is a local maximum in radiative timescales where the temperature cold point is located. Similar results are obtained when the amplitude of the heating perturbation is halved and when a sine wave perturbation is used instead.

Unlike the previous SEFDH experiments, we have allowed the temperatures to vary across the whole of the atmosphere. The imposed perturbation leads to a large temperature change below 100 hPa and non-local aspect of radiative transfer means that temperatures in the region above will be affected. Moreover, the temperature changes between 100 and 200 hPa would be lower if "tropospheric" temperatures were clamped below 200 hPa similar to the SEFDH calculation in Section 5.3.2, again affecting both the magnitude and location of the maximum higher up. For this reason, we have allowed temperatures to change at all levels. This is different to the previous section where temperature changes from ozone and water vapour were small (less than 2 K in amplitude) and the results are not affected by having a "tropopause".

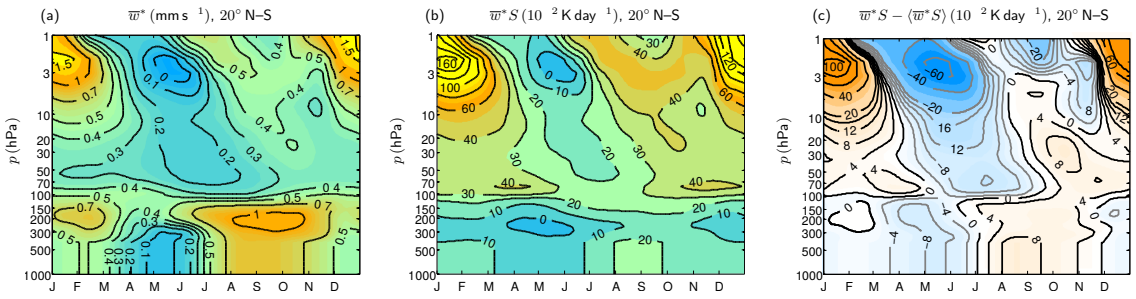


**Figure 5.18:** Data from ERA-Interim averaged between 1991 to 2010 and 20° N–S. Monthly averages interpolated to daily values to smooth out noisy upwelling field. (a) Mean residual vertical velocity, $\overline{w}^*$. (b) Dynamical heating term $\overline{w}^* \overline{S}$. (c) Same as (b) but with the annual mean removed.

The dynamical heating is now perturbed with the annual cycle in $\overline{w}^* \, \overline{S}$ taken from ERA-Interim (Figure 5.18(c)). For this calculation, the monthly means of the quantity $\overline{w}^* \, \overline{S} - \langle \overline{w}^* \, \overline{S} \rangle$ are calculated and interpolated to daily values to obtain a smoother field. The corresponding temperature change is shown in Figure 5.20(b). A comparison of

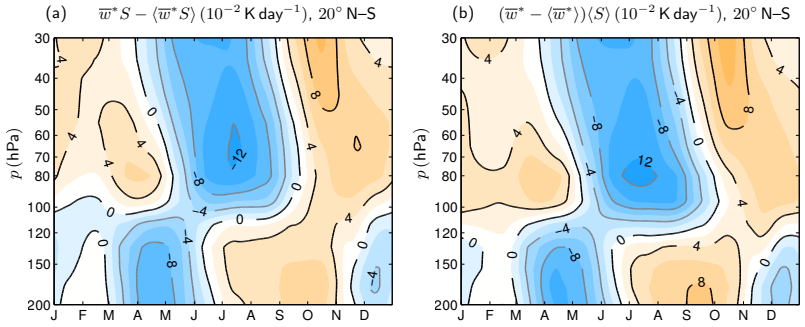


**Figure 5.19:** (a) Same as Figure 5.18(c) showing the tropical lower stratosphere in more detail. (b) The term $(\overline{w}^* - \langle \overline{w}^* \rangle)\langle S \rangle$ which only takes into account the annual cycle in $\overline{w}^*$.

Figures 5.20(a) and (b) reveals that the vertical structure in the annual cycle in the ERA-Interim upwelling term causes a more complex structure in the annual cycle in temperatures which is consistent with the structure in $\overline{w}^* \, \overline{S} - \langle \overline{w}^* \, \overline{S} \rangle$ shown in Figure 5.18(a). The larger forcing at 70 hPa leads to the temperature being large in this region. The weaker forcing lower down at 100 hPa (where the radiative timescale is largest) leads to a smaller temperature change there. Our analysis differs from Randel et al. (2007a) since it takes into account both the strength of the forcing and the structure of the radiative timescale.

Figure 5.20(c) which shows the solution to Equation 5.3 if a constant radiative relaxation timescale of 25 days is used following an estimate from Hitchcock et al. (2010). The vertical structure in the annual cycle in $\overline{w}^* \, \overline{S}$ produces a temperature change that is a good first approximation to that in Figure 5.20(b) but with a smaller magnitude. This suggests that radiative relaxation timescale is larger than 25 days at 70 hPa. Comparing this calculation to the ERA-Interim annual cycle in Figure 5.20(d), again the magnitude is smaller and the amplitude peaks lower down at around 80 hPa compared to 70 hPa in ERA-Interim.

There is an annual cycle in the dynamical heating above 110 hPa where the vertical motion is dominated by stratospheric processes whilst below 110 hPa, tropospheric processes lead to a different variation with time of the dynamical heating [Fueglistaler et al. (2009a)]. A similar separation of the dynamical regimes can be seen in the ERA-Interim annual cycle shown in Figure 5.20(c) where there is a prominent annual cycle above about 130 hPa with a large amplitude at 70 hPa and smaller variation in temperature below 130 hPa. To include this effect into the calculation, we now reintroduce a clamp of the temperature below 130 hPa.

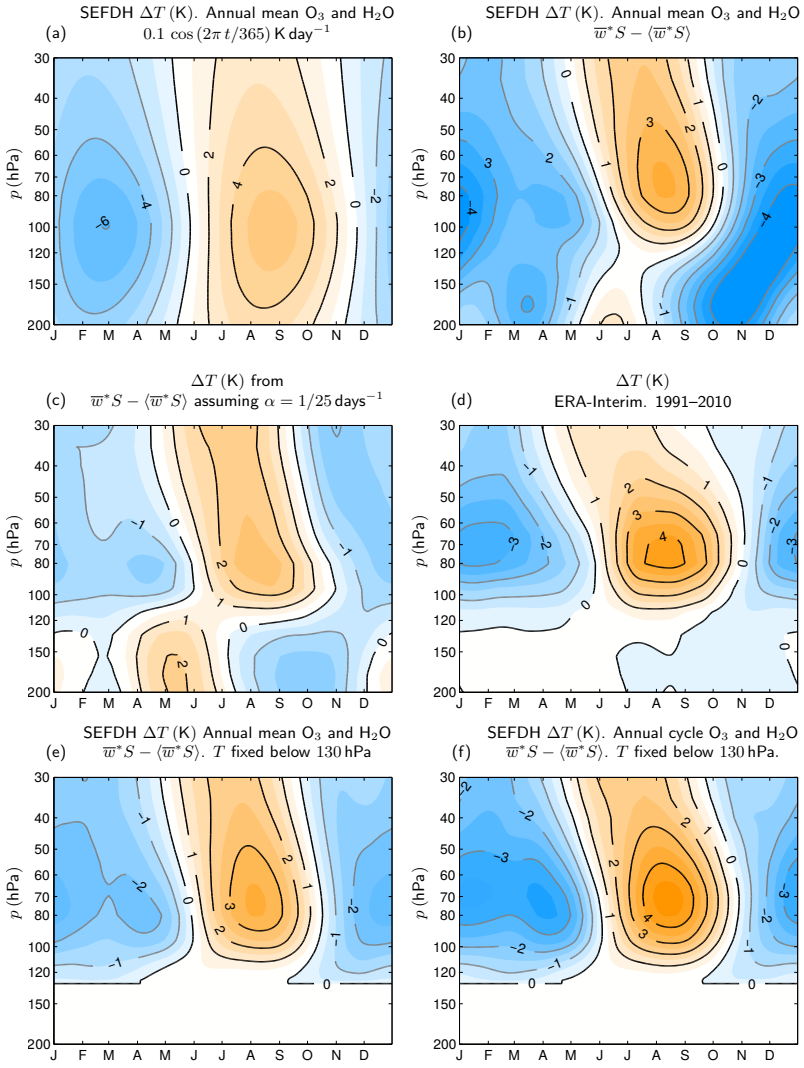


**Figure 5.20:** Temperature change from the annual mean averaged between 20°N–S. (a) An SEFDH like calculation with a perturbation of $-0.1\cos(2\pi\, t/365)\,\mathrm{K\,day^{-1}}$ is added to the dynamical heating with annual mean ozone and water vapour. (b) The temperature change from the annual cycle in the ERA-interim dynamical heating, $\overline{w}^* S - \langle \overline{w}^* S \rangle$, shown in Figure 5.18(c). (c) Temperature change due to the annual cycle in the ERA-interim dynamical but assuming a constant radiative relaxation rate of $1/25\,\mathrm{days^{-1}}$. (d) ERA-Interim annual mean temperature averaged between 1991 to 2010. Same as Figure 5.1(c). (e) Similar to (b) but with temperature held fixed at the annual mean below 130 hPa. (f) Similar to (e) but with the additional perturbation from the annual cycle in ozone and water vapour included.

Figure 5.20(d) shows the temperature change when the dynamical annual cycle perturbation, $\overline{w}^*\,\overline{S} - \langle \overline{w}^*\,\overline{S} \rangle$ is applied in the SEFDH like calculation but with the temperature below 130 hPa kept at the annual mean. This causes the maximum amplitude in temperature change to occur at around 70 hPa with a decrease in magnitude compared to Figure 5.20(b).

We build on this previous calculation and include the perturbations from the ozone and water vapour annual cycle to produce Figure 5.20(e). The net effect of the ozone and water vapour annual cycle, as shown in Section 5.3.4, is to increase the annual cycle in temperatures. This calculation produces an annual cycle with a structure that is close to the ERA-Interim annual cycle, Figure 5.20(c). Figure 5.21 shows the same data plotted at 70 hPa. The inclusion of the annual cycles in ozone, water vapour and dynamical heating produces an annual cycle with an amplitude of 8.4 K at 70 hPa compared to 7.5 K in ERA-Interim with good agreement in some months of the year and some differences of up to 2 K between March to May and July to September. Again perturbations to the dynamical heating and constituents are additive. Overall we have managed to reproduce the magnitude and phase of the annual cycle in ERA-Interim temperature using the dynamical heating from ERA-Interim and the annual cycle in ozone and water vapour. Whilst this calculation would appear to be a satisfactory answer, it does not provide any insight into what causes the upwelling and does not include the fact that an imposed heating can lead to a meridional circulation. We will look at the adjustment of the zonal mean circulation to the imposed heating in the next section and its effect on the temperatures.

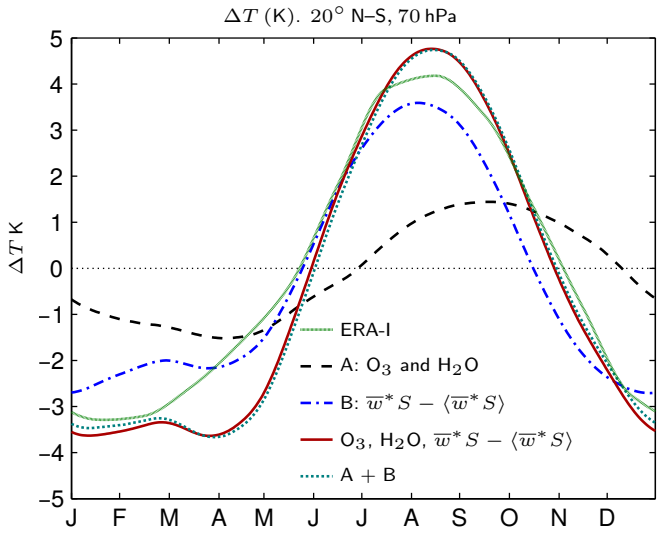


**Figure 5.21:** Change in temperature from the annual mean averaged between 20°N–S at 70 hPa. The green ERA-Interim curve is the same data as shown in Figure 5.1(c). The dashed black curve labelled A shows the SEFDH temperature change from the annual cycles in ozone and water vapour (same as in Figure 5.16(a)). The dash-dotted blue curve labelled B is from an SEFDH like calculation where the annual cycle in the dynamical heating from ERA-Interim is imposed as a perturbation (same data as in Figure 5.20(e)). The solid red curve is with the annual cycles in ozone, water vapour and dynamical heating imposed as a perturbation (same data as in Figure 5.20(f)).

In this part of the chapter, we have shown that both the radiative environment and the structure of the dynamical heating are important in determining the temperature change. We have found that ozone and water vapour together contribute to about 30% of the total amplitude in the annual cycle in temperatures at 70 hPa. Whilst ozone changes drive temperature changes that are mostly local to the perturbation, water vapour changes from the region below and above a region of interest affect the temperature there. This provides a coupling in the vertical between the water vapour both below and above the cold point that determines the temperature there. Hence, this affects the resulting water vapour distribution in the whole of the stratosphere by controlling the amount of dehydration. We have also found that radiative timescales maximise around 100 hPa but the annual cycle in temperatures maximise around 70 hPa because the forcing is largest there.

In the following sections, we will look a series of idealised dynamical experiments where different aspects of the interaction between the radiation and the dynamics are explored.

## 5.4 Zonal mean dynamical adjustment

We will now consider the influence of the annual cycle in ozone on the zonal mean dynamics as shown in the schematic diagram in Figure 5.22. The dynamical heating is no longer prescribed and it aim is to understand how the zonal mean dynamical adjustment resulting from the imposed heating will affect the temperatures. We make use of an idealised dynamical model, the Reading IGCM version 3.1 which is described in Section 2.4.1, with a resolution of T42L60 and the model top at 50 km. The model is run in a zonal mean configuration without any non zonal wavenumbers. Four longitudes are kept for computational stability but the values of all the variables are the same at each longitude. The label T42 in this case does not imply a triangular truncation since the model only has zonal mean quantities but it is kept in the interest of simplicity as it implies the right number of Gaussian latitudes. The model uses the same Zhong and Haigh radiation code to calculate the temperature tendency from radiative terms. The radiation code generates diurnal averages but is called four times a day as this minimises oscillations in temperature when radiative perturbations are imposed. We have verified that the standalone and model radiation codes produce consistent heating rates.

The model is initialised with the ERA-Interim annual mean temperature, $T_0$ and

SWOOSH annual mean ozone and water vapour, collectively denoted by $\chi_0$. The aim is to have a control state of the model which is statistically steady, with temperatures close to the ERA-Interim annual mean but in which perturbation experiments can then be done by imposing changes in the trace gases. In the troposphere, the model is relaxed to $T_0$ with a relaxation time scale of 10 days. In the stratosphere, the heating term required to keep the model temperatures at the ERA-Interim annual mean is calculated and subtracted from the temperature tendency. The same linear damping of velocities as the Held and Suarez (1994) case is used in the layer near the surface where $\sigma > 0.7$ (see Section 2.4.4). The temperature tendency in the model is given by:

$$\partial_t T = [\ldots] + (1 - G(\phi, \sigma))(Q_{\text{rad}}(T(t), \chi(t)) - Q_{\text{rad}}(T_0, \chi_0)) - G(\phi, \sigma)\,\alpha(T - T_0)$$

where the $[\ldots]$ represents other advective processes in the model and $G(\phi, \sigma) = 0.5(1 + \tanh(50(\sigma - \sigma_t(\phi) - 0.1)))$ with $\sigma_t(\phi)$ being the sigma value of the lapse rate tropopause obtained from $T_0$. $G(\phi, \sigma)$ is one at the ground and zero at the top.

A control run of 60 years is performed after a spin up of 50 years. During this time, the temperature slowly changes and reaches a statistical steady state. The temperature in the tropics in the stratosphere differs from the initial annual mean ERA interim temperature by up to 2 K. The model state evolves during this time due to diabatic processes such as surface drag and the model hyperdiffusion.

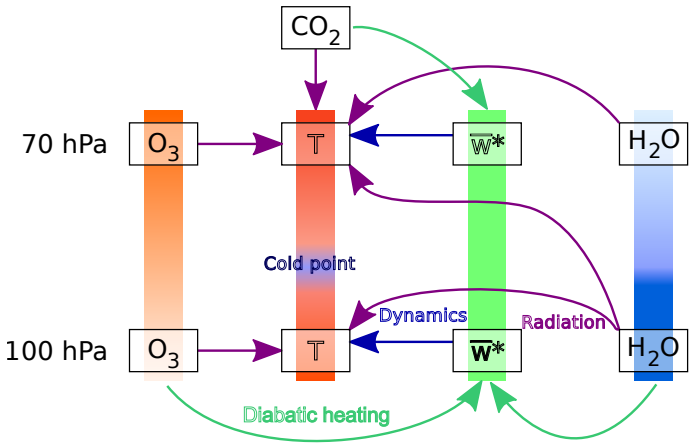


**Figure 5.22:** Schematic diagram illustrating some of the processes included in the idealised dynamical model experiment.

At the end of the control run period, a perturbation is switched on in the form of an annual cycle in a trace gas. The trace gas concentrations are read into the model at daily intervals. The radiative effect of the perturbations will bring about dynamical

changes in the stratosphere. The model adjusts with a temperature and circulation change. The perturbation run is 70 years long with the first 10 years of data discarded. The changes plotted in the following sections are differences between the perturbed and control runs.

The perturbation is around a steady temperature in the model and around an annual cycle in temperature in the SEFDH case. One way of setting of the model experiment in way more directly comparable to the SEFDH experiment would be to maintain a model state with the ERA-Interim annual cycle in temperatures and apply a perturbation to the ozone and water vapour. In the region of interest, additional SEFDH calculations show that perturbations in trace gases about a state with an annual cycle in temperature and about a state with the annual mean in temperature both lead to similar temperature changes with a maximum difference of less than 0.09 K. We chose to perturb around a steady temperature in the model because it is more convenient to obtain a model state with the ERA-Interim annual mean temperature rather than an annual cycle.

### 5.4.1 Ozone annual cycle

Figures 5.23(a) and (b) compare the temperature change in the idealised dynamical model and SEFDH calculation 70 hPa for the ozone annual cycle. The plots show that the temperature change in the model calculation is overall smaller than in the SEFDH calculation. The off equatorial maximum at about 10° N in the SEFDH calculation is not present in the model. The dynamics in the model adjust such that the meridional temperature gradients are small whilst in the SEFDH calculation, the radiative temperature changes are obtain at each individual latitude independently. This is a crucial difference between a purely radiative SEFDH calculation and the zonally symmetric model. Latitudinal gradients in the ozone field result in similar gradients in the heating rates which would imply similar gradients in the temperature change in an SEFDH calculation.

Figure 5.24 shows the major terms in the thermodynamic equation at 68.8 hPa. The dynamical case does not give the same result as the SEFDH case. The structure in heating, Figure 5.24(a) tends to be balanced by the vertical velocity response as shown in Figure 5.24(b). The structure of the upwelling term, $\overline{w}^*\overline{S}$, looks similar to the total diabatic heating term (which includes the relaxational terms), $Q$, especially in the region around 10° N where the annual cycle in heating is large. In contrast,

the rate of change of temperature with time has small meridional gradients over the equator Figure 5.24(c). The sum of $\overline{w}^*\overline{S}$ and $\partial_t\overline{T}$, Figure 5.24(d) balances most of the heating, $\Delta Q$, in the tropics showing that other terms are negligible. We will discuss the thermodynamic balance further in Section 5.5.

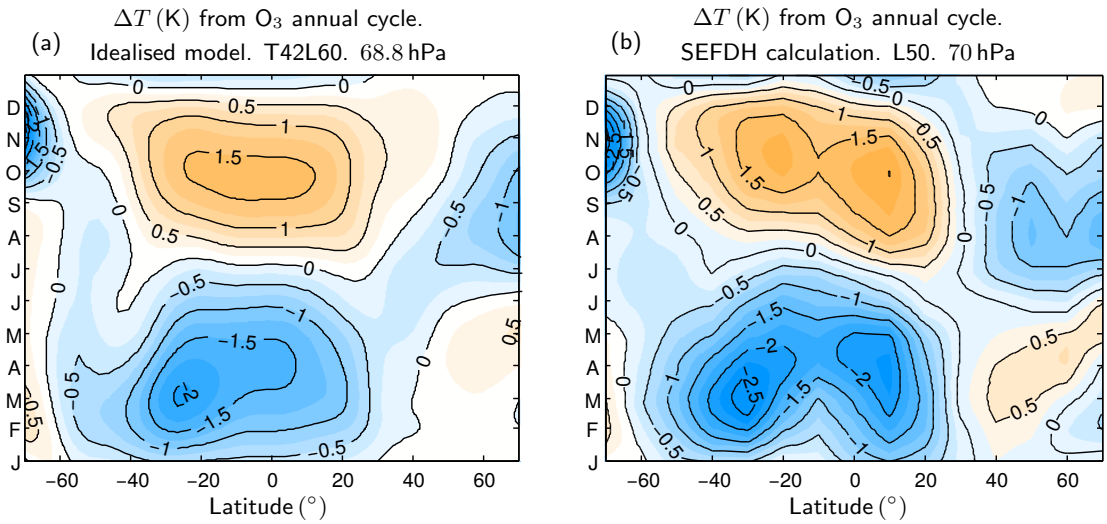


**Figure 5.23:** (a) Temperature changes (K) showing the annual cycle at 68.8 hPa calculated using the idealised dynamical model (with resolution T42L60) with an annual cycle in ozone. (b) Figure 5.9(e) is reproduced here for comparison and shows the corresponding SEFDH calculation at 70 hPa. Coloured contours are at intervals of 0.25 K.

The idealised dynamical model calculation also differs from the SEFDH calculation in that extratropical circulation changes driven by the heating can affect the tropical temperatures. To quantify this effect, we restrict the ozone annual cycle perturbation to the tropical region between 30° N–S using a mask of the form $0.5\,[\tanh((\phi+\phi_1)/c) - \tanh((\phi-\phi_1)/c)]$ where $\phi_1 = 30°$, $c = 2\times10^{-2}$. The results are shown in Figure 5.25. The net effect of having an annual cycle in temperature in the extratropics from the ozone is to increase the amplitude of the annual cycle in the tropics from 2.5 K to 3 K peak to peak. The main contribution to the annual cycle change in temperature from ozone is due to local ozone.

### 5.4.2 Water vapour annual cycle

An idealised dynamical model is now perturbed with a water vapour annual cycle in a similar way to the ozone perturbation above. The temperature change at 70 hPa (Figure 5.26(a)) is compared to the SEFDH temperature change (Figure 5.26(b)). Unlike the ozone case, the temperature change in the idealised dynamical model in

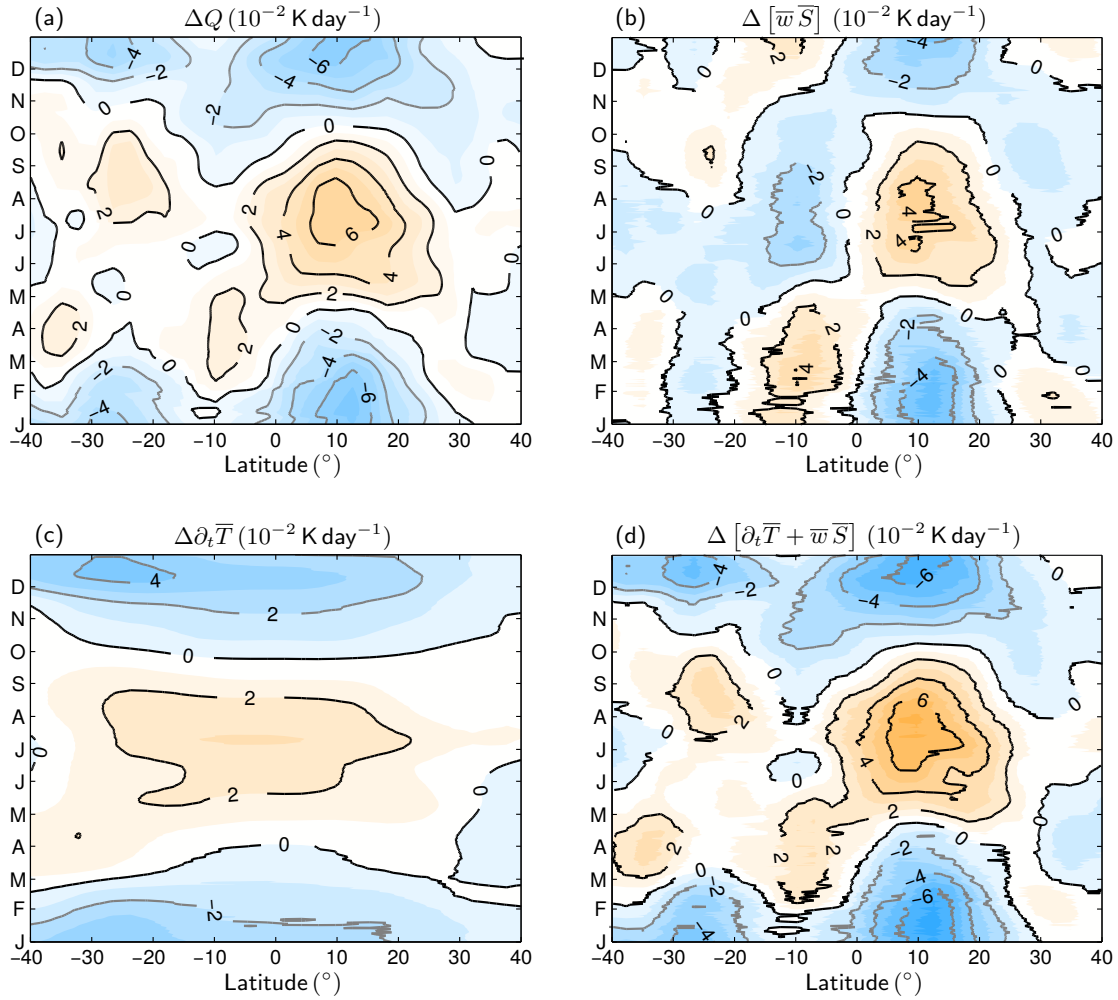


**Figure 5.24:** Changes in the various terms in the thermodynamic equation at 68.8 hPa when an ozone annual cycle is imposed in the idealised dynamical model (T42L60). (a) Heating term, $Q$ ($10^{-2}\,\mathrm{K\,day^{-1}}$). (b) Upwelling term, $\overline{w}^*\overline{S}$ ($10^{-2}\,\mathrm{K\,day^{-1}}$). (c) Rate of change of temperature, $\overline{T}_t$ ($10^{-2}\,\mathrm{K\,day^{-1}}$) (d) Sum of (b) and (c). Coloured contours are at intervals of $2 \times 10^{-2}\,\mathrm{K\,day^{-1}}$

the tropical region due to water vapour is larger than the SEFDH case and this is the case throughout the region from about 50 to 120 hPa (compare Figure 5.15(d) and Figure 5.26(b)). The structure in Figure 5.26(a) does not appear to be the result of a simple flattening of the meridional temperature gradients over the equator in the idealised dynamical model.

The difference in behaviour between the idealised dynamical model and the SEFDH case is due to a number of factors. There is a large influence from the annual cycle in water vapour on the temperatures in the tropics. A similar experiment to that described in the previous section with ozone is performed with the water vapour annual

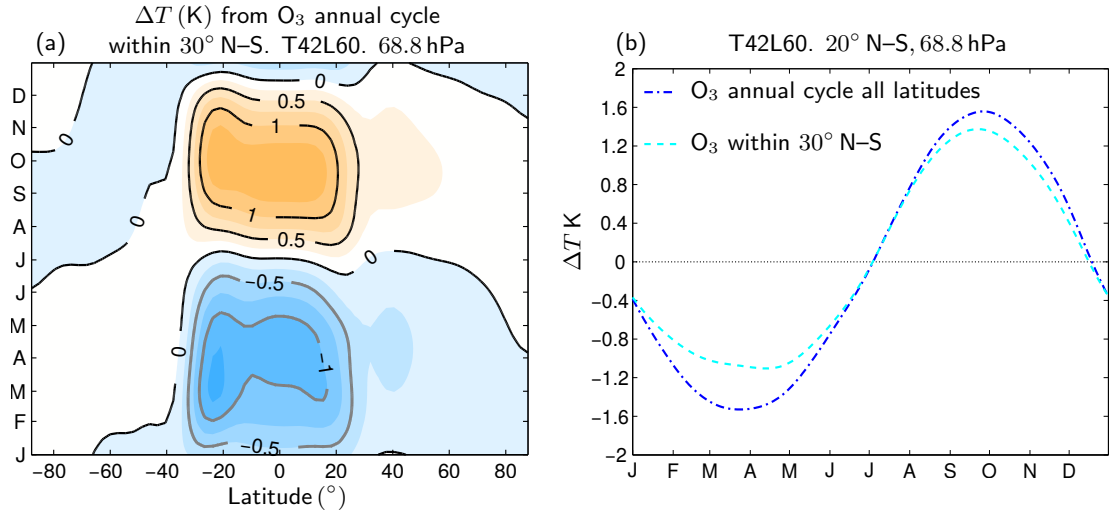


**Figure 5.25:** (a) Temperature change (K) in an idealised dynamical model (T42L60) calculation with the ozone annual cycle imposed between 30° N–S only (see text for more details). (b) Temperature change at 68.8 hPa and averaged between 20° N–S calculated with the ozone annual cycle perturbation applied everywhere in the stratosphere (dash-dotted line) and only within 30° N–S (dashed line).

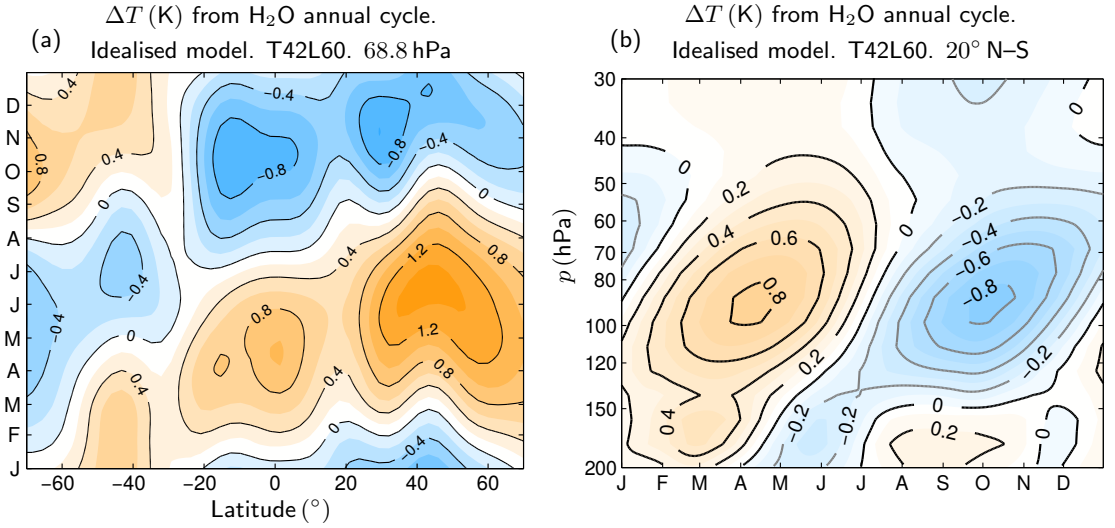


**Figure 5.26:** Temperature changes (K) calculated using the idealised dynamical model (with resolution T42L60) with an annual cycle in water vapour (a) at 68.8 hPa and (b) averaged over 20° N–S.

cycle limited to the region within 30° N–S. The results are shown in Figure 5.27.

Comparing Figure 5.27(a) with Figure 5.26(a) shows that the extratropics have a significant influence on the tropical annual cycle in temperature for water vapour. When the annual cycle is confined to 30° N–S, the dynamics in the idealised dynamical model act to reduce the latitudinal gradients in temperatures over the tropics (Figures 5.27(a)

and (b)) compared to the SEFDH calculation (Figures 5.27(c) and (d)), an effect also observed in the ozone case in the previous section. The temperature change in the idealised dynamical model averaged between 20° N–S at 98.3 hPa is smaller when the extratropical annual cycle in ozone is excluded as shown in Figure 5.27(f) again consistent with the ozone case.

When the water vapour annual cycle is applied at all latitudes in the stratosphere, the heating perturbation drives a large annual cycle in the upwelling in the region around 100 hPa (Figure 5.28(a)) compared to the case with the water vapour annual cycle limited to 30° N–S (Figure 5.28(b)). This in turn has a large influence on the upwelling and the temperature at 70 hPa. The phase of the upwelling also leads to a dynamical heating that acts to increase the amplitude of the temperature annual cycle seen in Figure 5.26.

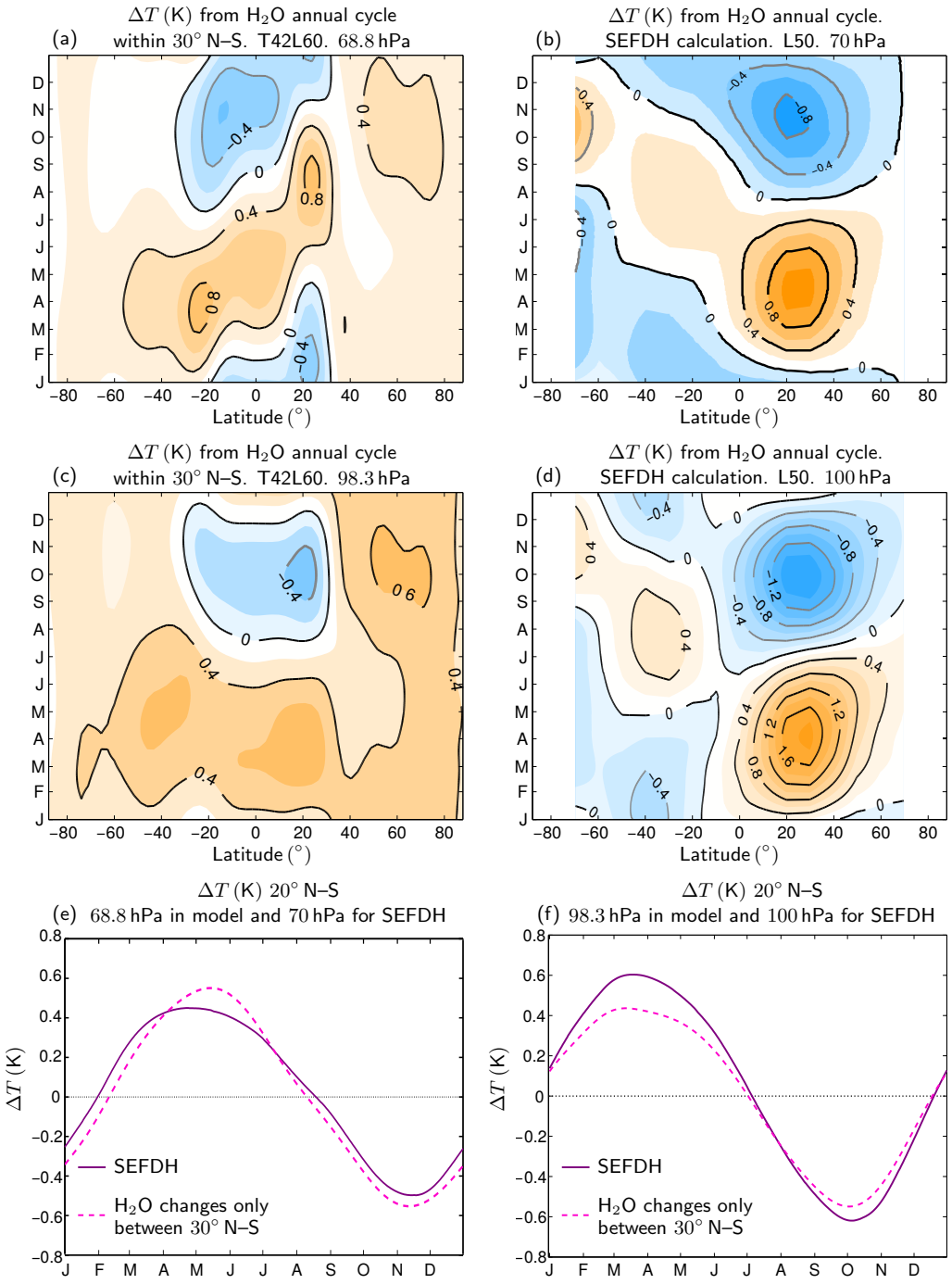


**Figure 5.27:** (a) and (c) Temperature changes (K), at 68.8 hPa and 98.3 hPa, respectively calculated using the idealised dynamical model (with resolution T42L60) with an annual cycle in water vapour that is imposed only between 30° N–S. (b) and (d) SEFDH temperature changes (K), at 70 hPa and 100 hPa respectively, from the annual cycle in water vapour (same as the calculation in Section 5.3.3). (e) Temperature change due to water vapour averaged between 20° N–S from the idealised dynamical model where water vapour is imposed in the region within 30° N–S (dashed line) and the SEFDH calculation (solid line). These are tropical averages to compare (a) and (b) around 70 hPa. (f) Similar to (e) but around 100 hPa to compare (c) and (d).

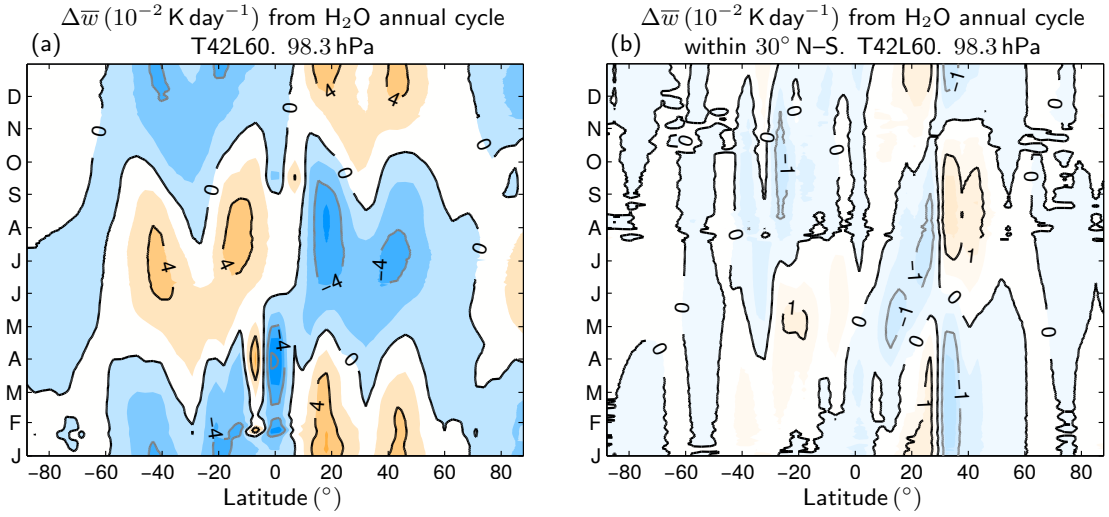


**Figure 5.28:** Change in vertical velocity, $\Delta\overline{w}\,(10^{-2}\,\mathrm{K\,day^{-1}})$, at 98.3 hPa calculated using the idealised dynamical model (with resolution T42L60) with an annual cycle in water vapour. (a) The water vapour annual cycle is imposed everywhere in the stratosphere. (b) The water vapour annual cycle is imposed only in the region within 30° N–S

## 5.4.3 Ozone and water vapour annual cycles

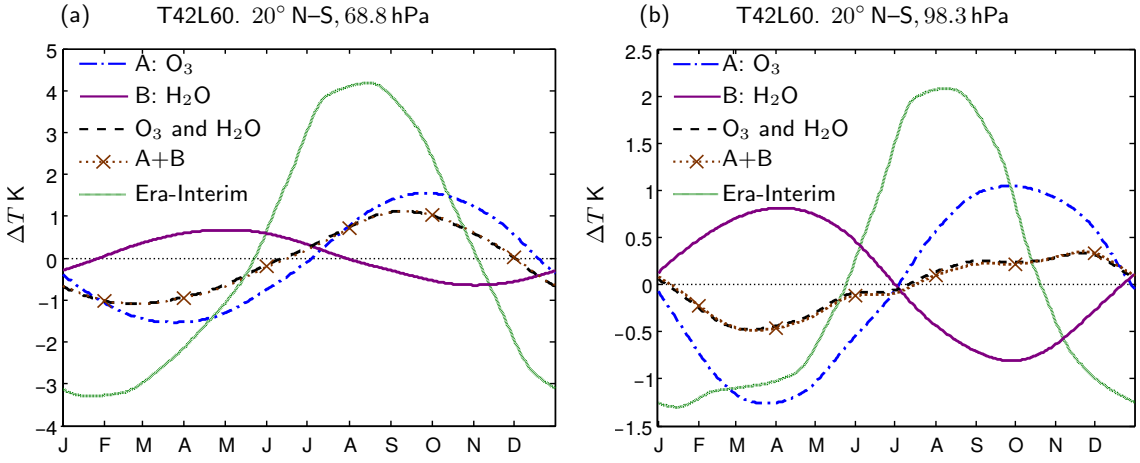


**Figure 5.29:** Temperature changes (K) calculated using the idealised dynamical model (with resolution T42L60) with annual cycles in ozone and water vapour imposed separately (A and B) and together to show that their radiative effects add linearly. The plots are averaged between 20° N–S at (a) 68.8 hPa and (b) 98.3 hPa. The ERA-Interim temperature annual cycle is also shown. Note that the vertical axes are different in (a) and (b).

The ozone and water vapour perturbation are now applied together in the dynamical model. Figure 5.29 shows the temperature changes from ozone and water vapour

applied individually and together at 70 hPa and at 100 hPa, averaged between 20° N–S. The temperature change in the model from the ozone annual cycle is smaller than the SEFDH calculation (compare to Figure 5.16) whilst the change from water vapour is larger. This leads to more compensation between the two cycles at 100 hPa. The combined effect of these two gases is to give a net annual cycle of 2.7 K peak to peak at 70 hPa and 0.8 K peak to peak at 100 hPa or about 36% and about 24% of the ERA-Interim annual cycle peak to peak value at these levels respectively. The contributions from water vapour and ozone are additive when both trace gases are perturbed.

These experiments have shown that the response to an ozone perturbation is dependent on the local radiative properties whilst the response to the water vapour perturbation depends on the radiative properties of the surrounding region as well as the upwelling response at different pressure levels. We will now explore this further in the next section.

## 5.5 Temperature dependent part of diabatic heating

When an annual cycle in constituents is imposed in the idealised dynamical model, the change in the total diabatic heating depends on the constituents and the temperature. We approximate the total diabatic heating as the sum of a component that depends on the change in constituents (and the annual mean temperature), $\Delta Q(\Delta\chi)$ and a component that depends on the change in temperature, $\Delta Q(\Delta T)$, as the system comes to a new equilibrium. The breakdown is approximate since there will be additional terms that depend on both the changes in the temperature and the constituents but these are small in our analysis. $\Delta Q(\Delta\chi)$ at each time can be calculated using the offline radiation code as the total instantaneous change in heating when a perturbation in $\chi$ (ozone or water vapour) is applied. $\Delta Q(\Delta T)$ will be estimated as the difference between the total diabatic heating, $\Delta Q$ from the model and $\Delta Q(\Delta\chi)$. This component can be regarded as relaxational. The aim of this section is to examine to what extent the diabatic heating changes can be regarded as proportional to the local temperature change and if possible to estimate the radiative relaxation timescale.

### 5.5.1 Ozone annual cycle

The terms described above are shown in Figure 5.30 for the ozone annual cycle perturbation imposed in the idealised dynamical model. Figure 5.30(b) shows the imposed heating calculated from the offline radiation code and is the same for both the model and SEFDH calculations. The latitudinal distribution in the heating is similar to the latitudinal distribution of the ozone perturbation at this level (Figure 5.9(a)). In the model, as the temperatures adjust, this leads to a relaxational component in the diabatic heating, shown in Figure 5.30(c). There is a strong similarity between the structure of $\Delta Q(\Delta T)$ at 68.8 hPa and the temperature change, Figure 5.23(a). We wish to test the assumption that $\Delta Q(\Delta T)$ is proportional to the local temperature change at each level, i.e it can be written as $-\alpha\,(\Delta T)$ with $\alpha$ representing a radiative relaxation rate. Comparing Figure 5.30(c) and Figure 5.23(a) shows that $\Delta Q(\Delta T)$ is roughly proportional to $(\Delta T)$. By taking the ratio of the amplitude of the heating averaged between 20°N–S to that of the temperature change in the same region, we estimate $1/\alpha$ to be about 25 days for the ozone annual cycle perturbation. This is consistent with estimates of the radiative timescale, $1/\alpha$, in this region which range from 25 days [Hitchcock et al. (2010)] to over 100 days [Mlynczak et al. (1999), Randel et al. (2002)]. The radiative relaxation rate is dependent on the structure of the perturbation and the temperature change produced [Fels (1982)].

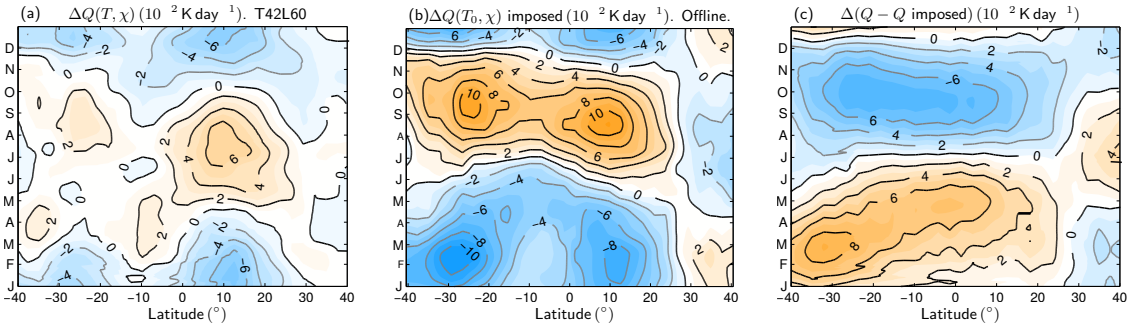


**Figure 5.30:** (a) Total diabatic heating at 68.8 hPa when an ozone annual cycle is imposed in the idealised dynamical model (T42L60) (Same as Figure 5.24(a)). (b) Imposed heating at 68.8 hPa calculated using the offline radiation code with the ERA-interim annual mean temperature and an annual cycle in ozone. (c) Difference between (b) and (a) which represent the part of the heating that can be regarded as relaxational.

To further illustrate that a value of $1/\alpha = 25$ days is a reasonable estimate for the ozone perturbation in this region, we solve the equation $\partial_t \Delta\overline{T} = \Delta Q(\Delta\chi) - \alpha\Delta\overline{T}$ for the temperature change $\Delta T$ with the imposed heating, $\Delta Q(\Delta\chi)$ and different values of $\alpha$. The results for three different values of $1/\alpha = 10,\ 25$ and 100 days are

shown in Figure 5.31. The temperature changes assume that relaxational response to a heating perturbation depends purely on the local temperature. These plots can be compared to the SEFDH temperature change (Figure 5.11(b)) and show that a value of $1/\alpha$ of about 25 days provides the closest estimate to the SEFDH temperature change at 70 hPa rather than 10 or 100 days. This calculation can be contrasted with the experiments to estimate the temperature change from the dynamical heating in ERA-Interim shown in Figure 5.20(b) and (c). In these calculations, it was shown that for the heating perturbation due to the dynamical heating, it was not possible to reproduce the structure of the temperature change using a constant $\alpha$ in the vertical and that a value of $1/\alpha$ of 25 days was not large enough to reproduce the temperature change at 70 hPa in the SEFDH calculation. This illustrates that any estimates of the value of $\alpha$ will depends on the structure of the imposed perturbation.

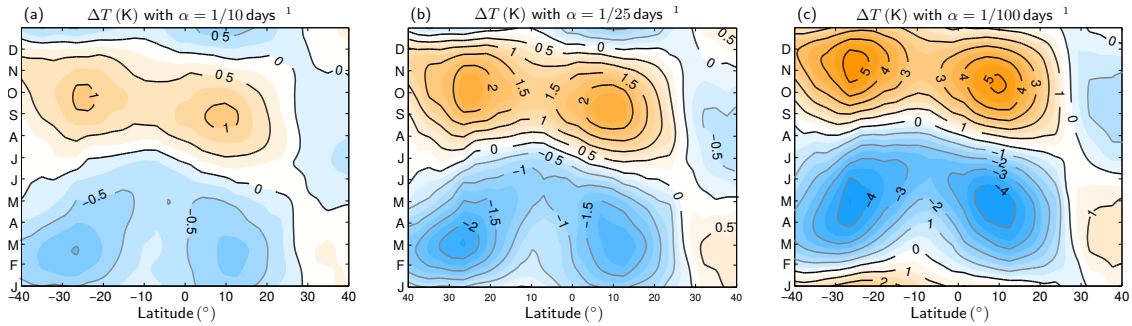


**Figure 5.31:** Temperature change (K) resulting from an imposed perturbation in heating, $\Delta Q(\Delta\chi)$, from the ozone annual cycle obtained by solving $\partial_t \Delta\overline{T} = \Delta Q(\Delta\chi) - \alpha\Delta\overline{T}$ with values of $1/\alpha$ equal to (a) 10 (b) 25 and 100 days.

### 5.5.2 Water vapour annual cycle

A similar analysis now performed for the water vapour annual cycle and the corresponding components of the total diabatic heating are shown in Figure 5.32. Figure 5.32(b) shows the imposed heating 68.8 hPa at calculated from the annual cycle in water vapour. The imposed heating takes into account effects of non-local contributions from water vapour in the region below 68.8 hPa. Unlike ozone, these effects are important for water vapour as discussed previously in Section 5.3.5. The diabatic heating component that can be regarded as relaxational is shown in Figure 5.32(c). Comparing this to Figure 5.15(c) shows that it is not possible to write a linear local relationship between the relaxational component of the diabatic heating and the temperature change for the heating perturbation induced by water vapour. A radiation code is required to

determine the radiative effects of changes in water vapour.

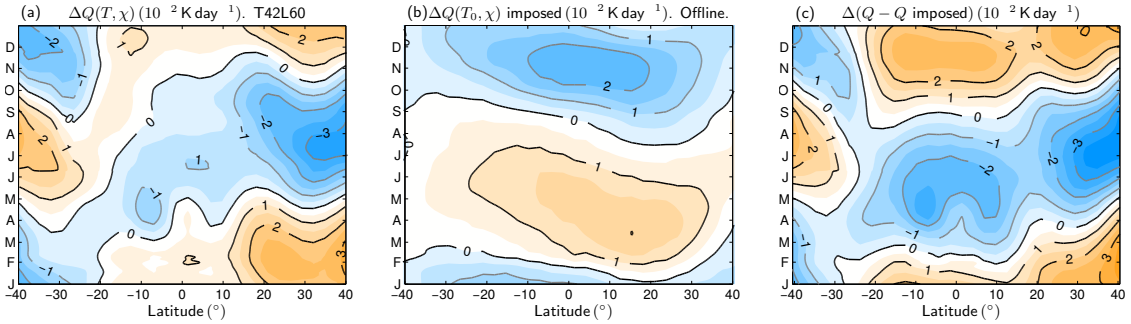


**Figure 5.32:** (a) Total diabatic heating at 68.8 hPa when a water vapour annual cycle is imposed in the idealised dynamical model (T42L60). (b) Imposed heating at 68.8 hPa calculated using the offline radiation code with the ERA-interim annual mean temperature and an annual cycle in water vapour. (c) Difference between (b) and (a) which represent the part of the heating that can be regarded as relaxational.

## 5.6 Discussion

In this chapter, we have first reviewed the radiative impact of changing ozone and water vapour in the tropical lower stratosphere using a fixed dynamical heating calculation and proceeded to explore the role of the annual cycle in constituents in driving the annual cycle in temperatures in this region with a seasonally evolving fixed dynamical heating approach. There is a 7 K peak to peak temperature difference observed in ERA-Interim at 70 hPa averaged between 20° N–S of which ozone causes a peak to peak temperature change of 3.5 K. The fact that ozone acts to produce an annual cycle in temperatures is consistent with previous findings by Fueglistaler et al. (2009b). We have further demonstrated that water vapour acts to decrease the annual cycle in temperatures and causes a change of 1 K peak to peak. The temperature change due to water vapour and ozone are additive and the combined effect of both trace gases is to produce an annual cycle of about 3 K peak to peak.

Whilst the temperature change due to ozone, at any given level in the lower stratosphere, was predominantly due to local perturbations in ozone, we found that water vapour changes below and above a certain level have a non negligible impact on the temperatures at that level. This can clearly be seen in imposed heating due to the annual cycle in ozone (Figure 5.30(b)) which has a structure in latitude and time similar to the change the ozone in Figure 5.11(a) whilst the imposed heating due to water vapour, Figure 5.32(b), differs from the local water vapour change (Figure 5.15(a)) and

has a structure that depends on the vertical distribution of the tape recorder signal. We have shown that for the ozone perturbation at 70 hPa, it is possible to think of the relaxational response to ozone as having a linear dependence on the temperature with a radiative relaxation timescale of about 25 days. In contrast, this is not possible for water vapour as the temperature change on a certain level has a different structure and lags behind the imposed heating, demonstrating the need to used a radiative transfer model to understand the radiative impacts of changes in trace gases versus a simple local Newtonian cooling approach.

An SEFDH-like calculation with a perturbation in the dynamical heating that is uniform in the vertical revealed that there was a preferred region around 100 hPa where the amplitude of the temperature change was a maximum. This suggested that the radiative timescales are also at a maximum. Despite this, the temperature annual cycle in ERA-Interim is observed to peak around 70 hPa and we have showed that this arises from a combination of the vertical structure in the dynamical heating (from structure in the upwelling and static stability) and the properties of the radiation (decreasing radiative timescale away from 100 hPa) in this region together with the radiative effects of both ozone and water vapour.

The water vapour content of the stratosphere is set by the amount freeze dried out the upwelling air at the cold point. The SEFDH calculations show that water vapour changes well below the cold point in the upper troposphere in the region around 120 to 150 hPa can influence the temperatures around the cold point as shown in Figure 5.17(a)). The radiative coupling between the upper troposphere and lower stratosphere on either side of the cold point demonstrates that the upper troposphere, which experiences different dynamical regimes to the stratosphere, has the ability to influence the dynamics of the stratosphere though the imposed radiative heating due to water vapour. The upper tropospheric water vapour together with the water vapour and ozone at the cold point have a key role in setting the magnitude and phase of the temperature annual cycle at the cold point and hence the subsequent water vapour concentrations in the stratosphere. The SEFDH calculations show that there is a significant amount of cancellation between the annual cycles due to the two trace gases at 100 hPa leaving a 1.5 K net contribution to the peak to peak temperature.

Having demonstrated the need for a radiative code to understand the effects of changes in trace gases, we have set up an experiment using an idealised zonally symmetric model and a radiation code in the stratosphere to investigate the annual cycle in temperature when the zonal mean dynamics are also allowed to adjust to the imposed

heating. The temperature annual cycle due to ozone in the model was smaller than the SEFDH calculation as would be expected from the thermodynamic equation if the perturbations in heating drive local changes in temperature and upwelling. This was not the case for water vapour where the extratropical changes in water vapour lead to heating perturbations that results in a large change in the upwelling over the tropics. This resulted in larger temperature change in the dynamical model compared to the SEFDH case.

The next effect of the annual cycles in ozone and water vapour, taking into account the zonally symmetric circulation response, is to produce an annual cycle in temperatures of 2.7 K peak to peak at 70 hPa and of 0.8 K peak to peak at 100 hPa. The amplitude annual cycle produced at 70 hPa is about 36% of that in ERA-Interim illustrating that the radiative contribution from ozone and water vapour is significant.

# Chapter 6

## Conclusions and further work

The focus of this work has been the radiative and dynamical processes in the tropopause region. The aim was to better understand the formation of some of the large scale features of the Upper Troposphere/Lower Stratosphere region using a combination of observations, radiative calculations and dynamical models with various levels of idealisation. Chapter 3 looks at the layer of stable air above the extratropical tropopause, the tropopause inversion layer, and the dynamics of its formation whilst Chapters 4 and 5 consider the tropical region. In Chapter 4, we examine the cause of the double peak structure in the upwelling and diabatic heating observed in the time mean and in Chapter 5 we look at how the large annual cycle in temperatures in the same region is driven. Several common themes emerge across the chapters. On the dynamical side, we repeatedly make use of the downward control principle and discuss the importance of considering whether the torque generated by waves on the atmosphere can be thought of as being imposed 'externally' or as part of the response. On the radiative side, we have shown that a key aspect of this exchange of energy is that part of it has a non-local influence and forms part of the imposed heating rather than being completely relaxational. We will now summarise the main conclusions and discuss some potential further work.

## 6.1 Tropopause inversion layer

### 6.1.1 Dynamical formation

We have demonstrated that a tropopause inversion layer can form in an idealised dynamical model and is a persistent feature of the steady state as demonstrated by its presence in the potential vorticity field. We argue that the TIL arises as a result of the wave driving leading to a certain pattern of upwelling consistent with a static stability maximum. This explanation contrasts with other theories of the formation of the TIL. In particular Wirth (2003) attributed the TIL to the compositing bringing out the asymmetry between the fact that transient anticyclones enhance the stability above the tropopause but cyclones do not whilst Birner (2010) proposed that the time dependent static stability equation involves a forcing term, the gradient of the mean vertical residual velocity, and the structure of the residual circulation is such that a TIL emerges. In our experiments, the vertical gradient in the mean vertical residual velocity is also important and is linked to the structure of the wave driving, a region of convergence of the Eliassen-Palm flux in the stratosphere. This structure is key to the structure of the static stability. In a model with the Haynes et al. (2001) restoration profiles, the distribution of waves is different to the Held and Suarez case where a TIL forms. The region of convergence in the Eliassen-Palm flux in the stratosphere is absent and a TIL does not form.

### 6.1.2 Tropopause based averaging

The tropopause inversion layer in CHAMP radio occultation data can be classified as two distinct types. The first is a broad layer in the static stability that arises from simply averaging the vertical profiles in time and the other is a much sharper TIL, that is about twice as strong, resulting from compositing the profiles with respect to the individual tropopause height in each profile. In contrast, it is not possible to obtain the sharp strong TIL in the dynamical model experiment. The presence of fluctuations in the individual CHAMP temperature profiles suggested that these fluctuations might be aligned under compositing to lead to the strong sharp TIL. We test this using a set of idealised fluctuations to determine if certain aspects of the fluctuations can composite to cause an artificial sharpening of the TIL.

Whilst we were unable to identify a specific class of fluctuations that would cause a

significant sharpening and doubling of the strength of the TIL observed in CHAMP data, our analysis revealed that large amplitude fluctuations (of a similar magnitude to those in the CHAMP data), on a base temperature profile that contains a TIL, tend to sharpen the existing TIL and bring the maximum closer to the tropopause but do not significantly change the strength.

The sole purpose of tropopause based averaging appears to be obtaining a TIL which is clearly distinguishable in the time mean and it is not clear that this process is of dynamical relevance to the propagation of large scale waves through this region of the atmosphere.

### 6.1.3 Further work

In this chapter, we have not addressed the variation in the strength and location of the TIL with seasons [Bell and Geller (2008)] and it is likely that the other proposed mechanisms also contribute to modulating the TIL. We have also not addressed why the structure in the wave driving exists and how it is modulated by the TIL. The TIL will affect wave propagation into the stratosphere and chemical transport across the tropopause. The timescales involved in these processes will determine which aspects of the TIL (sharp peaks in individual profiles or broad maximum in static stability) are relevant. Furthermore, radiative effects have not been taken into account. All these aspects of the TIL are likely to be relevant to stratospheric-tropospheric coupling in the extratropics.

The analysis of the sharpening and strengthening of the TIL under tropopause based averaging aimed to better understand the underlying fluctuations in the temperature profile. We speculate that the TIL in the steady state arising from the structure in the wave driving changes the amplitude and wavelength of gravity waves propagating through this region. This in turn creates a set of perturbations that have a large amplitude and smaller wavelength in the region of the background TIL. Compositing then lines up these profiles to give the sharp strong TIL. Whilst we have been not been able to demonstrate this, further experiments could look at the effect of static stability maximum on gravity wave propagation.

This Chapter has also made it clear that the detailed effect of tropopause-based averaging in dynamical studies needs to be understood. This methodology is also widely used in chemical tracer analysis in the UTLS [Hegglin et al. (2008), Hoor et al. (2004), Pan et al. (2007)] and it is important to investigate if tropopause-based

averaging introduces artefacts in the data in each of these applications.

## 6.2 Structure in tropical upwelling

### 6.2.1 Imposed double peak structure in diabatic heating

The double peak in diabatic heating in the tropical lower stratosphere with prominent peaks around 20° N–S and 70 hPa can, in part, be considered a forcing on the atmosphere. We have shown that the major contributions to the double-peak structure in diabatic heating are the latitudinal variations in ozone concentration which give rise to a corresponding variation in heating. Latitudinal variations in temperature and ozone in the atmospheric layers below and above the level of the double peak cause differences in longwave absorption. For the clear-sky longwave heating rates between 1991 to 2010, 60% of the difference between 20 ° N and the Equator at 70 hPa can be attributed to the ozone meridional gradient and 30% to the temperature changes with smaller contributions from water vapour. The cloud and shortwave (from ozone) contributions can directly be classified as forcing and contribute to 28% of the difference in diabatic heating rates between 20 ° N and the Equator at 70 hPa. Added to this imposed forcing are the contributions from the non-local temperature and ozone changes in the clear sky longwave just described. Hence, a substantial part of the double peak in diabatic heating, which is largely confined to the 90 hPa to 60 hPa layer, is forced by aspects of radiative heating that are external to the temperature structure and indeed the dynamics of that layer. This is consistent with the structure in the temperature field which does not show a double peak and is relatively flat across latitudes. The alternative hypothesis would have been that the latitudinal structure in upwelling was due to a dynamically determined (e.g by wave dynamics) structure in the wave force in the absence of any latitudinal structure in the external radiative forcing. The structure of the temperature field would then correspond to that of the upwelling which is not the case.

### 6.2.2 Circulation response to imposed heating

When a heating, similar to the double peak in ERA-interim, is imposed in an idealised three dimensional model, a double peak in the mean residual vertical velocity is generated and has a similar magnitude to that observed in ERA-Interim. This represents a dynamical regime in which the dominant balance to a heating is an upwelling. In such a regime, to achieve the required upwelling, the waves form part

of the response so as to maintain angular momentum consistency. The upwelling generated can simply be deduced from the heating perturbation and is insensitive to the details of the dependence of the wave force on the zonal velocity. We also set out some scaling arguments that show that if the dynamical aspect ratio $K\,N^2\,D_Q^2/\alpha\,f^2\,L_Q^2 \gg 1$ (4.2), i.e if the heating is deep and narrow, for example for large $K$ and/or small $f$ (i.e. low latitude), the dominant response to the heating is more likely to be in the form of an upwelling with a similar structure in latitude and height. These scaling arguments are a more general form of those previously stated by various authors (e.g. Fels et al. (1980), Garcia (1987)) in the context of a zonally symmetric response to heating when the wave force is represented by Rayleigh friction ($K$ is then simply the Rayleigh friction coefficient).

### 6.2.3 Sensitivity to location and width of heating

Various parameters of the idealised heating perturbation are then varied. The latitude of the perturbation is varied and the same balance between the upwelling and the heating holds even at high latitudes suggesting that the scaling relation in (4.2) is large at all latitudes from $K$ being sufficiently large. This behaviour could potentially be relevant for a localised narrow heating arising from the Antarctic ozone hole [Orr et al. (2013)].

Increasing the width of the heating revealed a different behaviour in which changes in the static stability become important in determining how the heating is balanced. For such heating perturbations, which could for example arise from the tropical ozone changes under climate change [Forster et al. (2007)], we cannot directly infer the response as was the case with a narrow and deep heating and it is necessary to use a dynamical model.

### 6.2.4 Similarity with an imposed force

We show that the same arguments relevant to a heating perturbation are applicable to the response to an applied force. This problem has been considered by Cohen et al. (2013) and Sigmond and Shepherd (2014) who have observed compensation of the imposed force leading to a small change in the meridional circulation. We have shown that there is a regime in which this is the case, similar to the narrow and deep heating and also that as the imposed force is made broader, less compensation is observed. A

similar aspect ratio (4.8) emerges to describe the response.

### 6.2.5 Further work

The understanding gained from the work in this chapter is currently being applied by Peter Hitchcock and Amanda Maycock to the circulation changes observed in the tropical lower stratosphere under climate change in a comprehensive chemistry climate model. Although it is a reasonable assumption that the balance between upwelling and heating in the narrow heating regime will hold in a more comprehensive model, this has not been explicitly tested. Similar experiments in a wider sample of models could be done to test the robustness of the hypothesis presented in this Chapter.

Various aspects of the forcing and response have also not been addressed in this work. These include changing the location in height and the vertical lengthscale of the heating perturbation and the effect of imposing the heating in a model with a radiative code as opposed to Newtonian cooling. We have shown that for the wide heating case, the response depends on the background state on which the perturbation is applied. The latitudinal profile of static stability is different further up from the tropopause and will likely have a significant effect on the response to a wide forcing located in the mid-stratosphere.

We have emphasised the need to identify structures in the diabatic heating that can be regarded as externally imposed in understanding the dynamical response. The method in Hitchcock et al. (2010) can, to some extent, be used to identify components of the radiative heating rates that can be represented by radiative relaxation. A further difficulty arises when trying to determine a suitable reference temperature profile. It would therefore be interesting to develop a method of extracting the "imposed" diabatic heating component given a perturbation in the trace gases (e.g. from the trends in ozone and water vapour).

In the imposed mechanical force experiments, we have varied the width of the perturbation but it would be interesting to extend this to a wider set of parameter sweep experiments. In a way analogous to the heating case, the strength and location could be varied.Watson and Gray (2015) reported on cases where there was over compensation of the imposed force–a phenomenon which we did not see in our runs.

## 6.3 Annual cycle in tropical lower stratospheric temperatures

### 6.3.1 Radiative contribution to annual cycle

A seasonally evolving fixed dynamical heating calculation demonstrates that ozone contributes to about 3.5 K and water vapour to about 1 K (both peak to peak values) at 70 hPa of the 7 K observed annual cycle in temperatures in ERA-Interim (averaged between 20° N–S). A key point of this study is that water vapour is important to the annual cycle and not negligible as was previously thought [Fueglistaler et al. (2011), Chae and Sherwood (2007)]. It also acts to decrease the amplitude of the annual cycle with the combined radiative effect of the two trace gases leading to an annual cycle with a 3 K peak to peak temperature change (about 40% of the total). The relative contribution compared to ozone is larger at 100 hPa with water vapour causing a change of 1.2 K peak to peak and ozone of 2.6 K peak to peak.

The SEFDH calculation provides a good framework to investigate the non-local aspect of radiative transfer. The ozone annual cycle was found to drive primarily local temperature changes whilst for water vapour, it was important to take into account non-local contributions from the water vapour below the level of interest to understand the temperature change at that level. This effect was important in the tropical lower stratosphere and the fact that the water vapour in the region below the cold point is able to affect the temperature above it is an important aspect of the radiative coupling. The importance of a non-local imposed heating was also discussed in Chapter 4 where the ozone and temperature structure contributed to the steady state double peak structure of the diabatic heating.

### 6.3.2 Location of peak in annual cycle

We find that the peak in the annual cycle at 70 hPa is primarily due to a combination of the vertical structure in the upwelling and the ozone annual cycle maximising there and not due to a maximum in the radiative timescale in this region [Randel et al. (2002)]. A set of SEFDH-like calculations was used to support this argument. When a dynamical heating perturbation with an annual cycle but no vertical structure was applied, the temperature change was greatest in a preferred region around 100 hPa.

This suggests a maximum in the radiative timescales not at 70 hPa but at 100 hPa. Combined with the vertical structure in the upwelling and the ozone heating, a large annual cycle in temperatures is obtained in the region around 70 hPa but this is also affected by the large temperature changes driven lower down below 130 hPa.

In ERA-Interim, the temperature below about 130 hPa does not display a large annual cycle. Fixing the temperatures below this level to the annual mean temperature in the SEFDH-like experiments has a significant effect on the temperatures at 70 hPa. This illustrates that processes in the lower part of the tropical tropopause layer are important in determining the location and magnitude of the annual cycle.

### 6.3.3 Zonal mean dynamical adjustment

The inclusion of the zonal mean dynamics reveals various non-local interactions not seen in the SEFDH calculation. The heating resulting from the annual cycle also drives an upwelling and there is a smoothing of the temperature meridional gradients over the Equator in the dynamical model compared to the SEFDH case. This leads to a lower temperature change compared to the SEFDH case. Furthermore, the extratropical heating also drives a circulation that affects tropical temperatures. When the trace gas annual cycle changes are constrained to the region between 30° N–S as opposed to being allowed to vary across the stratosphere, the peak to peak temperature change averaged 20° N–S falls from 3 K to 2.5 K for ozone and 1.4 K to 1.1 K for water vapour.

### 6.3.4 Further work

The next step that naturally follows from this work would be to study the full three dimensional response in a model with an eddy field and a radiation code and to compare the results with a different set of idealisations where the heating due to the trace gases is imposed in a model with Newtonian cooling in a way similar to that done in Chapter 4 but to study the time dependent response. Both these sets of experiments would give some insight of different aspects of the radiative-dynamical coupling. Such a framework, where the radiative and dynamical interaction are first studied separately and then with different interactions included could be applied to other problems relevant to the atmosphere. For instance, one of the main challenges in modelling the TTL is the presence of large inter-model differences and large biases in the temperature at the cold point compared to observations [Hardiman et al. (2015)].

Models do not agree on the sign of the temperature trend at the cold point tropopause which leads to a similar uncertainty in the sign of the stratospheric water vapour trend. Our idealised experiments could be useful in identifying the processes that would reduce these biases. The vertical resolution can also easily be increased to match that of the observational data.

The question of estimating radiative timescale in the atmosphere is one that needs to be addressed and whilst various studies have made progress towards quantifying this quantity, one must be cautious in generalising the results since the timescales depends on the structure of the perturbation and the temperature change. The idealised calculations described could be extended to provide estimates of these timescales for various perturbations relevant to the atmospheric flow [Fels (1982)].

The way in which extratropical changes affect the tropics requires more careful study. In our model set-up, it was convenient to perturb about a base state which is the annual mean ERA-Interim temperature. Our FDH calculations (as well as other studies such as Maycock et al. (2011)) have shown that the background value of the trace gas has a non-negligible effect on the temperature change. The extratropics also experience a large annual cycle in temperature which will affect the longwave emission and the diabatic heating forcing; an effect not present in our calculation. It would be interesting to include these extratropical effects in the model and investigate how they affect the tropical annual cycle in temperature.

# Bibliography


Andrews, D. G., J. R. Holton, and C. B. Leovy, 1987: *Middle atmosphere dynamics*. Academic Press, Orlando.

Batchelor, G. K., 2000: *An Introduction to Fluid Dynamics*. Cambridge Mathematical Library, Cambridge University Press.

Bell, S. W. and M. A. Geller, 2008: Tropopause inversion layer: Seasonal and latitudinal variations and representation in standard radiosonde data and global models. *Journal of Geophysical Research (Atmospheres)*, **113**, D05 109.

Birner, T., 2006: Fine-scale structure of the extratropical tropopause region. *Journal of Geophysical Research*, **111 (D4)**, D04 104.

Birner, T., 2010: Residual Circulation and Tropopause Structure. *Journal of the Atmospheric Sciences*, **67 (8)**, 2582–2600.

Birner, T., A. Dörnbrack, and U. Schumann, 2002: How sharp is the tropopause at midlatitudes? *Geophysical Research Letters*, **29 (14)**, 1700.

Birner, T., D. Sankey, and T. G. Shepherd, 2006: The tropopause inversion layer in models and analyses. *Geophysical Research Letters*, **33**, L14 804.

Brasseur, G. P., J. J. Orlando, and G. S. Tyndall, 1999: *Atmospheric Chemistry and Global Change*. Oxford University Press.

Brewer, A. W., 1949: Evidence for a world circulation provided by the measurements of helium and water vapour distribution in the stratosphere. *Quarterly Journal of the Royal Meteorological Society*, **75**, 351–363.

Brühl, C., et al., 1996: Halogen occultation experiment ozone channel validation. *J. Geophys. Res.*, **101 (D6)**, 10 217–10 240, doi:10.1029/95JD02031.

Bühler, O., 2009: *Waves and Mean Flows*. Cambridge Monographs on Mechanics, Cambridge University Press.

Butchart, N., M. Office, and H. Centre, 2014: Reviews of Geophysics The Brewer-Dobson circulation. *Reviews of geophysics*, **52**, 157–184, doi:10.1002/2013RG000448. One.

Butchart, N. and A. A. Scaife, 2001: Removal of chlorofluorocarbons by increased mass exchange between the stratosphere and troposphere in a changing climate. *Butchart, Neal*, **410 (6830)**, 799–802, doi:10.1038/35071047.

Butchart, N., et al., 2006: Simulations of anthropogenic change in the strength of the Brewer-Dobson circulation. *Climate Dynamics*, **27 (7-8)**, 727–741, doi:10.1007/s00382-006-0162-4.

Butchart, N., et al., 2010a: ChemistryClimate Model Simulations of Twenty-First Century Stratospheric Climate and Circulation Changes. *Journal of Climate*, **23 (20)**, 5349–5374.

Butchart, N., et al., 2010b: *SPARC Report on the Evaluation of Chemistry-Climate Models, CCMVal (2010)*. SPARC, 109–148 pp.

Butchart, N., et al., 2011: Multimodel climate and variability of the stratosphere. *Journal of Geophysical Research: Atmospheres*, **116 (5)**, 1–21, doi:10.1029/2010JD014995.

Chae, J. H. and S. C. Sherwood, 2007: Annual temperature cycle of the tropical tropopause : A simple model study. *Journal of Geophysical Research*, **112**, 1–10.

Clough, S. A. and M. J. Iacono, 1995: Line-by-line calculation of atmospheric fluxes and cooling rates: 2. Application to carbon dioxide, ozone, methane, nitrous oxide and the halocarbons. *Journal of Geophysical Research: Atmospheres*, **100 (D8)**, 16 519–16 535.

Clough, S. A., M. J. Iacono, and J.-L. Moncet, 1992: Line-by-line calculations of atmospheric fluxes and cooling rates: Application to water vapor. *Journal of Geophysical Research: Atmospheres*, **97 (D14)**, 15 761–15 785.

Cohen, N. Y., E. P. Gerber, and O. Buhler, 2013: Compensation between Resolved and Unresolved Wave Driving in the Stratosphere : Implications for Downward Control. *Journal of Atmospheric Sciences*, **70**, 3780–3798.

Cohen, N. Y., E. P. Gerber, and O. Buhler, 2014: What Drives the Brewer-Dobson Circulation? *Journal of Atmospheric Sciences*, **71**, 3837–3855, doi: 10.1175/JAS-D-14-0021.1.

Dee, D. P., et al., 2011: The ERA-Interim reanalysis: configuration and performance of the data assimilation system. *Quarterly Journal of the Royal Meteorological Society*, **137 (656)**, 553–597, doi:10.1002/qj.828.

Dickinson, R. E., 1971: Analytic model for zonal winds in the tropics. *Monthly Weather Review*, **99**, 501–510.

Dickinson, R. E., 1973: Method of Parameterization for Infrared Cooling between. *Journal of Geophysical Research*, **78 (21)**, 4451–4457.

Dobson, G. M. B., D. N. Harrison, and J. Lawrence, 1929: Measurements of the Amount of Ozone in the Earth's Atmosphere Conditions -Part III. *Proceedings of the Royal Society of London. Series A, Containing Papers of a Mathematical and Physical Character*, **122 (790)**, 456–486.

Doherty, G. M., R. E. Newell, and E. F. Danielsen, 1984: Radiative heating rates near the stratospheric fountain. *Journal of Geophysical Research*, **89 (D1)**, 1380–1384.

Fels, S. B., 1982: A Parameterization of Scale-Dependent Radiative Damping Rates in the Middle Atmosphere. *Journal of the Atmospheric Sciences*, **39**, 1141–1152.

Fels, S. B., 1985: Radiative-dynamical interactions in the middle atmosphere. *Advances in Geophysics*, **28A**, 277–300.

Fels, S. B., J. D. Mahlman, M. D. Schwarzkopf, and R. W. Sinclair, 1980: Stratospheric Sensitivity to Perturbations in Ozone and Carbon Dioxide: Radiative and Dynamical Response. *Journal of Atmospheric Sciences*, **37**, 2265–2297.

Foelsche, U., M. Borsche, A. K. Steiner, A. Gobiet, B. Pirscher, G. Kirchengast, J. Wickert, and T. Schmidt, 2008: Observing upper troposphere-lower stratosphere climate with radio occultation data from the CHAMP satellite. *Climate Dynamics*, **31 (1)**, 49–65, doi:10.1007/s00382-007-0337-7.

Forster, P. M., M. Blackburn, R. Glover, and K. P. Shine, 2000: An examination of climate sensitivity for idealised climate change experiments in an intermediate general circulation model. *Climate Dynamics*, **16 (10-11)**, 833–849.

Forster, P. M., G. Bodeker, R. Schofield, S. Solomon, and D. Thompson, 2007: Effects of ozone cooling in the tropical lower stratosphere and upper troposphere. *Geophysical Research Letters*, **34 (23)**, 1–5, doi:10.1029/2007GL031994.

Forster, P. M., R. S. Freckleton, and K. P. Shine, 1997: Climate Dynamics On aspects of the concept of radiative forcing. *Climate Dynamics*, **13**, 547–560.

Forster, P. M. D. F. and K. P. Shine, 1999: Stratospheric water vapour changes as a possible contributor to observed stratospheric cooling. *Geophysical Research Letters*, **26 (21)**, 3309–3312.

Forster, P. M. D. F. and K. P. Shine, 2002: Assessing the climate impact of trends in stratospheric water vapor. *Geophysical Research Letters*, **29 (6)**, 10–1–10–4.

Fortuin, J. P. and U. Langematz, 1994: Update on the global ozone climatology and on concurrent ozone and temperature trends. *Proc. SPIE, Atmospheric Sensing and Modelling*, R. P. Santer, Ed., Vol. 2311, 207–216, doi:10.1117/12.198578.

Fortuin, J. P. F. and H. Kelder, 1998: An ozone climatology based on ozonesonde. *Journal of Geophysical Research*, **103 (D24)**, 31 709–31 734.

Fouquart, Y. and B. Bonnel, 1980: Computations of solar heating of the earths atmosphere: A new parameterization. *Beitr. Phys. Atmos.*, **53**, 35–62.

Fu, Q., 2003: Radiation (solar). *Encyclopedia of Atmospheric Sciences: Potential vorticity*, Holton JR, Curry J A, and P. JA, Eds., London: Academic/Elsevier, Vol. 2, 685–694.

Fueglistaler, S., A. E. Dessler, T. J. Dunkerton, I. Folkins, Q. Fu, and P. W. Mote, 2009a: Tropical tropopause layer. *Reviews of Geophysics*, **47 (1)**, RG1004, doi: 10.1029/2008RG000267.

Fueglistaler, S., P. H. Haynes, and P. M. Forster, 2011: The annual cycle in lower stratospheric temperatures revisited. *Atmospheric Chemistry and Physics*, **11 (8)**, 3701–3711.

Fueglistaler, S., B. Legras, A. Beljaars, and J. Morcrette, 2009b: The diabatic heat budget of the upper troposphere and lower / mid stratosphere in ECMWF reanalyses. *Quarterly Journal of the Royal Meteorological Society*, **135 (638)**, 21–37, doi: 10.1002/qj.

Gall, R., 1976: A Comparison of Linear Baroclinic Instability Theory with the Eddy Statistics of a General Circulation Model. *Journal of the Atmospheric Sciences*, **33 (3)**, 349–373.

Garcia, R. R., 1987: On the Mean Meridional Circulation of the Middle Atmosphere. *Journal of Atmospheric Sciences*, **44 (24)**, 3599–3609.

Garcia, R. R. and W. J. Randel, 2008: Acceleration of the Brewer-Dobson Circulation due to Increases in Greenhouse Gases. *Journal of Atmospheric Sciences*, **65 (8)**, 2731–2739.

Gettelman, A., P. M. Forster, M. Fujiwara, Q. Fu, H. Vomel, L. K. Gohar, C. Johanson, and M. Ammerman, 2004: Radiation balance of the tropical tropopause layer. *Journal of Geophysical Research*, **109 (D07103)**, 1–12.

Gettelman, A., P. Hoor, and L. Pan, 2011: The extratropical upper troposphere and lower stratosphere. *Reviews of Geophysics*, **49**, 1–31.

Gettelman, A., et al., 2010: Multimodel assessment of the upper troposphere and lower stratosphere: Tropics and global trends. *Journal of Geophysical Research*, **115 (D3)**, D00M08, doi:10.1029/2009JD013638.

Goody, R. M. and Y. L. Yung, 1989: *Atmospheric Radiation*. 2d ed., Oxford University Press.

Grise, K. M., D. W. J. Thompson, and T. Birner, 2010: A Global Survey of Static Stability in the Stratosphere and Upper Troposphere. *Journal of Climate*, **23 (9)**, 2275–2292.

Hardiman, S. C., N. Butchart, and N. Calvo, 2014: The morphology of the Brewer-Dobson circulation and its response to climate change in CMIP5 simulations. *Quarterly Journal of the Royal Meteorological Society*, **140 (683)**, 1958–1965.

Hardiman, S. C., et al., 2015: Processes controlling tropical tropopause temperature and stratospheric water vapor in climate models. *Journal of Climate*, **28 (16)**, 6516–6535, doi:10.1175/JCLI-D-15-0075.1.

Harries, J. E., J. M. R. Iii, A. F. Tuck, L. L. Gordley, P. Purcell, K. Stone, R. M. Bevilacqua, and W. A. Traub, 1996: Validation of measurements of water vapour from the Halogen Occulatation Experiment (HALOE). *Journal of Geophysical Research*, **101 (D6)**, 10 205–10 216.

Hartmann, D. L., J. R. Holton, and Q. Fu, 2001: The heat balance of the tropical tropopause, cirrus and stratospheric dehydration. *Geophysical Research Letters*, **28 (10)**, 1969–1972.

Haynes, P., 2005: Stratospheric Dynamics. *Annual Review of Fluid Mechanics*, **37 (1)**, 263–293.

Haynes, P., J. Scinocca, and M. Greenslade, 2001: Formation and maintenance of the extratropical tropopause by baroclinic eddies. *Geophysical Research Letters*, **28 (22)**, 4179.

Haynes, P. H., 1998: The latitudinal structure of the quasi-biennial oscillation. *Quarterly Journal of the Royal Meteorological Society*, **124 (552)**, 2645–2670.

Haynes, P. H., M. E. McIntyre, T. G. Shepherd, C. J. Marks, and K. P. Shine, 1991: On the 'Downward Control' of Extratropical Diabatic Circulations by Eddy-Induced Mean Zonal Forces. *Journal of Atmospheric Sciences*, **48**, 651–680.

Hegglin, M. I., et al., 2008: Validation of ACE-FTS satellite data in the upper troposphere/lower stratosphere (UTLS) using non-coincident measurements. *Atmospheric Chemistry and Physics*, **8 (6)**, 1483–1499, doi:10.5194/acp-8-1483-2008.

Hegglin, M. I., et al., 2010: Multimodel assessment of the upper troposphere and lower stratosphere: Extratropics. *Journal of Geophysical Research*, **115 (D3)**, D00M09.

Held, I. M. and M. J. Suarez, 1994: A Proposal for the Intercomparison of the Dynamical Cores of Atmospheric General Circulation Models. *Bulletin of the American Meteorological Society*, **75**, 1825–1830.

Hitchcock, P., T. G. Shepherd, and S. Yoden, 2010: On the Approximation of Local and Linear Radiative Damping in the Middle Atmosphere. *Journal of the Atmospheric Sciences*, **67 (6)**, 2070–2085.

Ho, S.-p., et al., 2009: Estimating the uncertainty of using GPS radio occultation data for climate monitoring: Intercomparison of CHAMP refractivity climate records from 2002 to 2006 from different data centers. *Journal of Geophysical Research*, **114 (D23107)**, 1–20.

Hoerling, M., T. Schaack, and A. Lenzen, 1991: Global objective tropopause analysis. *Monthly Weather Review;(United States)*, **119**.

Holton, J. R., P. H. Haynes, M. E. Mcintyre, A. R. Douglass, and B. Rood, 1995: Stratosphere-Troposphere. *Reviews of Geophysics*, **33 (4)**, 403–439.

Holton, J. R. and H.-C. Tan, 1980: The Influence of the Equatorial Quasi-Biennial Oscillation on the Global Circulation at 50 mb. *Journal of the Atmospheric Sciences*, **37 (10)**, 2200–2208, doi:10.1175/1520-0469(1980)037⟨2200:TIOTEQ⟩2.0.CO;2.

Hoor, P., C. Gurk, D. Brunner, M. I. Hegglin, H. Wernli, and H. Fischer, 2004: Seasonality and extent of extratropical TST derived from in-situ CO measurements during SPURT. *Atmospheric Chemistry and Physics Discussions*, **4 (2)**, 1691–1726, doi:10.5194/acpd-4-1691-2004.

Hoskins, B. J. and A. J. Simmons, 1975: A multi-layer spectral model and the semi-implicit method. *Quarterly Journal of the Royal Meteorological Society*, **101**, 637–655.

Hoskins, B. J. J., M. E. E. McIntyre, and A. W. W. Robertson, 1985: On the use and significance of isentropic potential vorticity maps. *Quarterly Journal of the Royal Meteorological Society*, **111 (470)**, 877–946.

Joseph Pedlosky, 1987: *Geophysical Fluid Dynamics*. 2d ed., Springer.

Joshi, M. M., A. J. Charlton, and A. a. Scaife, 2006: On the influence of stratospheric water vapor changes on the tropospheric circulation. *Geophysical Research Letters*, **33 (9)**, 2–5, doi:10.1029/2006GL025983.

Kerr-Munslow, A. M. and W. A. Norton, 2006: Tropical Wave Driving of the Annual Cycle in Tropical Tropopause Temperatures. Part I: ECMWF Analyses. *Journal of the Atmospheric Sciences*, **63 (5)**, 1420–1431, doi:10.1175/JAS3698.1.

Konopka, P., J.-U. Grooß, G. Günther, F. Ploeger, R. Pommrich, R. Müller, and N. Livesey, 2010: Annual cycle of ozone at and above the tropical tropopause: observations versus simulations with the Chemical Lagrangian Model of the Stratosphere (CLaMS). *Atmospheric Chemistry and Physics*, **10 (1)**, 121–132, doi:10.5194/acp-10-121-2010.

Kuo, Y.-H., T.-K. Wee, S. Sokolovskiy, C. Rocken, W. Schreiner, D. Hunt, and R. Anthes, 2004: Inversion and Error Estimation of GPS Radio Occultation Data. *Journal of the Meteorological Society of Japan*, **82 (1B)**, 507–531, doi:10.2151/jmsj.2004.507.

Lacis, A. and V. Oinas, 1991: A Description of the Correlated k Distribution Method for Modeling Nongray Gaseous Absorption , Thermal Emission , and Multiple Scattering in Vertically Inhomogeneous Atmospheres. *Journal of Geophysical Research*, **96 (D5)**, 9027–9063.

Lambert, A., et al., 2007: Validation of the Aura Microwave Limb Sounder middle atmosphere water vapor and nitrous oxide measurements. *Journal of Geophysical Research: Atmospheres*, **112 (24)**, 1–24, doi:10.1029/2007JD008724.

Lauritzen, P., C. Jablonowski, M. Taylor, and R. Nair, 2011: *Numerical Techniques for Global Atmospheric Models*, Vol. 80. 1st ed., Springer.

MacKenzie, I. a., 2004: Middle-atmospheric response to a future increase in humidity arising from increased methane abundance. *Journal of Geophysical Research*, **109 (D2)**, 1–18, doi:10.1029/2003JD003590.

Maycock, a. C., M. M. Joshi, K. P. Shine, S. M. Davis, and K. H. Rosenlof, 2014: The potential impact of changes in lower stratospheric water vapour on stratospheric temperatures over the past 30 years. *Quarterly Journal of the Royal Meteorological Society*, **2007**, 2176–2185, doi:10.1002/qj.2287.

Maycock, a. C., K. P. Shine, and M. M. Joshi, 2011: The temperature response to stratospheric water vapour changes. *Quarterly Journal of the Royal Meteorological Society*, **137 (657)**, 1070–1082, doi:10.1002/qj.822.

McIntyre, M. E., 2003: Potential vorticity. *Encyclopedia of Atmospheric Sciences*, H. JR, C. J. A, and P. JA, Eds., London: Academic/Elsevier, Vol. 2, 685–694.

Ming, A., P. Hitchcock, and P. Haynes, 2016a: The Double Peak in Upwelling and Heating in the Tropical Lower Stratosphere. *Journal of the Atmospheric Sciences*, **73 (5)**, 1889–1901, doi:10.1175/JAS-D-15-0293.1.

Ming, A., P. Hitchcock, and P. Haynes, 2016b: The Response of the Lower Stratosphere to Zonally Symmetric Thermal and Mechanical Forcing. *Journal of the Atmospheric Sciences*, **73 (5)**, 1903–1922, doi:10.1175/JAS-D-15-0294.1.

Miyazaki, K., S. Watanabe, Y. Kawatani, K. Sato, Y. Tomikawa, and M. Takahashi, 2010: Transport and Mixing in the Extratropical Tropopause Region in a High-Vertical-Resolution GCM. Part II: Relative Importance of Large-Scale and Small-Scale Dynamics. *Journal of the Atmospheric Sciences*, **67 (5)**, 1315–1336, doi:10.1175/2009JAS3334.1.

Mlawer, E. J., S. J. Taubman, P. D. Brown, M. J. Iacono, and S. A. Clough, 1997: Radiative transfer for inhomogeneous atmospheres: RRTM, a validated correlated-k model for the longwave. *Journal of Geophysical Research: Atmospheres*, **102 (D14)**, 16 663–16 682.

Mlynczak, M. G., C. J. Mertens, R. R. Garcia, and R. W. Portmann, 1999: A detailed evaluation of the stratospheric heat budget: 2. Global radiation balance and diabatic circulations. *Journal of Geophysical Research: Atmospheres*, **104 (D6)**, 6039–6066.

Morcrette, J.-J., 1991: Radiation and cloud radiative properties in the European Centre for Medium Range Weather Forecasts forecasting system. *Journal of Geophysical Research: Atmospheres*, **96 (D5)**, 9121–9132.

Morcrette, J.-J., E. J. Mlawer, M. J. Iacono, and S. A. Clough, 2001: 91. Changes to the Operational Forecasting System. ECMWF Newsletter No 91, 1–15 pp.

Mote, P. W., T. J. Dunkerton, M. E. McIntyre, E. A. Ray, P. H. Haynes, and J. M. I. Russell, 1998: Vertical velocity, vertical diffusion, and dilution by midlatitude air in the tropical lower stratosphere. *Journal of Geophysical Research*, **103 (D8)**, 8651–8666.

Mote, P. W., et al., 1996: An atmospheric tape recorder ' The imprint of tropical tropopause temperatures on stratospheric water vapor s observed phase lag agrees with the phase lag calculated assuming advection by the The phase agreement confirms the overall robustness of the calc. *Journal of Geophysical Research*, **101 (D2)**, 3989–4006.

Orr, A., T. J. Bracegirdle, J. S. Hosking, W. Feng, H. K. Roscoe, and J. D. Haigh, 2013: Strong Dynamical Modulation of the Cooling of the Polar Stratosphere Associated with the Antarctic Ozone Hole. *Journal of Climate*, **26 (2)**, 662–668, doi:10.1175/JCLI-D-12-00480.1.

Pan, L. L., J. C. Wei, D. E. Kinnison, R. R. Garcia, D. J. Wuebbles, and G. P. Brasseur, 2007: A set of diagnostic for evaluating chemistry-climate models in the extratropical tropopause region. *Journal of Geophysical Research Atmospheres*, **112 (9)**, 1–12, doi:10.1029/2006JD007792.

Plumb, R. a., 2002: Stratospheric transport. *Journal of the Meteorological Society of Japan*, **80 (4)**, 793–809, doi:10.2151/jmsj.80.793.

Plumb, R. A. and J. Eluszkiewicz, 1999: The Brewer-Dobson Circulation: Dynamics of the Tropical Upwelling. *Journal of the Atmospheric Sciences*, **56 (6)**, 868–890.

Ramachandran, S., V. Ramaswamy, G. L. Stenchikov, and A. Robock, 2000: Radiative impact of the Mount Pinatubo volcanic eruption: Lower stratospheric response. *Journal of Geophysical Research*, **105 (D19)**, 24 409.

Ramanathan, V. and R. E. Dickinson, 1979: The Role of Stratospheric Ozone in the Zonal and Seasonal Radiative Energy Balance of the Earth-Troposphere System. *Journal of Atmospheric Sciences*, **36**, 1084–1104.

Ramaswamy, V., et al., 2001: Stratospheric temperature trends: Observations and model simulations. *Reviews of Geophysics*, **39 (1)**, 71–122.

Randel, W. J., R. Garcia, and F. Wu, 2008: Dynamical Balances and Tropical Stratospheric Upwelling. *Journal of the Atmospheric Sciences*, **65 (11)**, 3584–3595, doi:10.1175/2008JAS2756.1.

Randel, W. J., R. R. Garcia, and F. Wu, 2002: Time-Dependent Upwelling in the Tropical Lower Stratosphere Estimated from the Zonal-Mean Momentum Budget. *Journal of Atmospheric Sciences*, **59**, 2141–2152.

Randel, W. J. and E. J. Jensen, 2013: Physical processes in the tropical tropopause layer and their roles in a changing climate. *Nature Geoscience*, **6 (3)**, 169–176.

Randel, W. J., M. Park, F. Wu, and N. Livesey, 2007a: A Large Annual Cycle in Ozone above the Tropical Tropopause Linked to the Brewer-Dobson Circulation. *Journal of the Atmospheric Sciences*, **64 (12)**, 4479–4488.

Randel, W. J., F. Wu, and P. Forster, 2007b: The Extratropical Tropopause Inversion Layer: Global Observations with GPS Data, and a Radiative Forcing Mechanism. *Journal of Atmospheric Sciences*, **64**, 4489–4496.

Randel, W. J., F. Wu, A. Gettelman, J. M. Russell, J. M. Zawodny, and S. J. Oltmans, 2001: Seasonal variation of water vapor in the lower stratosphere observed in Halogen Occultation Experiment data. *Journal of Geophysical Research*, **106 (D13)**, 14 313, doi:10.1029/2001JD900048.

Reed, R. J. and C. L. Vicek, 1969: The Annual Temperature Variation in the Lower Tropical Stratosphere. *Journal of Atmospheric Sciences*, **26**, 163–167.

Reid, G. C. and K. S. Gage, 1981: On the Annual Variation in Height of the Tropical Tropopause. *Journal of the Atmospheric Sciences*, **38 (9)**, 1928–1938.

Rind, D. and P. Lonergan, 1995: Modeled impacts of stratospheric ozone and water vapour perturbations with implications for high-speed civil and transport aircraft. *Journal of Geophysical Research*, **100 (D4)**, 7381–7396.

Rosenlof, K. H., A. F. Tuck, K. K. Kelly, J. M. Russell, and M. P. McCormick, 1997: Hemispheric asymmetries in water vapor and inferences about transport in the lower stratosphere. *Journal of Geophysical Research*, **102 (D11)**, 13 213–13 234, doi:10.1029/97JD00873.

Schmidt, T., J.-P. Cammas, H. G. J. Smit, S. Heise, J. Wickert, and A. Haser, 2010: Observational characteristics of the tropopause inversion layer derived from CHAMP/GRACE radio occultations and MOZAIC aircraft data. *Journal of Geophysical Research*, **115 (D24)**.

Scott, R. K., 2002: Wave-Driven Mean Tropical Upwelling in the Lower Stratosphere. *Journal of the Atmospheric Sciences*, **59 (18)**, 2745–2759.

Seviour, W. J. M., N. Butchart, and S. C. Hardiman, 2012: The Brewer-Dobson circulation inferred from ERA-Interim. *Quarterly Journal of the Royal Meteorological Society*, **138 (665)**, 878–888.

Shepherd, T. G., 2007: Transport in the Middle Atmosphere. *Journal of the Meteorological Society of Japan*, **85B**, 165–191.

Shepherd, T. G. and C. McLandress, 2010: A Robust Mechanism for Strengthening of the Brewer-Dobson Circulation in Response to Climate Change : Critical-Layer Control of Subtropical Wave Breaking. *Journal of Atmospheric Sciences*, **68**, 784–797.

Shepherd, T. G. and C. McLandress, 2011: A Robust Mechanism for Strengthening of the Brewer-Dobson Circulation in Response to Climate Change : Critical-Layer Control of Subtropical Wave Breaking. *Journal of Atmospheric Sciences*, **68**, 784–797, doi:10.1175/2010JAS3608.1.

Sigmond, M. and T. G. Shepherd, 2014: Compensation between resolved wave driving and parameterized orographic gravity wave driving of the Brewer-Dobson circulation and its response to climate change. *Journal of Climate*, **27 (14)**, 5601–5610, doi: 10.1175/JCLI-D-13-00644.1.

Solomon, S., K. H. Rosenlof, R. W. Portmann, J. S. Daniel, S. M. Davis, T. J. Sanford, and G.-K. Plattner, 2010: Contributions of stratospheric water vapor to decadal changes in the rate of global warming. *Science (New York, N.Y.)*, **327 (5970)**, 1219–1223, doi:10.1126/science.1182488.

Son, S.-W. and L. M. Polvani, 2007: Dynamical formation of an extra-tropical tropopause inversion layer in a relatively simple general circulation model. *Geophysical Research Letters*, **34**.

Stolarski, R. S., D. W. Waugh, L. Wang, L. D. Oman, A. R. Douglass, and P. A. Newman, 2014: Seasonal variation of ozone in the tropical lower stratosphere: Southern tropics are different from northern tropics. *Journal of Geophysical Research: Atmospheres*, **119 (10)**, 6196–6206.

Uppala, S. M., et al., 2005: The ERA-40 re-analysis. *Quarterly Journal of the Royal Meteorological Society*, **131 (612)**, 2961–3012.

Vallis, G. K., 2006: *Atmospheric and Ocean Fluid Dynamics*. Cambridge University Press, 24–25 pp.

von Storch, H. and F. W. Zwiers, 2001: *Statistical Analysis in Climate Research*. Cambridge University Press, 111–116 pp.

Watson, P. a. G. and L. J. Gray, 2015: The stratospheric wintertime response to applied extratropical torques and its relationship with the annular mode. *Climate Dynamics*, 1–60, doi:10.1007/s00382-014-2359-2.

Wirth, V., 2003: Static Stability in the Extratropical Tropopause Region. *Journal of the Atmospheric Sciences*, **60 (11)**, 1395–1409.

WMO, 1957: Meteorology–A three-dimensional science. *WMO Bull. 6 (Oct)*, 134—-138.

Wright, J. S. and S. Fueglistaler, 2013: Large differences in reanalyses of diabatic heating in the tropical upper troposphere and lower stratosphere. *Atmospheric Chemistry and Physics*, **13 (18)**, 9565–9576.

Young, P. J., D. W. J. Thompson, K. H. Rosenlof, S. Solomon, and J. F. Lamarque, 2011: The seasonal cycle and interannual variability in stratospheric temperatures and links to the Brewer-Dobson circulation: An analysis of MSU and SSU data. *Journal of Climate*, **24 (23)**, 6243–6258.

Yulaeva, E., J. R. Holton, and J. M. Wallace, 1994: On the cause of the annual cycle in tropical lower-stratospheric temperatures. *Journal of the Atmospheric Sciences*, **51 (2)**, 169–174.

Zhong, W. and J. D. Haigh, 1995: Improved Broadband Emissivity Parameterization for Water Vapor Cooling Rate Calculations. *Journal of Atmospheric Sciences*, **52 (1)**, 124–138.

Zwiers, F. W. and H. von Storch, 1995: Taking serial correlation into account in tests of the mean. *Journal of Climate*, **8**, 336–351.